



HAL
open science

Light Up–conversion in Rare Earth doped Thin Films. Synthesis, Characterization, Luminescence and Prospects for Solar Cell Application

Elisabeth L. Payrer

► **To cite this version:**

Elisabeth L. Payrer. Light Up–conversion in Rare Earth doped Thin Films. Synthesis, Characterization, Luminescence and Prospects for Solar Cell Application. Material chemistry. Université de Grenoble; Instituto Superior Tecnico de Lisboa, 2014. English. NNT: . tel-01122208

HAL Id: tel-01122208

<https://theses.hal.science/tel-01122208>

Submitted on 4 Mar 2015

HAL is a multi-disciplinary open access archive for the deposit and dissemination of scientific research documents, whether they are published or not. The documents may come from teaching and research institutions in France or abroad, or from public or private research centers.

L'archive ouverte pluridisciplinaire **HAL**, est destinée au dépôt et à la diffusion de documents scientifiques de niveau recherche, publiés ou non, émanant des établissements d'enseignement et de recherche français ou étrangers, des laboratoires publics ou privés.

THESE

Pour obtenir le grade de

DOCTEUR DE L'UNIVERSITÉ DE GRENOBLE

**préparée dans le cadre d'une cotutelle entre
l'Université de Grenoble et Instituto Superior
Técnico**

Spécialité : **Matériaux, Mécanique, Génie Civil, Electrochimie**

Arrêté ministériel : 6 janvier 2005 – 7 aout 2006

Présentée par

Elisabeth L. Payrer

These dirigée par **Jean-Luc Deschanvres**
et codirigée par **Rui M. Almeida**

préparée au sein des **Laboratoire des Matériaux et du Génie Physi-
que, Grenoble INP et Departamento de Engenharia Química/ ICEMS,
IST Lisbon**
dans les Écoles Doctorales **I-MEP-2 et Engenharia de Materiais**

Light Up–conversion in Rare Earth doped Thin Films

**Synthesis, Characterization, Luminescence
and Prospects for Solar Cell Application**

These soutenue publiquement le **12.02.2014**,
devant le jury composé de :

Monsieur Daniel Bellet

Professeur, LMGP, Grenoble INP, Président

Monsieur Bernard Moine

Directeur de recherche CNRS, LPCML, UCBL, Rapporteur

Monsieur Constantin Vahlas

Directeur de recherche CNRS, CIRIMAT–ENSIACET, Rapporteur

Monsieur Jorge Manuel Morgado

Professeur, Departamento de Bioengenharia, IST Lisbon, Examineur

Monsieur Jean-Luc Deschanvres

Chargé de recherche CNRS, LMGP, Grenoble INP, Directeur de these

Monsieur Rui M. Almeida

Professeur, Departamento de Engenharia Química/ ICEMS, IST Lisbon, Co-
Directeur de these



Abstract

Photon up-conversion (UpC) allows the generation of light of shorter wavelengths compared to the excitation wavelength. In this work the synthesis of thin films doped with optically active rare earth (RE^{3+}) ions, their structural characterization, as well the optical and photoluminescence properties are highlighted. The emphasis lies on two different routes of film deposition on silicon and transparent substrates: first, metalorganic chemical vapor deposition (LI-MOCVD, AA-MOCVD) is introduced for the deposition of Er/Yb-doped YF_3 and Y_2O_3 films and it is demonstrated, how the UpC emission of Er^{3+} upon 972 nm excitation is influenced by the host lattice. Secondly, sol-gel processing, a wet-chemical technique, is used for the fabrication of Er/Yb-doped Y_2O_3 , SiO_2 and TiO_2 thin films by spin-coating. Optimization of the up-converted light emission was achieved through adjusting the RE concentration and the processing temperature. Moreover, in a different approach for achieving an enhanced UpC emission, sol-gel derived Fabry-Pérot dielectric microcavities, consisting of a multilayer stack of silica and titania layers and Er/Yb: Y_2O_3 as the cavity layer, are investigated. The aim of this work is to address the questions, how does the nature of the host lattice and doping level influence the radiative emission in Er^{3+} , what are the requirements for a good upconverter material and what are the limitations? We also include a discussion of the application of an upconverter to a solar cell device, which may debatably enhance the response in the infrared.

Keywords: Up-conversion, rare earths, thin films, YF_3 , oxides, Y_2O_3 , MOCVD, sol-gel, Fabry-Pérot microcavities

Résumé

Le phénomène d'up-conversion de photon (UpC) permet de générer de la lumière à longueurs d'onde plus courtes que la longueur d'onde d'excitation. Dans cette recherche, la synthèse de couches minces dopées avec des ions de terres rares (RE^{3+}) optiquement actifs, leurs caractérisations structurales, ainsi que leurs propriétés optiques et de photoluminescentes ont été étudiées. Les couches ont été élaborées par deux voies de dépôt de couche sur du silicium et des substrats transparents : tout d'abord, un dépôt chimique organométallique en phase vapeur (LI-MOCVD, AA-MOCVD) est utilisé pour le dépôt des couches minces de YF_3 et Y_2O_3 co-dopées Er/Yb. Il est démontré que l'émission d'UpC de Er^{3+} avec une excitation à 972 nm est influencée par le réseau hôte. Par ailleurs, le traitement sol-gel, une technique chimique par voie humide, est utilisé pour la fabrication de couches minces Y_2O_3 , SiO_2 et TiO_2 co-dopées Er/Yb par spin-coating. Une optimisation de l'émission de lumière par UpC a été atteinte grâce à l'ajustement de la concentration de RE et de la température de traitement thermique. De plus, une approche différente a été étudiée pour atteindre une émission UpC renforcée : l'utilisation de microcavités diélectriques de Fabry-Pérot obtenues par sol-gel, constitués d'un empilement de couches de silice et d'oxyde de titane, avec Er/Yb : Y_2O_3 comme couche de cavité. Le but de ce travail est de répondre aux questions suivantes : comment la nature du réseau hôte et le niveau de dopage influencent l'émission radiative de l' Er^{3+} ? Quelles sont les conditions pour un bon matériau d'UpC et ses limites ? Nous incluons également une discussion sur les perspectives d'une application possible d'une couche d'UpC dans un dispositif de cellule solaire, qui pourrait améliorer la réponse dans l'infrarouge.

Mots-clefs : Up-conversion, terres rares, couche mince, YF_3 , oxydes, Y_2O_3 , MOCVD, sol-gel, microcavités de Fabry-Pérot

Resumo

A up-conversion (UpC) permite a produção de luz de comprimentos de onda menores do que os de excitação. Neste trabalho realça-se a síntese de filmes finos dopados com iões de terras raras opticamente activos (RE^{3+}), a sua caracterização estrutural, assim como as suas propriedades ópticas e de fotoluminescência. O ênfase reside em duas formas diferentes de deposição do filme em substratos de silício e substratos transparentes: primeiro, deposição de vapor metalorgânico químico é (MOCVD) introduzido para a deposição de filmes de Er/Yb-dopado YF_3 e Y_2O_3 e é demonstrado, como a emissão UpC de Er^{3+} até à excitação de 972 nm é influenciada pela rede do hospedeiro. Segundo, o processamento sol-gel, uma técnica de química húmida, é utilizada para a fabricação de filme finos de Er/Yb-dopado Y_2O_3 , SiO_2 e TiO_2 por spin-coating. Uma optimização da luz emitida por UpC foi conseguida através do ajuste da concentração de RE e da temperatura de processamento. Para além disso, numa aproximação diferente para conseguir uma emissão UpC melhorada, microcavidades dieléctricas de Fabry-Pérot derivadas de sol-gel, consistindo de um empilhamento multicamadas com camadas de sílica e titânia e Er/Yb: Y_2O_3 como camada da cavidade, são investigadas. O objectivo deste trabalho é responder à questão, como a natureza da rede do hospedeiro e o nível de dopagem influencia a emissão radiactiva em Er^{3+} , quais os requisitos para um bom material conversor e quais as suas limitações. Também incluímos uma discussão sobre perspectivas de uma aplicação discutível de um conversor para uma célula solar, que pode aumentar a resposta desta no infravermelho.

Palavras-chave: Up-conversion, terras raras, filmes finos, YF_3 , óxidos, Y_2O_3 , MOCVD, sol-gel, microcavidades de Fabry-Pérot

Acknowledgments

I want to express my gratitude to my two supervisors, Prof. Rui M. Almeida and Dr. Jean-Luc Deschanvres, for their guidance throughout the thesis. Jean-Luc, I want to thank you especially, for giving me the opportunity and financial support to take part in international conferences.

Furthermore, I thank all my colleagues at LMGP Grenoble: especially Dan, for your motivation, science discussions and proof-reading of the thesis; Pierre-David, for your assistance in SEM and your joyful way to do science; Carmen, for your work efforts, as well as giving me lots of helpful advice.

Martin, ich danke dir für deinen unermühtlichen Einsatz bei Problemen aller Art, einschliesslich der AFM Messungen und vor allem die zahlreichen Kaffeepausen, und dass du immer ein geduldiger Zuhörer warst. Birgit und du, haben dazu beigetragen, dass Grenoble immer ein besonderer Ort für mich sein wird.

Carole and Ana, we have become great friends during my stay in Lisbon and I will always carry the memories in my heart. Yigang, Luís Fortes and Luís Santos, I want to thank you for always taking the time for discussions and giving me assistance in technical matters – muito obrigado. Florian, danke, dass du für mich da bist und für deine Unterstützung.

This project was part of the “ERASMUS MUNDUS II 2009–2013” IDS-FunMat programme (project n° 2010–11).

Ich lerne, weil ich das Leben liebe - I do science, because I love life

Table of Contents

Acknowledgments	vii
Executive summary	1
1 Introduction and theoretical background	5
1.1 High efficiency solar cells	7
1.2 Materials for light up-conversion	10
1.2.1 Upconverters based on rare earth ions	12
1.2.2 Upconverters based on transition metal ions	17
1.2.3 Efficiency improvement using 1D-PBG structures	18
1.3 Theoretical description of UpC processes	20
1.3.1 Energy transfer: Dexter's and Förster's theories	24
1.4 Thin film deposition techniques	28
1.4.1 Chemical vapor deposition	28
1.4.2 Sol-gel processing	33
2 RE³⁺-doped YF₃ thin films by LI-MOCVD	39
2.1 Introduction	41
2.2 Experimental details	42
2.3 Film deposition	42
2.4 Investigation of the film microstructure and composition	44
2.5 Optical performance and Raman spectra of Er/Yb:YF ₃ films	51
2.6 Summary	54
3 Three-photon UpC of RE³⁺-doped YF₃ thin films	55
3.1 Introduction	57
3.2 Experimental details	58
3.3 Results and discussion	59
3.3.1 Stokes luminescence of Er/Yb-doped YF ₃ thin films	59
3.3.2 Anti-Stokes (UpC) luminescence spectra of Er/Yb-doped YF ₃ thin films	62

3.4	Lifetimes of Er: ⁴ S _{3/2} and ⁴ F _{9/2} states	67
3.4.1	Power dependence studies of Er/Yb:YF ₃	69
3.5	Summary	73
4	RE³⁺-doped Y₂O₃ thin films grown by AA-MOCVD	75
4.1	Experimental	77
4.2	Quantitative element analysis: EPMA results	78
4.3	Structural characterization of Er/Yb:Y ₂ O ₃ thin films	79
4.3.1	Spectroscopic characterization: FTIR and Raman studies	81
4.4	Luminescence spectra of Er/Yb:Y ₂ O ₃ films deposited by AA-MOCVD	85
4.4.1	Up-conversion after 972 nm excitation	86
4.5	Lifetimes of Er: ⁴ I _{13/2} and Yb: ² F _{5/2} states in Er/Yb:Y ₂ O ₃ films deposited by AA-MOCVD	90
4.6	Summary	92
5	RE³⁺-doped Y₂O₃ thin films grown by LI-MOCVD	95
5.1	Introduction	97
5.2	Film deposition	97
5.3	Film microstructure	99
5.3.1	Dispersion of refractive index and Raman spectra of Er/Yb:Y ₂ O ₃ films	103
5.4	Three-photon UpC emission and power dependence study on Er/Yb:Y ₂ O ₃ thin films	105
5.4.1	Lifetimes of Er: ⁴ S _{3/2} and ⁴ F _{9/2} states in Er/Yb:Y ₂ O ₃ films	109
5.5	Summary	111
6	Light UpC in RE³⁺-doped Y₂O₃, SiO₂ and TiO₂ thin films by the sol-gel method	113
6.1	Sol-gel processing	115
6.2	Results: Y ₂ O ₃	116
6.2.1	Structural characterization	116
6.2.2	Optical properties of Er/Yb:Y ₂ O ₃ films	120
6.2.3	Light UpC of Er/Yb-doped yttria sol-gel films at 972 nm	121
6.3	Results: Aluminosilicate glass	124
6.3.1	Structural characterization	124
6.3.2	Light UpC of Er/Yb-doped silicate sol-gel films at 972 nm	126
6.4	Results: TiO ₂	128
6.4.1	Structural characterization	128
6.4.2	Light UpC of Er/Yb-doped titania sol-gel films at 972 nm	130
6.5	Summary	132
7	1D-Photonic bandgap structures: Fabry-Pérot microcavities	133
7.1	Introduction	135
7.2	Methods and characterization	136
7.2.1	F-P microcavities	136
7.2.2	Characterization	137

7.3	Results	138
7.3.1	Reflectance spectra and UpC emission at 972 nm excitation	138
7.4	Summary and Outlook	144
	Application of an upconverter to a solar cell device	147
8	General conclusions and outlook	151
	References	155
	Appendix	169
	List of abbreviations	169
	Résumé	170

Executive summary

Light up-conversion (UpC) has been widely investigated for its use in biomedical applications, luminescent materials, lasers and solar cell devices. The development of efficient upconverters is one of the main goals with regard to potential applications in photovoltaics. In this thesis we investigate the design of lanthanide-based thin film upconverters and therefore, the factors that influence the UpC luminescence, such as the nature of the host lattice into which the rare earth ions are embedded, and the microstructure-luminescence relationship.

The main questions addressed in this thesis are: 1.) the evaluation of what kind of materials possess a good light UpC performance 2.) the importance of film deposition technique and 3.) whether it is reasonable to apply an upconverter layer to a solar cell device.

In the first part of the thesis we focus on the film deposition by metalorganic chemical vapor deposition, using liquid source precursors. Chapter 2 unveils the influence of the processing parameters on the microstructure of Er/Yb-doped YF_3 thin films, grown onto Si(111) substrates by LI-MOCVD. A lot of effort has been devoted to the optimization of the deposition parameters in order to obtain films of good optical and mechanical properties. The deposition temperature, the total gas flux and oxygen partial pressure were determined to be the most crucial factors influencing crystallinity and film adherence to the substrate. The characterization of the microstructure was performed by SEM and AFM, judging the influence of the processing parameters. Vibrational spectroscopies including Micro-Raman and FTIR techniques, allowed confirmation of the formation of polycrystalline, orthorhombic YF_3 .

The luminescent properties of Er/Yb: YF_3 films are described in Chapter 3. The spectroscopic characterization involved the analysis of the Stokes luminescence as well as the anti-Stokes emission, when excited at 972 nm. In the latter case, a strong green, a weaker red and violet up-converted emission was observed; therefore, we give an extensive description of the most probably excitation pathways leading to the up-converted emission in Er^{3+} . Measurements of the temporal evolution of the luminescence of the green and red light emitting levels in Er^{3+} showed

a dependence on the Yb concentration, and supported the idea that an Er-to-Yb energy back transfer could be responsible for the luminescence quenching at high Yb concentrations. For a better understanding of the population mechanisms of the excited states in Er^{3+} , power dependence studies were performed. The chapter concludes with a detailed description of the rate equations used in modeling the power dependence of the emission intensity.

Chapter 4 introduces another variant of MOCVD used for the deposition of Er/Yb-doped Y_2O_3 films on Si(100) wafers, namely the aerosol-assisted MOCVD. This method allows for a film deposition at atmospheric pressure using a rather simple experimental set-up and, therefore, film fabrication at low cost. A detailed study of the film microstructure and composition was performed, using XRD, SEM, AFM and EPMA. Spectroscopic properties were measured using ellipsometry, Raman and FTIR spectroscopies. Although deposition rates of ~ 500 nm/h can be achieved with this technique, the as-deposited films contain organic contamination attributed to the acetylacetonate precursors needed in the deposition; therefore, high post-deposition annealing temperatures are used to reduce multiphonon relaxation caused by organic residues, improving the luminescence properties. Under the conditions of thermal annealing, cracks are formed in the film microstructure, which can hardly be avoided due to film shrinkage and the difference between the CLTE of the substrate and the film. Among the Er/Yb: Y_2O_3 films fabricated by AA-MOCVD, only the annealed samples showed up-converted emission in the violet, green and red wavelength region. A study of the lifetimes of $\text{Er}^{4\text{I}}_{13/2}$ and $\text{Yb}^{2\text{F}}_{5/2}$ states, allowed an estimate of the energy transfer quantum yield between Yb and Er.

In Chapter 5, the synthesis of Er/Yb-doped Y_2O_3 films by LI-MOCVD and the evolution of their microstructure and the dependence of the UpC emission on the post-deposition annealing temperature are presented. The annealing of the samples in air, at two different temperatures, showed the total UpC emission to be enhanced by a factor 6, in comparison to the as-deposited film. This emphasizes the importance of thermal annealing as a tool to eliminate impurities, which act as luminescence quenchers and to reduce lattice defects due to the increasing grain size. The evolution of the $\text{Er}^{4\text{S}}_{3/2}$ and $\text{Er}^{4\text{F}}_{9/2}$ lifetimes in Er/Yb: Y_2O_3 with increasing annealing temperature, confirmed the relationship of microstructure and spectroscopic properties.

The second part of the thesis describes a different synthetic approach for oxide-based film deposition, namely the sol-gel processing. To date, this wet-chemical procedure has proven to be successful in the fabrication of many different materials, including glasses, powders, fibers and coatings. We deposited Er/Yb-doped Y_2O_3 , SiO_2 and TiO_2 thin films by spin-coating of sol-gels onto Si wafers, and characterized their emission properties as a function of the processing conditions. Chapter 6 concentrates on the description of the synthetic routes of Er/Yb-doped Y_2O_3 , SiO_2 and TiO_2 films, their microstructure and related UpC performance. Chapter 7 deals with the fabrication of Fabry-Pérot dielectric microcavities by sol-gel processing. These consist of an Er/Yb: Y_2O_3 cavity layer inserted between two Bragg mirrors consisting of alternating $\text{SiO}_2/\text{TiO}_2$ layers. We studied

the modifications of the NIR-to-Vis up-converted luminescence in Er/Yb:Y₂O₃, when placed between two Bragg mirrors, compared to the emission properties outside the cavity structure. An enhancement in intensity was measured only for the green emission due to the position of the resonance peak. And again, a gain in the total emission intensity was determined for samples annealed at 1050 °C, compared to a baking temperature of 900 °C. This confirms the importance of a thermal treatment after the final coating cycle; first, to eliminate particularly functional groups of high-energy quanta, such as OH, and secondly, to increase the grain size.

The present work is concluded with a short essay dealing with the challenges and prospects of an upconverter-solar cell device, and addresses the limitations of light UpC used for enhancing the infrared response of a solar cell.

Introduction and theoretical background

This chapter deals with the motivation behind the present work and summarizes in a quite compact manner the concepts of light up-conversion and the materials involved. In the beginning of the chapter, the limitations in the efficiency of solar cells are briefly discussed and up-conversion systems are introduced as an emerging concept for increasing the efficiency of solar cells. Furthermore, some attention is given to the physical description of light up-conversion, especially to the theories of Förster and Dexter, which are the foundation of energy transfer processes. To conclude this chapter, the two main routes of thin film deposition used in this thesis are introduced: first, film growth by chemical vapor deposition (CVD), which found implementation in the fabrication of Y_2O_3 and YF_3 -derived host lattices, and further – to conclude this chapter – the sol-gel processing, used for the deposition of oxide-based host lattices.

1.1 High efficiency solar cells

The solar technology is a remarkable growing industry achieving a global capacity just over 100 GW in 2012, as shown in Fig. 1.1, an amount sufficient to cover more than 30 million European households [1]. The competitiveness of photovoltaics (PV), PV, is in general due to the increasing energy prices and partly due to the state subsidies of PV for urban–residential use. An increasing amount of effort and resources is focused on the quest for sustainable energy sources, since the main resources of energy supply still depend on fossil fuels such as coal, crude oil and natural gas. Since the predictions about the end of the hydrocarbon era estimate that crude oil might last 30 years more and that the coal reserves will last another 100 years, worldwide research has evolved that aims to find sustainable forms of energy [2]. The solar cell technology is one possibility, allowing a getting–off from fossil fuels, which release huge quantities of CO₂ into the atmosphere and thereby assists the greenhouse effect. Therefore, the concept of using the energy from the sun by converting it into an accessible energy form, has a huge potential.

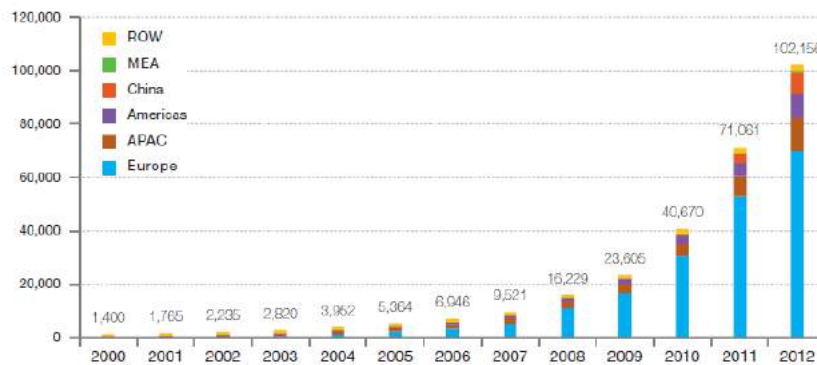


Figure 1.1: Global PV capacity in [MW]; ROW: rest of the world, MEA: middle east and africa, APAC: asia pacific. Adapted and slightly modified from [1].

The solar cell market is presently still dominated by silicon wafer technology, due to its excellent inherent properties. Its large abundance in the earth crust, as well as its non–toxicity, self–passivation, appropriate band gap energy and ease of doping, led it to be the most studied semiconductor material and hence to its predominance in the solar cell market [3]. However, a lot of effort has been done to replace the Si wafer–based *first generation* solar cells by the *second generation* thin film technology in order to reduce the costs of the starting materials. The costs of the starting materials and encapsulants of a mature technology seem to be the most critical factor for the overall process costs. Thin film manufacturing allows one to reduce the material costs and to achieve a higher production throughput compared to first generation solar cells. The most promising candidates include polycrystalline and amorphous silicon, cadmium sulphide, copper indium diselenide and cadmium telluride [4]. However, for developing a solar cell technology into a truly competitive alternative to other energy sources, a reduction in costs has to be achieved. The costs (\approx US–\$ 30/m²) determine – together with the efficiency (e. g. 15 %/m² or 150 W/m²) – the lower limit on solar cell module

costs (US-\$ 0.2/W) and the electricity generation costs [5]. Since the costs are predominantly controlled by the materials used, the only way to progress further is through an increase in the solar cell efficiency.

The *third generation* devices consolidate the benefits of the first and second generation, achieving high efficiency, low cost solar cells. Seven different approaches are considered for the 3rd generation [5, 6]:

1. Tandem or multicolor cells
2. Dye sensitized solar cells, DSSCs
3. Multiple carrier excitation
4. Hot carrier cells
5. Intermediate band and impurity photovoltaic cells
6. Thermophotovoltaic and thermophotonic devices
7. **Modulation of the solar spectrum: Light down- and up-conversion**

All these concepts are considered for the third generation solar cells, where the efficiencies achieved are getting closer to the maximum thermodynamic efficiency of 93 %, which is the theoretical maximum for energy conversion of sun light into useful energy [7]. To approach the thermodynamic limit, a stacking of multiple solar cell materials with varying E_g matching the polychromatic solar spectrum, so-termed tandem cells, is considered as a possible route. In Table 1.1, selected examples of solar cell efficiencies presently reached are summarized. As can be seen, the efficiencies achieved reside in the 10–20 % range, with exceptions for the high-efficiency tandem solar cells.

In comparison, the Shockley–Queisser (SQ) limit sets the upper efficiency limit for a p–n junction to 30 % at 300 K (at 5800 K black body radiation) for an energy gap E_g of 1.1 eV [9]. This efficiency limit is obtained by considering two intrinsic loss mechanisms which decrease the efficiency in real solar cells: first, that the discrete band structure of a semiconductor does not properly match the width of the solar spectrum and that secondly, losses through radiative recombination occur. Other extrinsic and intrinsic loss mechanisms responsible for lowering the efficiency are summarized in Table 1.2.

An incomplete charge carrier collection and radiative carrier recombination occur at the defects within the material microstructure, at interfaces and grain boundaries, and can hardly be avoided. Thermalization is a process where high energy photons ($h \cdot \nu > E_g$) generate an electron–hole pair, and the excess energy is dissipated as heat, while the electron relaxes to the conduction band edge and the hole to the valence band edge, respectively. Transmission is another type of loss mechanism and concerns the non-absorption of the incident photons coming from the sun, which are of energy lower than the band gap of the solar cell material. Depending on the E_g , a part of the solar spectrum is not accessible to the cell and hence does not add to its photocurrent. In the case of c-Si solar cells, the

Table 1.1: Selected terrestrial cell and module efficiencies, respectively, under AM1.5 solar spectrum (1000 W/m^2) at 25°C ; an excerpt from [8].

Cell type	Efficiency %	Concentrator cell efficiency %
Si technology		
Si (crystalline)	25 ± 0.5	27.6 ± 1.0
Si (multicrystalline)	20.4 ± 0.5	
Si (thin film polycrystalline submodule)	10.5 ± 0.3	
III–IV cells		
GaAs (thin film)	28.8 ± 0.9	
GaAs (multicrystalline)	18.4 ± 0.5	29.1 ± 1.3
Thin film chalcogenides		
CIGS (cell)	19.6 ± 0.6	
CIGS (submodule)	17.4 ± 0.5	
CdTe (cell)	18.3 ± 0.5	
Amorphous–nanocrystalline Si		
amorphous Si	10.1 ± 0.3	
nanocrystalline Si	10.1 ± 0.2	
Dye sensitized SC	11.9 ± 0.4	
Organic thin film	10.7 ± 0.3	
Multijunction technology (tandem SC)		
InGaP/GaAs/InGaAs	37.7 ± 1.2	43.5 ± 2.6
a-Si/nc-Si (thin film cell)	12.3 ± 0.3	
a-Si/nc-Si (thin film submodule)	11.7 ± 0.4	

Table 1.2: Intrinsic and extrinsic loss mechanisms in real solar cells [10].

Loss mechanism	
Extrinsic	Intrinsic
Light reflection	Incomplete charge carrier collection
Contact shadowing	Radiative recombination
Series resistance	Thermalization, $h \cdot \nu > E_g$
-	Transmission, $h \cdot \nu < E_g$

transmission loss accounts for about 20% of the incident solar energy.

One of the 3rd generation concepts listed above differs significantly from the others: the purpose of photon conversion aiming to modify the solar spectrum with the objective to match the absorption of the cell material. In contrast to the other concepts, light conversion devices can be treated and optimized as an optical process, separately from the cell [11]. There are three conversion processes of interest including the down–shifting, the down–conversion and the up–conversion (UpC) of photons as illustrated in Fig. 1.2.

Photon down–shifting and down–conversion are the two processes that can be utilized to reduce losses through thermalization. On the other hand, light UpC has the potential to increase the overall efficiency by dealing with the transmission losses by up–converting IR photons into photons of higher energy. By these means, sub–band gap photons become accessible to the solar cell and an increase in its efficiency can be expected. In this thesis, we are dealing in more detail with the

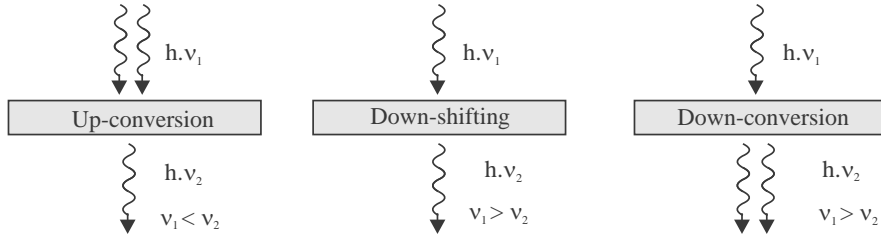


Figure 1.2: Concepts of light conversion, from the left to the right: photon up-conversion, down-shifting and photon down-conversion.

concept of using light UpC, converting low energy photons to a higher energy range. The upper limit for the conversion efficiency of a single-junction solar cell combined with an upconverter was estimated by Trupke *et al.* [12]. The maximum efficiency was determined at 63.2% for a semiconductor with an E_g of 1.955 eV, considering the minimum emission case (i.e. the solid angle of the emission of the system equals the solid angle of the solar disk). In the case of light concentration, the efficiency limit decreases to 61.4% ($E_g = 1.86$ eV) and for a system with no restrictions in the solid angle and non-concentrated light, the upper limit of efficiency was found to be 47.6% (for $E_g = 2$ eV). One can understand that the UpC efficiency is dependent on the semiconductor (SC) energy band gap and the zenith angle of the sun, hence the air mass coefficient AM of the incident solar radiation. UpC systems could be a good option for achieving an efficiency improvement, especially in case the energy band gap is > 1.25 eV and sub-band gap losses are dominant [11]. Band gaps < 1.25 eV have larger thermalization losses, hence down-conversion would be suitable.

1.2 Materials for light up-conversion

UpC as a physical phenomenon was described as early as 1959 by Bloembergen, who proposed a visual detection of infrared radiation by certain ions in a solid [13]. It is a physical process where two or more low energy photons are converted into one high energy photon. Transition group ions and rare earth ions embedded as impurities (dopants) in host lattices have the ability to perform light UpC due to the richness of their energy level structure. In general, the UpC material (upconverter) is able to absorb photons via ground state absorption (GSA), followed by the generation of a higher excited state via excited state absorption (ESA) or energy transfer (ETU, energy transfer UpC), from where subsequent emission takes place. Since the first UpC process based on ETU was reported, a large number of suitable inorganic materials in the solid state, including crystals and glasses in bulk, nanoparticles and thin films, has been described in the literature [14]. The technological interests for using UpC processes include laser materials [15, 16], waveguide amplifiers [17], displays [18], data storage [19], IR radiation detection [20] and medical applications [21]. Furthermore, UpC materials offer an emerging technology for their use in photovoltaics. In principle, an UpC material must have its excitation range towards longer wavelength relative to the band gap of the solar cell material and, furthermore, allow for an emission

slightly above the band gap, where the cell has ideally its maximum response. Wide band gap solar cells such as GaAs, a-Si, dye sensitized (DSSC) and organic solar cells have their absorption limit at ≈ 900 nm, and would benefit from implementing an UpC layer in their device structure, since transmission losses are dominant [22]. Typically, UpC phosphors are dispersed into a transparent adhesive medium, which has a matching refractive index to minimize scattering effects, and are attached to the back side of the cell. The first report of using an UpC layer on the rear side of a bifacial GaAs cell, was made by Gibart *et al.* in 1996 [23]. An efficiency increase of 2.5 % was achieved by a 100 μm thick glass ceramic doped with Er^{3+} and Yb^{3+} , at 1.391 eV laser excitation ($P = 1$ W, see Fig. 1.3).

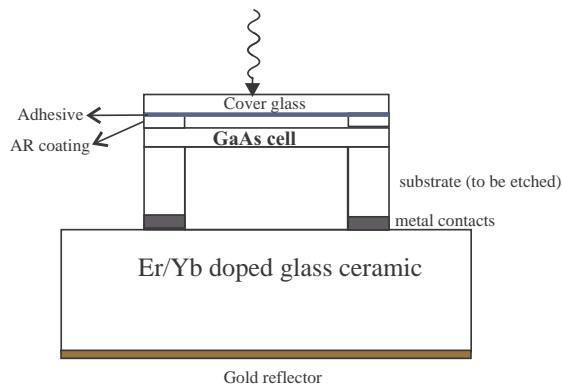


Figure 1.3: Schematic diagram of an Er/Yb-doped glass ceramic as an UpC layer, attached to the rear side of a GaAs cell. A layer of gold used for the back reflection of the up-converted photons is additionally applied. Adapted and slightly modified from [23].

A responsivity enhancement of a bifacial c-Si solar cell in the NIR was also realized by using a polycrystalline $\text{NaYF}_4:\text{Er}^{3+}$ (20%) phosphor dispersed into a polymeric matrix and adhered to the rear side of the cell [11]. Since the c-Si solar cell is able to absorb light just above the band gap of 1.12 eV, sub-band gap photons will be transmitted through the device. Under 1523 nm laser excitation of Er^{3+} , a gain in external quantum efficiency (EQE) of 2.5 % was achieved when placing the upconverter phosphor on the rear side of the cell. Other examples of applying UpC phosphors to solar cells are shown in Table 1.3. The absolute efficiency enhancement strongly depends on the upconverter quantum efficiency (QE) and the illumination intensity. The absolute gains in efficiency which were achieved so far are too small for a practical application due to some parasitic losses when attaching an UpC layer to the cell. These losses originate from an absorption of sub-band gap photons within the components of the UpC layer and a deterioration of the rear reflectivity [24]. To overcome these constraints, high efficiency UpC materials have to be developed.

Table 1.3: UpC materials tested on real solar cells and their corresponding efficiency η improvement given in absolute values.

Upconverter	Solar cell	η improvement	Exc./Em. λ [nm]	Lit.
Er ³⁺ , Yb ³⁺ doped glass ceramic	GaAs thin film	2.5 %	1.39 eV/ 525, 550, 650	[23]
NaYF ₄ :Er ³⁺ , polycrystalline	c-Si	2.5 %	1523 / 550, 660, 800, 980	[24]
NaYF ₄ :Er ³⁺ , film	c-Si	0.7 %	980 / 550, 660	[25]
NaYF ₄ :Er ³⁺ , Yb ³⁺ , polycrystalline	a-Si:H	0.02 %	980/ 522, 540, 653	[26]
NaYF ₄ :Er ³⁺ , Yb ³⁺ , colloidal	DSSC	0.1 %	980/ 540, 640, 660, 680	[27]
YAG:Er ³⁺ , Yb ³⁺	DSSC	-	980/ 520, 563, 677	[28]
Er ³⁺ - doped fluorozirconate glass	c-Si	1.6 %	1540/ 530, 550, 660, 800, 980	[29]

1.2.1 Upconverters based on rare earth ions

In the following section, light UpC processes carried out in trivalent rare earth (RE³⁺) ions are shortly discussed. To begin with, the choice of the right host material for embedding the RE³⁺ ions is shown to be a decisive factor for designing efficient upconverter materials. We further describe a sample of UpC materials which was assembled from numerous works in the literature.

Influence of the host material. The exact spectral positions and intensities of the luminescence will vary with different host lattices due to their inherent optical and magnetic properties and will cause a host–ion interaction through phonons, sensitization and a perturbation by exchange mechanisms [30]. Some important effects are shortly discussed in the following section.

Nephelauxetic effect. The spectral positions tend to shift slightly to higher energy in e. g. fluorides compared to the oxides, due to the nephelauxetic effect. The nephelauxetic effect is described by the degree of covalency within the constituting ions – when increasing the covalency the electronic transitions will shift to lower energy. This is due to a reduction in the electronic interaction, since the electrons spread out over wider orbitals [31].

Crystal field. Another factor influencing the optical properties of a given ion is the crystal field (CF), the electric field at the site of the ion considering the surrounding. In particular, the effect of CF on the optical transitions of transition metal ions is known to strongly influence the spectral positions and the splitting patterns.

Phonon properties. The choice of host lattice should result in a close lattice match allowing for the incorporation of impurities without a lattice distortion, and furthermore, take the host–dopant interaction influenced by multiphonon effects into account. An example is the incorporation of 1% Er³⁺ in Cs₃Lu₂X₉ (X = Cl, I, Br) lattices, which allows a long-lived ⁴I_{9/2} excited state to achieve efficient 3- and 4-photon UpC processes [30, 32]. In oxide and fluoride host lattices a different behavior is observed due to a fast phonon–assisted relaxation of the ⁴I_{9/2} state to the lower-lying state ⁴I_{11/2}. These processes are illustrated in Fig. 1.4. Some energetic parameters of other host materials are listed in Table 1.4.

It is expected that a lower nonradiative decay rate is guaranteed for hosts with low phonon energies, leading to an increase of the emission efficiency. A low phonon energy reduces the probability of a multiphonon process along with large energy

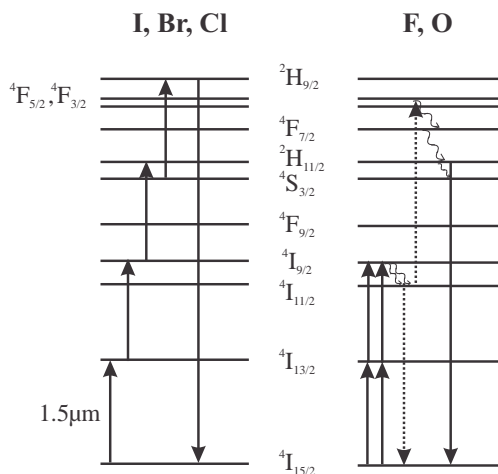


Figure 1.4: Energy level diagram of the Er^{3+} ion upon excitation at $1.5 \mu\text{m}$ within high and low phonon host matrices, i. e. I, Br, Cl (left) and F, O host lattices (right). A 4-photon absorption results in the population of the ${}^2\text{H}_{9/2}$ state (420 nm luminescence) in low phonon energy hosts, whereas high phonon hosts yield green luminescence from the ${}^4\text{S}_{3/2}$ state. Curly arrows indicate multiphonon relaxation processes. The system is dominated by ETU processes in all excitation steps. Adapted and slightly modified from [30].

gaps between the emitting and terminal levels. Basically, this is adequately described by the energy-gap law.

Energy-gap law. The probability of nonradiative decay rate A_{nr} can be expressed as [40, 41]:

$$A_{\text{nr}} = A_{\text{nr}}(0) \cdot e^{-\alpha\Delta E} \quad (1.1)$$

where $A_{\text{nr}}(0)$ and α are two parameters dependent on the material but not on the luminescent center itself and ΔE the energy gap between two adjacent energy levels within the ion. The energy-gap law gives the nonradiative rate from

Table 1.4: Highest lattice phonon energy, $\hbar\omega_{\text{max}}$ and average ${}^4\text{I}_{9/2}$ - ${}^4\text{I}_{11/2}$ energy gap of Er^{3+} in halide and oxide lattices; n_{phonons} is the minimum number of phonons required to bridge the energy gap. In addition, the data of host matrices partly investigated within the thesis are listed [32].

Host lattice	$\hbar\omega_{\text{max}}$ [cm^{-1}]	Gap [cm^{-1}]	n_{phonons}
Oxide	600	1894	3.1
Fluoride	355	2036	5.8
Chloride	260	2117	8.1
Bromide	172	2135	12.3
Iodide	144	2138	14.9
YF_3	500, [33]	2196, [34]	4.4
Y_2O_3	600, [35]	2065, [36]	3.4
TiO_2	641, [37]	2120	3.5
SiO_2	1100, [38]	1596, [39]	1.5

1 Introduction and theoretical background

each level of a RE^{3+} ion in a given material through the simple knowledge of ΔE . Fig. 1.5 shows the exponential decrease of the nonradiative decay rate with increasing gap in a double-logarithmic form for various host materials.

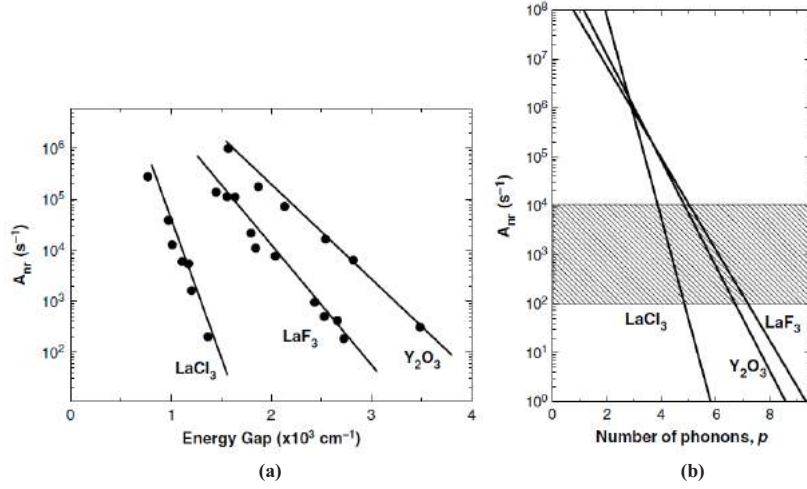


Figure 1.5: (a) Experimentally obtained nonradiative decay rates A_{nr} as a function of the separation between two adjacent energy levels, the energy gap ΔE for LaCl_3 , LaF_3 and Y_2O_3 . (b) The exponential decrease in the multiphonon rate is due to the increased number of emitted effective phonons: the higher the number of effective phonons required to bridge ΔE , the lower the multiphonon nonradiative rate. Highest energy phonons of LaCl_3 , LaF_3 and Y_2O_3 are at $\sim 260 \text{ cm}^{-1}$, 350 cm^{-1} and $430\text{--}550 \text{ cm}^{-1}$. The shadowed area indicates the typical nonradiative rates of RE^{3+} ions in crystals. Adapted from [40, 41].

The decrease in the nonradiative decay rate is due to an increase in the number of emitted phonons taking part in the relaxation process and are usually the highest energy phonons $\hbar\omega_{max}$, also called effective phonons. The multiphonon relaxation rate is hence expressed as

$$A_{nr} = A_{nr}(0) \cdot e^{-\alpha(\hbar\omega_{max}) \cdot p} \quad (1.2)$$

with p the number of effective phonons required to bridge the energy gap. As a rule of thumb, multiphonon relaxation processes are competitive up to a number of 5–6 phonons involved in rare earth doped systems [42]. The ranking of different host matrices according to their highest energy phonons is [43]:

Iodide (160 cm^{-1}) < bromide ($175\text{--}190 \text{ cm}^{-1}$) < chalcogenide, chlorides ($200\text{--}300 \text{ cm}^{-1}$) < fluoride ($500\text{--}600 \text{ cm}^{-1}$) < tellurite ($600\text{--}850 \text{ cm}^{-1}$) < germanate ($800\text{--}975 \text{ cm}^{-1}$) < silicate ($1000\text{--}1100 \text{ cm}^{-1}$) < phosphate (1100 cm^{-1}) < borate (1400 cm^{-1})

To this effect, hosts with a low phonon energy are likely to decrease the probability of nonradiative transitions and hence halide materials are found to be the most promising hosts for UpC phosphors.

1 Introduction and theoretical background

1.55 μm telecommunication wavelength. The Er^{3+} ion is most commonly used for UpC phosphors in combination with c-Si solar cells, due to GSA in the IR domain at 1480–1580 nm (${}^4\text{I}_{15/2} \rightarrow {}^4\text{I}_{13/2}$). The up-converted luminescence shows then four emission bands: ${}^4\text{I}_{11/2} \rightarrow {}^4\text{I}_{15/2}$, 980 nm; ${}^4\text{I}_{9/2} \rightarrow {}^4\text{I}_{15/2}$, 810 nm; ${}^4\text{F}_{9/2} \rightarrow {}^4\text{I}_{15/2}$, 660 nm and ${}^4\text{S}_{3/2} \rightarrow {}^4\text{I}_{15/2}$, 550 nm [22].

Table 1.5: A selection of rare earth based UpC materials found in the published literature.

Rare earth ion(s)	Host material	$\lambda_{\text{exc.}}$	Emission [nm]	Lit.
Er^{3+}	BaX_2 ($X = \text{I, Br, Cl, F}$)	1.5 μm	410, 550, 660, 810	[45]
Er^{3+}	CaF_2	1.55 μm	550, 660, 980	[46]
Er^{3+}	NaYF_4	1.523 μm	660, 550, 800, 980	[24]
Er^{3+}	NaGdF_4	1.53 μm	527, 540, 653, 980	[47]
Er^{3+}	$\text{Gd}_2(\text{MoO}_4)_3$	1.510–1.565 μm	545, 665, 800, 980	[48]
Er^{3+}	$\text{Cs}_3\text{Lu}_2\text{Cl}_9$	1.54 μm	420, 550, 800	[49]
Er^{3+}	Ba_2YCl_7	800 nm	382, 407	[49]
Er^{3+}	$\text{SiO}_2\text{-TiO}_2$	979 and 1532 nm	660, 560	[50]
Ho^{3+}	oxyfluoride glass ceramic	1170 nm	650, 910	[51]
$\text{Er}^{3+}, \text{Tm}^{3+}$	YF_3	1.5 μm	410, 550, 660	[34]
$\text{Er}^{3+}, \text{Yb}^{3+}$	PbF_2 nanocrystals in oxyfluoride glass	980 nm	545, 660	[52]
$\text{Er}^{3+}, \text{Yb}^{3+}$	NaYF_4	980 nm	420, 525, 550, 660	[53]
$\text{Er}^{3+}/\text{Tm}^{3+}, \text{Yb}^{3+}$	$\text{Y}_2\text{O}_2\text{S}$	980 nm	560, 670 (Er); 480, 660, 710 (Tm)	[49]
$\text{Er}^{3+}, \text{Yb}^{3+}$	Y_2O_3	980 nm	560, 660	[49]
$\text{Tm}^{3+}, \text{Yb}^{3+}$	NaYF_4	976 nm	350, 370, 470, 490, 660	[53, 54]
$\text{Er}^{3+}/\text{Ho}^{3+}/\text{Tm}^{3+}, \text{Yb}^{3+}$	YF_3	980 nm	-	[44]
$\text{Tm}^{3+}, \text{Yb}^{3+}$	YF_3	970 nm	475, 810	[55]
$\text{Ho}^{3+}, \text{Yb}^{3+}$	fluoroindate glasses	1155 nm	550, 750, 650, 905, 980 (Yb)	[51]

A selection of RE^{3+} -doped upconverter phosphors is listed in Table 1.5. Fluoride materials out of all halides have the advantages of non-hygroscopicity and thermal stability. Vetrone *et al* in Ref. [56] gave an overview of RE^{3+} -doped fluoride nanoparticles, including LaF_3 and NaYF_4 , and showed that some of the outstanding features compared to the bulk material, are the size-dependent optical properties of nanoparticles, including the size-dependent lifetime of the excited states. Another fluoride-based UpC material, namely, PbF_2 nanocrystals embedded in an oxyfluoride glass, has been reported to show even higher efficiencies than NaYF_4 due to its lower maximum phonon energy (340 cm^{-1} for NaYF_4 vs. 250 cm^{-1} for PbF_2 , respectively) [52].

Ytterbium. Upconverters applicable for the wider band gap solar cell materials, e. g. a-Si (1.75 eV), GaAs (1.43 eV), DSSCs and organic SCs are usually $\text{Er}^{3+}/\text{Yb}^{3+}$ co-doped in order to achieve an enhancement in the UpC efficiency [57]. Yb^{3+} is successfully used as a sensitizer for the Er^{3+} emission, when excited in the 900–1100 nm wavelength region corresponding to the ${}^2\text{F}_{7/2} \rightarrow {}^2\text{F}_{5/2}$ transition of Yb^{3+} . It is also successfully used to sensitize the UpC emission in other ions such as Ho^{3+} , Tm^{3+} , Pr^{3+} and Tb^{3+} by increasing the absorption oscillator strength

in the infrared region [58].

Nanoparticles of NaYF_4 doped with Er^{3+} (2%) and Yb^{3+} (20%) are one of the most promising UpC materials aiming at high quantum yields. However, the quantum yield (QY) of the nanoparticles (NP) strongly depends on the particle size; a drastic decrease in the QY was found for 100 to 10 nm sized colloidal NaYF_4 NPs from 0.3% to 0.005% upon excitation at 980 nm. In contrast, a μm -sized sample of NaYF_4 doped with Er^{3+} and Yb^{3+} gives a QY of 3%, a value which is quite close to the QY found for the bulk sample (QY = 4%) [59]. The increase in surface area of smaller-sized NPs accounts for the decrease in the QY, thus a decrease in the UpC luminescence. This can be explained by the fact that a higher surface area gives rise to more surface defects and a smaller particle size brings a percentage of the lanthanide ions closer to the surface. Both effects together provide luminescence quenching and a further decrease for the QY. New synthetic strategies in NP fabrication, e.g. core/shell structures, allow to overcome these issues and yield better results in the QY.

Other RE^{3+} ions. As a blue-light emitter, Tm^{3+} is known to convert IR radiation by a 3-photon UpC process when relaxing from the $^1\text{G}_4$ excited state to the ground state. Other examples of RE^{3+} ions showing UpC upon excitation at $\lambda > 900$ nm include Pr^{3+} and Tb^{3+} and are thoroughly described in the work of Strümpel *et al.* [60].

1.2.2 Upconverters based on transition metal ions

Transition metal (TM) ions have the larger ability to interact with their structural environments due to a smaller orbital shielding. This allows to some extent for an optimization of the spectral positions of the absorption and emission bands by changing the host lattice. Spectra of TM ions present broad and intensive bands due to a strong lattice-host coupling and are thus of high interest for UpC processes. All TM ion-doped systems show in general the same UpC mechanisms as observed and proposed for RE^{3+} -doped systems, and possess the same building blocks consisting of host-activator-sensitizer (see definitions in Section 1.3). Many TM ion-doped UpC phosphors studied use Ti^{2+} ($3d^2$), Ni^{2+} ($3d^8$), Re^{4+} ($5d^3$) and Os^{4+} ($5d^4$) to perform the light UpC and some examples are presented in Table 1.6 [61, 62].

Table 1.6: Transition metal ions doped as impurities in various host lattices and corresponding light UpC processes. Adapted and slightly modified from [30].

TM ion	Electrons	Host lattice	UpC mechanism(s)
Ti^{2+}	$3d^2$	MgCl_2	GSA/ESA
Ni^{2+}	$3d^8$	CsCdCl_3	GSA/ESA, Avalanche
Mo^{3+}	$4d^3$	$\text{Cs}_2\text{NaYCl}_6$	GSA/ESA
Re^{4+}	$5d^3$	Cs_2ZrCl_6	ETU
Os^{4+}	$5d^4$	Cs_2ZrBr_6	GSA/ETU, GSA/ESA, Avalanche

Another promising UpC phosphor is based on the sensitization of the red emission of Cr^{3+} at ≈ 700 nm by Yb^{3+} in YGG ($\text{Y}_3\text{Ga}_5\text{O}_{12}$), where a large spectral overlap gives rise to a resonant energy transfer due to the broad d-d band of the

Cr³⁺ ion [63].

A manipulation of the UpC process is possible by utilizing perturbations through the sensitization by the host itself or by a lanthanide co-doping. For example, co-doping with Yb³⁺ ions in Re⁴⁺:Cs₂ZrCl₆ allows one to expand the excitation range, leading to a broad red luminescence of Re⁴⁺ [61]. Host perturbation through a magnetic interaction influences the spectroscopic properties by lifting the spin selection rules. For example, substituting Ti²⁺-doped MgCl₂ by MnCl₂ allows to overcome the spin selection rules due to a weak magnetic exchange mechanism between Ti²⁺ and Mn²⁺. RE-based upconverters are by far more investigated in the literature compared to TM upconverters; therefore, our choice fell on using RE³⁺ ions as the luminescent species.

1.2.3 Efficiency improvement using 1D-PBG structures

In this work, Fabry-Pérot microcavities have been prepared for achieving an intensity enhancement of the Er³⁺ emission when doped within the defect layer of the microcavity. The following section comprises the basic concepts concerning the optical microcavities.

Optical microcavities. Photonic bandgap structures (PBG) or photonic crystals are characterized by periodic variations in the refractive index [64]. One type of a 1-dim. PBG structure is a distributed Bragg reflector (DBR), which shows a high reflectivity region where electromagnetic wave propagation is forbidden. This region is conveniently designated as the *stop band*, with its maximum reflectivity determined at a wavelength for which $n \cdot d = \lambda_f/4$, where n is the refractive index and d the physical thickness of the layer (Fig. 1.7).

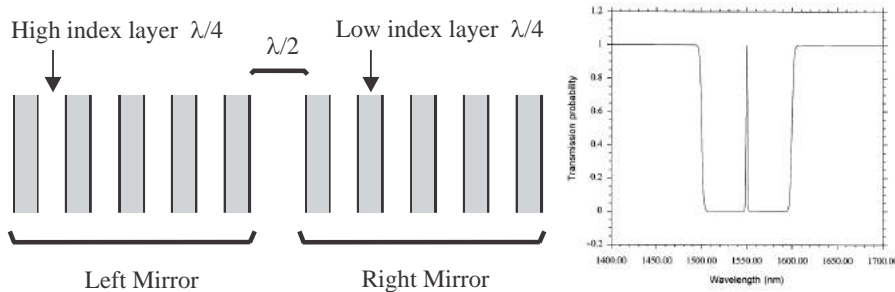


Figure 1.7: Left: Structure of a Fabry-Pérot (F-P) microcavity made of alternating quarter-wavelength thick films of high and low refractive index materials (Bragg mirrors) separated by a one-half wavelength thick layer. Right: The transmission spectrum of a F-P cavity with the pass band centered at 1.5 μm ; adapted from [17, 64].

When two DBRs are placed on the two sides of an active layer, a defect is introduced by the suppression of one layer in the multilayer stack and a *pass band* is obtained, localized at a certain resonance wavelength within the stop band [65]. Such structures are called optical microcavities or Fabry-Pérot (F-P) cavities and exhibit interesting physical properties [64–66]. The microcavity allows a confinement of light by resonant recirculation and can be utilized for the enhancement of spontaneous emission. When doping the cavity layer, a modifica-

tion in the optical properties, e. g. photoluminescence intensity, can be observed due to a coupling of the excited species to the cavity modes as a consequence of the Purcell effect [65]. The enhancement of the emission, when resonant with the cavity, reaches the order of magnitude of the cavity Q factor, expressed as $Q = \lambda_f / \Delta\lambda$, λ_f being the resonance wavelength and $\Delta\lambda$ the resonance full width at half maximum (FWHM) [67]. F-P microcavities possess a small cavity volume and a large cavity mode selectivity and are hence ideal structures for manipulating the spontaneous emission. Numerous examples can be found in the literature that deal with an emission enhancement, along with a change in the observed lifetime and emission profile of RE^{3+} ions, when embedded in dielectric materials [68–72]. Since the difference in the refractive index, together with the number of layers, control the width of the stop band and the reflectivity within the stop band, the choice of material often falls on SiO_2 ($n \sim 1.5$), as low refractive index material and TiO_2 ($n \sim 2.4$), as high refractive index material.

Such photonic structures find application in photovoltaics, aiming for an efficiency enhancement of solar cells. PBG structures are used, amongst others, for antireflective coatings, light concentrators and spectrally selective filters [73, 74]. An example is a PV system, shown in Fig. 1.8, which utilizes different mechanisms for light harvesting in the solar cell, including such fluorescent concentrators and spectrally selective filters in combination with an upconverter.

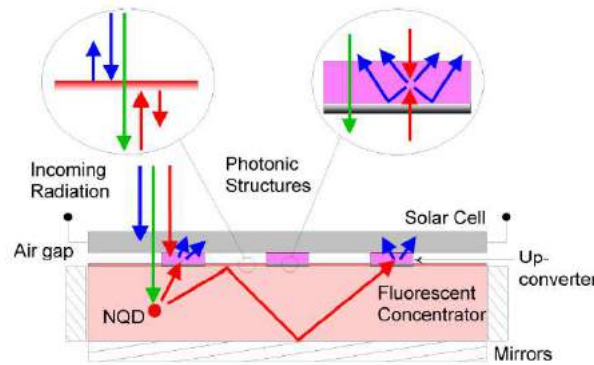


Figure 1.8: An advanced PV structure utilizing PBG structures, such as fluorescent concentrator and spectrally selective filters together with an upconverter and quantum dots (NQD). The fluorescent concentrator is able to emit and guide light to the upconverter; spectrally selective filters are placed between the interfaces of the solar cell and the upconverter and/or the concentrator and between the upconverter and the concentrator to enhance the light intensity and reduce escape cone losses. Adapted from [73].

The fluorescent concentrator performs a spectral concentration by broadband absorption and a subsequent light emission in the absorption region of the upconverter. Furthermore, a geometric concentration is realized since light is only allowed to leave the concentrator where the upconverter is placed. In addition, spectrally selective filters can be placed between the upconverter and the solar cell, to increase the light intensity, and/or the fluorescent concentrator, for reflection of the light being absorbed by the upconverter, or between the solar cell and

the concentrator to reduce reflection losses.

1.3 Theoretical description of UpC processes

This section deals with the fundamental description of the processes which lead to light UpC. Most of the concepts discussed in this chapter are described in more detail in Ref. [14, 30, 31, 75]. A number of different mechanisms have been proposed so far for the generation of anti-Stokes shifted photons. These mechanisms include excited state absorption (ESA), energy transfer up-conversion (ETU), cooperative effects, classical second harmonic generation (SHG) and two-photon absorption (TPA), which are schematically illustrated in Fig. 1.9. Additionally another process, photon avalanche, has to be mentioned to complete this list [30].

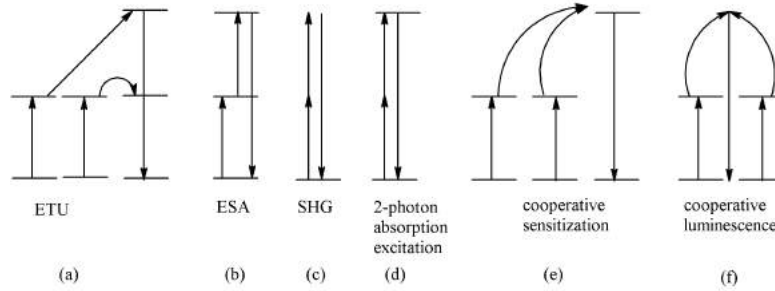


Figure 1.9: Various UpC processes; adapted from [14, 31].

The first UpC process based on ETU was reported by Auzel for $\text{Er}^{3+}/\text{Yb}^{3+}$ co-doped CaWO_4 crystals, able to convert near-IR radiation into green light and it changed the existing perception about the generation of anti-Stokes emission [76]. UpC processes have been since reported for a wide range of inorganic materials in the solid state, including bulk crystals and glasses, nanoparticles and thin films [14]. UpC processes involve usually a first absorption step (ground state absorption, GSA), followed by a second photon absorption or one or several energy transfer (ET) steps.

GSA/ESA. The simplest UpC process is a combination of GSA/ESA, a ground state absorption, succeeded by an excited state absorption step, taking place within one single luminescent center.

GSA/ETU. However, the most efficient UpC process, relative to the processes shown in Fig. 1.9, is ETU – originally denoted as APTE, “l’addition de photon par transferts d’energie” – where the generation of excited states is realized by succeeding energy transfer steps from a sensitizer to an activator [14]. The theoretical description of energy transfer based on the theories of Förster and Dexter will be described in more detail in Section 1.3.1.

Cooperative processes, on the other hand, comprise the interaction of two ions to populate an excited state within a third one, or the generation of a Stokes-shifted emission by two ions via the presence of a virtual state when relaxing back to their corresponding ground state. One talks of cooperative sensitization in the first case and of cooperative luminescence in the latter case. Processes of lower efficiency include **second harmonic generation (SHG)** and **two-photon absorption excitation (TPA)** which are, per se, not related to UpC

processes in the original sense, since energy transfer steps are not involved and the presence of a metastable state is not required. Efficiencies achieved for different UpC processes are listed in Table 1.7.

Table 1.7: Normalized efficiencies η achieved through different UpC mechanisms in selected materials; n_{photons} ...number of photons involved in the UpC process. Adapted from [14].

Host matrix	RE ³⁺ ion(s)	Predominant UpC mechanism	η at 300 K (cm ² /W) ⁿ⁻¹	n_{photons}
YF ₃	Er ³⁺ /Yb ³⁺	ETU	10 ⁻³	2
NaYF ₄	Er ³⁺ /Yb ³⁺	ETU	10 ⁻² -2·10 ⁻⁴	2
NaYF ₄	Tm ³⁺ /Yb ³⁺	ETU	5.5·10 ⁻²	3
YF ₃	Tm ³⁺ /Yb ³⁺	ETU	4.25·10 ⁻²	3
YF ₃	Er ³⁺ /Tb ³⁺	Coop. sensitization	10 ⁻⁶	2
YbPO ₄	Yb ³⁺ /Tb ³⁺	Coop. luminescence	10 ⁻⁸	2
SrF ₂	Er ³⁺	ESA	10 ⁻⁵	2
KDP		SHG	10 ⁻¹¹	2
CaF ₂	Eu ²⁺	Two-photon absorption	10 ⁻¹³	2

The ETU effect is the most efficient one, since it is close to resonance and the photons are able to interact with the medium for a long time. Importantly, UpC processes show a nonlinear behavior, hence the UpC efficiency shows a dependence on the excitation power. The values must then be normalized relative to the incident flux given in (cm²/W)ⁿ⁻¹ for a n -photon process [14].

The theoretical and experimental discrimination of ETU and ESA [14]

For a first distinction between the GSA/ESA and GSA/ETU mechanisms, the energy level scheme given in Fig. 1.10 can be used. The probability W for a particular process is given by [14]:

$$\text{ESA} \quad W_{13} = W_{12} \cdot W_{23} \quad (1.3)$$

$$\text{ETU} \quad N_A \cdot W_{13} = N_A N_{S^*} W_{SA1} \cdot W_{SA2} N_{S^*} \quad (1.4)$$

which can be further simplified – assuming that all W_{ij} have the same magnitude – to:

$$\text{ESA} \quad W_{13} \approx W_{12}^2 \quad (1.5)$$

$$\text{ETU} \quad W_{13} \approx N_{S^*}^2 W_{SA}^2 = N_S^2 \cdot W_{12}^2 \cdot W_{SA}^2 \quad (1.6)$$

From Eq. 1.6, a gain of $N_S^2 \cdot W_{SA}^2$ for ETU over ESA follows, identifying ETU as the more efficient process. ETU is a 2-ion process, where the absorption and emission do not take place in the same center and it is moreover dependent on the sensitizer concentration, N_S . This concentration dependence is a direct result of the dependence of the energy transfer rate k_{ET} on the interionic distance r , as will be discussed later in Section 1.3.1. ESA, on the other hand, is a single-ion process and relatively independent on the concentration of the luminescent

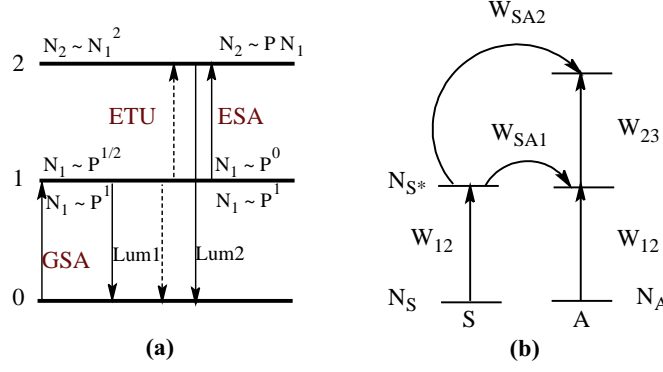


Figure 1.10: Energy level diagram for the GSA/ETU and GSA/ESA processes: (a) UpC mechanisms for a three level scheme and corresponding dependence of the population density N on the excitation power P and (b) a two-photon ETU mechanism with the symbols used in Eq. 1.3–1.6; adapted from [14, 49].

ion [30]. Hence, for a low dopant concentration $< 0.1\%$, the distance r is so large that GSA/ESA will be the dominant UpC mechanism. The distinction between particular UpC mechanisms is essential and can in general be done by two methods which are shortly mentioned in the following.

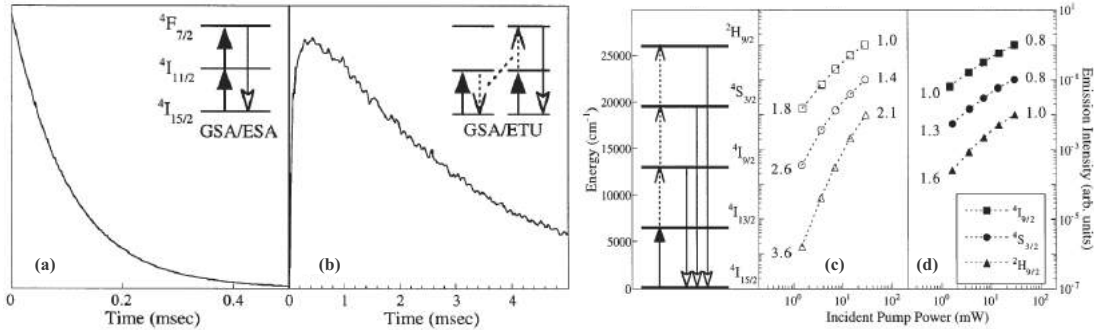


Figure 1.11: Luminescence decay profiles from the ${}^4F_{7/2}$ state for (a) GSA/ESA and (b) GSA/ETU based UpC in 1% Er:RbGd₂Br₇ following a 10 nm excitation pulse and measured slopes of UpC power dependence study in (c) 1% Er:Cs₃Lu₂Cl₉ and (d) Cs₃Er₂Cl₉ excited with 1.5 μm photons; adapted from [30].

First, time-dependent measurements help to distinguish between the ESA and the ETU mechanism and, as an example, we give the decay profiles of 1% Er³⁺ doped RbGd₂Br₇ in Fig. 1.11 [30]. As for ESA, the decay profile is identical to that of a direct excitation of the ${}^4F_{7/2}$ level and, furthermore, the decay signal is only observed within the laser pulse. The decay profile of the ETU mechanism features a delayed maximum and with the luminescence only occurring subsequent the laser pulse; a decrease in the rate constant and the rise time correlates with the decay time of the ${}^4F_{7/2}$ state. These two very distinctive features allow an identification of the underlying UpC mechanism.

Another very powerful tool for understanding the UpC mechanism is to study the

pump power dependence of the luminescence intensities [49]. Since UpC cannot maintain its nonlinear behavior up to an infinite excitation energy, the emitted intensity I_{em} depends on the incident light intensity I_i according to

$$I_{\text{em}} \propto I_i^n \quad (1.7)$$

where the exponent n equals the number of photons required for the population of the emitting state. A saturation effect is to be expected at high excitation power, however, shown by a decrease of the slope in a double-logarithmic representation of the luminescence intensity versus the excitation pump power. So the statement that a two-photon excitation process follows a quadratic power dependence is only valid under certain experimental conditions.

For example, Fig. 1.11 shows the power dependence of the two-, three- and four-photon excitation processes of $\text{Cs}_3\text{Lu}_2\text{Cl}_9$ doped with (c) 1% and (d) 100% Er^{3+} , thus $\text{Cs}_3\text{Er}_2\text{Cl}_9$ [49]. At a low doping level of Er^{3+} both GSA/ESA and GSA/ETU mechanisms are found; at low excitation power, the luminescence intensity of all excited states show a power dependence of P^n with slopes of 1.8, 2.6 and 3.6. At higher excitation power, however, the increase in power leads to a reduction of the slopes, indicating that some saturation effect takes place. In the case of $\text{Cs}_3\text{Er}_2\text{Cl}_9$, the dominant mechanism is GSA/ETU and the power dependence at lowest pump power shows a slope comparable to the highest power behavior of the sample with low erbium concentration. At an even higher power regime, the slopes decrease to only ~ 1 , revealing that the power dependency becomes itself power dependent [30]. Although the behavior in a high power regime resembles a saturation effect, it does not originate from a depletion of the ground state population but rather from the branching kinetics of the intermediate level or to put it differently, from the competition between the linear and nonlinear decay rate. To understand such a behavior, solving the rate equations for the excitation mechanism of a three level system as depicted in Fig. 1.10 yields, for GSA/ETU:

Low power limit (low excitation power): $N_1 \propto P^1$ and $N_2 \propto P^2$

Upper power limit (high excitation power): $N_1 \propto P^{1/2}$ and $N_2 \propto P^1$

and for GSA/ESA:

Low power limit (low excitation power): $N_1 \propto P^1$ and $N_2 \propto P^2$

Upper power limit (high excitation power): $N_1 \propto P^0$ and $N_2 \propto P^1$

Table 1.8 lists the power dependence of an excited state population N_i for the different cases of low and high power excitation for the two UpC mechanisms GSA/ESA and GSA/ETU, respectively.

Table 1.8: Power dependence behavior of excited state population via n–photon excitation. Limits are set for a (1) small (low excitation power) and (2) large (high excitation power) UpC rate based on ETU and ESA and further, a distinction made by the decay route into (a) next lower–lying state and (b) to the ground state. Adapted from [49].

Regime	ETU or ESA	Predominant decay route	Power dependence	Level
(1) small UpC rate	ETU or ESA	next lower state or ground state	$N_i \propto P^i$	$i = 1 \dots n$
(2) large UpC rate	ETU	(a) next lower state	$N_i \propto P^{i/n}$	$i = 1 \dots n$
		(b) ground state	$N_i \propto P^{1/2}; N_n \propto P^1$	$i = 1 \dots n-1$
	ESA	(a) next lower state	$N_i \propto P^i$	$i = 1 \dots n$
		(b) ground state	$N_i \propto P^0; N_n \propto P^1$	$i = 1 \dots n-1$

1.3.1 Energy transfer: Dexter’s and Förster’s theories

The phenomenon of energy transfer (ET) is well described by the theories of Förster and Dexter [77,78]. As a photo–physical process, ET studies are a powerful tool to determine the distances in biomolecules and supramolecular assemblies (“molecular ruler”) and furthermore, suited to obtain some information about the conformations of biomolecules. They are also used as the underlying principle to describe processes in transition metal and rare earth ions doped solids.

Generally speaking, ET can be considered as an alternative possible deactivation pathway for luminescent centers to return to their ground state by decaying from an excited state, besides the known radiative and nonradiative multiphonon decay channel. If we consider two species, the activator A, sometimes also referred to as the acceptor, and the sensitizer S, also referred to as the donor, a non–vanishing interaction exists over a short distance, denoted by r . In case the sensitizer is in its excited state, S^* , an energy transfer may occur to the acceptor A, in its ground state, if a suitable interaction between both exists: $S^* + A \rightarrow S + A^*$. Moreover, a resonance condition should be fulfilled, i. e. the energy gap between ground and excited states of S and A should be equal or very similar. The theoretical description requires a distinction between radiative, nonradiative ET and homo– and hetero–transfer, and must take into account whether the activator and sensitizer are identical or different (see Fig. 1.12).

One may further consider a phonon–assisted ET, in case the resonance condition is not fulfilled. Some characteristic features of radiative and nonradiative ET are summarized in Table 1.9. In radiative transfer, a real photon is emitted by the sensitizer and is subsequently absorbed by the activator, whereas in nonradiative transfer no real photons are emitted.

Resonant nonradiative energy transfer. The theory of resonant nonradiative electric dipole–dipole (Coulombic) ET was first formulated by Förster [77] and later extended by Dexter [78]. Förster described the rate of energy transfer k_{ET} in molecular systems by a classical approach (and later by quantum–mechanics) considering the interaction of two oscillating electric dipoles. One can imagine the sensitizer to be an oscillating electric dipole that progressively transfers its

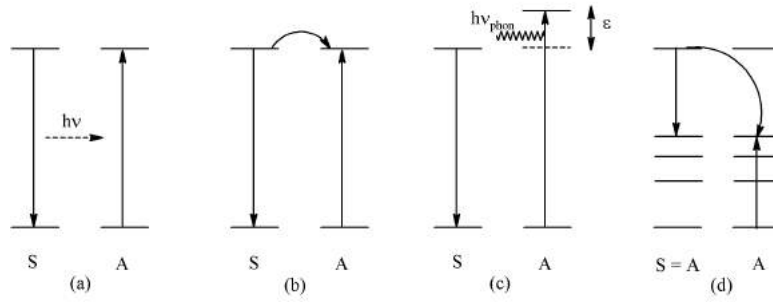


Figure 1.12: Energy transfer mechanisms: (a) radiative (b) nonradiative (c) phonon-assisted and (d) cross relaxation between two identical centers; S = sensitizer, A = activator.

Table 1.9: Distinctive features of radiative and nonradiative ET; r ...distance between S–A, $[A]$...activator concentration, τ_S ...lifetime of the sensitizer, IA...interaction [75].

Radiative ET	Nonradiative ET
$r > \lambda$	$r < \lambda$ (20 nm for dipole–dipole IA)
No IA between S–A required	Requires IA between S–A
Spectral overlap and $[A]$ important	-
Fluorescence spectrum changed in the overlap region (Inner filter effect)	Fluorescence spectrum unchanged
τ_S : unchanged	τ_S : shortened

excitation energy to the activator which is initially at rest. The activator will absorb an emitted power P' when placed at a distance r from the dipole according to [75]:

$$P' = \frac{3\sigma\lambda^4}{64\pi^5 r^6} P^0 \quad (1.8)$$

where P^0 is the power emitted by the oscillating sensitizer dipole. Dividing both sides of Eq. 1.8 by $h \cdot \nu$ yields the quantities k_T , k_r and the absorption coefficient ϵ . This is an important step, since now radiative properties are introduced and we move away from the classical dipole model. Considering all assumptions, the rate constant for the ET can be expressed as [75]:

$$k_{ET} = \frac{1}{\tau_0} \frac{3ln10\Phi_F^0}{64\pi^5 N_a n^4 r^6} \int_0^\infty F_S(\lambda) \epsilon(\lambda) \lambda^4 d\lambda = \frac{1}{\tau_0} \left(\frac{R_0}{r} \right)^6 \quad (1.9)$$

where R_0 is the critical or Förster radius, r the distance between the two dipoles, τ_0 the radiative lifetime and Φ_F^0 the fluorescence quantum yield of the sensitizer S in absence of a transfer. The spectral integral considers the absorption coefficient of the activator and the quantity F_S represents the normalized emission spectrum of the excited sensitizer.

Radiative energy transfer. In radiative transfer no interaction between the partners is required, and it is observed at average distances larger than the wavelength. The probability of radiative ET is expressed as [14]:

$$k_{\text{ET}} = \frac{\sigma_A}{4\pi r^2 \tau_S} \int g_S(\nu) g_A(\nu) d\nu \quad (1.10)$$

considering an absorption cross section σ_A of the activator and the spectral overlap integral of the emission spectrum of S and the absorption spectrum of A, expressed by the integral over the line shape functions $g(\nu)$. Consequently, we see that the radiative transfer rate does not depend on a critical radius, but on the absorption ability of A, hence the concentration of A and the spectral overlap are of crucial importance. On the contrary, nonradiative ET requires an interaction between S and A and an overlap of the emission and absorption spectra.

The rate of energy transfer strongly depends on the type of interaction present and the degree of resonance. As can be seen in Fig. 1.13, the existing interaction may be of Coulombic nature and/or orbital overlap. While in Coulombic interaction the oscillating dipole of S^* induces an electric dipole in A (\rightarrow Förster mechanism), an exchange of two electrons between S and A is associated with the electron exchange mechanism due to the orbital overlap, which is also referred to the Dexter mechanism.

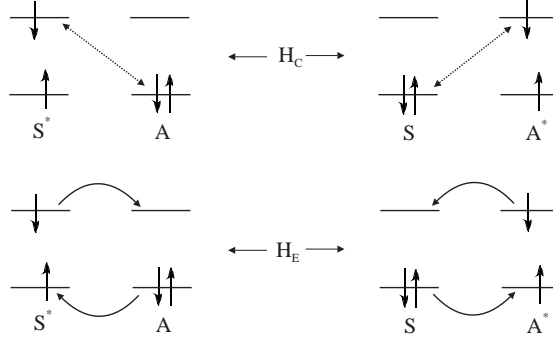


Figure 1.13: Dipole–Dipole (H_C , Förster) and electronic (H_E , Dexter) interaction mechanisms between two centers A, activator or acceptor, and S, sensitizer or donor, in the ground and in the excited state (indexed by *), respectively. H_C and H_E are the electric dipole–dipole interaction and exchange interaction Hamiltonians. Adapted and slightly modified from [79].

The total interaction energy between S and A is expressed by a quantum–mechanical approach using Fermi’s Golden rule by [79]:

$$k_{\text{ET}} \propto \left[\underbrace{\langle \psi(S^*)\psi(A) | H_e | \psi(S)\psi(A^*) \rangle^2}_{\text{Exchange}} + \underbrace{\langle \psi(S^*)\psi(A) | H_c | \psi(S)\psi(A^*) \rangle^2}_{\text{Coulombic}} \right] \quad (1.11)$$

and

$$k_{\text{ET}} \propto E^2 \approx \left(\frac{\mu_S \mu_A}{r^3} \right)^2 \quad (1.12)$$

where the transfer rate is proportional to the sum of an electronic exchange term and the Coulombic interaction term and consequently to the electric dipole

moments μ . Förster used a semi-classical quantum approach to determine the transfer rate for Coulombic interaction proportional to r^{-6} as expressed in Eq. 1.9. The Coulombic interaction (Förster mechanism) is the predominant mechanism for a long range action up to 20 nm and its probability strongly decreases for multipole interactions. The exchange mechanism (Dexter mechanism), on the contrary, is just relevant at short distances since an overlap of orbitals is required (<1 nm). The exchange interaction is a purely quantum-mechanical effect arising from the symmetry properties of the wavefunctions and is independent of any experimental quantities or the oscillator strengths of the relevant transitions, however, does depend on the spectral overlap integral J [79]:

$$k_{\text{ET}} = K \cdot J \cdot \exp\left(\frac{-2r}{L}\right) \quad (1.13)$$

where the parameter K is related to the orbital interactions, J the normalized spectral overlap and L the van der Waals radius. Various types of interactions and their distance dependencies on the transfer rate can be specified as follows:

Dipole–dipole (electric)	$1/R^6$
Dipole–quadrupole	$1/R^8$
Quadrupole–quadrupole	$1/R^{10}$
Magnetic dipole	$1/R^6$
Exchange interaction	$\exp(-2r/L)$

It is important to mention that the dipole–dipole interaction is the strongest in case the transitions are allowed. When forbidden transitions occur, e.g. in inorganic solids, an extension of the Förster theory was given by Dexter [78] and Inokuti and Hirayama [80] to include higher order multipole and exchange interactions. The transfer probability p_{ET} , formulated by Dexter is extended for electrostatic multipolar interaction in the form [81]:

$$p_{\text{ET}} = \frac{2\pi}{\hbar} \langle SA^* | H | S^* A \rangle^2 \int g_S(\nu) g_A(\nu) d\nu \quad (1.14)$$

with

$$H = \sum_{i,j} \frac{e^2}{|\vec{r}_i - \vec{r}_j|} = \sum_{k_1, q_1} \sum_{k_2, q_2} \frac{e^2}{R^{k_1+k_2+1}} C_{q_1 q_2}^{k_1 k_2} D_{q_1}^{(k_1)}(S) \cdot D_{q_2}^{(k_2)}(A) \quad (1.15)$$

where $C_{q_1 q_2}^{k_1 k_2}$ is an angular factor depending on the orientation of the coordinate axes and k represents the rank of the pole. For example, an electric dipole transition has $k = 1$; an electric quadrupole transition $k = 2$. Eq. 1.15 shows

H_{SA} as a product of tensor operators related to the spherical harmonics, where one operator acts on the wavefunction on the sensitizer only and the other on the wavefunction of the acceptor only. Energy transfer in RE-doped samples are mostly interpreted by means of electric multipole interactions, while exchange interactions are important for 3d ions.

1.4 Thin film deposition techniques

In this thesis, thin film materials with light UpC properties were synthesized using chemical vapor deposition and the sol-gel processing route. Both techniques are now subject of a rather basic theoretical treatment.

1.4.1 Chemical vapor deposition

Chemical vapor deposition (CVD) can be described as the dissociation and/or chemical reactions of gaseous reactants on a heated substrate to form a solid product [82]. Heat, plasma or light introduce homogeneous and/or heterogeneous reactions, depending on whether the chemical reactions occur in the gaseous phase or on/near the vicinity of a hot substrate surface, respectively. The unique advantages of CVD over other coating techniques facilitate the fabrication of electronic/optoelectronic materials, surface modifying coatings (e. g. protective coatings against corrosion, wear) and the extraction and pyrometallurgy of metallic films and ceramic fibres. Since CVD is based on molecular reactions, a large spectrum of materials can be obtained due to a wide range of precursors, including halides, hydrides and organometallics:

- Semiconductors: Si, Ge, etc. for micro/optoelectronics, photovoltaic devices
- Dielectrics and ceramic materials for protective coatings: SiC, BN, Al₂O₃, ZrO₂, SiO₂
- Metallic films: W, Pt, Mo, Cu, Al for electronics
- Ceramic fibers and ceramic matrix composites: SiC, C, etc.

Table 1.10 summarizes the advantages of CVD that outweigh its drawbacks and make it to an attractive and versatile technique for thin film fabrication.

Other CVD techniques were developed not only to fabricate films, but also powders, composites and nanotubes. Several CVD variants exist in addition to the conventional CVD which uses thermal energy for the activation of chemical reactions. The use of other energy sources enables e. g. plasma-enhanced and photo-assisted CVD, which use plasma or light, respectively, for the activation process. Furthermore, the type of precursor supply system for the generation of vapor-phase precursors yields different CVD variants. MOCVD is another CVD variant, relying on metalorganic rather than the inorganic precursors used in the conventional CVD. In particular, the aerosol-assisted metalorganic CVD (AA-MOCVD) and liquid injection (LI) MOCVD are described in more detail in the following subsections, since these two techniques were used throughout the thesis work.

Table 1.10: Selected advantages and drawbacks of chemical vapor deposition.

Advantages
<ul style="list-style-type: none"> - Highly dense and pure materials in nanometer scale - Wide range of materials for single-/multi-layer deposition - Reasonable processing cost - Non-line-of-sight deposition of complex-shape objects - High sample throughput, reproducibility - Control of morphology, crystallinity - Low sample contamination - Relatively low deposition temperatures
Drawbacks
<ul style="list-style-type: none"> - Multi-component materials using multi-source precursors: problems with stoichiometry - Hazardous, toxic precursors - High costs for more sophisticated CVD systems, e. g. plasma-assisted CVD

i.) Aerosol-assisted MOCVD [83,84]

Two specific issues in conventional CVD play a limiting role in its application, the availability of precursors with sufficient volatility and the difficulties in controlling the stoichiometry, especially for multicomponent systems. Aerosol-assisted (AA) MOCVD is a variant of the conventional CVD which involves the generation of an aerosol from a liquid source to volatilize the precursors. This allows a wider range of precursors to be used, since volatility is not crucial and the precursors just have to be soluble in an appropriate solvent. Metalorganic precursors used in MOCVD can also be used for AA-MOCVD, including alkoxides, β -diketones and amides. Thin films of oxides, chalcogenides and metals have been synthesized using AA-MOCVD. Further advantages of AA-MOCVD include a simpler reactor set-up and the associated lower costs, a high deposition rate and a more flexible reaction environment, since the operational pressure is flexible.

The key steps of the process are described in Fig.1.14 and involve, firstly, the atomization of a liquid precursor solution into micrometer-sized aerosol droplets. The precursor aerosol is then delivered into a heated reaction zone, where solvent evaporation is followed by the vaporization of the precursors. Subsequently, homogeneous and/or heterogeneous reactions take place. Homogeneous gas phase reactions involve a decomposition and/or chemical reactions of the gaseous precursors into fine powders at a high temperature, before they can even reach the heated substrate surface. On the other hand, when the vaporized precursors adsorb onto the substrate surface, subsequent heterogeneous reactions occur, including chemical reactions and decomposition, yielding the desired material.

Atomization of the precursor liquid can be achieved by three different methods: by an ultrasonic aerosol generator, by a pneumatic aerosol jet or an electrostatic

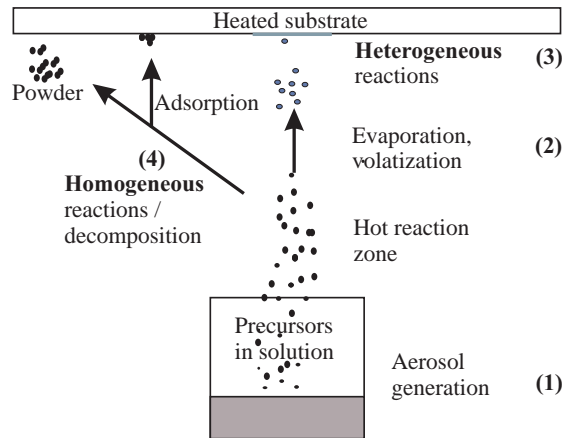


Figure 1.14: The key components of an AA-MOCVD process.

atomization. The three methods differ in their aerosol formation mechanism and the size and size distribution of the aerosol droplets. The most common method is the ultrasonic aerosol generator, which was also used in our AA-MOCVD set-up. A piezoelectric transducer causes the formation of droplets when a high frequency field is applied and the transducer begins to vibrate. The droplet size is expressed by [85]:

$$d = k \cdot \left(\frac{2\pi \cdot \gamma}{\rho \cdot f^2} \right)^{1/3} \quad (1.16)$$

where k is a constant, γ and ρ are the surface tension and the viscosity of the solution, respectively, and f is the ultrasonic frequency. Eq. 1.16 indicates that the droplet size is inversely proportional to the applied frequency, i. e. applying a higher frequency decreases the droplet size. A smaller droplet size favors the vaporization of the precursors and is desirable. However, the power setting of the transducer together with the carrier gas flow influence the amount of aerosol produced. The droplet sizes achieved by the use of an ultrasonic generator usually vary between 1 – 10 μm .

ii.) Pulsed liquid injection MOCVD [86, 87]

Metalorganic chemical vapor deposition (MOCVD) is a variant of the conventional CVD method, using metalorganic precursors rather than inorganic sources. Problems arising when using metalorganic precursors may range from a low thermal stability due to hydrolysis and polymerization reactions and a low vapor pressure, to changes in the rate of evaporation during the CVD process which lead to variations in the film composition. The injection method offers a solution to overcome these issues. Pulsed liquid injection (LI) MOCVD can use liquid precursors (or in solution of organic solvents), sealed in a tube which is kept at room temperature under inert gas. Micro-amounts of the liquid precursors are sequentially injected into a heated evaporation chamber (the evaporator), where the precursor is then flash-volatilized. The evaporation chamber is close to the deposition zone

and allows a short transfer time and high deposition rates. The vapor pressure is highly stabilized and controlled, due to the precise injection of the precursors. A stabilized vapor pressure and composition allows the synthesis of more complex materials, such as high temperature superconductors (YBCO) with high reproducibility. Another advantage is that only one source containing all the precursors is needed. Not only liquid precursors for the injection have been developed, but also powder mixtures. However, the introduction of micro-amounts of powders is more complex and difficult to control and creates a disadvantage over liquid precursor feeding. For introducing liquids into the evaporator, micro-pumps, syringes, liquid mass flow controllers, aerosols and high-speed electro-valves can be used. The principle of electro-valves is similar to the injectors used for fuel injections in thermal motors. The MOCVD injector is controlled by a computer or an electric pulse generator and the amount of liquid precursor is determined by the following parameters: the pulse duration, the injection frequency, the precursor concentration, the differential pressure between the injection tube and the evaporator and the viscosity of the solution. The use of such an injector allows an accurate injection of precursors and a “digital” growth, since the layer thickness can be easily controlled by changing the number of pulses, keeping all other parameters constant. After the injection and vaporization of the precursors, the reactants are delivered into the reaction chamber onto a heated substrate by a carrier gas flow (inert or reactive gas). The peculiarities of LI-MOCVD facilitate the growth of multilayers, superlattices of complex structures, digital film growth and the use of unstable metalorganic precursors of low volatility.

Deposition mechanism. The most important key steps of the deposition process are depicted in Fig. 1.15. To begin with, the liquid-source precursors are volatilized into gaseous reactants which then undergo gas phase reactions forming intermediate species (Fig. 1.15, step [1]).

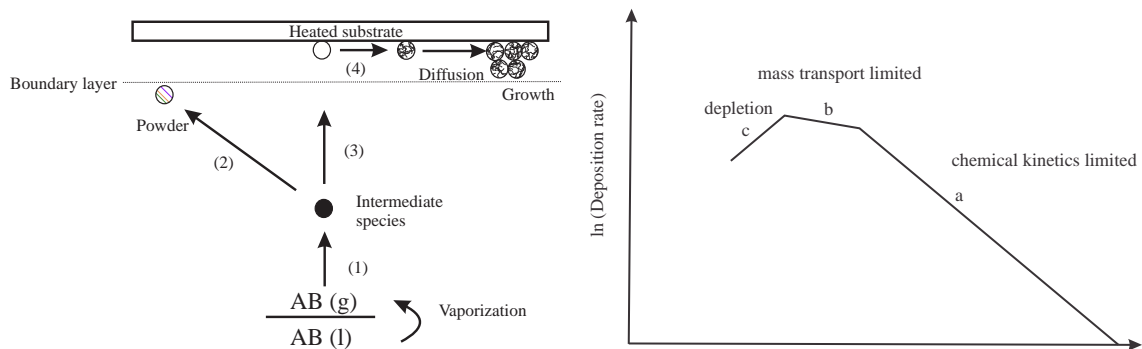


Figure 1.15: Key steps in the CVD process of a material AB (left) and a typical Arrhenius plot (right) divided into three main kinetic regimes (a) depletion (b) mass transport limited and (c) chemical kinetics limited; adapted and modified from [82].

These intermediate species can then obey two different pathways, depending on the temperature: first, at temperatures higher than the decomposition temperature of the intermediate species, homogeneous gas phase reactions occur, followed by decomposition and the formation of powders and volatile byproducts (Fig. 1.15,

step [2]). The powder particles will deposit on the surface and can act as crystallization centers. The as-formed films have usually a poor adhesion.

The second pathway occurs at a temperature lower than the decomposition temperature of the intermediate species, and is described by the diffusion/convection of the species across the boundary layer (Fig. 1.15, step [3]). The intermediate species is adsorbed onto the substrate and a heterogeneous gas–solid reaction takes place. Thereby, a deposit is formed onto the substrate, which will diffuse along the surface and act as a crystallization center. Heterogeneous reactions allow to realize a dense film, compared to films derived from homogeneous gas phase reactions. By specific tailoring of the process conditions, hetero- or homogeneous reactions can be favored to obtain a porous or a dense material.

The kinetics of a CVD process are quite intricate, since chemical reactions are involved in the gas phase and/or at the solid–gas interface and further chemisorption and desorption have to be considered. However, for the kinetic description of a CVD process, it is widely accepted to experimentally determine the deposition rate as a function of the deposition temperature and match it to rate-limiting models. The Arrhenius equation describes exactly the relationship of the deposition rate k_D with temperature and is expressed by:

$$k_D = A \cdot \exp(-E_a/RT) \quad (1.17)$$

where A is a constant, E_a the activation energy, R the gas constant and T the absolute deposition temperature. Three main kinetic regimes can be identified, depending on the deposition temperature:

- (a) Surface reaction kinetics
- (b) Mass transport kinetics
- (c) Depletion

In the regime of *surface chemical kinetic* limitation, processes like chemisorption, desorption, chemical reaction and surface migration occur. The deposition temperature strongly influences the deposition rate. At higher temperature the mass transport limited regime is reached, where the surface kinetic processes become so fast that the overall process is mass transport limited due to the limiting step of the diffusion of reactants across the boundary layer onto the substrate surface. At even higher temperature, the reactants start to deplete and the desorption rate may also increase drastically, which leads to an overall decrease in the deposition rate. In what kind of kinetic regime the CVD process is actually carried out depends not only on the temperature, but also on the pressure during the deposition. CVD at atmospheric pressure is mass transport or diffusion limited, since surface reactions are very rapid. Non-uniform thicknesses may occur in mass transport limited reactions, due to the depletion of reactants. The rate of mass transport is higher than the surface reaction rate in the case of low pressure CVD. Hence, low pressure CVD is usually surface reaction rate limited, where the reactants undergo slow chemical reactions on the surface, leading to the formation of uniform films.

1.4.2 Sol–gel processing

Since the beginning of sol–gel science, a very large number of materials has been produced, including catalysts, ceramics, films, coatings, composites, aerogels and fibres [88, 89]. In Fig. 1.16, different routes of sol–gel processing are illustrated for the fabrication of various materials.

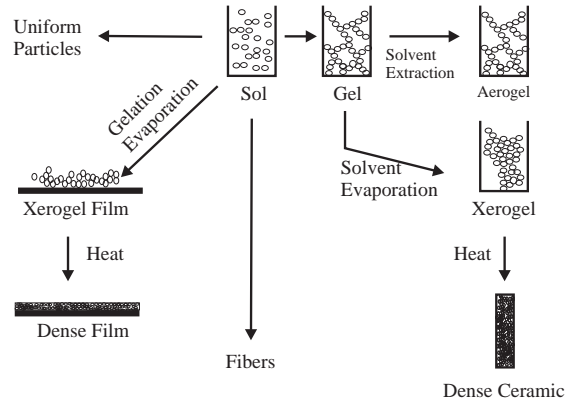
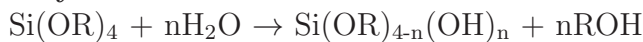


Figure 1.16: Sol–gel processing leading to various end products; adapted and slightly modified from [88].

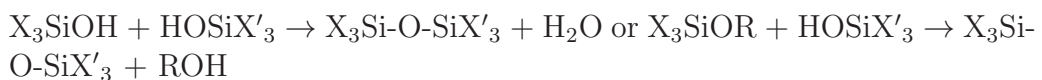
All sol–gel derived materials share a common preparation strategy: their synthesis involves the generation of a sol, which is then subsequently converted into a viscous gel (sol–gel transition) and then to a solid material. A sol is described as a colloidal suspension of particles between 1 nm and 1 μm moving under Brownian motion in a fluid [89]. The size of the initial colloidal particles depends on nucleation and growth and both processes may cause a precipitation of the particles. Colloids are only obtained if the nucleation rate, which is determined by the solubility of the materials, is faster than the growth rate, which depends on factors such as the amount of material available, the diffusion rate, or the presence of impurities able to act as growth inhibitors. As any other technology, the sol–gel process has many advantages, as well as limitations, for a number of reasons summarized in Table 1.11.

The different stages in the sol–gel processing of silica (silicon alkoxide sol–gel process) are illustrated in detail below as an example how the chemical links are formed. Following key steps can be defined [89]:

Hydrolysis:



Condensation:



Gelation:

Formation of a network of high viscosity entrapping the remaining solution

Table 1.11: Sol–gel synthesis: advantages and limitations, adapted and slightly modified from [89].

Advantages

- Required temperature rather low (except densification), close to room temperature; thermal degradation minimized
- Precursors such as metal alkoxides are easily purified and yield high purity and stoichiometry products
- Mild chemical conditions: no extreme pH levels, pH sensitive species including enzymes, cells may be entrapped
- Highly porous and nanocrystalline materials synthesis
- Porosity, pore size control via chemistry: chem. modifications of precursors lead to changes in hydrolysis and condensation rate
- Use of liquid precursors allow casting of ceramic materials of complex shape, as well as thin films, fibers
- Synthesis of materials of high optical quality for optical components
- Process temperature below crystallization temperature of oxides, allows the production of amorphous materials

Limitations

- Time consuming process
 - Expensive precursors, sensitive to moisture
 - Problems of the dimensional change during densification, shrinkage and stress cracking during drying
-
-

Aging:

Includes processes like the formation of further cross–links and shrinkage of the gel, structural evolution with changes in pore size and pore wall strengths

Drying: The loss of volatile components, e. g. water, alcohol; first in form of an expulsion of the liquid during gel shrinkage, then as evaporation of liquid from the pore structure

Densification:

Thermal treatment to densify the open structure

The reaction mechanisms for silica sol–gels under acid– and base–catalyzed conditions are shown in Fig. 1.17. The first step involves the hydrolysis of the silicon alkoxy groups, and depends strongly on the pH value, the temperature and the steric effects of the substituents on the alkoxy groups. Larger alkoxy groups lead to more steric hindrance and a decrease in the hydrolysis rate: e. g. tetramethoxy silane, TMOS, hydrolyzes faster than tetraethoxy silane, TEOS. The use of a higher alcohol as a solvent leads to a replacement of the ethoxide groups in TEOS during the first step of hydrolysis and, consequently, reduces the rate of the 2nd hydrolysis step. In general, the gel structure can be modified, namely the pore size and surface area, through the reactivity and the bulkiness of the precursors;

for example, the replacement of the alkoxy groups by other ligands such as acetate or acetylacetonate leads to a retardation of the hydrolysis and condensation reaction. Moreover, the ethanol:TEOS ratio must be taken into account, since a certain amount of solvent is needed to achieve miscibility with water to facilitate the hydrolysis.

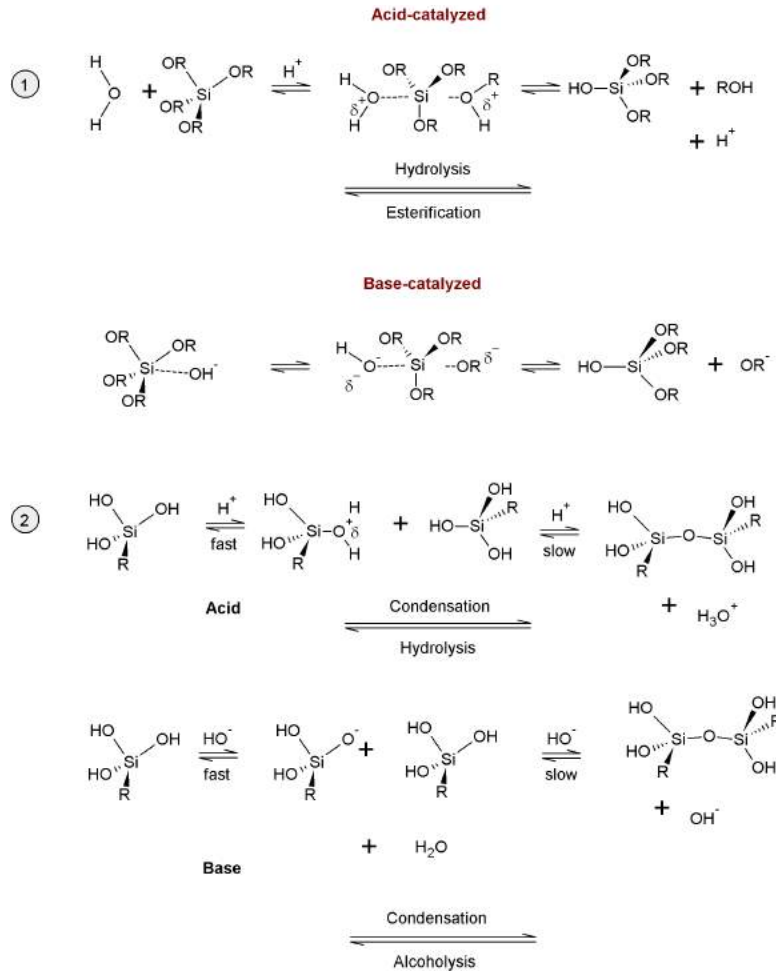


Figure 1.17: Acid- and base-catalyzed reaction mechanism for the sol-gel processing of silica.

Fig. 1.18 shows the gel time as a function of the water:TEOS and ethanol:TEOS ratios. At least 4 molecules of water are needed for a complete hydrolysis of TEOS. However, less water can be used, since the condensation reaction (Fig. 1.17, step [2]) forms water as a product. If the amount of water becomes small, the gel time becomes long. A similar effect is observed if the quantity of water becomes too large, because then the dilution of reactants becomes too high to achieve effective hydrolysis rates. The role of the catalyst in the hydrolysis reaction is clearly to accelerate the conversion of the silicon alkoxides into trialkoxy silanols (see Fig. 1.17). For acid-catalyzed hydrolysis, the positively charged transition state is stabilized by electron donating groups, i.e. $(\text{RO})_3\text{Si}(\text{OH})$ will condense faster than $(\text{RO})_2\text{Si}(\text{OH})_2$ and so on. This indicates that the first catalyzed reaction is

1 Introduction and theoretical background

the fastest and hence is quickly followed by a condensation reaction. To put it differently, only partially hydrolyzed monomers will play a significant role in the reaction.

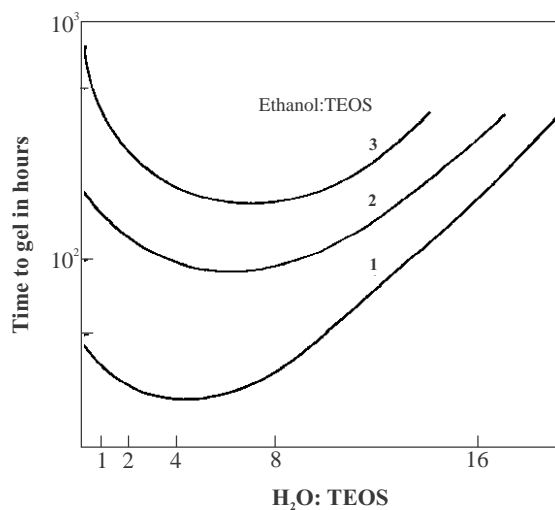


Figure 1.18: Gel time in [hours] for different ethanol:TEOS and H₂O:TEOS ratios, adapted and slightly modified from [90].

An open network structure of linear polymer chains is formed, as shown in Fig. 1.19, and cross-linking of the chains is achieved through hydrolysis of the Si-OR side groups, leading to a relatively dense gel with small pores. On the contrary, base-catalyzed reactions yield a negatively stabilized transition state, which becomes more stable the more -OR groups are replaced by -OH groups. As a consequence, almost completely hydrolyzed monomers are formed, since successive hydrolysis steps proceed faster, and the hydrolyzed species undergo condensation reactions at an early stage of the reaction. Highly cross-linked and large sol particles are formed under basic catalysis, yielding ultimately gels with large pores. Hence the choice of acid or base catalysis influences the charge of the transition state, the reaction rate and the nature of the gel formed.

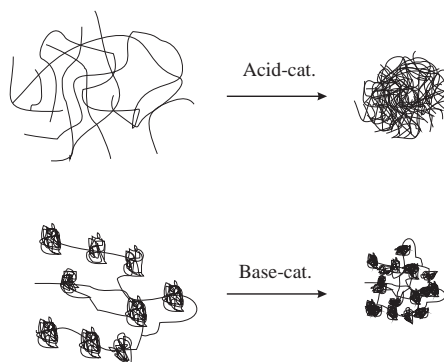


Figure 1.19: Schematic illustration of gel structures formed under acid- and base-catalyzed reactions, respectively.

Since the sol-gel process has such a complex pattern involving a number of

reactions which may also proceed simultaneously, one can control the properties of sol-gel materials by modifying the conditions during the individual process stages. Hydrolysis, condensation, aging, drying and densification can be tuned to obtain materials with the required characteristics. One serious problem encountered at the drying stage, for example, is the crack formation and material fracture. This is due to the evaporation of the solvent and the associated capillary forces.

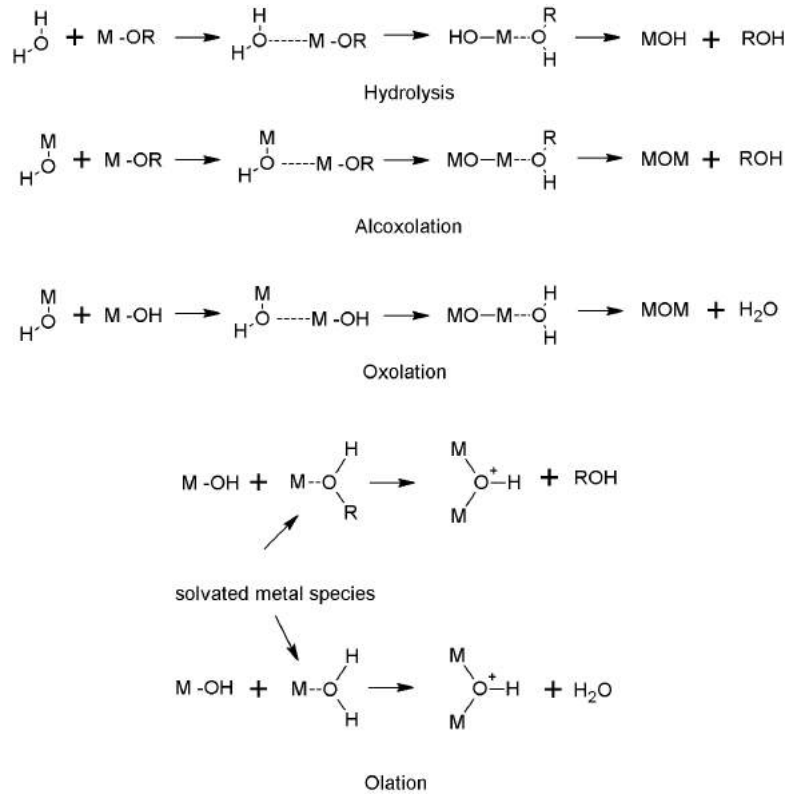


Figure 1.20: Hydrolysis and condensation reactions of metal oxide precursors for sol-gel processing; adapted and slightly modified from [89].

One method to overcome this problem is the use of so-called drying control chemical additives (DCCA), such as formamide, dimethylformamide (DMF), or acetonitrile [89]. These agents allow a drying process without crack formation even at high temperatures. Due to the formation of large pores, the capillary forces will be weakened and the stress on the gel during drying becomes much smaller. On the other hand, an increase in the pore size will promote the evaporation of the solvent (Kelvin equation, pp. 152 from [91]). Another reason for reducing the drying stress is the binding of the DCCA to the silica through the H-bond formation. The removal of water is then eased by reducing the interaction of water with the silanol groups on the pore walls. The same effect as DCCA has the addition of surfactants, since the hydrophilic alkyl groups prevent the interaction of water with the pore wall and consequently reduce the stress during drying. The silica sol-gel process in Fig. 1.17 was chosen to illustrate the possible reactions in sol-gel processing. In a similar manner, metal oxide sols can be prepared by two classes of sol-gel methods, whether metalorganic precursors or inorganic salts

are used in the process. In general, the chemical reactions are much faster for metal oxide sol-gels compared to silica sol-gels: e. g. the hydrolysis rate for TEOS is $5 \cdot 10^{-9} \text{ M}^{-1}\text{s}^{-1}$ and it is $10^{-3} \text{ M}^{-1}\text{s}^{-1}$ for $\text{Ti}(\text{OEt})_4$ [89]. This can be explained by the highly electropositive character of the metal, which facilitates the nucleophilic attack on the central atom and their greater ability to vary the coordination number and geometry.

The reactions involved for metal alkoxide precursors are illustrated in Fig. 1.20, describing the hydrolysis and condensation reactions in the absence of an acid or a base catalyst. All the different reactions shown depend strongly on the partial positive charge of the metal and the partial negative charge of the incoming nucleophile, as well on the partial charge and stability of the leaving group. Moreover, the ability of the metal to expand its coordination sphere facilitates the hydrolysis and condensation reactions, which is not feasible for silicon alkoxides. In the case where an acid or base catalyst is present during the reaction, the progress of the condensation reaction can be predicted due to the charges present on the reacting species. In acid-catalyzed systems, the least positively charged species will react fastest, whereas with basic catalysis the most positively charged species will react fastest, e. g. $\text{Ti}(\text{OR})(\text{O}^-)_3 > \text{Ti}(\text{OR})_3\text{O}^-$. The choice of catalysts allows to control the structural evolution of the metal oxide formed, since base-catalyzed systems will lead to highly branched networks, as already discussed for the silica sol-gel process.

RE³⁺-doped YF₃ thin films by LI-MOCVD

Yttrium fluoride (YF₃) is a potential candidate as an ideal host material for rare earth (RE³⁺) ions to allow the up- and down-conversion of light. We describe the deposition of Er/Yb co-doped YF₃ thin films on Si(111) wafers using low pressure pulsed liquid injection MOCVD. Films were grown through the thermal decomposition of Y/RE(hfac)₃ precursors dissolved in dimethoxyethane (0.05 M), under 5 torr of an O₂/Ar atmosphere, at different substrate temperatures between 450 °C and 650 °C. The film microstructure strongly depends on the deposition conditions and an optimization of the gas flow, oxygen content, pulse duration and deposition temperature was achieved. Under optimized conditions, films deposited at 590 °C showed the best quality and no crack formation was observed on Si(111) for a film thickness < 100 nm. These films have been characterized by SEM, AFM, XRD and Raman techniques. Optical measurements, including the dispersion of the refractive index and light transmission, were performed on the Er/Yb:YF₃ films grown under optimized conditions.

2.1 Introduction

Thin films of rare earth metal fluorides have a great potential as optical coating materials covering the UV to the IR wavelength region [92]. This is foremost due to their low refractive indices and their wide range of transmission, attributed to the low molar weight and high ionicity of fluorides, which, together with their low phonon energies, are advantages over oxide materials [93]. Different applications include optical waveguides, phosphors for flat panel appliances, multilayer storage devices and interference coatings [19, 94–96]. The two main categories of film growth processes from vapor phase are physical vapor deposition (PVD) and chemical vapor deposition (CVD). Since the properties of thin films inherently depend on the film deposition technique and its parameters, the choice of method is crucial for the microstructure and film performance. In PVD, targets containing the cations are most commonly thermally evaporated in molecular form from Knudsen cells, crucibles or sputtered by an argon plasma. The limitations of PVD for the growth of thin films are the low packing density of the film and the lack of control over the film thickness in multilayer stacks. CVD is a suitable method to produce dense, large area, high quality thin films through the deposition of a solid from the gaseous phase onto a heated substrate. The deposition process includes an activated (thermal, plasma- or photo-) decomposition of volatile precursors. Examples for the film growth of rare earth fluorides include LaF_3 [97], YF_3 [98], GdF_3 [99] and CeF_3 [100], all using metalorganic compounds as source materials (MOCVD).

We are particularly interested in yttrium fluoride (YF_3) which is potentially an ideal candidate for replacing radioactive ThF_4 as anti-reflective coating due to its low absorption in the 8–12 μm region [101, 102]. Moreover, the Y^{3+} ionic radius, which is similar to that of other RE ions ($\text{Y}^{3+} = 0.90 \text{ \AA}$; $\text{Er}^{3+} = 0.89 \text{ \AA}$; $\text{Yb}^{3+} = 0.87 \text{ \AA}$ [103]), allows the incorporation of optical centers that are capable of light conversion.

Our emphasis is towards the UpC of light, a physical process where two low energy photons are combined into one high energy photon. This process is well described in the literature and the most commonly reported UpC processes involve lanthanide ions in a solid host matrix [14]. A promising technological application of these materials is, amongst others, in photovoltaics, since the efficiency of conventional solar cells can be increased by simply applying an UpC layer on the rear side of the cell [23, 24]. Nanocrystalline YF_3 phosphors are reported to be successful systems for both up- and down-conversion of light, due to their low phonon energy and their chemical and thermal stability [104, 105].

In this work, we describe the deposition of doped polycrystalline $\text{Er}:\text{YF}_3$ and $\text{Er}/\text{Yb}:\text{YF}_3$ thin films on $\text{Si}(111)$ substrates by pulsed liquid injection (LI) MOCVD. Processing parameters were optimized to achieve the best film quality. Among the various deposition conditions, the substrate temperature and the oxygen concentration in the carrier gas flux were shown to be the most critical parameters influencing the film microstructure. In this paper, we focus on correlating the deposition parameters with structural film properties characterized by XRD, SEM

and AFM measurements. The film composition was checked both by EDS and WDS techniques. Micro-Raman studies on RE:YF₃ films have also been performed to elucidate the nature of the crystalline phase and the material refractive index was characterized as well.

2.2 Experimental details

Microstructural characterization. X-ray diffraction (XRD) patterns of the thin films were recorded between 10° and 70° with a scan rate (2θ) of 1°/min in Bragg-Brentano geometry with a Bruker Advance D8 diffractometer, using CuK α radiation ($\lambda = 0.1541$ nm). A FEI Quanta 250 FEG-SEM was used to determine the film surface morphology and to measure the film thickness. The micrographs were obtained in secondary electron imaging (SEI) mode. Atomic force microscopy (AFM) was performed using a SPM/AFM Veeco Dimension 3100 in tapping mode in order to further characterize the film surface morphology. For qualitative film composition analysis, energy dispersive X-ray spectroscopy (EDS) was performed with a PGT detector installed on a Philips XL30 SEM. Electron probe microanalysis (EPMA) was used for the quantitative film analysis, performed on a Cameca SX50 system equipped with a WDS (wavelength-dispersive) spectrometer. The EPMA data was analyzed using the Stratagem program dedicated to the analysis of thin films [106].

Spectroscopic characterization. The dispersion of the refractive index was determined by spectroscopic ellipsometry, using a HORIBA Jobin-Yvon model UVISSEL NIR spectroscopic ellipsometer, over the spectral range of 300–1200 nm, at a 70° angle of incidence. FTIR spectra were recorded on a Digilab Excalibur FTS 3000 IR spectrometer, in absorption mode. The spectra were measured at a resolution of 8 cm⁻¹, in the range of 100–4000 cm⁻¹. Raman spectra were recorded on a high resolution Micro-Raman spectrometer (LabRAM HR 800 Evolution, Jobin-Yvon Horiba) with a 100X objective and a 633 nm laser excitation wavelength (14 mW power). Optical transmission spectra of fluoride films were measured with a Lambda 950 UV/Vis/NIR spectrophotometer (Perkin Elmer).

2.3 Film deposition

Er/Yb:YF₃ thin films were grown by pulsed liquid injection metalorganic chemical vapor deposition (LI-MOCVD) on 2" Si(111) wafers over a temperature range of 450–650 °C. For the optical transmission measurements, additional films were deposited on fused silica substrates. The temperature control and heating of the substrates was performed by an induction heating system. A schematic illustration of the MOCVD reactor used in this work is depicted in Fig. 2.1. The experimental set-up is based on the injection of micro-amounts of a solution of Ln(hfac)₃ (hfac = 1,1,1,5,5,5-hexafluoroacetylacetonato; Ln = Y, Er, Yb) precursors in 1,2-dimethoxyethane (monoglyme) into an evaporator. The precursor solution was kept at room temperature in a sealed tube pressurized under 1.2 bar of Ar, and connected with the injector to the evaporation chamber. The injector used in the LI-MOCVD experiments consists of high-speed electro-valves driven by a computer. The amount of solution injected during the experiment is controlled by the

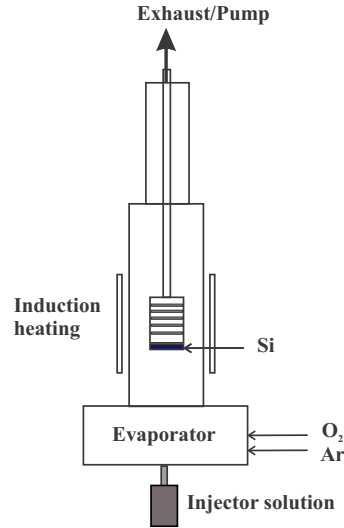


Figure 2.1: Experimental set-up of the pulsed LI-MOCVD apparatus used to deposit rare earth doped YF_3 thin films.

opening time of the injector, the frequency and the number of pulses [87]. This has the advantage of a controlled (“digital”) film growth, since the thickness is determined by the number of pulses, when all other parameters are fixed. Immediately after the solution is injected (~ 1 mg) into the evaporator, flash-vaporization takes place. The vaporized precursors are then carried by an O_2/Ar gas flow into the reaction chamber onto a hot substrate, where a decomposition/reaction of the precursors leads to the film deposition. All relevant processing parameters are shown in Table 2.1.

Table 2.1: Processing parameters for RE: YF_3 film growth by LI-MOCVD.

Substrate temperature [$^{\circ}\text{C}$]	450–650
Evaporation chamber temperature [$^{\circ}\text{C}$]	250
Carrier gas O_2/Ar flow rate [sccm]	560
Oxygen concentration in total gas flow [%]	50–80
Total work pressure [torr]	5
Pulse frequency [Hz]	1
Injector aperture time [ms]	1.5
Concentration precursor solution [M]	0.05
Deposition time [min]	20–40

2.4 Investigation of the film microstructure and composition

Growth conditions were studied on singly doped Er:YF₃ films and, subsequently, Er/Yb co-doped films were fabricated in the same manner. The growth rate and structural properties of the films were not affected by the additional presence of Yb³⁺ ions.

Influence of the oxygen gas flow on the film microstructure. The effect of processing parameters such as the oxygen concentration and deposition temperature on the final microstructure has been investigated in detail. Oxygen acts both as a carrier gas and reaction gas in the CVD process, where it is required in the decomposition pathway of Y/RE(hfac)₃, with the formation of trifluoroketones or -aldehydes and CO₂ as decomposition products [98]. The independence of the film composition on the oxygen flow was demonstrated by qualitative EDX analysis.

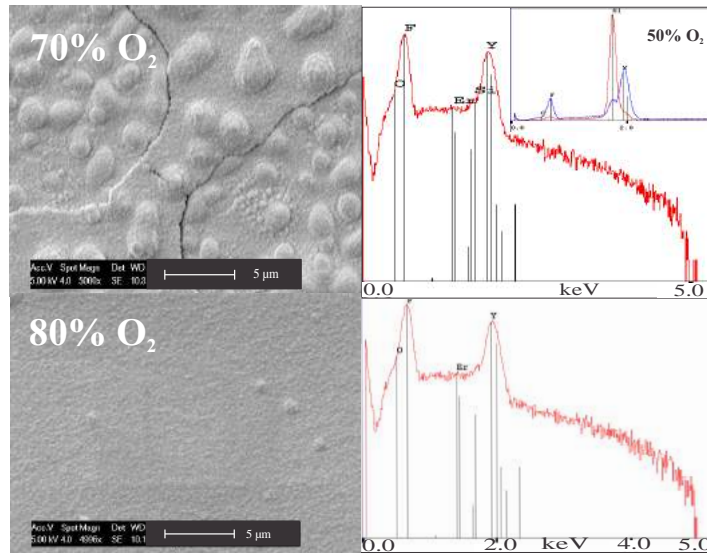


Figure 2.2: SEM micrographs of Er:YF₃ films deposited at 590 °C with 70% (top) and 80% (bottom) oxygen concentration in the carrier gas flow. The EDX spectra show the intensity of the X-ray lines K α of F, O, Si (substrate), L α line of Y and the M line of Er in log-scale. As an inset graph added is the EDX spectrum of an Er:YF₃ film deposited at 590 °C and 50% for two measuring points of the film (blue: center, red: edge); since the film thickness is rather low, the emission line of Si is clearly visible in the spectrum.

Since the film properties at 50% and 70% oxygen flow are similar, Fig. 2.2 shows only the SEM images of the films grown under 70% and 80% oxygen concentrations. Additionally, the EDX spectrum of a film deposited at 50% oxygen in the gas flow is shown as an inset in Fig. 2.2. The EDX spectra were obtained with an electron beam energy of 5 keV and reveal a film composition consisting of the elements Y, Er and F. The spectral features of the O K α peak are very close to the F K α peak and cannot be resolved at low energy (O K α = 0.525 keV; F

$K\alpha = 0.677$ keV). Therefore, a quantitative EPMA analysis was used to confirm the absence of oxygen in the film composition, yielding a chemical composition of $Y_{1-x}Er_xF_3$ with $x = 0.017$ for films grown both at 70% and 80% O_2 . This confirms the actual formation of YF_3 and the clean decomposition of the precursors, since no O peaks were detected in the analysis, hence the oxygen partial pressure used in these experiments does not influence the film composition.

The infrared spectra in Fig. 2.3, showed well-defined absorption peaks with maxima at 143(w), 220(s), 239(m), 262(s), 362(m), 395(m) and 434(w) cm^{-1} , corresponding to Y–F vibrations, and no residual compounds were detected [107]. The FWHM of the Y–F peak at ~ 363 cm^{-1} decreases when increasing the oxygen partial pressure: from 58 cm^{-1} (50%) to 39 and 19 cm^{-1} for an oxygen content of 70 and 80%, respectively. This indicates an increase of the nanostructure and crystallinity of the films.

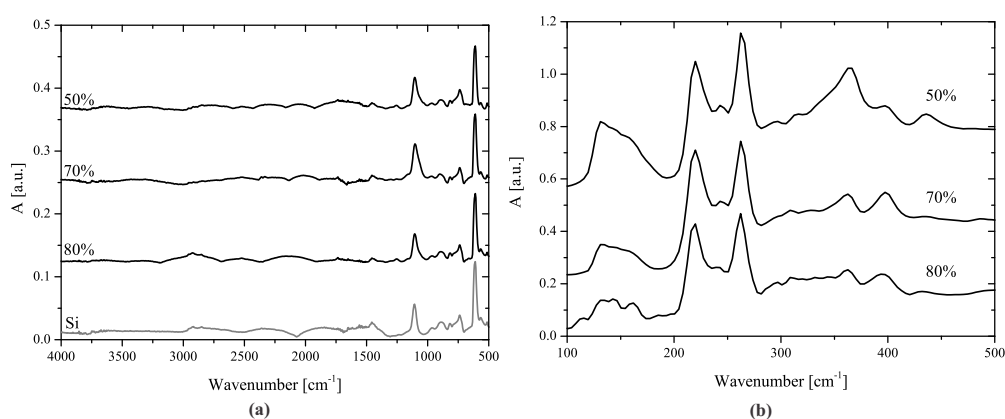


Figure 2.3: (a) MIR spectra of Er:YF₃ films deposited at 590 °C under 50%, 70% and 80% oxygen concentration in the carrier gas flux, depicted with a spectrum of the neat Si substrate and (b) Far-IR spectra of the same. The band assignment corresponds to the vibrational modes of the Y–F bond, as discussed in the text.

Up to an oxygen ratio of 70% in the carrier gas flow, the formation of micro-cracks and mounds in the film surface occurs as shown in Fig. 2.2, for film growth at 590 °C. Increasing the oxygen gas flow to 80% leads to a dense microstructure with small grain size. This effect can be related to the formation of a larger number of nuclei at higher oxygen flow and a higher decomposition efficiency of the precursors. The nuclei will begin to grow in a columnar structure and coalesce into a smooth homogeneous surface at high oxygen flow and also at higher temperature. The cross-section images of films grown at a high oxygen flow (80%) and elevated temperatures such as 590 °C and 650 °C are depicted in Fig. 2.4, exhibiting in both cases a densely packed microstructure.

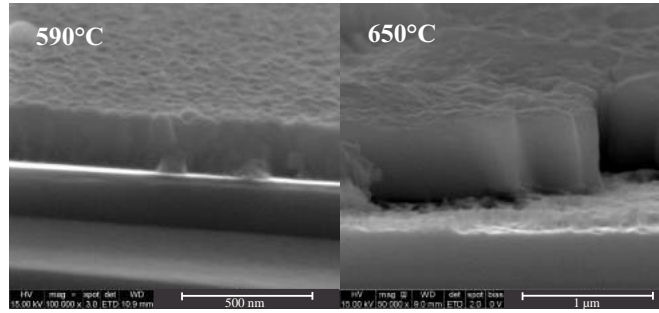


Figure 2.4: Cross-section SEM images of RE:YF₃ films grown at 590 °C (left) and 650 °C (right) under high oxygen gas flow of 80% in the total gas flow.

Influence of the deposition temperature on the film microstructure.

Fig. 2.5 shows the FTIR spectra of a series of Er:YF₃ thin films grown at different deposition temperatures while all other processing parameters are kept constant. The vibrational features become more distinct at higher deposition temperatures due to an increased film thickness and a higher degree of crystallinity of the film.

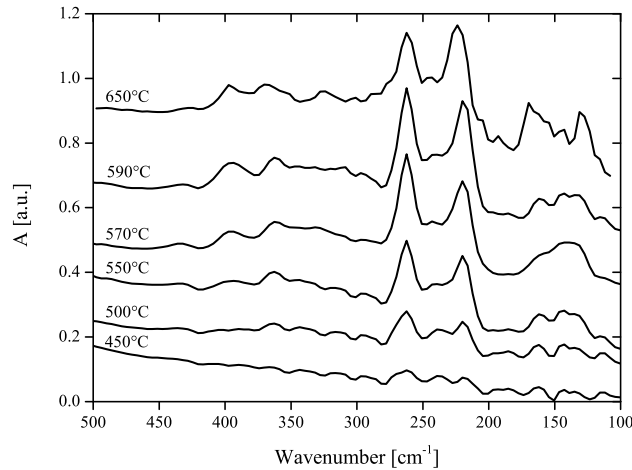


Figure 2.5: FTIR spectra in the 500–100 cm⁻¹ range of Er:YF₃ films deposited over a temperature range between 450–650 °C under 80% oxygen concentration in the carrier gas flux. The bands correspond to vibrational modes involving the Y–F bonds.

The deposition temperature and film thickness have both a crucial impact on the film microstructure. Therefore, Er/Yb:YF₃ films were grown on Si(111) over a temperature range between 450 and 650 °C, keeping all other process parameters constant. The deposition rate increases strongly with temperature, from 60 nm·h⁻¹, at 450 °C, to 750 nm·h⁻¹, at 650 °C. However, films deposited with 80% O₂ in the gas flux in a lower temperature range, i.e. 450–500 °C, show poor crystallinity, indicated by the low reflection intensities in the XRD analysis (Fig. 2.6).

These films are moreover easily scratched off the substrate and exhibit low durability.

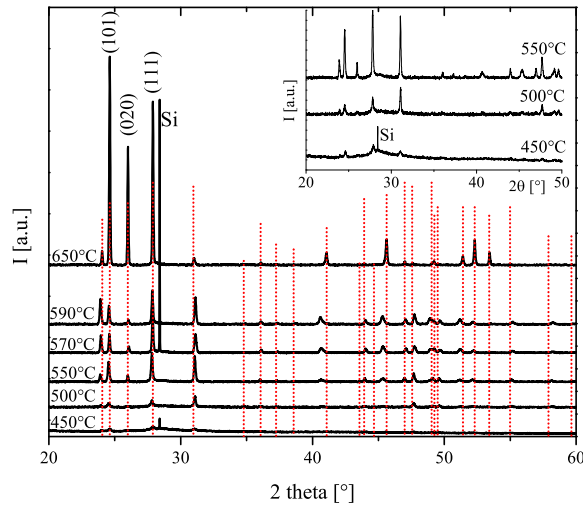


Figure 2.6: XRD patterns of Er:YF₃ thin films grown by MOCVD on Si(111) and deposited at temperatures ranging from 450 to 650 °C. The inset depicts for a better view the diffraction patterns of films grown at lower deposition temperatures. The reference patterns of orthorhombic YF₃ are indicated by the vertical lines (ICDD No. 32–1431).

By increasing the temperature, the reflected intensities become more pronounced, not only due to the temperature effect on the film thickness as a consequence of an increased deposition rate, but also due to an increase in crystallinity. For films deposited at 450–590 °C, the peak positions are shifted compared to the powder diffraction reference patterns of orthorhombic YF₃ (ICDD No. 32–1431), possibly due to residual stresses in the film structure, which are released at higher deposition temperature. The films deposited at 650 °C show furthermore a preferential orientation along the [101] direction with unusually high intensity at 24.6°, compared to the 100 % reflection intensity at 27.9° in the [111] direction for the reference pattern. This might support the idea that the crystallites tend to minimize their surface free energy by developing a texture. The grain size was determined from the line broadening β (full width of half maximum, FWHM) of the most intense reflection in the [111] direction, by applying the Scherrer formula $\beta = 0.9 \cdot \lambda / D \cdot \cos(\theta)$, D being the average crystalline domain size. The grain size increases with the temperature: a value of ~ 40 nm was obtained for films grown at 500 °C, films grown between 550–590 °C have a grain size of ~ 60 nm and films deposited at 650 °C yielded ~ 80 nm for the 111 reflection.

The influence of the Yb co-doping on the structural properties is shown by the XRD patterns, depicted in Fig. 2.7. It seems that increasing the concentration of RE³⁺ ions has an effect on the reflection intensities similar to the use of a higher deposition temperature during film growth. Up to a doping concentra-

tion of 12% Yb, the most intense peak is along the [111] direction; this behavior changes for a doping concentration of 14% Yb, where the preferential orientation is along the [101] direction, as was observed for the sample deposited at 650 °C.

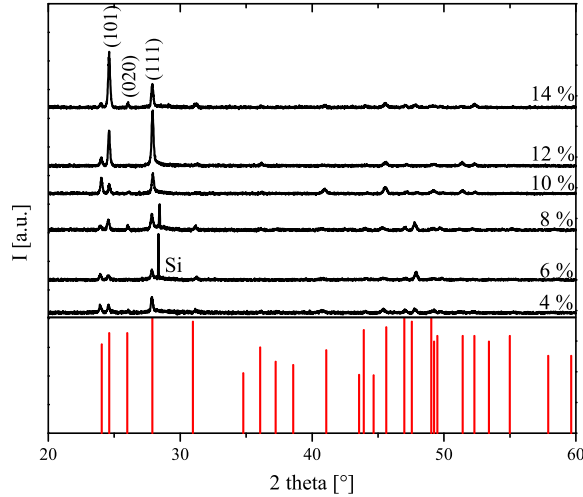


Figure 2.7: XRD diffraction patterns of YF_3 thin films co-doped with 1.5 at.% Er and x at.% Yb, with $x = 4, 6, 8, 10, 12$ and 14 (at.% in solution). The reference patterns of orthorhombic YF_3 are indicated by the vertical lines at the bottom of the graph (ICDD No. 32-1431).

The grain size and shape distribution in Er/Yb: YF_3 films deposited at different substrate temperatures were analyzed by SEM (Fig. 2.8). The top-view SEM micrographs show that films deposited at 590 °C are crack-free, while those deposited at 450 °C and 650 °C show cracks. The films deposited at 450 °C ($d_f \sim 50$ nm) have a mirror-like appearance and consist of small grains up to ~ 40 nm, showing very fine micro-cracks, barely visible in the SEM analysis.

However, the mechanical stability of films grown at 450 °C is low and the films can easily be scratched off the substrate. Films grown at 650 °C ($d_f \sim 630$ nm) have many micro-cracks in their structure, hence their surfaces appear opaque to the naked eye due to light scattering. The particle size distribution is non-homogeneous: some of them are rod-shaped up to $1 \mu\text{m}$ in length, while others have a length of a few hundred nm. This is due to the fact that smaller grains will coalesce at higher temperatures to form aggregates. At 590 °C, films also have a mirror-like appearance and show a homogeneous surface with grains of ~ 60 – 70 nm in size. The morphology of a typical Er/Yb: YF_3 film grown at 590 °C was studied by AFM. The RMS value of the surface roughness of such a film was 5.5 nm and became larger for films grown at 450 °C and 650 °C, with RMS values of 6.8 nm and 41 nm, respectively. However, the as-grown films show a dense columnar microstructure, which provides good film stability.

Crack formation. The thickness is another important factor influencing the microstructure of the films. It was found that cracks are related to a minimum

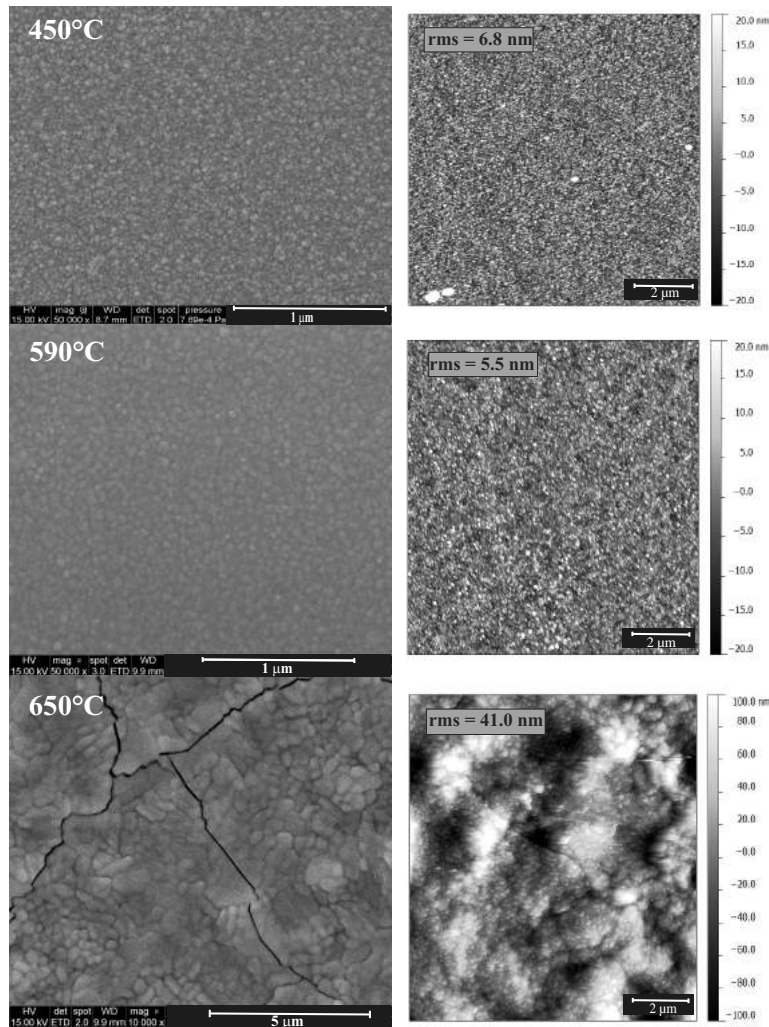


Figure 2.8: Left: FEG–SEM images of an Er/Yb:YF₃ film surface, grown on Si(111) by MOCVD at 450 °C, 590 °C and 650 °C. Images of a higher magnification of films deposited at 450 °C and 590 °C are shown for a better view of the crystalline features. The corresponding AFM morphologies of a 10x10 μm² area of the same film are shown on the right, where additionally the RMS values of the roughness are given.

film thickness: for YF₃ films deposited at 590 °C with a thickness higher than 100 nm, the formation of micro–cracks is favored. The formation of cracks is due to the occurrence of high tensile stresses originating from the thermal expansion coefficient difference between Si and YF₃ (CLTE at 300 K: Si = 2.6·10⁻⁶/K, YF₃ = 16.9·10⁻⁶/K [108,109]) and it limits the total thickness of a crack–free film. Growth of YF₃ films up to a total thickness of about 500 nm on Si(111) substrates can be realized at a deposition temperature of 590 °C. Beyond this critical thickness, macro–cracks occur and the film may craze and lift off the substrate due to high tensile stresses during cooling–down to room temperature (Fig. 2.9).

Film composition. The best results in terms of film microstructural quality (no cracking) and optical performance at the temperatures studied were achieved

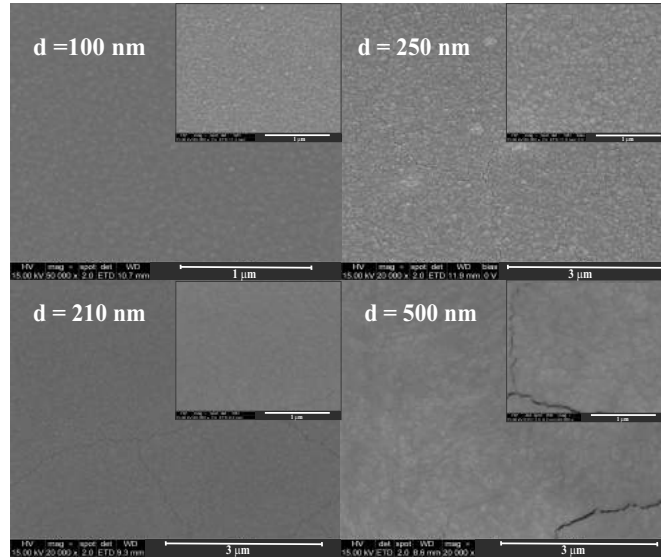


Figure 2.9: Evolution of the crack formation of Er/Yb-doped YF_3 thin films on Si(111). Films were deposited at 590°C with the final thickness indicated in the figure.

with film deposition at 590°C and 80% oxygen concentration in the carrier gas flux, allowing a growth rate of $270\text{ nm}\cdot\text{h}^{-1}$. Since the XRD patterns of the isostructural Er/Yb/Y fluorides are almost identical due to similar lattice parameters, a distinction between them could not be achieved. For Er/Yb co-doped YF_3 films, EPMA was performed to determine the film composition, and a Y/F ratio of 1:3 was obtained, as expected for YF_3 . However, the atomic concentration of RE^{3+} ions in the film depends strongly on the deposition temperature. This is illustrated in Fig. 2.10, where, for a fixed Er concentration of 1 at.% in the precursor solution (cationic ratio $\text{Er}/(\text{Er} + \text{Y})$), the Er concentration in the film is expressed as a function of the substrate temperature.

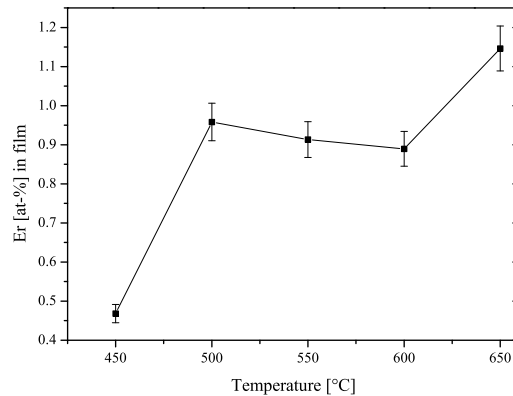


Figure 2.10: Influence of deposition temperature on the final atomic concentration of Er in YF_3 films, with an initial Er content fixed at 1 at.% in the precursor solution.

For a low deposition temperature of 450 °C, about half (0.46 at.%) of the initial concentration of Er in solution (1 at.%) is obtained in the film. Increasing the substrate temperature leads to a strongly increased rare earth concentration in the film and it is shown that between 500–600 °C the concentration is rather constant. However, at 650 °C the deposition activity (i. e. efficiency) of the metalorganic precursors is further increased and leads to an even higher Er concentration in the film. The concentrations of Er/Yb (RE) in the films (atomic ratio RE/(RE+Y) at.%) grown at 590 °C for a solution with different molar ratios of RE(hfac)₃/(RE(hfac)₃+Y(hfac)₃) are depicted in Fig. 2.11.

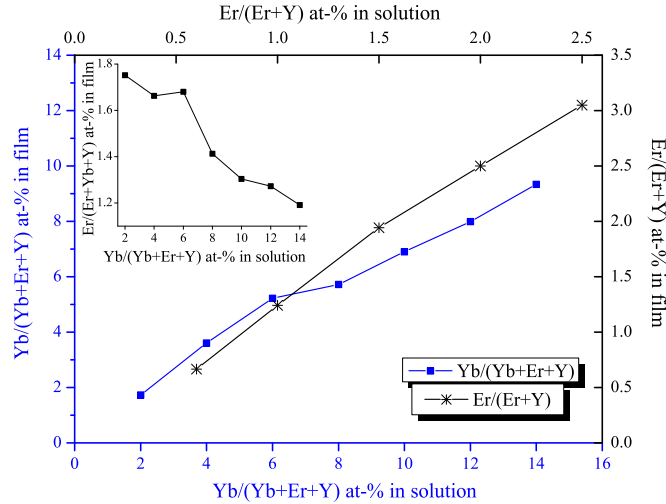


Figure 2.11: Rare earth (Er, Yb) concentration in the film (RE/(RE+Y) at.%) for different concentration of RE(hfac)₃/(RE(hfac)₃+Y(hfac)₃) in solution, for films grown by MOCVD at 590 °C. The inset shows the Er concentration in the film dependent on the Yb concentration in solution, for Er/Yb co-doped YF₃.

The Er/(Er+Y) ratios for singly Er-doped YF₃ films indicate that the Er(hfac)₃ precursor shows more deposition activity than the Y(hfac)₃ precursor, explaining the higher concentration of Er in the film compared to the solution. As for the Er/Yb co-doped films, both RE³⁺ ions influence each other during the deposition process, causing a lower Yb concentration in the films compared to the initial concentration in solution. Furthermore, the Yb³⁺ ions have an effect on the deposition rate of the Er³⁺ ions, as can be seen in the inset graph of Fig. 2.11: for a fixed concentration of 1.5 at.%, the concentration of Er in the film decreases when the Yb concentration in solution increases. This indicates that the Yb(hfac)₃ precursor reduces the deposition yield of Er(hfac)₃ and vice versa.

2.5 Optical performance and Raman spectra of Er/Yb:YF₃ films

A high optical transmission in the visible region for RE doped materials is desirable in order to obtain effective light emission. The optical transmission spectrum

depicted in Fig. 2.12, was obtained from an Er/Yb:YF₃ thin film grown on fused silica.

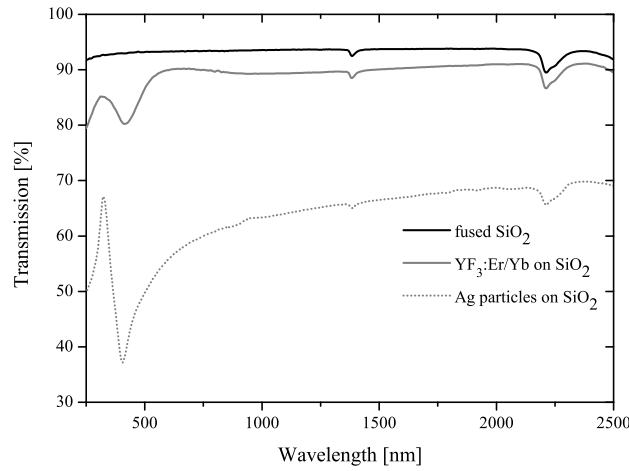


Figure 2.12: Optical transmission spectrum of Er/Yb-doped YF₃ film on fused silica (grey solid line). The black solid line shows the transmission of the neat substrate and, the dotted black line shows the spectrum from the edge of the sample, where the silver paste was applied.

We do find a slight decrease in light transmission of about 3% for a ~ 100 nm thin film grown on fused SiO₂ compared to the neat substrate, caused by scattering of visible light by aggregated particles and by the reflection on the different interfaces. However, from these results we can still conclude that the RE-doped films have a high transparency due to the dense and homogeneous film structure formed by nanometer-sized grains. Furthermore, the spectra exhibit a sharp absorption at 405 nm, which can be assigned to the absorption of silver particles [110]. This is due to the fact that a silver paste is applied on the edges of the rear side of the substrate, to achieve a substrate fixation onto the sample holder. During the reaction, Ag particles may diffuse from the edges toward the center of the substrate, and thus will influence the transmission measurements.

The refractive index was studied by spectroscopic ellipsometry (SE) over the 300–1200 nm spectral range. The analysis of the SE data was achieved by fitting the experimental spectra to the calculated spectra of a model. The dispersion of the refractive index was expressed by the Sellmeier equation, $n^2 = A + B(\lambda^2 / (\lambda^2 - \lambda_0^2))$, with the single effective oscillator with a characteristic wavelength λ_0 . For the three unknown fitting parameters, the following values were determined: $A = 1$, $B = 1.27$ and $\lambda_0 = 38.5$. Our results show that the value of refractive index at 600 nm is 1.51 with a difference of 0.02 compared to the value of 1.53 reported for neat YF₃ thin films [111]. In principle this can have several reasons, including the method of film deposition and inhomogeneity of the film which may cause the difference in optical constants. We applied a multi-layer model for the fitting of the data, using a void function to determine the void fraction in the film. Since

the obtained results included a void fraction $< 1\%$, we believe the as-grown films to be homogeneous. Furthermore, it should be emphasized at this point that the obtained refractive index depends on the selection of the final model for the analysis of the SE data. For instance, when expressing the dispersion using the Cauchy formula, $n(\lambda) = A + B \cdot 10^4/\lambda^2 + C \cdot 10^9/\lambda^4$, one obtains a refractive index of 1.57 at 600 nm, a value also found elsewhere in the literature [112]. The Cauchy coefficients used in the fitting of the SE data were determined with $A = 1.53$, $B = 1.62$ and $C = -1.37$. Since the difference in the refractive index derived from the Sellmeier and Cauchy equations is lower than 5%, both results are within the margin of error and thus considered to be reliable.

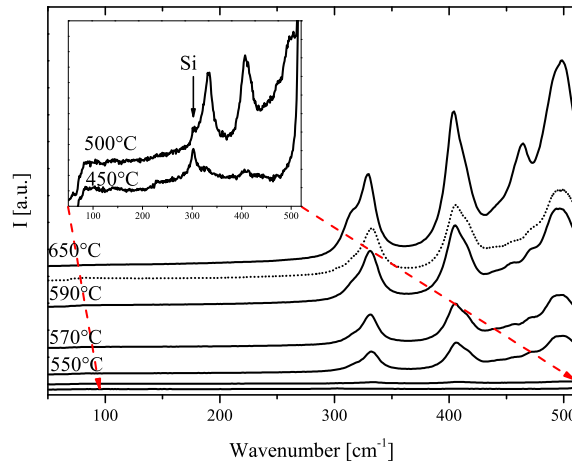


Figure 2.13: Raman spectra of Er:YF₃ films grown by MOCVD at different temperatures indicated in the figure. For a better view, the spectra of films grown at lower temperature are depicted in the inset figure. For comparison, the dotted line shows an Er/Yb co-doped YF₃ film grown at 590 °C. A Raman peak at $\sim 300 \text{ cm}^{-1}$ of c-Si can be seen in the spectra for films of lower thickness grown at lower temperature.

Room temperature Raman spectra of Er:YF₃ thin films deposited at different temperatures have been studied over the 50–510 cm^{-1} range (Fig. 2.13). For comparison, the spectra are depicted together with that of an Er/Yb co-doped film. The main bands are located at 329, 404, 469 and 498 cm^{-1} , so the highest phonon energy of YF₃ should be $\sim 500 \text{ cm}^{-1}$. These bands are assigned to the Raman-active vibrational modes of orthorhombic YF₃, but due to the polycrystalline nature of the material, mode identification is not possible [113]. Neglecting the thickness effect on the Raman mode intensities, it can be seen that higher temperatures induce film crystallization. A small peak shift of $\sim 2 \text{ cm}^{-1}$ to lower frequency for the film grown at 650 °C is observed.

A slight decrease in the FWHM values for the band centered at $\sim 400 \text{ cm}^{-1}$, from 20 cm^{-1} for films grown $< 600 \text{ °C}$ to 18 cm^{-1} for growth at 650 °C, is also observed. This can be explained by the increasing crystallinity of the YF₃ phase. The poor crystallinity of films grown at 450 °C is in agreement with the results obtained by

XRD. The Raman peak at $\sim 300\text{ cm}^{-1}$, observed in films of lower thickness, are overtones of the transverse acoustic 2 TA phonons in c-Si [114].

2.6 Summary

Er/Yb-doped YF_3 films were successfully grown by LI-MOCVD on Si(111) wafers and fused silica. Of all growth parameters studied, the substrate temperature and the oxygen flow were found to have the most crucial effect on the film microstructure. These RE fluorides may be easily deposited as smooth thin films, if the substrate is heated to 590°C and the carrier gas flux consists of 80% oxygen. The optical properties allow us to conclude that these films were grown in a dense and homogeneous structure. Furthermore, the effect of the film thickness and tensile stress on the microstructure has to be taken into account in order to obtain crack-free films.

Based on

E.L. Payrer, R.M. Almeida, C. Jimenez, P.-D. Szkutnik, J.-L. Deschanvres
Surface & Coatings Technology 230 (2013) 22–27

Three-photon UpC of RE³⁺-doped YF₃ thin films

We investigated the Stokes and anti-Stokes luminescence characteristics of singly Er-doped and Er/Yb co-doped YF₃ thin films. A strong green (Er:²H_{11/2},⁴S_{3/2} →⁴I_{15/2}), as well as a red (Er:⁴F_{9/2} →⁴I_{15/2}) and a violet (Er:²H_{9/2} →⁴I_{15/2}) emission band was observed for all films after 972 nm excitation. The up-converted emission was studied as a function of the Yb concentration, and a change in the red/green emission ratio observed when increasing the sensitizer concentration. An Er-to-Yb back transfer corresponding to ⁴S_{3/2} →⁴I_{13/2}:²F_{7/2} →²F_{5/2} starts to take place with increasing Yb concentration. As a consequence, the red emission is shown to be enhanced through an upward energy transfer ⁴I_{13/2} →⁴F_{9/2}. The excitation power dependence of an intermediate state, *i*, showed slopes of P^{i/2} at high pump power and slopes converging to Pⁱ for lower excitation power. Further, luminescence decay characteristics of ⁴S_{3/2} and ⁴F_{9/2} states showed the influence of Yb co-doping in the relaxation processes of Er³⁺.

3.1 Introduction

Photon up-conversion (UpC) is an important nonlinear optical process to achieve light conversion and has been extensively investigated over the last decades [14,30]. Since an UpC process strongly relies on the presence of metastable energy states, rare earth and transition metal ions as optically active species doped in host lattices are most commonly used. In particular, for the conversion of $\sim 1\ \mu\text{m}$ IR light, host materials doped with rare earth ions such as Er^{3+} , Ho^{3+} , Tm^{3+} and additionally sensitized by Yb^{3+} , are frequently used because of their large variety in energy levels [14, 44, 62]. Upconverters find important applications in various fields of science and technology, including their use as biolabels, in flat panel displays, lasers and photovoltaics [16, 21, 60, 115–118].

Although IR-to-visible light conversion was first proposed by Bloembergen [13], the breakthrough for a deeper understanding of UpC processes was achieved by Auzel with the description of ETU (energy transfer up-conversion) or APTE (l'addition des photons par transfer d'energie). Auzel discovered that higher excited states in the light-emitting ion might be populated through successive energy transfer steps from a neighboring ion [76].

Since the spectral features and the overall efficiency of the UpC process strongly depend on the host material, dopant levels and nanostructural properties, a lot of effort has been done to produce efficient upconverter materials under consideration of all influencing factors. For instance, it is well known that the cut-off phonon energy of the host material influences the rate of nonradiative multiphonon relaxation due to electron-phonon interactions. Thus one can control the predominance of the red or green emission in Er-doped phosphors: in oxide host lattices, the red emission may dominate over the green, and vice-versa in fluoride hosts, where the green emission usually dominates over the red [119]. Other important factors for the total emission output are the excitation power and the ion doping level, which influences the ion-ion interactions [120].

Among the well-known fluoride host materials, such as alkali metal rare earth fluorides, rare earth oxyfluorides and rare earth fluorides, the latter are promising candidates for highly efficient UpC materials. Particularly YF_3 has been shown to be a highly efficient upconverter material, due to its good chemical and physical properties such as high durability, a wide band gap ($\sim 10\ \text{eV}$), low phonon energy and suitable sites to substitute Y^{3+} with other trivalent rare earth ions [121–123]. While a large amount of research has been done on nano-structured YF_3 phosphors [104, 117, 121, 124–126], fewer attention has been drawn to thin films of RE-doped YF_3 [95, 98]. These films might be used for photovoltaic cells, where an additional UpC layer on the rear side of the cell can be used to enhance the photocurrent of the device, due to a reduced transmission loss of the cell.

In this chapter, we discuss the UpC behavior of Er/Yb-doped YF_3 thin films, deposited on Si(111) substrates by pulsed liquid injection MOCVD (LI-MOCVD). We observed a strong green up-converted emission after excitation of singly Er

and Er/Yb co-doped YF_3 films at 972 nm. The visible emission was investigated as a function of the sensitizer concentration, in order to achieve a maximum emission output. Lifetimes of intermediate states $^4S_{3/2}$ and $^4F_{9/2}$ were determined, to show the influence of the Yb concentration in the relaxation processes of Er^{3+} . Furthermore, we elucidate the most probable excitation routes for the population of the higher excited states in the Er^{3+} ion by the assignment of the luminescence spectra and the analysis of the excitation dependence of the up-converted emission. Power dependence studies of the intermediate states are an especially powerful tool for the interpretation of the underlying UpC mechanism and allow one to investigate whether ESA or ETU is the predominant process. The predicted slopes of P^i , for an intermediate state i , are only to be expected in the limit of low UpC rates and converge to P^1 when the UpC rates are larger than the linear decay rates. In the case of intermediate pump powers, the measured slopes are between the two limits attained at large and small UpC rates. Furthermore, several nonlinear processes might coexist during the actual UpC process, leading to a more complicated situation, which makes the interpretation of the experimentally measured slopes more challenging.

3.2 Experimental details

Stokes luminescence spectra were recorded between 500–750 nm with a Jobin-Yvon/ Horiba LabRam Micro-Raman spectrometer and 488 nm excitation from an Ar^+ laser ($P = 75 \mu W$). The UpC luminescence spectra were recorded under 972 nm laser diode excitation focused with a 10X microscope objective on each sample, and the up-converted luminescence was collected by a multimode fiber (core diameter 600 μm) and in the following analyzed by a spectrometer consisting of a 0.85 m double monochromator coupled to a photomultiplier tube detector (Hamamatsu R 928).

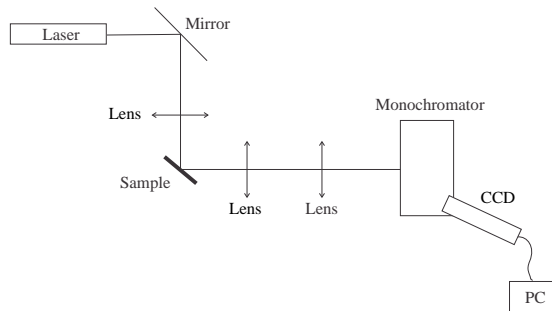


Figure 3.1: Experimental set-up for the luminescence decay measurements of thin films.

The luminescence decay curves of the $^4S_{3/2}$ and $^4F_{9/2}$ energy levels of Er^{3+} were recorded under pulsed laser excitation (EKSPLA YAG pumped by OPO, 10 Hz, pulse duration: 6 ns) at 980 nm. The signal was collected through two lenses with focal lengths of 50 and 100 mm by a Jobin-Yvon HR 250 monochromator (3001/mm, blaze at 500 nm), coupled to an EGG Princeton (Roper) ICCD camera with 1024 diodes, and a detection range from 200 to 920 nm (Fig. 3.1).

3.3 Results and discussion

3.3.1 Stokes luminescence of Er/Yb-doped YF₃ thin films

In Table 3.1 the initial rare earth doping concentrations in the precursor solution and the final composition for RE:YF₃ films are summarized. For reasons of simplicity, we always refer in the following to the rare earth ion content in the precursor solution, instead of the actual film composition.

Table 3.1: Rare earth concentrations (RE/(RE+Y)·100 [at.%]; RE = Er, Yb) in solution and film for singly-doped Er and Er/Yb co-doped YF₃ films, grown by pulsed LI-MOCVD.

RE [at.%] in solution	RE [at.%] in film
0.6 Er	0.7 Er
1 Er	1.1 Er
1.5 Er	1.8 Er
2 Er	2.5 Er
2.5 Er	3.0 Er
1.5 Er/ 2 Yb	1.8 Er/ 1.7 Yb
1.5 Er/ 4 Yb	1.7 Er/ 3.6 Yb
1.5 Er/ 6 Yb	1.7 Er/ 5.2 Yb
1.5 Er/ 8 Yb	1.4 Er/ 5.7 Yb
1.5 Er/ 10 Yb	1.3 Er/ 6.9 Yb
1.5 Er/ 12 Yb	1.3 Er/ 8.0 Yb
1.5 Er/ 14 Yb	1.2 Er/ 9.3 Yb
1.5 Er/ 20 Yb	1.3 Er/ 13.1 Yb

The Stokes luminescence spectra of singly Er-doped films were recorded in the 500–750 nm range using a Micro-Raman spectrometer upon excitation with the 488 nm line of an Ar⁺ laser. As shown in Fig. 3.2 (a), the most intensive luminescence bands are observed at ~ 520 and 540 nm, corresponding to transitions $^2H_{11/2}$ and $^4S_{3/2} \rightarrow ^4I_{15/2}$, and a weaker band at ~ 660 nm, corresponding to the transition $^4F_{9/2} \rightarrow ^4I_{15/2}$. Due to the overlap of the two emission bands originating from $^2H_{11/2}; ^4S_{3/2}$, these transitions are simply referred to as the green emission, and no attempt is made to separate these two emission bands. With 488 nm pumping, the green light emitting levels are fed due to multiphonon relaxation from the $^4F_{7/2}$ level and constitute the most prominent band in the emission spectrum. Much weaker red luminescence from the $^4F_{9/2}$ is observed due to relaxation from the upper state $^4S_{3/2}$.

Fig. 3.2 (b) displays the integrated luminescence intensities associated with the optical emissions at ~ 540 nm and 660 nm, and the sum of these emission bands as a function of the Er contents in the films.

The luminescence intensities in the green and red spectral domains peak at an Er content of 2 at.% and drop when the Er concentration is further increased. The luminescence emissions from the $^4S_{3/2}$ and $^4F_{9/2}$ states are both significantly quenched with an Er concentration > 2 at.% in YF₃. The concentration dependence of the emission intensities of Er³⁺ is due to self-quenching (cross-relaxation)

3 Three-photon UpC of RE^{3+} -doped YF_3 thin films

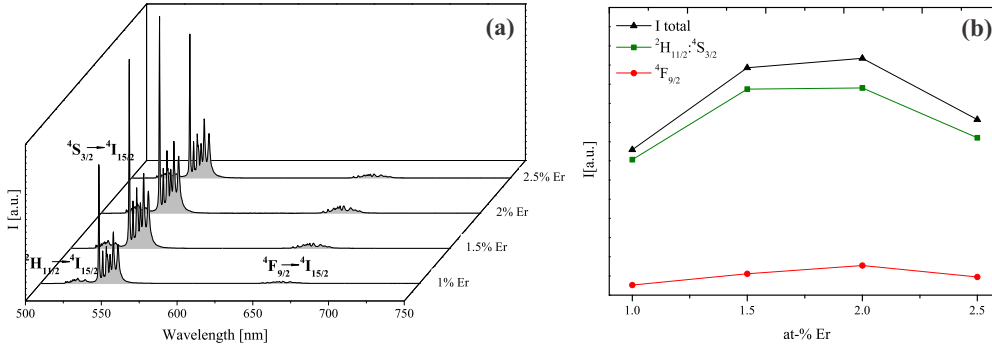


Figure 3.2: (a) Measured PL intensities from the $^2H_{11/2}$, $^4S_{3/2}$ and $^4F_{9/2}$ levels centered at 540 and 660 nm in Er:YF₃ thin films under 488 nm excitation; the Er dopant level is denoted in the figure. (b) Integrated PL intensities at 540 nm ($^2H_{11/2}:^4S_{3/2}$) and 660 nm ($^4F_{9/2}$), respectively, for different Er concentrations in YF₃ films. The total emission intensity is represented by the sum of the integrated green and red emission intensities.

of the higher-lying states and the occurrence of energy migration among closely-spaced ions. In fact, at high Er concentrations, the distance r between the ions becomes smaller, inducing electric dipole-dipole interactions between the ions, which obey Förster's theory with scaling behavior r^{-6} [77]. This effect causes a reduced light emission due to energy transfer between the ions and is usually observed in fluoride hosts for an Er concentration of $> 1-2$ at.% [127, 128].

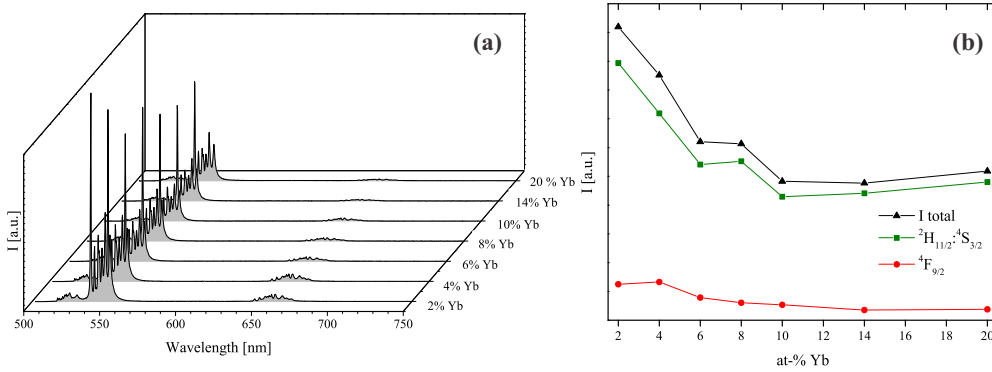


Figure 3.3: (a) PL spectra of YF₃ co-doped with Er (1.5 at.%) and varying contents of Yb as indicated in the graph, under $\lambda_{exc.} = 488$ nm ; (b) concentration dependence of the integrated Vis-luminescence intensities originated from the $^2H_{11/2}$, $^4S_{3/2}$ and $^4F_{9/2}$ levels as a function of x at.% Yb in Er/Yb co-doped YF₃. The triangles show the sum of the integrated red and green emission bands of each sample.

A detailed study on the self-quenching of luminescence was done for NYF:Er (NYF = Na_{0.4}Y_{0.6}F_{2.2}) by Tkachuk *et al.* [129]. It was shown that the $^4S_{3/2}$ level is significantly quenched with increasing Er concentration, leading to the transitions $^4S_{3/2} \rightarrow ^4I_{9/2}$, $^4I_{13/2}: ^4I_{15/2} \rightarrow ^4I_{13/2}$, $^4I_{9/2}$, as well as energy migration according to the transitions $^4S_{3/2} \rightarrow ^4I_{15/2}: ^4I_{15/2} \rightarrow ^4S_{3/2}$. The luminescence self-quenching for the red emission from $^4F_{9/2}$ was found to be concentration independent and mostly due to nonradiative multiphonon transitions and/or quenching due to impurities

acting as traps. However, since population of the ${}^4F_{9/2}$ level is mainly due to multiphonon relaxation processes from the higher energy ${}^4S_{3/2}$ state, concentration quenching of this level will reduce the red emission. The gain in the total luminescence intensity is shown to be rather small when increasing the Er concentration from 1.5 to 2 at.%, hence the final Er concentration in Er/Yb co-doped samples was fixed at 1.5 at.%, assuming that concentration quenching already occurs.

The photoluminescence spectra of Er/Yb co-doped YF_3 films were recorded under 488 nm laser excitation and illustrate the influence of the Yb co-doping on the Er emission (Fig. 3.3). The luminescences from the excited states ${}^2H_{11/2}$, ${}^4S_{3/2}$ and ${}^4F_{9/2}$ are gradually reduced when increasing the Yb content in the film. This can partly be explained by means of the energy level scheme of the Er–Yb ion couple depicted in Fig. 3.4, which allows one to identify the most probable processes that lead to the de-excitation of the higher excited states in the Er^{3+} ion. Since the Yb^{3+} ions show no optical absorption at 488 nm, only the Er^{3+} ions are directly excited into the ${}^4F_{7/2}$ energy levels.

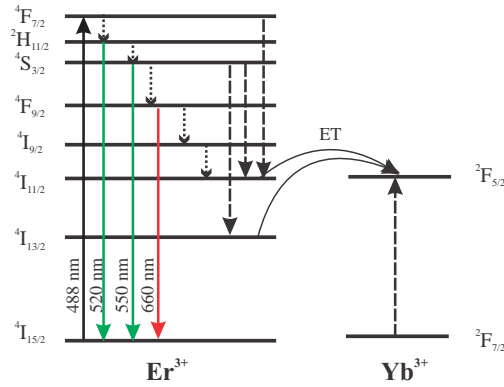


Figure 3.4: Energy level scheme of the Er–Yb ion couple, showing the most probable de-excitation processes at 488 nm pump wavelength. Solid and dotted arrows indicate the radiative and nonradiative de-population mechanisms. Transitions involved in an Er-to-Yb energy transfer are indicated by dashed arrows. For convenience, only the energy levels which take part in the down-conversion process in the visible λ -range are considered.

Due to the small energy gap separation of ${}^4F_{7/2}$ to the next lower-lying energy levels, fast nonradiative multiphonon relaxations are responsible for the depopulation of ${}^4F_{7/2}$ towards the ${}^2H_{11/2}$ and ${}^4S_{3/2}$ energy levels. Subsequently, intensive green emission, attributed to transitions ${}^2H_{11/2}$, ${}^4S_{3/2} \rightarrow {}^4I_{15/2}$, takes place. The population pathway of level ${}^4F_{9/2}$ will most probable occur via another multiphonon relaxation transition, since the ${}^4S_{3/2}$ – ${}^4F_{9/2}$ energy gap separation is only $\sim 3000 \text{ cm}^{-1}$. A total of ~ 6 lattice phonons are required to bridge the gap, for a cut-off phonon frequency of $\sim 500 \text{ cm}^{-1}$ in YF_3 , which makes nonradiative multiphonon relaxation a competitive process [42]. More nonradiative multiphonon relaxation processes might occur through ${}^4F_{9/2} \rightsquigarrow {}^4I_{9/2} \rightsquigarrow {}^4I_{11/2}$. In the case of Yb co-doping, a resonant nonradiative energy transfer from the Er-to-Yb is feasible by ${}^4F_{7/2} \rightarrow {}^4I_{11/2}$ (Er) : ${}^2F_{7/2} \rightarrow {}^2F_{5/2}$ (Yb) or a phonon-assisted energy

transfer according to the transitions $^4S_{3/2} \rightarrow ^4I_{11/2}$ (Er) : $^2F_{7/2} + \hbar\omega \rightarrow ^2F_{5/2}$ (Yb) might occur [119]. Furthermore, since the energy gap between $^4S_{3/2} \rightarrow ^4I_{13/2}$ (Er) is just slightly larger than $^2F_{7/2} \rightarrow ^2F_{5/2}$ (Yb), yet another energy transfer from Er-to-Yb is possible [130]. This explains the observed reduction in the total emission intensity and it becomes clear that for a Yb concentration larger than 10 at.%, the energy transfer rate among Er-Yb pairs cannot be further increased, due to the restricted number of Er^{3+} ions. This finally leads to a leveling off in the total emission intensities.

3.3.2 Anti-Stokes (UpC) luminescence spectra of Er/Yb-doped YF_3 thin films

Fig. 3.5 (a) shows the emission spectra for a range of concentrations of Er-doped YF_3 films, measured under laser excitation at 972 nm ($P = 0.90$ W). Strong green emission is obtained by the absorption of two photons at this pump wavelength and shall be discussed in more detail when the excitation routes for the UpC emission in Er/Yb co-doped YF_3 are treated. The UpC luminescence intensity studied as a function of the Er concentration, achieves a maximum for a 2.5 at.% Er incorporation (2 at.% in solution) and luminescence self-quenching starts to take place when the Er concentration is further increased.

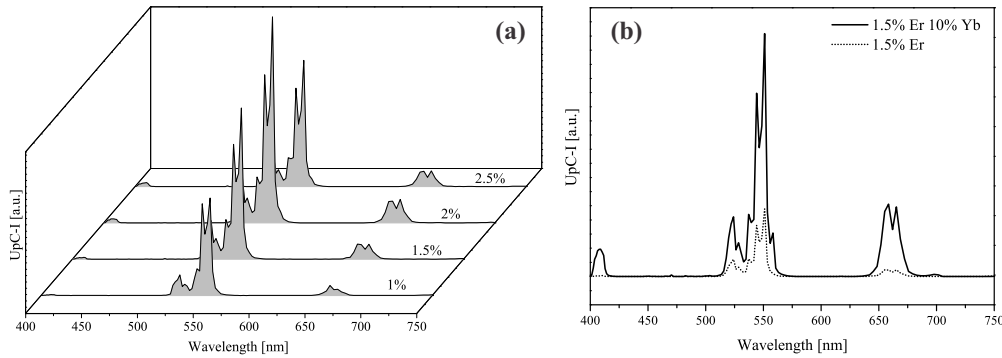


Figure 3.5: (a) UpC luminescence spectra of Er: YF_3 thin films pumped at 972 nm laser wavelength; $P = 0.90$ W. (b) Sensitization effect of the UpC emission in Er^{3+} through additional 10 at.% co-doping of Yb in 1.5 at.% Er: YF_3 .

Since the maximum in UpC emission possible for singly Er-doped systems is limited by the available number of Er^{3+} ions – before self-quenching takes place – a sensitization of the Er^{3+} emission by Yb^{3+} ions allows to increase the UpC emission by a multiple. This is due to the higher absorption oscillator strength of Yb, which is about 10 times that of Er at 972 nm [119]. Fig. 3.5 (b) illustrates the sensitization effect of Yb on the Er^{3+} emission, achieving an increase in the total UpC emission intensities by a factor of 5 due to co-doping of a sample containing 1.5 at.% Er with 10 at.% Yb. Thus, the effect of Yb co-doping was studied for a series of 1.5 at.% Er-doped samples in order to achieve the best UpC intensities. The Vis-UpC luminescence spectra of Er/Yb co-doped YF_3 thin films excited by a 972 nm laser diode are shown in Fig. 3.6 (a). In all samples, the most dominant emission bands are observed in the green spectral range at $\lambda_{max} \sim 550$ nm and in

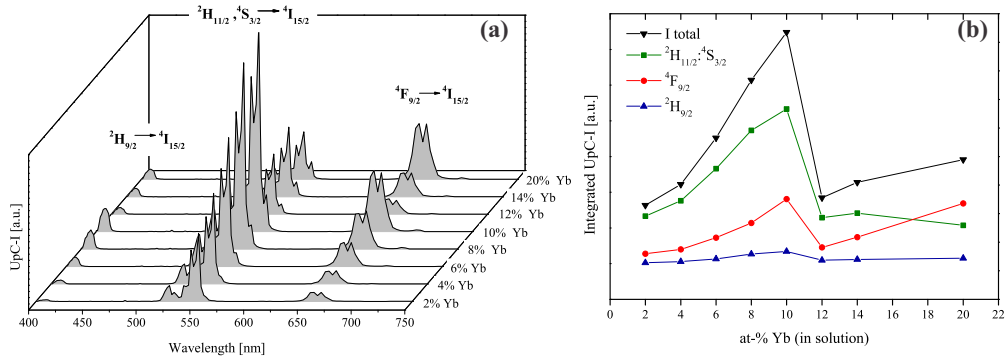


Figure 3.6: (a) Visible UpC luminescence of (1.5%)Er/(x%)Yb:YF₃ excited at 972 nm, P = 0.90 W, with the at.% Yb indicated in the graph. (b) Concentration dependence of the violet ($\lambda_{max} \sim 410$ nm), total green ($\lambda_{max} \sim 550$ nm) and red emission ($\lambda_{max} \sim 660$ nm) intensities of Er/Yb:YF₃ on the at.% fraction of Yb. In addition, the sum of the integrated luminescence intensities is depicted.

the red region at $\lambda_{max} \sim 660$ nm. A weaker luminescence band is found in the violet ($\lambda_{max} \sim 410$ nm) spectral domain, which, however, is overpowered by the strong green up-converted luminescence of the films, that can even be observed by the naked eye. The UpC spectra exhibit features comparable to those reported in the literature for Er/Yb co-doped YF₃ nanocrystals, although the relative green and red emission intensities might vary depending on the RE³⁺ ion concentration and the preparation methods used [104, 120, 121, 131].

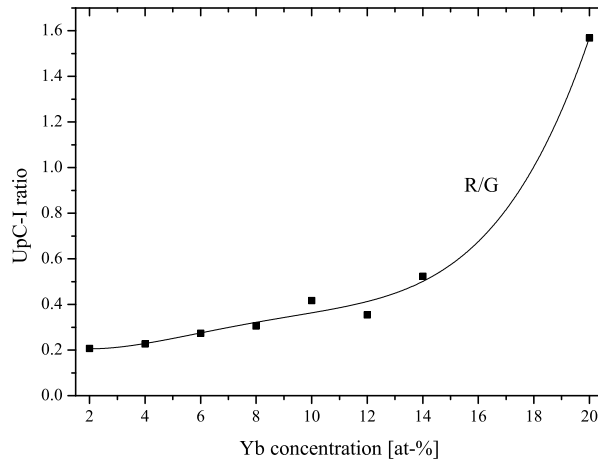


Figure 3.7: Red to green (R/G) emission intensity ratio as a function of the Yb concentration in (1.5 at.%)Er/Yb:YF₃ at 972 nm excitation.

The ratios of the green and red (G/R) emission in RE:YF₃ films are different for 488 nm and IR excitation, whereupon the red emission is enhanced under 972 nm excitation. For instance, for 1.5 at.% Er:YF₃, the G/R integrated luminescence intensity ratio decreases from about 10 for the Stokes emission at 488 nm pumping

– depicted in Fig. 3.2 – to a G/R ratio of 7 for the anti-Stokes emission pumped at 972 nm, see Fig. 3.5. This indicates that the population mechanisms for the green and red up-converted emissions are of a different nature.

Significant changes in the emission intensities are observed for films containing a Yb concentration up to ~ 10 at.%, showing a maximum in the up-converted luminescence, followed by a strong decrease in the emission intensities when the Yb concentration is further increased (Fig. 3.6 (b)). Films with Yb dopant levels larger than ~ 12 at.% exhibit again a slight increase in the total UpC intensities, mainly due to the increase in the red emission.

Moreover, the following interesting aspect can be observed: in samples containing a high sensitizer concentration, the ratio of the red to green emission intensities (R/G) changes and the UpC spectrum for ~ 20 at.% Yb shows a predominance of the red content in the emission spectrum. The relative UpC intensity ratio of the red to green emission as a function of the Yb concentration in Er/Yb:YF₃ is illustrated in Fig. 3.7. The R/G ratio increases from 0.21 for a Yb concentration of 2 at.% Yb, to 1.57 for 20 at.% Yb. In order to understand these observations, one has to consider the various population and de-population processes in the energy level scheme of the Er/Yb couple, which are summarized in Fig. 3.8.

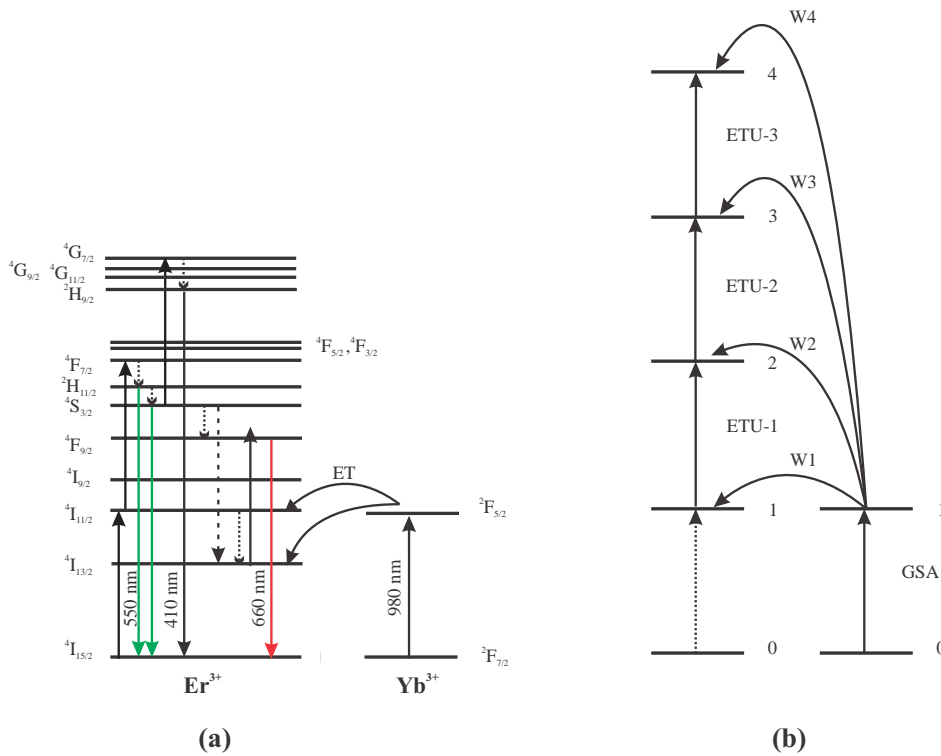


Figure 3.8: (a) Energy level scheme of Er^{3+} and Yb^{3+} showing the most probable processes to generate up-converted luminescence, when excited at ~ 980 nm. Solid and dashed arrows indicate radiative and nonradiative transitions, respectively, curved arrows energy transfer processes. (b) Four-level energy scheme for ETU with corresponding symbols used in Section 3.4.1. For convenience, only the sequential four-step excitation pathway is shown.

The absorption of an incoming 972 nm photon causes mainly the transition ${}^2F_{7/2} \rightarrow {}^2F_{5/2}$ in Yb, since the absorption oscillator strength of Yb is about 10 times larger than that of Er: ${}^4I_{15/2} \rightarrow {}^4I_{11/2}$ [119]. Although excitation of the Er^{3+} ions via ground state absorption (GSA), followed by excited state absorption (ESA) might in any case coexist with the ETU mechanism, we mainly focus on ET and ETU when describing the underlying UpC mechanism. We expect that ESA in Er^{3+} will play a minor role at the Yb dopant level present in the samples. Therefore, due to nearly perfect resonance conditions for Er: ${}^4I_{11/2}$ and Yb: ${}^2F_{5/2}$, ${}^4I_{11/2}$ is mainly populated due to energy transfer from ${}^2F_{5/2}$ [120]. A successive second energy transfer step from Yb allows for the population of the higher excited state ${}^4F_{7/2}$ (ETU), followed by fast nonradiative multiphonon relaxation (MPR) to the lower-lying states ${}^2H_{11/2}$ and ${}^4S_{3/2}$. The relaxation of these levels back to the ground state ${}^4I_{15/2}$ causes intensive green emission. The ${}^2H_{11/2}$ level is thermally populated from ${}^4S_{3/2}$ and hence is observed in the spectra recorded at room temperature [132, 133].

Violet light emission at $\lambda_{\text{max}} \sim 410$ nm from the ${}^2H_{9/2}$ state is caused by a second ETU step, which provokes the transition ${}^4S_{3/2} \rightarrow {}^4G_{7/2}$, followed by a MPR transition towards the ${}^2H_{9/2}$. We summarize the most probable processes leading to the 410 and 550 nm up-converted luminescence under 972 nm excitation as follows:

- (1) Yb: ${}^2F_{7/2} \rightarrow {}^2F_{5/2}$
- (2) ET: Yb: ${}^2F_{5/2} + \text{Er}: {}^4I_{15/2} \rightarrow \text{Er}: {}^4I_{11/2} + \text{Yb}: {}^2F_{7/2}$
- (3) ETU-1: Er: ${}^4I_{11/2} + \text{Yb}: {}^2F_{5/2} \rightarrow \text{Er}: {}^4F_{7/2} + \text{Yb}: {}^2F_{7/2}$
- (4) MPR: ${}^4F_{7/2} \rightsquigarrow {}^2H_{11/2}$ and ${}^2H_{11/2} \rightsquigarrow {}^4S_{3/2}$
- (5) Green emission: ${}^2H_{11/2}, {}^4S_{3/2} \rightarrow {}^4I_{15/2}$
- (6) ETU-2: Er: ${}^4S_{3/2} + \text{Yb}: {}^2F_{5/2} \rightarrow \text{Er}: {}^4G_{7/2} + \text{Yb}: {}^2F_{7/2}$
- (7) MPR: ${}^4G_{7/2} \rightsquigarrow {}^2H_{9/2}$
- (8) Violet emission: ${}^2H_{9/2} \rightarrow {}^4I_{15/2}$

Based on the assumptions made with regard to the excitation and de-excitation pathways, we conclude that for efficient emission from ${}^4S_{3/2}$, the population of the intermediate state ${}^4I_{11/2}$, through energy transfer from Yb: ${}^2F_{5/2}$, plays a key role. Increasing the population density of ${}^4I_{11/2}$ by increasing the Yb concentration is successful until energy back transfer from Er-to-Yb becomes competitive and limits the UpC efficiency. This explanation is supported by the long lifetime of the ${}^4I_{11/2}$ state in Er (~ 10 ms [119]) and energy conditions close to resonance with Yb: ${}^2F_{5/2}$, allowing efficient energy forward and back transfer. We hence observe a decrease in the green emission for high Yb concentrations. As it was discussed earlier for the Stokes emission in Er/Yb:YF₃, a reduced green emission is due to nonradiative resonant and phonon-assisted energy transfers (PAT) from Er-to-Yb, which correspond to ${}^4F_{7/2} \rightarrow {}^4I_{11/2}$ (Er) : ${}^2F_{7/2} \rightarrow {}^2F_{5/2}$ (Yb) and ${}^4S_{3/2} \rightarrow$

⁴I_{11/2} (Er) : ²F_{7/2} → ²F_{5/2} (Yb) transitions [119]. Another reason for a reduced luminescence from ⁴S_{3/2} is that the energy separation of the ⁴S_{3/2} → ⁴I_{13/2} transition is only slightly larger than ²F_{7/2} → ²F_{5/2}, which facilitates another efficient Er-to-Yb energy back transfer [120, 130]. We will see in the following that ⁴I_{13/2}, which represents an intermediate level for the population of the red-emitting state ⁴F_{9/2}, is fed by the energy back transfer from ⁴S_{3/2} to Yb:²F_{5/2}. Furthermore, migration processes among Yb³⁺ ions become important at high Yb concentration: studies have shown that in Yb-doped fluorindate glasses, which have a similar phonon energy as in YF₃, migration processes among Yb³⁺ ions are only negligible for a concentration of 0.1 mol-% [134].

Based on the spectroscopic data and the energy level scheme, we can make the following considerations for the red emission from the ⁴F_{9/2} state: first, the nonradiative decay from the upper energy level ⁴S_{3/2} towards ⁴F_{9/2} is unlikely to occur, since the Stokes emission spectra showed only weak luminescence in the red when excited at 488 nm. Secondly, the Er:⁴F_{9/2} state can be fed by level ⁴I_{13/2} as a result of an upward energy transfer corresponding to ²F_{5/2} + ⁴I_{13/2} → ²F_{7/2} + ⁴F_{9/2}. For the population of ⁴I_{13/2}, a multiphonon transition from ⁴I_{11/2} or the Er-to-Yb back transfer from ⁴S_{3/2} → ⁴I_{13/2} (Er) : ²F_{7/2} → ²F_{5/2} (Yb) might be responsible, as mentioned above. The energy transfer described in the latter case might, on the other hand, also affect distant Yb³⁺ ions and hence an increase in the Yb concentration causes simultaneously the red emission to be enhanced and the green emission to be reduced.

In case of internal multiphonon relaxation according to ⁴I_{11/2} ↔ ⁴I_{13/2}, the energy gap is compensated by the emission of phonons. However, since the energy gap is rather large with ~3700 cm⁻¹, accounting for ~7 phonons in YF₃ matrix, the multiphonon relaxation rate is rather low and the observed red emission, due to ⁴I_{13/2} (Er) + ²F_{5/2} (Yb) → ⁴F_{9/2} (Er) + ²F_{7/2} (Yb), is weak [120]. A third population pathway for ⁴I_{13/2} in YF₃ was proposed by Kuroda and involves a direct energy transfer from Yb:²F_{5/2} → ⁴I_{13/2} and again is accompanied by the emission of about 7 phonons (accounting for an energy gap of ~3700 cm⁻¹) [120].

Considering that multiphonon relaxation involving ≤6 phonons are not as likely [42], the red emission output in Er/Yb:YF₃ is weaker than the green emission. However, at high Yb doping levels, population of the intermediate ⁴I_{13/2} level is increased due to the de-excitation of the green-emitting ⁴S_{3/2} state by energy back transfer to Yb.

To sum up the preceding discussion, we list the processes involved in the red emission from level ⁴F_{9/2}:

- (1) MPR: ⁴S_{3/2} ↔ ⁴F_{9/2}
- (2) MPR: ⁴I_{11/2} ↔ ⁴I_{13/2}
- (3) PAT: Yb:²F_{5/2} + Er:⁴I_{13/2} → Yb:²F_{7/2} + ⁴F_{9/2}
- (4) ETU-3: Er:⁴I_{13/2} + Yb:²F_{5/2} → Er:⁴F_{9/2} + Yb:²F_{7/2}
- (5) ⁴F_{9/2} → ⁴I_{15/2}

3.4 Lifetimes of $\text{Er}:\text{}^4\text{S}_{3/2}$ and $\text{}^4\text{F}_{9/2}$ states

Lifetime measurements were performed for the $\text{}^4\text{S}_{3/2}$ green- and $\text{}^4\text{F}_{9/2}$ red-emitting energy states of Er^{3+} upon pumping at 980 nm. The results allow us to draw conclusions for the influence of the sensitizer concentration in Er/Yb co-doped YF_3 films on the relaxation processes in Er^{3+} .

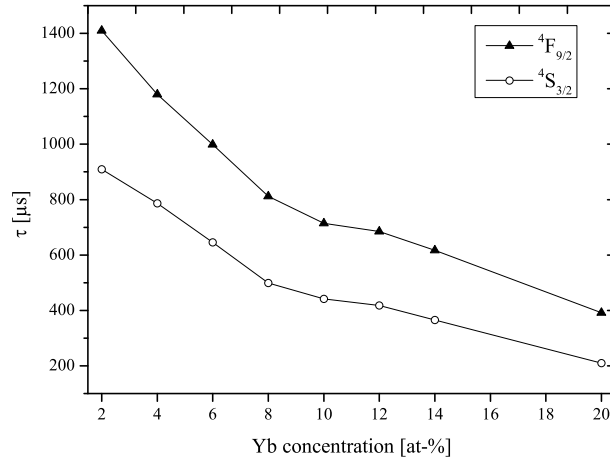


Figure 3.9: Lifetimes τ of $\text{Er}:\text{}^4\text{S}_{3/2}$ and $\text{}^4\text{F}_{9/2}$ states as a function of the Yb concentration in Er/Yb: YF_3 .

In Fig. 3.9 the measured lifetimes of the $\text{}^4\text{S}_{3/2}$ and $\text{}^4\text{F}_{9/2}$ states are depicted as a function of the Yb concentration. The shortening of the observed lifetimes with increasing Yb concentration is due to relaxation processes in the Er^{3+} ion. In general, the nonradiative rate is enhanced by ion-phonon interactions or energy transfer to another ion. Relaxation of the higher excited state $\text{}^4\text{S}_{3/2}$ by downward non-resonant energy transfer to a neighboring Yb^{3+} ion in manners of $\text{Er}:\text{}^4\text{S}_{3/2} \rightarrow \text{}^4\text{I}_{13/2}$ and $\text{Yb}:\text{}^2\text{F}_{7/2} \rightarrow \text{}^2\text{F}_{5/2}$ results in an observed shortening of the lifetime. This explains the decrease in the lifetime with the increase of Yb concentration. The same applies for the red-emitting $\text{}^4\text{F}_{9/2}$ state, where relaxation due to $\text{}^4\text{F}_{9/2} \rightarrow \text{}^4\text{I}_{15/2}$ and $\text{}^2\text{F}_{7/2} \rightarrow \text{}^2\text{F}_{5/2}$ (Yb) shortens the radiative lifetime of the state. The experimental lifetimes τ of the two intermediate levels $\text{}^4\text{S}_{3/2}$ and $\text{}^4\text{F}_{9/2}$ were determined from the luminescence decay curves for films with different sensitizer concentration by pumping the $\text{Yb}:\text{}^2\text{F}_{7/2}$ level with a 980 nm laser.

The temporal evolution of the green and red emission band for samples with varying Yb concentration is shown in Fig. 3.10. For a better view, Fig. 3.11 shows selected films containing 0, 2, 10 and 20 at.% Yb, which represent characteristic observed decay curves. The luminescence kinetics for both $\text{Er}:\text{}^4\text{S}_{3/2}$ and $\text{Er}:\text{}^4\text{F}_{9/2}$ states exhibit deviations from an exponential behavior, which is more conspicuous for samples containing a higher Yb concentration. The intensity was normalized and represented in a logarithmic scale for better comparison with an exponential decay behavior and the lifetimes were obtained by fitting the luminescence decay curves corresponding to $I=I_0+A\cdot\exp^{-t/\tau}$. The lifetime of $\text{}^4\text{S}_{3/2}$ is about 1.51 ms

3 Three-photon UpC of RE^{3+} -doped YF_3 thin films

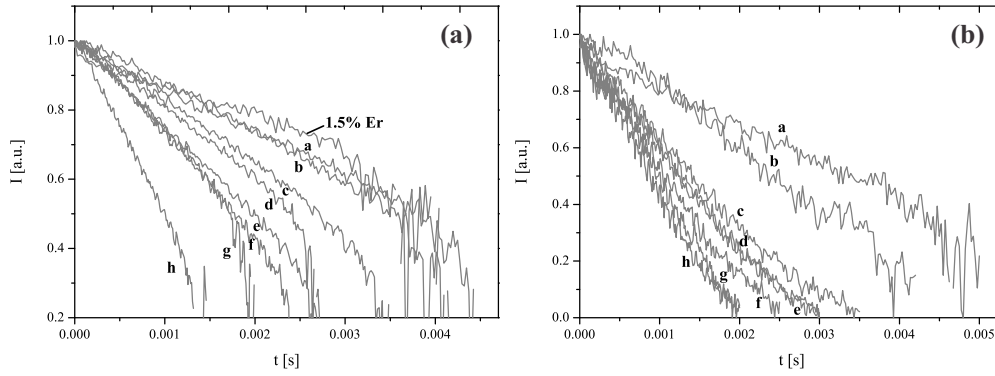


Figure 3.10: Dynamics of the Vis-UpC emissions corresponding to (a) $Er:4S_{3/2}$ and (b) $4F_{9/2}$ states as a function of the Yb doping level in Er/Yb:YF₃ films, under 980 nm excitation. The decay curves correspond to the following Yb concentrations: (a) 2% (b) 4% (c) 6% (d) 8% (e) 10% (f) 12% (g) 14% (h) 20%. The intensities are normalized and represented in a log-scale for better comparison with an exponential decay behavior.

in singly Er-doped YF₃ and is shortened to about 442 μ s and 209 μ s due to the addition of 10 and 20 at.% Yb (Fig. 3.11 (a)). As can be seen from Fig. 3.11 (b), the lifetime of the $4F_{9/2}$ level is dependent on the Yb concentration as well and decreases from 1.4 ms (2 at.% Yb) to 714 μ s (10 at.% Yb) and 392 μ s (20 at.% Yb), respectively. In case of singly Er-doped YF₃, no experimental decay of $4F_{9/2}$ could be determined, since the detectable intensities were too low to be measured with our experimental set-up. From the lifetime measurements of states $4S_{3/2}$ and $4F_{9/2}$, one cannot easily deduce the optimal Yb concentration which yields the highest UpC emission in the visible (i. e. 10 at.% Yb, see Fig. 3.6), just by determining the longest lifetime. This is because the Yb³⁺ ions take part in the relaxation process of Er³⁺, as a result of the Er-to-Yb energy transfer. For a deeper understanding of the UpC mechanism, knowledge of the decay kinetics of the intermediate level $Er:4I_{11/2}$ and the excited state of Yb³⁺ ($2F_{5/2}$), is additionally needed.

Various lifetime measurements are reported in the literature. The results mainly depend on the system, ion concentration and temperature. However, the observed lifetimes are close to each other when similar conditions are used [119, 120, 130]. For example, Auzel reported a decay time of 1.2 ms for the red and 0.82 ms for the green emission in an Er/Yb:YF₃ phosphor (2 % Er, 20 % Yb) [119]. As reported in Ref. [135], the calculated radiative lifetimes of Er³⁺ in fluorindate glass, which has a phonon energy comparable to YF₃, is 1.06 ms for $4S_{3/2}$ and 0.623 ms for the $4F_{9/2}$ state. However, a lengthening of the $4F_{9/2}$ state lifetime is to be expected in the UpC process, since the red-emitting level is mainly populated via the $4I_{13/2}$ state, which has a lifetime of \sim 10 ms in fluoride systems [104, 136].

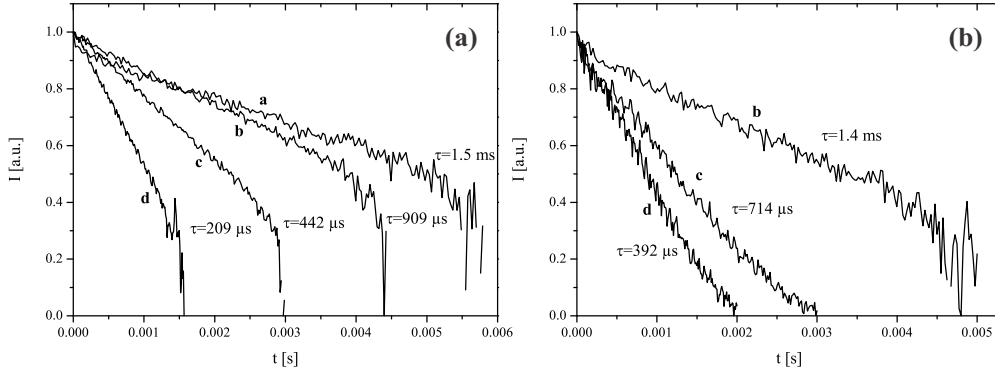


Figure 3.11: Luminescence decay kinetics from (a) $^4\text{S}_{3/2}$ and (b) $^4\text{F}_{9/2}$ states as a function of the Yb concentration in (1.5 at.%)Er/Yb:YF₃, with a Yb concentration of (a) 0 at.% (b) 2 at.% (c) 10 at.% and (d) 20 at.%. The lifetime of $^4\text{F}_{9/2}$ in Er:YF₃ was not measured, due to limitations of our experimental set-up. The intensities are normalized and shown in a logarithmic scale, for better comparison with the exponential decay behavior.

3.4.1 Power dependence studies of Er/Yb:YF₃

For the population of the $^4\text{F}_{9/2}$, $^4\text{S}_{3/2}$ and $^2\text{H}_{9/2}$ energy levels in Er^{3+} , at least two photons, in the former two cases, and three excitation photons in the latter case, are needed. Since UpC is a nonlinear optical process, it strongly depends on the intensity of the excitation light. The number of photons n required for the population of the emitting energy levels can be derived from the slope of a double-logarithmic representation of the UpC emission intensity, I_{em} , versus the pump power, P , according to

$$I_{\text{em}} \propto P^n \quad (3.1)$$

However, eq. 3.1 is only valid when the UpC rate is negligible compared to the linear decay rate [30, 42, 49]. A measured decrease in the slope is often referred to as a saturation effect and is, in fact, determined by the competition between linear and nonlinear (UpC) decay. The characteristic slopes for a n -photon excitation process can be derived by solving the appropriate rate equations in the limiting regimes for very low and large UpC rates, as shown in detail by Pollnau *et al.* [49]. Moreover, a distinction of the underlying UpC process, namely ESA or ETU, can be derived in certain cases from the slopes of the intermediate levels, in case the UpC process dominates over linear decay routes (large UpC rate). The measured slopes for the UpC luminescence from the levels $^2\text{H}_{9/2}$, $^2\text{H}_{11/2}$: $^4\text{S}_{3/2}$ and $^4\text{F}_{9/2}$ for YF₃ doped with 1.5% Er/10% Yb and 1.5% Er/20% Yb, respectively, are depicted in Fig. 3.12.

The dominant UpC process present in our samples, used for the power-dependence studies, is ETU, since the rare earth doping level is rather high. We expect further, that emission to the ground state dominates over relaxation to lower-lying states due to the low phonon energy of YF₃. In 1.5% Er/10% Yb-doped YF₃, the measured slopes for the $^4\text{S}_{3/2}$ luminescence change from 1.6 to 1.2 with increasing

3 Three-photon UpC of RE^{3+} -doped YF_3 thin films

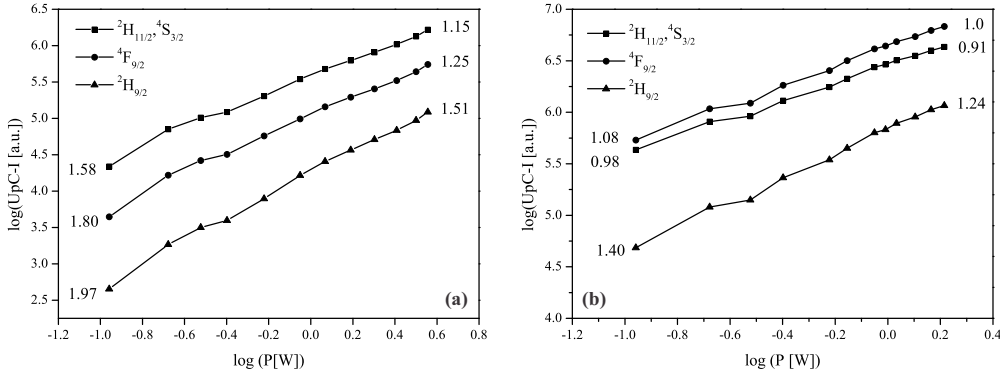


Figure 3.12: Power dependence of UpC luminescence from the ${}^2H_{9/2}$, ${}^2H_{11/2}$: ${}^4S_{3/2}$ and ${}^4F_{9/2}$ of (a) 1.5% Er/10% Yb and (b) 1.5% Er/20% Yb doped YF_3 thin films, under laser excitation at 972 nm.

pump power excitation. Assuming that the first ETU step (ETU-1, Fig. 3.8 (b)) for populating ${}^4S_{3/2}$ is more efficient than the second and third ETU step (ETU-2 and ETU-3 in Fig. 3.8 (b)), we can expect for each excited state i a slope of $P^{i/2}$, assuming high UpC rates at high power (see derivations in the end of the chapter). The experimentally obtained slope of 1.2 is in good agreement with the predicted slope of P^1 . At low pump power, the slope converges to the lower limit of P^i , yet one expects slopes between the limiting cases, because the dopant level and the applied power yield a competitive situation between linear and nonlinear processes [32]. The measured slopes for the emission from ${}^2H_{9/2}$ and ${}^4F_{9/2}$ at high pump power yield 1.5 and 1.3, respectively, and agree quite well with the predicted values of $P^{1.5}$ and P^1 in the latter case. Again, for decreasing pump powers we find slopes between the two limiting cases $P^{i/2}$ and P^i , indicating a competition of linear and nonlinear behavior.

In 1.5% Er/20% Yb-doped YF_3 the measured slopes show a similar behavior as discussed above for the 1.5% Er/10% Yb-doped sample, however, the situation becomes more complex when increasing the rare earth dopant concentration. This is due to the fact that cross-relaxation, energy migration among ions, photon avalanche and other nonlinear processes might coexist with ETU, and result in experimentally observed slopes different from the ones predicted by the simple model [128].

PD of UpC luminescence in singly Er-doped YF_3 . Fig. 3.13 shows the dependence of the UpC luminescence on the pump power for 1.5% Er: YF_3 . At this doping concentration, both ESA and ETU processes might be responsible for the population of the higher excited states. The measured slopes of luminescence for the ${}^2H_{9/2}$ (410 nm), ${}^4S_{3/2}$ (550 nm) and ${}^4F_{9/2}$ (660 nm) levels exhibit a dependence of $P^{1.1}$, $P^{0.9}$ and $P^{0.7}$ at high pump power. In case we have an UpC process purely based on ETU and with large UpC rates, the slopes show a dependence of $P^{1/2}$ for intermediate levels and P^1 for the upper level, assuming all transitions take place to the ground state. On the other hand, if one considers ESA, one finds a power dependence of the luminescence of P^0 for intermediate states, and P^1 for the upper level at high pump power. This indicates that probably both ESA

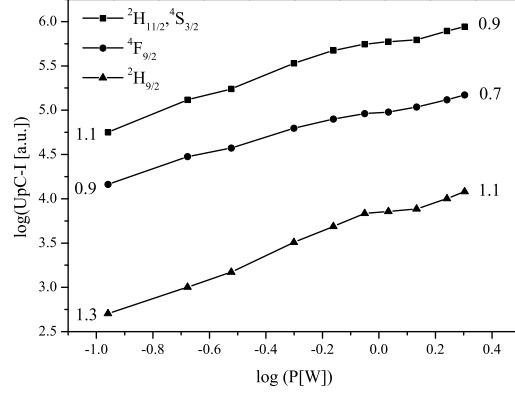


Figure 3.13: Double-log. representation of the emission intensities from the ${}^2H_{9/2}$, ${}^2H_{11/2}:{}^4S_{3/2}$ and ${}^4F_{9/2}$ levels in 1.5% Er:YF₃ vs. the excitation pump power (pumped at 972 nm). The obtained slopes are indicated by the number in the figure for the low and high pump power regime, respectively.

and ETU processes coexist during the excitation period. A decrease in the pump power as in Fig. 3.13 leads to a slight increase in the slopes, from which we draw the conclusion that we remain in an intermediate pump power regime, since the slopes indicate a competition between linear decay and light UpC; therefore, their power dependence lies between P^i , for small UpC rates, and the predicted slopes have characteristic values for ETU and ESA, as it was discussed before.

Steady-state solutions for the n -photon excitation of a four-level system and their characteristic power dependencies, following Ref. [49]

For a four-level system as shown in Fig. 3.8 (b), the rate equations for sequential ETU excitation are:

$$\begin{aligned} dN_1/dt &= \rho_p \sigma_0 N_0 - 2W_1 N_1 N_1 - W_2 N_1 N_2 - W_3 N_1 N_3 - A_1 N_1 + \beta_2 A_2 N_2 \\ dN_2/dt &= W_1 N_1 N_1 - W_2 N_1 N_2 - A_2 N_2 + \beta_3 A_3 N_3 \\ dN_3/dt &= W_2 N_1 N_2 - W_3 N_1 N_3 - A_3 N_3 + \beta_4 A_4 N_4 \\ dN_4/dt &= W_3 N_1 N_3 - A_4 N_4 \end{aligned}$$

with the pump constant $\rho_p \propto P$ and σ_0 the absorption cross section of the ground state and β the branching ratio. In the limit of large UpC rates, the linear decay terms are negligible and we obtain the following power dependencies for a n -photon excitation:

$$\begin{aligned} dN_1/dt = 0 &\implies \rho_p \sigma_0 N_0 = 2W_1 N_1 N_1 + W_2 N_1 N_2 + W_3 N_1 N_3 \\ dN_2/dt = 0 &\implies W_1 N_1 N_1 = W_2 N_1 N_2 \\ dN_3/dt = 0 &\implies W_2 N_1 N_2 = W_3 N_1 N_3 \\ dN_4/dt = 0 &\implies W_3 N_1 N_3 = A_4 N_4 \end{aligned}$$

3 Three-photon UpC of RE³⁺-doped YF₃ thin films

and since $\rho_p \propto P$, it follows that:

$$\begin{aligned} N_1 &\propto P^{1/2} \\ N_2 &\propto N_1 \propto P^{1/2} \\ N_3 &\propto N_3 \propto P^{1/2} \\ N_4 &\propto \rho_p \sigma_0 N_0 \propto P^1 \end{aligned}$$

We obtain characteristic slopes of $P^{1/2}$ for intermediate states and P^1 for the upper state. For the lower limit of small UpC rates, and thus linear decay as the dominant depletion mechanism, we find

$$\begin{aligned} dN_1/dt = 0 &\implies \rho_p \sigma_0 N_0 = A_1 N_1 \\ dN_2/dt = 0 &\implies W_1 N_1 N_1 = A_2 N_2 \\ dN_3/dt = 0 &\implies W_2 N_1 N_2 = A_3 N_3 \\ dN_4/dt = 0 &\implies W_3 N_1 N_3 = A_4 N_4 \end{aligned}$$

and the characteristic slopes of

$$\begin{aligned} N_1 &\propto P^1 \\ N_2 &\propto N_1^2 \propto P^2 \\ N_2 &\propto N_1 N_2 \propto P^3 \\ N_2 &\propto N_1 N_3 \propto P^4 \end{aligned}$$

or generally expressed as P^i for the predicted slopes of luminescence. In case that (a) ETU-1 is more efficient than ETU-2 and ETU-3 and (b) luminescence takes place predominately to the ground state, hence $\beta = 0$, we can write the solutions for the case of large UpC rates (linear decay is negligible):

$$dN_1/dt = 0 \implies \rho_p \sigma_0 N_0 = 2W_1 N_1 N_1 \quad (3.2)$$

$$dN_2/dt = 0 \implies W_1 N_1 N_1 = A_2 N_2 \quad (3.3)$$

$$dN_3/dt = 0 \implies W_2 N_1 N_2 = A_3 N_3 \quad (3.4)$$

$$dN_4/dt = 0 \implies W_3 N_1 N_3 = A_4 N_4 \quad (3.5)$$

and the power dependence for each excited state i

$$N_1 \propto P^{1/2} \quad (3.6)$$

$$N_2 \propto N_1^2 \propto P^1 \quad (3.7)$$

$$N_3 \propto N_1 N_2 \propto P^{3/2} \quad (3.8)$$

$$N_4 \propto N_1 N_3 \propto P^2 \quad (3.9)$$

or $P^{i/2}$ for an i -step UpC process. It has to be noted that for intermediate pump powers, slopes between the two limiting cases will be found since a situation of competition between linear decay and UpC processes occurs in the system. Furthermore, a differentiation between ESA and ETU is possible just in the regime of large UpC rates, from the slopes of intermediate states.

3.5 Summary

Measurements of IR-to-visible light conversion (UpC) have been performed on Er/Yb:YF₃ under 972 nm laser excitation. The relative intensity ratio of red to green emission depends on the Yb concentration and increases with the Yb doping level. The violet emission at 410 nm is produced by three successive energy transfer steps from the Yb:²F_{5/2} state via Er:⁴I_{11/2}→⁴S_{3/2}→⁴G_{7/2} and a multiphonon relaxation to ²H_{9/2}. The population of the green-emitting states ²H_{11/2}:⁴S_{3/2} originates from two energy transfers from Yb-to-Er, while the red-emitting state ⁴F_{9/2} is populated by an upward ET from level ⁴I_{13/2}. The population of the intermediate level ⁴I_{13/2} is due to multiphonon relaxation from ⁴I_{11/2} or directly by an ET from Yb through ²F_{5/2}→⁴I_{13/2}, assisted by the emission of phonons. Since the number of phonons needed to bridge the energy gap is about 7, the red emission is weak. Another excitation route for the ⁴I_{13/2} state was mentioned which involves the relaxation of ⁴S_{3/2} → ⁴I_{13/2} due to an energy back transfer to Yb. This route might explain the increase in the red emission intensity when increasing the Yb concentration. Furthermore, it was shown that the dependence of the luminescence intensity on the pump power exhibits slopes of an excited state i of $P^{i/2}$ at high UpC rates, and intermediate situations are found at lower pump power with slopes converging to P^i . Luminescence kinetics of the ⁴S_{3/2} and ⁴F_{9/2} were measured as a function of the Yb concentration and exhibited a shortening of the lifetimes of both states, when the sensitizer concentration was increased.

 RE^{3+} -doped Y_2O_3 thin films grown by AA-MOCVD

In the present study, singly-doped Er, Yb and Er/Yb co-doped Y_2O_3 films were grown on Si(100) wafers at 540°C and atmospheric pressure by AA-MOCVD. This technique is based on the generation of an aerosol from a liquid source precursor of $\text{RE}(\text{acac})_3$ ($\text{RE} = \text{Y}, \text{Yb}$) and $\text{Er}(\text{tmhd})_3$ in 1-butanol (0.03 M) and allows a rather high film deposition rate of $\approx 500 \text{ nm}\cdot\text{h}^{-1}$. The as-grown films were subjected to post-deposition annealing at 600°C , 800°C and 900°C , respectively, for 1 h, in air. The resultant changes in the film microstructure, as well as optical and luminescent properties were studied in detail. We have used XRD, SEM and AFM for the structural elucidation of the films, and further, FTIR, Raman, ellipsometry, transmission and emission measurements to investigate their spectroscopic and optical behavior. The weak green and dominant red up-conversion emission of Er^{3+} was only observed in Er/Yb: Y_2O_3 films upon 972 nm excitation after a post-deposition annealing step, but not in the as-synthesized films. This, and the measured increase in the photoluminescence intensity with the annealing temperature was attributed to thermal effects, such as the increase in grain size and the removal of organic impurities from the film matrix. The longest $\text{Er}^{4}\text{I}_{13/2}$ lifetime in 900°C annealed films was determined to be approximately 1.6 ms.

4.1 Experimental

CVD variants that operate at ambient processing conditions, allow a film growth under a rather simple experimental set-up. In the present work, the aerosol-assisted (AA) MOCVD technique was used for the growth of Er/Yb-doped Y_2O_3 films on Si(100) and fused SiO_2 substrates, at atmospheric pressure and a deposition temperature of 540°C .

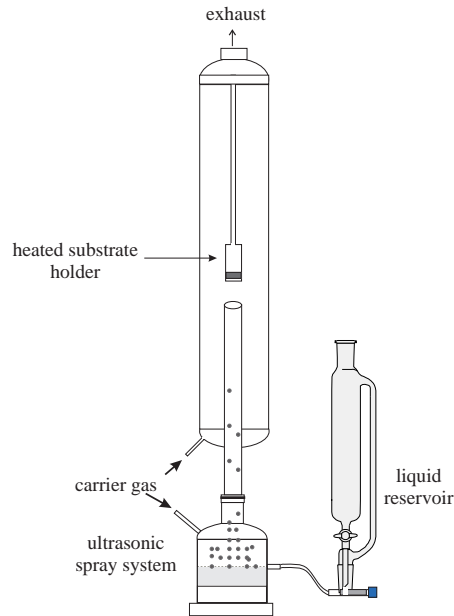


Figure 4.1: Schematic drawing of the AA-MOCVD chamber used for the deposition of RE: Y_2O_3 films, based on an ultrasonic spray system for the vaporization of the liquid source precursor.

The AA-MOCVD process is based on the deposition of an aerosol onto a heated substrate as shown in the schematic drawing in Fig. 4.1 [137]. The aerosol is generated at the surface of the precursor solution by an ultrasonic piezoelectric transducer ($f = 800 \text{ kHz}$), which creates ultrasonic oscillations in the solution resulting in aerosol formation [138]. The aerosol is then transported to the heated substrate by a carrier gas and a heterogeneous vapor/solid reaction takes place on the heated substrate. For the precursor solution, acetylacetonates of yttrium ($\text{Y}(\text{acac})_3 \cdot x \text{H}_2\text{O}$, 0.03 M, Alfa Aesar, 99.9%), ytterbium ($\text{Yb}(\text{acac})_3 \cdot x \text{H}_2\text{O}$, 99.9%, Strem Chemicals) and tris(2,2,6,6-tetramethyl-3,5-heptanedionato) erbium ($\text{Er}(\text{tmhd})_3 \cdot x \text{H}_2\text{O}$, 99.9%, Strem Chemicals) were dissolved in 1-butanol (Aldrich, 99%). The carrier gas consists of two dry air gas fluxes, the first one flows at $12.7 \text{ L} \cdot \text{min}^{-1}$ and is mainly responsible for transporting the aerosol to the substrate, the second gas flux of $10.1 \text{ L} \cdot \text{min}^{-1}$, helps to extend the time that the vapor stays in the vicinity of the substrate. For the substrate heating and temperature control, an electrical resistance with a built-in thermocouple was used and the substrate temperature was fixed at 540°C for all depositions. This temperature was chosen to obtain polycrystalline films of good mechanical stability [138]. The deposition rate was about 500 nm/h at 540°C , accounting for a solution vol-

ume of about 120 mL. The as-synthesized films were subsequently annealed at 600 °C, 800 °C and 900 °C for 1 h, in air. The obtained film thicknesses range from ~770 nm to 600 nm for films as-deposited and after annealing at 900 °C, respectively.

For a detailed description of the film characterization methods including SEM, AFM, FTIR, Micro-Raman, ellipsometry and film composition by electron probe micro-analysis (EPMA), the reader is referred to Chapter 2, Section 2.2. X-ray diffraction (XRD) patterns of the films were recorded between 10° <2θ <70° with a scan rate (2θ) of 1°/min in θ/2θ geometry with a Bruker Advance D8 diffractometer, using Cu Kα radiation (λ = 0.1541 nm).

UpC luminescence spectra in the visible region were recorded with two different experimental set-ups. First, using a 972 nm pulsed laser excitation from an OPO pumped tunable EKSPLA NT342 laser which delivered 10 ns pulses at a 10 Hz repetition rate. The excitation laser was focused on the sample by a lens with a 100 mm focal length. The optical emission was collected by an optical fiber and analyzed by a Triax 320 Jobin Yvon monochromator with a 500 grooves/mm grating, coupled to a Hamamatsu photomultiplier tube. Secondly, UpC spectra were recorded under continuous excitation by a 972 nm laser diode focused with a 10X microscope objective on each sample, and the emission was collected by a multimode fiber (core diameter 600 μm) and in the following analyzed by a spectrometer consisting of a 0.85 m double monochromator coupled to a photomultiplier tube detector (Hamamatsu R 928).

The luminescence decay curves of Er:⁴I_{13/2} were recorded under pulsed laser excitation at 977 nm (repetition rate 10 Hz, 7 ns pulse width). The temporal evolution of state Yb:²F_{5/2} was studied after excitation at 941 nm on the 1040 nm emission line. The signal was collected through two lenses with focal lengths of 50 mm and 100 mm by a Jobin Yvon HR250 monochromator, coupled to a liquid N₂-cooled Ge detector. The luminescence decays were monitored using a Lecroy model LT342 digital oscilloscope interfaced with a computer.

4.2 Quantitative element analysis: EPMA results

The cationic rare earth ratios, RE/(RE + Y) at.%, in singly-doped films for different RE(acac)₃/ (RE+Y)(acac)₃ at.% concentrations in solution are depicted in Fig. 4.2. Note that even though we used an Er(tmhd)₃ precursor, we denote all rare earth precursors by RE(acac)₃, for reasons of simplicity. The deposition reactivity of the Er and Yb precursors are higher than that of Y(acac)₃, hence their atomic ratios are higher in the film than in solution. This effect is much more pronounced for the Yb than for the Er precursor. Furthermore, the film composition does not show any significant changes after the post-deposition annealing, as shown in Fig. 4.2 (a). The dashed lines show the ideal case of depositing the same RE concentration in film as used in the precursor solution.

The presence of the two rare earth ion species in the solution did slightly influence their concentration in the film and, moreover, the Er concentration is decreased by increased co-doping of Yb, as shown in the inset graph of Fig. 4.2 (b). The

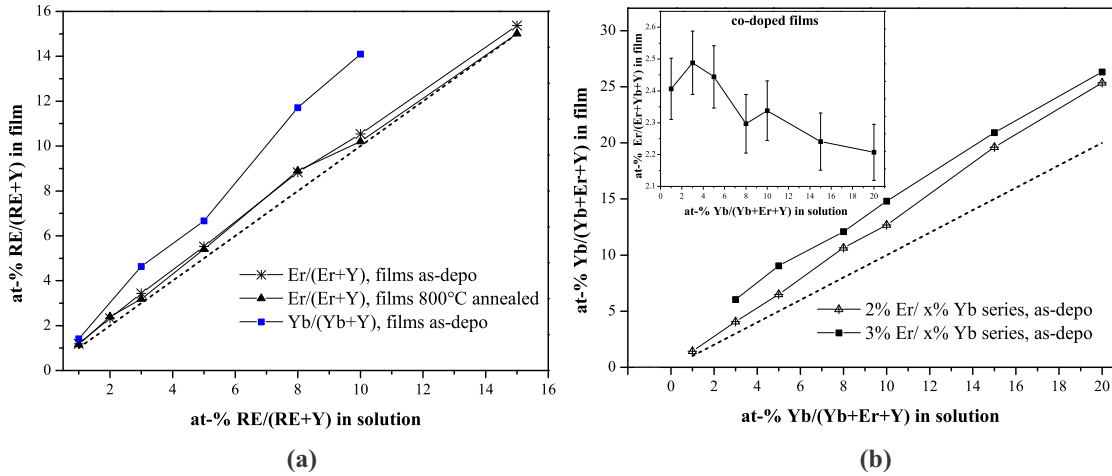


Figure 4.2: Rare earth (RE) concentrations in solution and in the films, grown at 540 °C; (a) Er/(Er+Y) at.% ratios in film vs. molar ratio in solution for films as-synthesized and after annealing at 800 °C; additionally the composition of singly Yb-doped films is depicted. (b) Yb/(Yb+Er+Y) at.% ratios in film for different molar concentrations in solution of Er/Yb:Y₂O₃ samples containing a fixed Er concentration of 2 at.% and 3 at.% in solution, respectively. The inset depicts the dependence of the Er concentration on the varying Yb content in Er/Yb co-doped films, with a fixed initial concentration of 2 at.% in solution. Dashed lines indicate the ideal case of finding the same RE concentration in film and solution.

doping concentration of Er in Er/Yb co-doped Y₂O₃ films was fixed at 3 at.% in solution or 1 at.% in the film (Er/(Er+Y+O) at.%) comparable to the Er dopant concentration reported in the literature for an optimal emission output [138, 139]. Note, that for reasons of simplicity, we always refer in the following to the RE concentration in the precursor solution, instead of the actual composition in the film matrix.

4.3 Structural characterization of Er/Yb:Y₂O₃ thin films

XRD results. The XRD studies for Er/Yb co-doped films (3%Er, 3%Yb), depicted in Fig. 4.3, reveal that the as-deposited film is of low crystalline quality. The crystallinity improves with the post-annealing temperature. The annealed films exhibit diffraction patterns indexed to polycrystalline c-Y₂O₃ (ICDD No. 41-1105). Moreover, one observes that the peak positions of the as-synthesized film are shifted compared to the powder diffraction reference patterns of c-Y₂O₃. This may be attributed to residual stresses in the film microstructure, which are released at higher annealing temperature. The most intense diffraction is found for the (222) peak, indicating a [111] texture of the film.

Furthermore, the increase of the RE doping level in Y₂O₃ does not alter the peak positions of the XRD patterns, indicating no lattice distortion. However, highly RE-doped samples exhibit an increased intensity for the 440 reflection (see sample 3% Er/15% Yb:Y₂O₃ in Fig. 4.3 (b)).

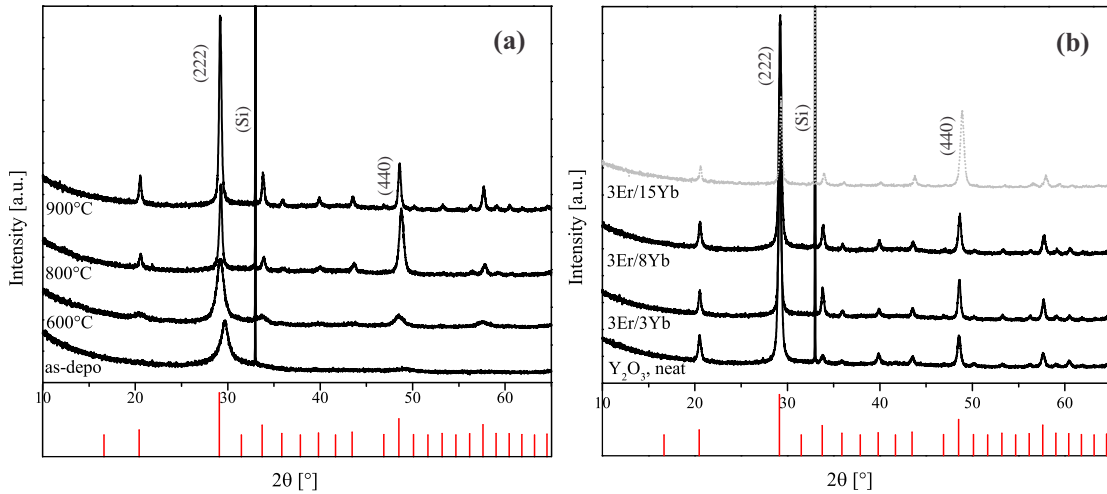


Figure 4.3: (a) XRD patterns of Er/Yb:Y₂O₃ (3%Er, 3%Yb) films as-grown and after post-annealing at 600, 800 and 900 °C, respectively. C-Y₂O₃ is shown as a reference pattern (ICCD No. 41-1105). (b) Influence of the RE doping concentration in Y₂O₃ on the diffraction patterns for films baked at 900 °C/1 h, in air.

SEM and AFM results. The film structure and morphological evolution with increasing post-deposition annealing temperature were analyzed by SEM and AFM (height images). The SEM micrographs of Er/Yb:Y₂O₃ films in Fig. 4.4 show the changes in the microstructure for different annealing temperatures. The as-deposited films are smooth in their appearance and no cracking was observed. Increasing the temperature leads to the occurrence of micro- and macro-cracks in the film structure. This effect is mainly due to shrinkage cracking and the mismatch in thermal expansion coefficients, leading to thermal stress in the film (CLTE Si = $3 \cdot 10^{-6}/K$ and $8 \cdot 10^{-6}/K$ for Y₂O₃ [109,140]). Thus thermal cracking can hardly be avoided and was repeatedly reported in the literature [140–145]. Along with the cracking, the RMS surface roughness increases. They were measured by AFM, for a $15 \times 15 \mu m^2$ area and an increase from 3.6 nm to 22 nm for the as-deposited and 900 °C/1 h films ($d_f \sim 700$ nm, see cross-section measurements in Fig. 4.5).

The grains on the surface are made clearly visible by AFM and the mean grain size for different thermal treatment were measured, and are summarized in Table 4.1, together with the crystallite sizes deduced from the Scherrer equation in the XRD analysis (see explanations in Chapter 2, Section 2.2). The high temperatures introduce grain growth through the coalescence of smaller grains into larger ones. The Scherrer equation, however, gives only an approximation of the crystallite size, since it works well only for nearly spherical particles, and possible stresses in the film result in a broadening of the Bragg peaks.

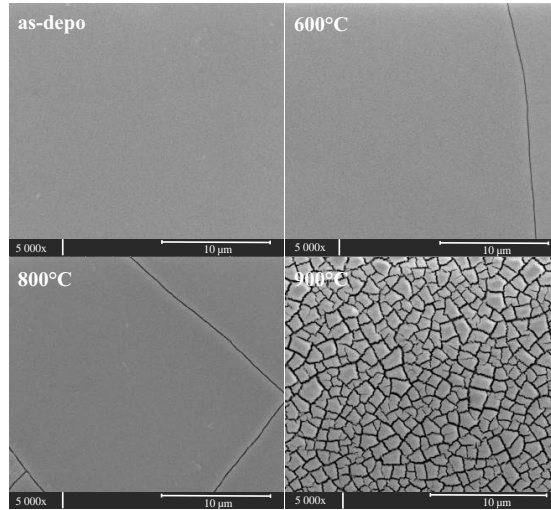


Figure 4.4: Influence of the annealing temperature on the film microstructure: Top-view SEM images of Er/Yb:Y₂O₃ (3 at.%Er, 10 at.%Yb) films, as-deposited and after thermal annealing at 600, 800 and 900 °C for 1 h, in air.

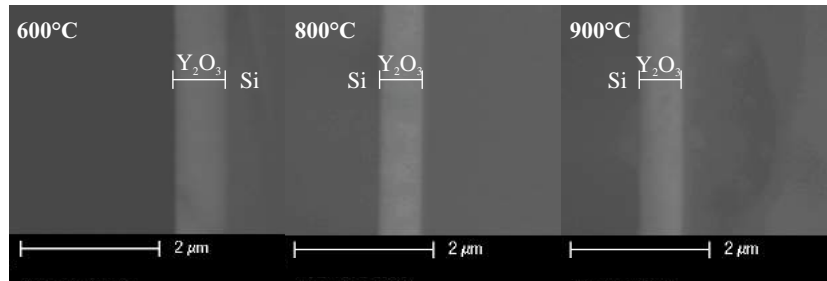


Figure 4.5: SEM cross-section images recorded in BSE mode of Er/Yb films (3 at.%Er, 10 at.%Yb) annealed at 600 °C, 800 °C and 900 °C. The corresponding film thicknesses are ~ 730 nm, 650 nm and 640 nm, respectively.

Table 4.1: Crystallite size D , derived by the Scherrer equation of the 222 diffraction peak after different thermal treatments of Er/Yb co-doped Y₂O₃ thin films and corresponding averaged AFM grain sizes.

Sample	D [nm]	AFM grain size [nm]
as-deposited	~ 10	30
600 °C	~ 10	30
800 °C	~ 20	30
900 °C	~ 30	50

4.3.1 Spectroscopic characterization: FTIR and Raman studies

FTIR and Raman spectroscopy allow us to obtain further information about the crystalline phases, the crystalline quality of the film through the intensity and the FWHM of the vibrational bands, and whether any other impurities are present. Y₂O₃ (yttrium sesquioxide) crystallizes in the cubic system, 22 Raman- and 16 IR-active modes can be deduced from the irreducible representations [146].

4 RE^{3+} -doped Y_2O_3 thin films grown by AA-MOCVD

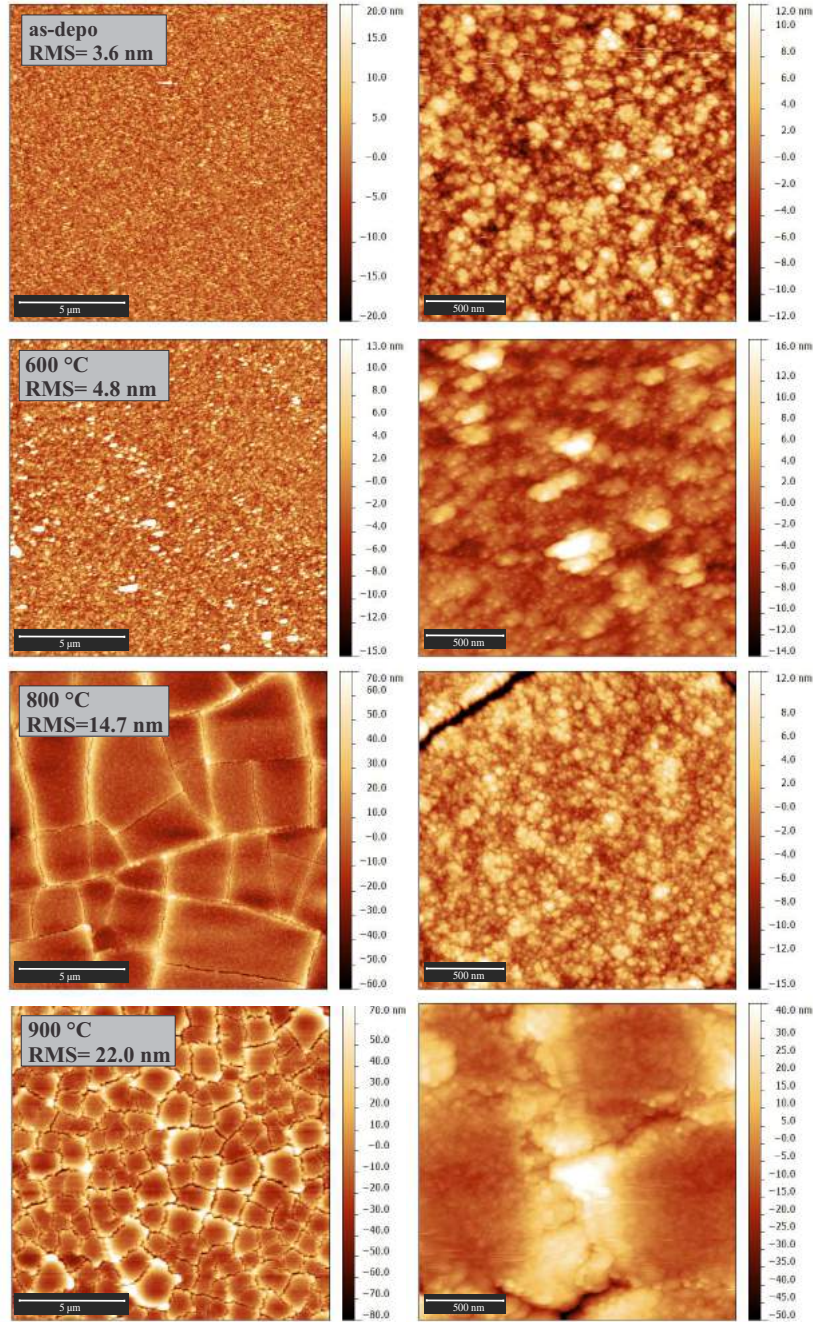


Figure 4.6: AFM height images of a $15 \times 15 \mu\text{m}^2$ (left) and a $2 \times 2 \mu\text{m}^2$ (right) area, respectively, of Er/Yb: Y_2O_3 (3 at.%Er, 10 at.%Yb) films, as-grown and annealed at 600°C , 800°C and $900^\circ\text{C}/1\text{h}$, in air. The RMS surface roughnesses are stated in the figure for a $15 \times 15 \mu\text{m}^2$ area.

In Fig. 4.7 the fundamental phonon transitions of $c\text{-}Y_2O_3$ are found between $50\text{--}600\text{ cm}^{-1}$, with line maxima at $\sim 367(\text{w})$, $403(\text{w})$, $468(\text{s})$, $542(\text{w})$, $557(\text{s})$ and $600(\text{s})\text{ cm}^{-1}$. However, fewer lines than the 22 expected are observed due to the polycrystalline nature of the film. The increase in intensity, together with the decrease in the line widths, are a function of the annealing temperature and indi-

cate an improved crystallinity of the films, which is in good agreement with the XRD results. For example, the FWHM at 468 cm⁻¹ decreases with the annealing temperature in the following order: 27 cm⁻¹, 22 cm⁻¹, 18 cm⁻¹ and 19 cm⁻¹ for films as-grown (540 °C) and annealed at 600, 800 and 900 °C, for 1 h, in air. Note, that we have removed the strong optical phonon mode of Si at ~520 cm⁻¹ from the spectra, due to its dominant intensity, as the film thickness is rather low.

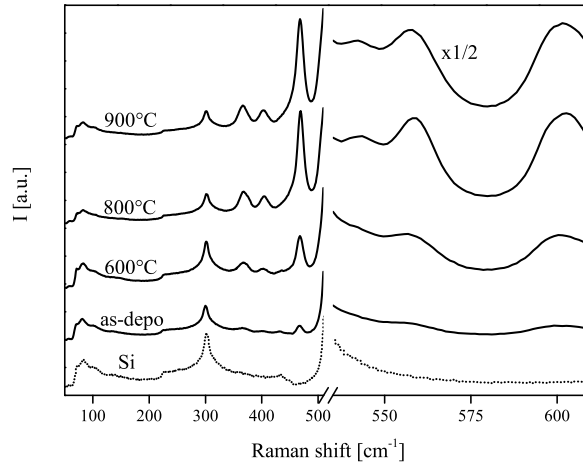


Figure 4.7: Raman spectra of RE:Y₂O₃ films deposited at 540 °C and after baking at 600 °C, 800 °C and 900 °C/1 h, in air. The spectrum of the 900 °C annealed film was divided by 2, for a better comparison with the other spectra.

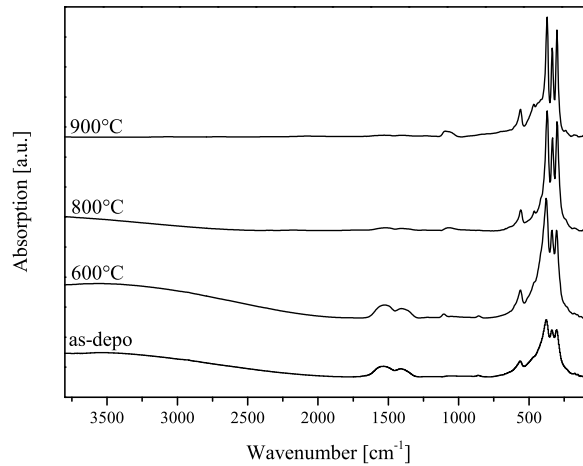


Figure 4.8: Influence of the annealing temperature on the IR vibrational modes of RE:Y₂O₃ films. The IR spectrum of the neat Si substrate was subtracted from the sample spectrum.

The FTIR spectra in Fig. 4.8 exhibit three important IR regions of the RE:Y₂O₃ films: first, the range between 100–600 cm⁻¹ presents the fundamental vibrational

bands of the Y–O bond of C-type Y_2O_3 , with peak maxima at ~ 300 (s), 336(s), 370(s), 466(shoulder) and 561(w) cm^{-1} .

The obtained peak positions are in good agreement with the reported data for the c- Y_2O_3 lattice absorptions [147]. The second region of interest is between 1300–1700 cm^{-1} and presents two intense bands due to the C–O and C–H vibrations originating from the acetylacetonate (and *tmhd*-) precursors. The traces of organic impurities are gradually eliminated as the annealing temperature is increased. It can be seen from the IR spectra that at least a temperature of 800 °C is required to eliminate the majority of the organic residues. Furthermore, a third region between 3000–3800 cm^{-1} shows a broad shoulder in the as-deposited and at 600 °C annealed sample due to hydroxyl groups, which vanish with increasing annealing temperature. The band at ~ 1100 cm^{-1} originates from the oxidation of the Si substrate and is assigned to the asymmetric Si–O–Si stretching vibration.

Optical properties of RE: Y_2O_3 thin films

An optical transmission spectrum of an Er/Yb: Y_2O_3 film ($d_f \approx 300$ nm) deposited on fused SiO_2 and annealed at 900 °C for 1 h, in air is depicted in Fig. 4.9. A decrease in transmission of the film compared to the neat substrate is mainly due to light scattering, which depends on the surface roughness and thus on the grain size of the film [141].

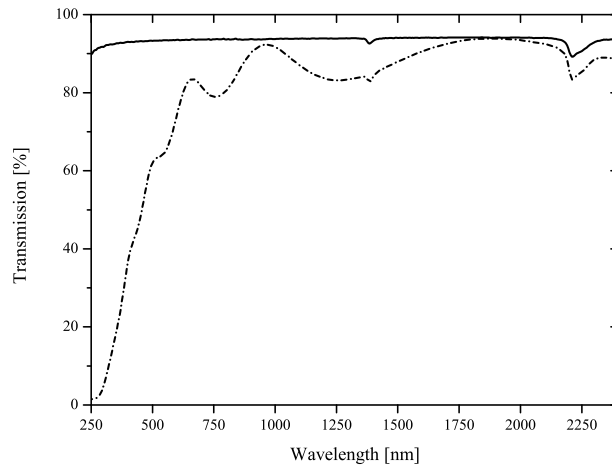


Figure 4.9: Transmission spectra of Er/Yb: Y_2O_3 , after post-deposition annealing at 900 °C, 1 h, in air (dashed line), and of the neat fused SiO_2 substrate.

The refractive indices were obtained by ellipsometric characterization of the Er/Yb: Y_2O_3 films deposited on Si substrates. The experimental data was modeled using the Cauchy dispersion function and its fitting parameters are summarized together with the values of refractive index at 500 nm in Table 4.2. The thermal annealing process showed little influence on the refractive indices, which are lower than the value of the bulk material (1.939 at 500 nm [148]).

Table 4.2: Fitting parameters A, B and C of the Cauchy dispersion function and refractive index n at 500 nm for Er/Yb:Y₂O₃ films as-deposited and after thermal annealing at 600 °C, 800 °C and 900 °C/1 h, in air.

Conditions	A	B	C	n(500 nm)
as-deposited	1.757	0.01120	0	1.80
600 °C	1.750	0.01152	0	1.80
800 °C	1.789	0.00558	0	1.81
900 °C	1.781	0.01324	0	1.83

4.4 Luminescence spectra of Er/Yb:Y₂O₃ films deposited by AA-MOCVD

Stokes emission in the visible, with a strong green emission band centered at ~ 550 nm and a weaker red component centered at ~ 670 nm, was detected in the samples upon pulsed laser excitation at 480 nm. In Fig. 4.10 the characteristic Stokes emission is shown for 3 at.% Er/ x at.% Yb:Y₂O₃ films annealed at 900 °C, with varying doping level of Yb ($x = 3, 5, 10$).

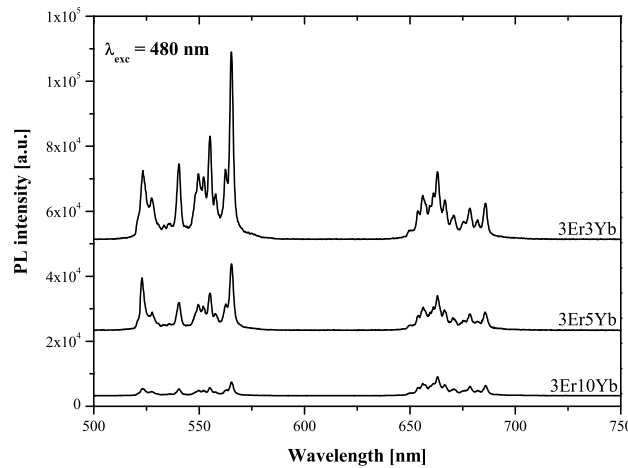


Figure 4.10: Photoluminescence spectra of Er/Yb:Y₂O₃ films baked at 900 °C/1 h, in air, with varying sensitizer concentration, as indicated in the graph. Excitation was performed at 480 nm.

Upon 480 nm photon excitation, initially the Er:⁴F_{7/2} energy state is populated and, after nonradiative relaxation to the lower-lying ⁴S_{3/2} state, a strong green emission is observed when relaxing back to the ⁴I_{15/2} ground state. The red luminescence band originates from the Er:⁴F_{9/2} level, which is populated due to nonradiative multiphonon relaxation from ⁴S_{3/2}. Since the number of phonons required to bridge the energy gap between ⁴S_{3/2} and ⁴F_{9/2} (~ 3000 cm⁻¹ [36]) accounts for about ~ 5 , this relaxation has been shown to be a competitive process [42]. Fur-

thermore, we observe a reduced emission for samples with increasing Yb dopant concentration due to the efficient phonon-assisted Er-to-Yb energy back transfer corresponding to the transitions Er:⁴S_{3/2} → ⁴I_{13/2} and Yb:²F_{7/2} → ²F_{5/2} [119].

4.4.1 Up-conversion after 972 nm excitation

Photon excitation of the films at around 980 nm leads to a visible up-converted luminescence from the Er³⁺ ion, as a result of its suitable energy level structure. Because of the weak absorption oscillator strength of the Er³⁺ ion at 980 nm, the luminescence is often sensitized through co-doping of Yb³⁺ ions. Er³⁺ can be excited to its ⁴I_{11/2} state by ground state absorption (GSA) or energy transfer (ET) from a neighboring Yb³⁺ ion (Fig. 4.11). During the up-conversion (UpC) process, two underlying excitation pathways of different nature may coexist, namely excited state absorption (ESA) and successive energy transfer from Yb-to-Er.

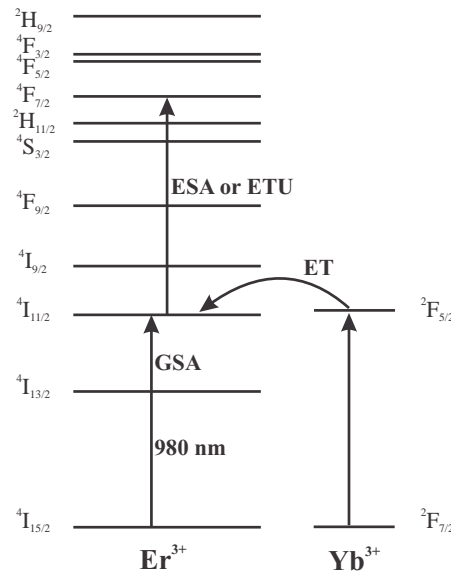


Figure 4.11: Energy level diagram of the Er³⁺ and Yb³⁺ ions showing the possible excitation pathways for populating state Er:⁴F_{7/2}, upon 980 nm excitation. GSA...Ground state absorption, ET...Energy transfer, ESA...Excited state absorption and ETU...Energy transfer UpC.

Once excited to ⁴I_{11/2}, a promotion to ⁴F_{7/2} by ESA or a successive ET from Yb can take place. Since we use a higher Yb than Er doping concentration in the host material and the oscillator absorption strength of Yb is larger than that of Er at 980 nm, we will mainly consider the energy transfer UpC (ETU) mechanism when discussing the UpC processes. With the current equipment available in our lab, we could only observe UpC phenomena for samples which were at least annealed at 600 °C/1 h, in air.

In Er/Yb:Y₂O₃ films, UpC luminescence upon ~980 nm is observed throughout the visible domain: a weak violet luminescence corresponding to the transition ²H_{9/2} → ⁴I_{15/2} at ~410 nm, a weak green luminescence band assigned to ²H_{11/2}:⁴S_{3/2} → ⁴I_{15/2} at ~540 nm and a strong red emission attributed to the transition ⁴F_{9/2} → ⁴I_{15/2} at ~660 nm, respectively. Fig. 4.12 shows the UpC spec-

4.4 Luminescence spectra of Er/Yb:Y₂O₃ films deposited by AA-MOCVD

tra for a series of Er/Yb:Y₂O₃ films with varying Yb concentration, once, under continuous laser excitation ($P = 4\text{ W}$, Fig. 4.12 (a)), and once under pulsed laser excitation, using another experimental set-up. The latter equipment has a significantly more sensitive detection method for the up-converted luminescence, and was able to detect the three-photon UpC emission at $\sim 410\text{ nm}$. Fig. 4.12 (b) depicts precisely two spectra recorded upon pulsed laser conditions, showing a 5-fold increase of the UpC emission intensity of an Er/Yb co-doped sample (3%Er, 10%Yb) compared to a singly Er-doped one (3%Er). This fact can be attributed to the previously mentioned improved absorption cross-section of Yb compared to Er at the pump wavelength used.

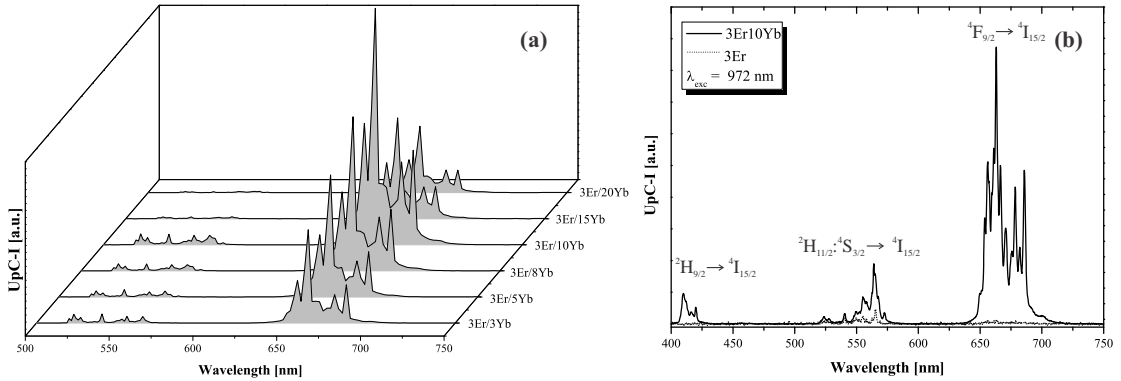


Figure 4.12: (a) UpC emission spectra of Er/Yb:Y₂O₃ films annealed at 800 °C, recorded upon 972 nm continuous laser excitation in the 500–750 nm range. (b) Influence of the Yb co-doping on the Er³⁺ up-converted emission in Y₂O₃. Spectra were recorded on thin films annealed at 900 °C with a pulsed tunable EKSPILA laser (see text for further explanations).

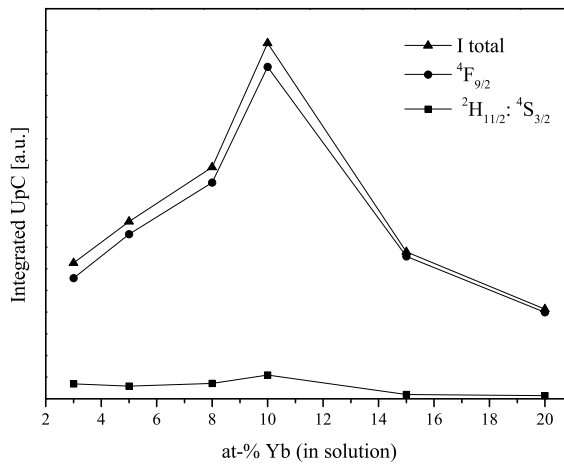
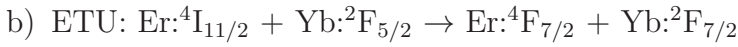
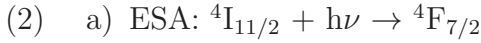
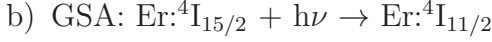
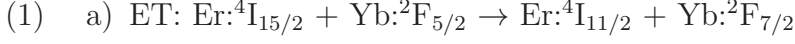
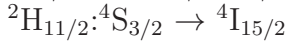


Figure 4.13: Integrated red ($^4F_{9/2} \rightarrow ^4I_{15/2}$), green ($^2H_{11/2}; ^4S_{3/2} \rightarrow ^4I_{15/2}$) and the total emission intensity as a function of the Yb concentration for Er/Yb doped Y₂O₃ films (annealed at 800 °C).

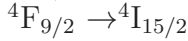
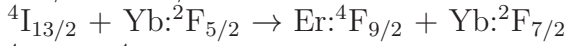
The maximum UpC emission was observed for the sample doped with 10 at.% Yb, as can be seen from Fig. 4.13. Further increase in the sensitizer concentration leads to concentration quenching of the luminescence. All light-emitting states are populated due to several consecutive UpC steps through feeding the intermediate level $Er:4I_{11/2}$. The most probable population mechanisms for the violet, green and red emissions are thoroughly discussed in Chapter 3 and 5, hence we can expect the following excitation sequences for higher excited states:



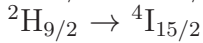
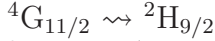
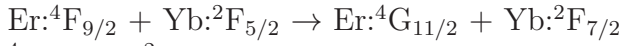
(3) **Green emission:**



(4) **Red emission:**



(5) **Violet emission:**



The *red* emission corresponds to the transition $4F_{9/2} \rightarrow 4I_{15/2}$ and is due to an energy transfer from a nearby excited Yb^{3+} ion to $Er:4I_{13/2}$. The population of $4I_{13/2}$ might occur as a result of a multiphonon relaxation from the higher state $4I_{11/2}$ or radiatively from state $4S_{3/2}$ [149]. Moreover, at high Yb concentration an Er-to-Yb energy back transfer becomes competitive and enables the population of the $4I_{13/2}$ state due to $Er:4S_{3/2} + Yb:2F_{7/2} \rightarrow Er:4I_{13/2} + Yb:2F_{5/2}$.

The *green* emission is due to a two-photon absorption, after the intermediate level $Er:4I_{11/2}$ is further promoted to level $4F_{7/2}$. After nonradiatively relaxing to the states $2H_{11/2}$ and $4S_{3/2}$, a radiative transition to $4I_{15/2}$ yields green luminescence.

The *violet* emission is associated with the transition $2H_{9/2} \rightarrow 4I_{15/2}$ and requires at least three ~ 970 nm quanta. A successive third ET from Yb promotes the transition $4F_{9/2} \rightarrow 4G_{11/2}$ followed by a fast relaxation towards state $2H_{9/2}$.

Influence of the annealing temperature on the UpC emission intensity

In Fig. 4.14 (a) the UpC emission spectra of Er/Yb:Y₂O₃ films (3%Er, 10%Yb) are shown as a function of the annealing temperature. The UpC emission intensity increases drastically by about a factor of 17, when increasing the annealing temperature from 600 °C to 900 °C.

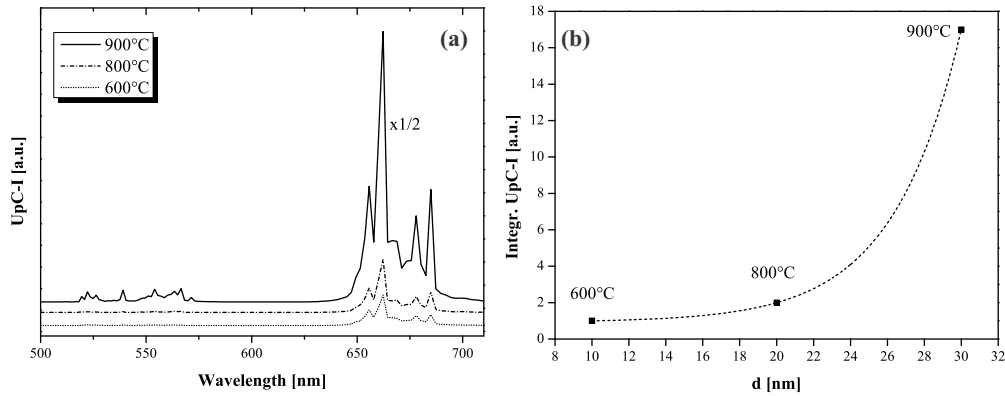


Figure 4.14: (a) Comparison of the UpC emission spectra of Er/Yb:Y₂O₃ films deposited at 540 °C and additionally baked at 600 °C, 800 °C and 900 °C, respectively, for 1 h, in air. The intensity of the 900 °C annealed sample spectrum was divided by 2. (b) Total integrated UpC emission intensity as a function of the crystallite size determined by the Scherrer formula in the XRD analysis. The UpC intensity was normalized with respect to the sample baked at 600 °C, which exhibits the lowest total UpC emission intensity.

We attributed this phenomenon to two main factors: reduction or elimination of organic impurities due to the acetylacetonates (and *tmhd*-) precursors reduces phonon losses (nonradiative multiphonon processes); furthermore, an increase in the grain size induced by annealing at elevated temperatures improves the UpC efficiency due to a minimization in the grain–boundary area (hence reduces defects). These thermal effects have been shown to be responsible for the improved luminescence in various materials [140]. Fig. 4.14 (b) shows the integrated Vis–UpC intensity of Er/Yb:Y₂O₃ films baked at different temperatures, as a function of their crystallite sizes, which were derived from the Scherrer equation in the XRD analysis. A sharp increase in the emission intensity is obtained after annealing the films at 900 °C for 1 h, in air.

Power dependence of UpC luminescence intensities

One method to study the UpC excitation mechanisms is to perform power dependence studies of the UpC luminescence. We can obtain the number of photons n , required to populate an excited state by the slope in a double–logarithmic representation of excitation power P versus the emission intensity I . The generalized expression, $I \propto P^n$, is only valid for the specific case, that the UpC rate is low compared to the linear decay [49].

The power dependence of the green and red UpC emission was studied under continuous laser excitation at 972 nm for a Er/Yb:Y₂O₃ film, shown in Fig. 4.15. The

blue emission band could not be recorded due to the weak intensity signal, especially at low excitation power. The measured slopes are 2 and 1.4 for the green and red emission band, respectively, and indicate that in both cases a two-photon absorption is responsible for the population of these states.

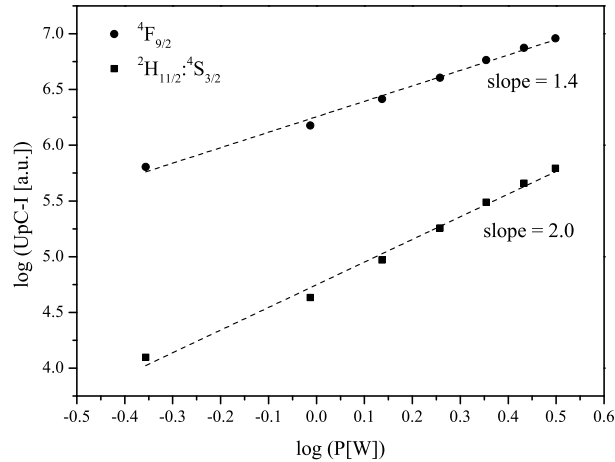


Figure 4.15: Power dependence of the green (emission from excited state ${}^2H_{11/2}, {}^4S_{3/2}$) and red (${}^4F_{9/2}$) UpC emission intensities of Er/Yb: Y_2O_3 (3%Er, 10%Yb), annealed at 900 °C. The measured slopes are noted in the graph.

4.5 Lifetimes of Er: ${}^4I_{13/2}$ and Yb: ${}^2F_{5/2}$ states in Er/Yb: Y_2O_3 films deposited by AA-MOCVD

The metastable Er: ${}^4I_{13/2}$ level plays an important role in many UpC processes. Therefore, we studied the time evolution of this level using 977 nm photon excitation and detection on the 1530 nm emission line of the Er^{3+} ion. Fig. 4.16 (a) shows the decay curves of Er/Yb: Y_2O_3 films (all annealed at 900 °C), as a function of the Yb concentration. The highest Er: ${}^4I_{13/2}$ lifetime obtained, shown in Fig. 4.16 (b), is about ~ 1.6 ms for a sample containing 3 at.% Er/3 at.% Yb.

This is in reasonable good agreement with values reported in the literature, as can be seen from Table. 4.3. At this point it has to be mentioned, that it is not always explicitly specified in the literature, if one uses the cationic RE concentration, RE/(RE+Y), or the film composition including oxygen, RE/(RE+Y+O); therefore, attention has to be paid when comparing experimental data with reference data from the literature.

At high Yb concentrations, the samples show exponential and non-exponential regions in the decay profile, e.g. the sample containing 15 at.% Yb shows in the beginning a non-single exponential behavior and converges slightly into an exponential part at the end. The non-exponential behavior is due to the energy transfer from Er-to-Yb, and the exponential part caused by the energy migration between Er^{3+} ions [155]. The experimental Er: ${}^4I_{13/2}$ lifetimes do not show a

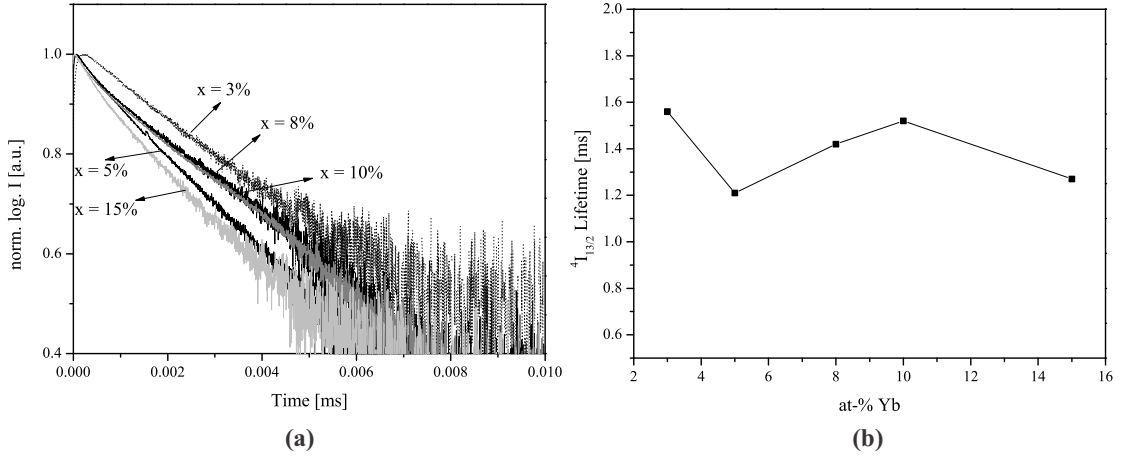


Figure 4.16: (a) Luminescence decay profiles of $\text{RE}:\text{Y}_2\text{O}_3$ films annealed at 900°C with compositions of 3 at.% Er and x at.% Yb, with x indicated in the graph. (b) $\text{Er}^{:4}\text{I}_{13/2}}$ lifetime dependence as a function of the Yb concentration. All decay curves were obtained at 977 nm excitation on the 1530 nm emission line of Er^{3+} .

Table 4.3: Lifetimes τ of excited states $\text{Er}^{:4}\text{I}_{13/2}}$ and $\text{Yb}^{:2}\text{F}_{5/2}}$ in $\text{Er}/\text{Yb}:\text{Y}_2\text{O}_3$ films, after NIR excitation and selected values found in the literature.

Sample	τ	Lit.
3% Er/ $x\%$ Yb: Y_2O_3 film, 900°C	1.6–1.2 ms ($^4\text{I}_{13/2}$)	this work
0.9% Er/ 7% Yb: Y_2O_3 film	2.4 ms ($^4\text{I}_{13/2}$)	[150]
0.5% Er/ 2.1% Yb: Y_2O_3 film	4.6 ms ($^4\text{I}_{13/2}$)	[150]
1% Er/ 2% Yb: Y_2O_3 NC	5.61–7.23 ms ($^4\text{I}_{13/2}$)	[151]
0.3% Er: Y_2O_3 film	7.5 ms ($^4\text{I}_{13/2}$)	[152]
0.75% Er: Y_2O_3 film	6 ms ($^4\text{I}_{13/2}$)	[153]
10% Yb: Y_2O_3 film, 900°C	$3\ \mu\text{s}$ ($^2\text{F}_{5/2}$)	this work
5% Yb: Y_2O_3 crystal	$950\ \mu\text{s}$ ($^2\text{F}_{5/2}$)	[154]
0.26% Yb: Y_2O_3 crystal	$790\ \mu\text{s}$ ($^2\text{F}_{5/2}$)	[155]

high dependence on the Yb concentration. This can be explained by considering several effects reported in the literature [156]. As it was already mentioned before, the excited Yb^{3+} ions in their $^2\text{F}_{5/2}$ state, transfer their excitation energy to $\text{Er}^{:4}\text{I}_{11/2}}$. The metastable $^4\text{I}_{13/2}$ level is then populated by nonradiative decay from $^4\text{I}_{11/2}$. With increasing Yb concentration, the population density of state $^4\text{I}_{13/2}$ is increased due to efficient Yb-to-Er energy transfer. On the other hand, other processes decrease the population of state $^4\text{I}_{13/2}$, hence the lifetime. First, due to UpC processes attributed to transitions $^4\text{I}_{11/2} \rightarrow ^4\text{F}_{7/2}$ and $^4\text{I}_{13/2} \rightarrow ^4\text{F}_{9/2}$, respectively. Secondly, back transfer from Er-to-Yb can lower the luminescence lifetime and ion-ion interactions between neighboring Yb^{3+} ions start to take effect when the Yb^{3+} concentration is increased. All these processes influence the $\text{Er}^{:4}\text{I}_{13/2}$ lifetime with similar situations reported in the literature [133, 150, 154, 156, 157]. Fig. 4.17 shows the decay curves of Yb^{3+} once in singly-doped $\text{Yb}:\text{Y}_2\text{O}_3$ and for an Er/Yb co-doped Y_2O_3 film.

It is evident that the $\text{Yb}^{:2}\text{F}_{5/2}$ lifetime is reduced when Er^{3+} ions are present due

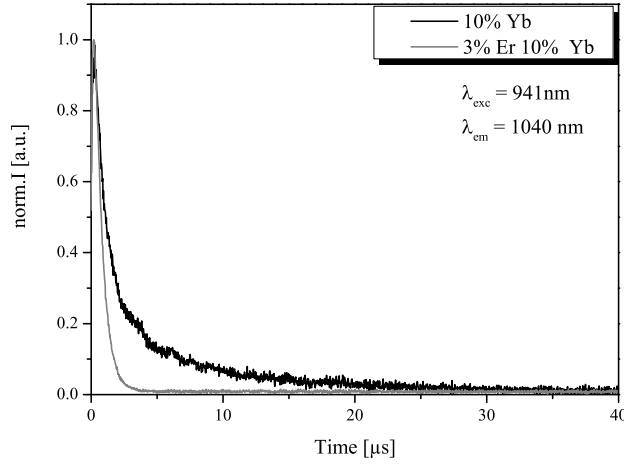


Figure 4.17: Measured exponential decay rates from $Yb:2F_{5/2}$ in singly-doped Yb and Er/Yb co-doped Y_2O_3 films. The decay curves were obtained at 941 nm excitation on the 1040 nm emission line of Yb.

to the quasi-resonant $2F_{5/2}$ (Yb) \rightarrow $4I_{11/2}$ (Er) energy transfer. The luminescence lifetimes of Yb^{3+} obtained in this work are $\sim 3 \mu s$ for 10 at.% Yb and $\sim 0.6 \mu s$ for 3 at.% Er/10 at.% Yb doped Y_2O_3 . Although the lifetimes achieved are lower than the values of other data on Yb^{3+} , by a few hundreds of μs , as shown in Table 4.3, we have to consider that the RE concentrations used in this work are much higher. The next stage of the investigation was to determine the Yb-to-Er energy transfer efficiency. For this, the $Yb:2F_{5/2}$ lifetimes τ_0 in the singly-doped Y_2O_3 film, and τ_e , in the Er/Yb co-doped sample, have been measured to obtain the energy transfer quantum yield through the equation:

$$\eta_{Yb \rightarrow Er} = 1 - \frac{\tau_e}{\tau_0} \quad (4.1)$$

Using Eq. 4.1, we obtain an energy transfer efficiency of about 80 % for a composition of 3 at.% Er and 10 at.% Yb, a value which is comparable to the literature [158]. A rather high transfer efficiency can be expected with high Yb concentration, owing to the strong interionic interactions between Er^{3+} and Yb^{3+} ions.

4.6 Summary

This work studied the influence of the annealing temperature on the structural and luminescence properties of Er/Yb: Y_2O_3 films, deposited at 540 °C onto Si(100) substrates by AA-MOCVD. Although the as-grown films are smooth and homogeneously deposited, a post-deposition treatment is essential to eliminate organic impurities to improve the luminescent properties of the films. High annealing temperature improves the crystallization and increases the grain sizes of the films. However, with the increase in temperature, the formation of micro-cracks in the

film microstructure appears due to the large difference in the thermal expansion coefficients of the film and substrate and also, due to film shrinkage. Even though the presence of micro-cracks has little influence on the efficiency of the UpC process, in certain cases when smooth and crack-free films are required, a change of the substrate of a higher CLTE than silicon, such as e.g. sapphire with a $CLTE = 8.3 \cdot 10^{-6}/K$, should be considered. NIR-to-Vis UpC emission was observed of the annealed films, with three main emission bands positioned at ~ 410 nm, 540 nm and 660 nm. An enhancement for the total UpC intensity of about 17 times was achieved for samples annealed at 900°C when compared to $600^\circ\text{C}/1\text{h}$, in air. We attributed this mainly to a consequence of diminishing multiphonon relaxation processes due to thermal effects. Finally, our investigation of the processes of luminescence kinetics showed a Yb-Er energy transfer efficiency of $\sim 80\%$ for the best light emitting sample. The lifetime of intermediate state $\text{Er}^4\text{I}_{13/2}$ was shown to be weakly influenced by the Yb concentration and was determined to be 1.6–1.2 ms. We explained this fact by other influencing factors such as UpC and energy transfer phenomena, which become competitive when the RE concentration is comparatively high.

 RE^{3+} -doped Y_2O_3 thin films grown by LI-MOCVD

$\text{RE}:\text{Y}_2\text{O}_3$ ($\text{RE} = \text{Er}, \text{Yb}$) thin films were deposited at 700°C via pulsed liquid injection MOCVD. The films were homogeneously grown on Si(100) wafers and exhibited a good optical quality.

We studied the microstructure and optical properties of the post-deposition annealing temperature applied to the films. Upon photon excitation at 972 nm, all films exhibited UpC phenomena in the visible wavelength range. A strong red emission according to the transition ${}^4\text{F}_{9/2} \rightarrow {}^4\text{I}_{15/2}$, weaker green emission from ${}^2\text{H}_{11/2}; {}^4\text{S}_{3/2}$ to the ground state, and a very weak emission band at ~ 410 nm due to a three-photon absorption process in Er^{3+} were observed. The up-converted emission was shown to gradually increase with the annealing temperature. Furthermore, luminescence decay kinetics of ${}^4\text{S}_{3/2}$ and ${}^4\text{F}_{9/2}$ states in Er^{3+} show a lengthening in the observed lifetimes after thermal annealing of the films. This was mainly attributed to the increased grain size due to the thermal annealing. Finally, we performed power-dependent UpC luminescence measurements to confirm our proposed excitation mechanisms.

5.1 Introduction

Owing to its excellent physical properties, Yttrium oxide (Y_2O_3) finds application in several areas of technology. Because of its wide band gap (~ 6 eV), thermal stability ($T_m = 2710$ K) and broad transparency range ($0.2\text{--}8\ \mu\text{m}$), high refractive index (~ 1.9 [148]) and relative low phonon energy [159], it is used for luminescent materials [160–162], protective/optical coatings [163–165] and waveguide applications [166, 167]. Furthermore, Y_2O_3 is investigated as a replacement of SiO_2 in microelectronics because of its small lattice mismatch with Si and high dielectric constant ($\approx 14\text{--}18$ [168, 169]). Y_2O_3 is an excellent host for the embedding of trivalent rare earth (RE^{3+}) ions due to their similar ionic radii (e. g. $\text{Y}^{3+} = 0.0892$ nm and $\text{Er}^{3+} = 0.0881$ nm [153]). We are in particular interested in RE^{3+} -doped thin films capable of performing light up-conversion (UpC), which might be useful in photovoltaics as one concept for third generation solar cells.

The numerous deposition techniques of RE^{3+} -doped Y_2O_3 thin films involve different variants of metalorganic chemical vapor deposition (MOCVD) [139, 140, 152, 161, 170], sputtering techniques [171], pulsed laser deposition [172–174] and wet-chemical methods such as the sol-gel method [162, 175, 176].

In this case, Er/Yb co-doped Y_2O_3 films were grown by pulsed liquid injection (LI) MOCVD on Si(100) wafers and their microstructure and light UpC properties were analyzed. Scanning electron microscope (SEM) analysis shows that the as-grown films are columnar in growth nature with fine crystallites and no micro-crack formation was observed. Further, we studied the effects of a post-deposition annealing step of the as-deposited films on structural and optical properties, and showed an increase in the UpC emission intensities after thermal annealing of the samples. We attribute this enhancement of the UpC emission intensities to the increased grain size caused by the annealing process. An increase in grain size leads to reduced grain boundaries, hence a reduced number of luminescence quenching areas. A lengthening of the lifetimes of the states $^4\text{S}_{3/2}$ and $^4\text{F}_{9/2}$ was observed for the annealed samples compared to the as-grown films. Moreover, we discuss the most probable UpC mechanisms responsible for the strong red, weak green and violet UpC emission, which is observed upon diode laser excitation at 972 nm.

5.2 Film deposition

Er/Yb co-doped Y_2O_3 films were grown by pulsed LI-MOCVD on 4" Si(100) wafers at 700 °C. A schematic diagram of the MOCVD reactor (Annealsys, MC200) is shown in Fig. 5.1. The process is based on the injection of microlitres of a solution containing the organometallic precursors $\text{Ln}(\text{tmhd})_3$ (2,2,6,6-tetramethyl-3,5-heptanedionate; Ln = Y, Er, Yb) in cyclohexane (0.05 M).

Immediately after the solution is injected into the evaporator, flash-vaporization takes place. The vaporized precursors are then carried by an O_2/Ar gas flow into the reaction chamber onto a heated and rotating substrate, where the decomposition/reaction of the precursors leads to the formation of a solid film. For the substrate heating a resistive heating is used. The substrate is mounted on a ro-

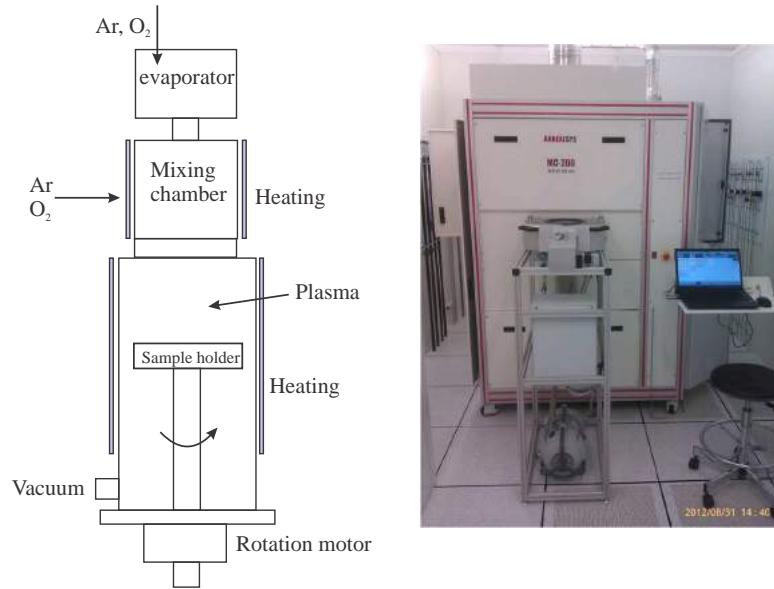


Figure 5.1: Left: LI-MOCVD reactor scheme for the deposition of RE-doped Y_2O_3 thin films. Right: Photographic image of the same.

tating stage to allow uniform deposition. The amount of solution injected during the experiment depends on processing parameters such as the opening time of the injector as well as the frequency and the number of pulses [87]. This has the advantage of a controlled (“digital”) film growth, since the film thickness is determined by the number of pulses, when all other parameters are fixed. Table 5.1 summarizes all relevant processing parameters for the optimized RE-doped Y_2O_3 film growth.

Table 5.1: Processing parameters for Er/Yb: Y_2O_3 film growth by pulsed LI-MOCVD.

Substrate temperature [°C]	700
Evaporation chamber temperature [°C]	150
Carrier gas flow rate [sccm]	Evaporator: 500 O_2 + 1500 Ar; Reaction chamber: 500 O_2 + 200 Ar
Oxygen concentration in total gas flow [%]	Evaporator: 25%; Reaction chamber: 71%
Total work pressure [mbar]	5
Pulse frequency [Hz]	3
Injection rate [g/min]	0.8
Substrate rotation [rpm]	30
Concentration precursor solution [M]	0.05

Compositional analysis using electron probe microanalysis (EPMA) yielded stoichiometric Y_2O_3 films doped with 1 at.% Er and 7 at.% Yb. After film deposition at 700 °C, the as-grown films underwent a thermal annealing process in air, for 1 h at 900 °C and 1050 °C. The aim of the present study was to investigate possible changes in the optical, microstructural and spectroscopic behavior of the films. For the description of the characterization methods used in this chapter, see Chapter 2, Section 2.2 and the experimental part of Chapter 3.

5.3 Film microstructure

XRD studies of Er/Yb:Y₂O₃ thin films on Si(100) reveal a polycrystalline nature with peaks mostly due to body-centered cubic Y₂O₃ and additional peaks for base-centered monoclinic Y₂O₃ (cubic Y₂O₃ ICDD No. 41–1105 and monoclinic Y₂O₃ No. 44–0399), see Fig. 5.2.

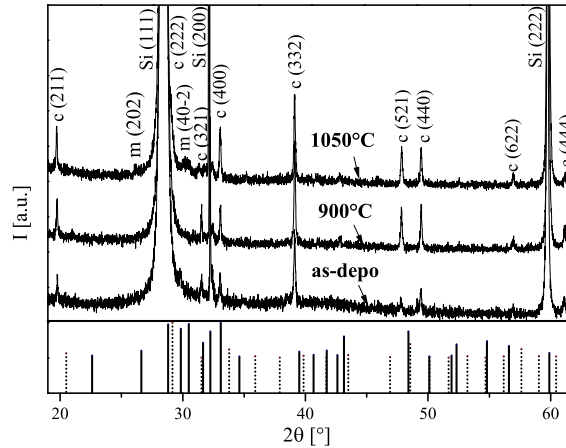


Figure 5.2: XRD patterns of films as-deposited and films undergone post-growth annealing at 900 °C and 1050 °C; shown are cubic Y₂O₃ (dotted line, ICDD No. 41–1105) and monoclinic Y₂O₃ (solid line, ICDD No. 44–0399) as reference patterns. Indexed reflections designated with ‘c’ and ‘m’ refer to the cubic and monoclinic phase, respectively.

Usually, high temperature and high pressure conditions are required for the monoclinic phase in bulk Y₂O₃ to be formed [177]. However, the same is found in nanocrystalline materials at ambient conditions due to the Gibbs–Thomson effect [178]. The coexistence of the monoclinic and cubic Y₂O₃ phases in thin films is supported by previous works and in fact strongly depends on the material synthesis used [140, 169, 179]. The XRD patterns of Y₂O₃ are shown in Fig. 5.2 as a function of the temperature: the as-deposited film as well as samples which were subject to a post-deposition annealing step, show peak positions slightly shifted compared to the powder diffraction reference patterns, possibly due to residual stress in the film structure. However, no major changes in the emerging peaks were observed. The main difference is that in films thermally annealed at 900 °C and 1050 °C, the reflection intensities become more pronounced, indicating an increase of crystallinity. The grain size was deduced from the Scherrer formula, $\beta = 0.9 \cdot \lambda / D \cdot \cos(\theta)$, with β the line broadening (full width at half maximum, FWHM) and D the crystalline domain size, for the 332 reflection at $2\theta \sim 39^\circ$. The Scherrer–crystallite size showed an increase from 46 to 62 nm for the as-synthesized sample and the one annealed at 1050 °C, respectively.

That the cubic phase is the dominant crystalline phase in the films is confirmed by FTIR spectroscopy studies in the far-IR region as shown in Fig. 5.3 (b), with peak maxima at 301, 332, 370, 463, 517 and 560 cm⁻¹, corresponding to the Y–O vibrational bands of cubic Y₂O₃ [146, 147]. The FWHM of the most intense peak (at ~ 370 cm⁻¹) shows a decrease from 49 cm⁻¹ to 27 cm⁻¹ for the as-grown film and after annealing at 1050 °C, respectively, which confirms an increase of the crystallinity of the films that underwent thermal annealing.

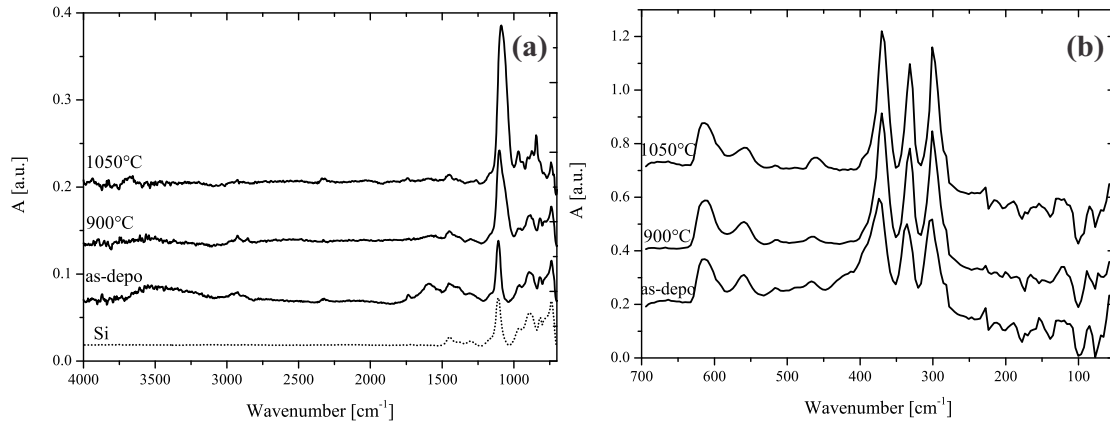


Figure 5.3: (a) MIR spectra of Y₂O₃ thin films grown on Si(100) wafers, as-deposited and after a post-annealing process during 1 h, in air. Additionally, the IR spectrum of a neat Si substrate is depicted (dotted line), whereby the absorption band at ~ 1100 cm⁻¹ corresponds to the Si–O–Si asymmetric stretching vibration. (b) FTIR spectra between 700–50 cm⁻¹ of the same. Note, that the absorption at ~ 615 cm⁻¹ is due to the Si–Si vibrational mode, and not due to Y₂O₃ [180].

Moreover, the analysis of the FTIR spectra between 4000–700 cm⁻¹, shown in Fig. 5.3 (a), reveals that the as-deposited film shows a broad OH absorption at ~ 3400 cm⁻¹ due to remaining OH impurities in the film. Vibrational bands located at between 1700 and 1400 cm⁻¹ are assigned to the mode vibrations of C=O, C=C, C–CH₃ and –CH₃ [181]. These originate from organic residues due to an incomplete decomposition of the metal β -diketones used as precursors in the film synthesis [182]. A clean decomposition of the precursors is achieved after post-annealing at ≥ 900 °C. The absorption band located at ~ 1100 cm⁻¹ corresponds to the Si–O–Si asymmetric stretching vibration due to the oxidation of the substrate at high temperature. From the analysis we can see, that IR spectroscopy can detect residual organic impurities which cannot be detected by XRD.

In Table 5.2 the Scherrer-derived crystallite sizes and FWHM of the most intensive IR band at 370 cm⁻¹ are listed for films as-grown and undergone thermal annealing. The obtained results from the XRD and FTIR studies reveal that a post-growth annealing of the films leads to an increase in crystallinity and grain sizes. The influence of post-deposition thermal annealing on the film microstructure was explored by SEM, as can be seen in Fig. 5.4. The top-view SEM images reveal rod-shaped grains of uniform length up to ~ 340 nm for all films. However, the rods became thicker when the films were thermally annealed, and show an increase

Table 5.2: Influence of the thermal annealing of Er/Yb-doped Y_2O_3 thin films on the grain size D , derived by the Scherrer formula and corresponding FWHM of the 322 reflection; moreover, the FWHM of the vibrational band at 370 cm^{-1} for thin films as-deposited and annealed at $900\text{ }^\circ\text{C}$ and $1050\text{ }^\circ\text{C}$ in air, are depicted.

Sample	D [nm]	FWHM [$^\circ$] at 322 reflection	FWHM [cm^{-1}] at 370 cm^{-1}
As-deposited	46	0.18	49
Annealed at $900\text{ }^\circ\text{C}$	59	0.14	28
Annealed at $1050\text{ }^\circ\text{C}$	62	0.13	27

in size, from $\sim 67\text{ nm}$ to 100 nm for the as-grown film and after an annealing step at $1050\text{ }^\circ\text{C}$, respectively. The grain size and shape distributions in Er/Yb: Y_2O_3 films are homogeneous.

Compared to the Scherrer-derived crystallite sizes in the XRD analysis, larger values are obtained in the SEM measurements. To explain this discrepancy, one has to take into account that one cannot accurately determine whether the particle is one single grain or composed of many grains. Thus the grain/particle size is usually larger than the crystallite size. Furthermore, the Scherrer equation works best for nearly spherical-shaped particles, hence the obtained values depend on the diffraction peak used to determine the size for non-spherical particles. Even though there is a large mismatch between the thermal expansion coefficients of c -Si and Y_2O_3 (CLTE c -Si: $2.6 \cdot 10^{-6}\text{ K}^{-1}$ (at 300 K) [109] and Y_2O_3 : $8.1 \cdot 10^{-6}\text{ K}^{-1}$ [140]), no micro-cracks were observed in the film, probably due to the existing discontinuity of grains in the film microstructure. The cross-section micrographs in Fig. 5.4 (right), reveal a columnar film growth caused by the polycrystalline growth process, initiated by nucleation at the substrate surface. At high temperatures, crystallites start growing and coalesce upon the formation of a dense microstructure [82].

Fig. 5.5 displays the AFM images of the as-deposited and annealed Er/Yb: Y_2O_3 films, with a thickness of $d_f \sim 500\text{ nm}$. The root-mean square (RMS) roughness increases with the post-deposition temperature from 15 to 22 nm for a $10 \times 10\ \mu\text{m}^2$ area, for films as-deposited and baked at $1050\text{ }^\circ\text{C}$, respectively. Furthermore, all films show a homogeneous, dense microstructure with small grains, and no micro- and macro-cracks were observed in the film structure.

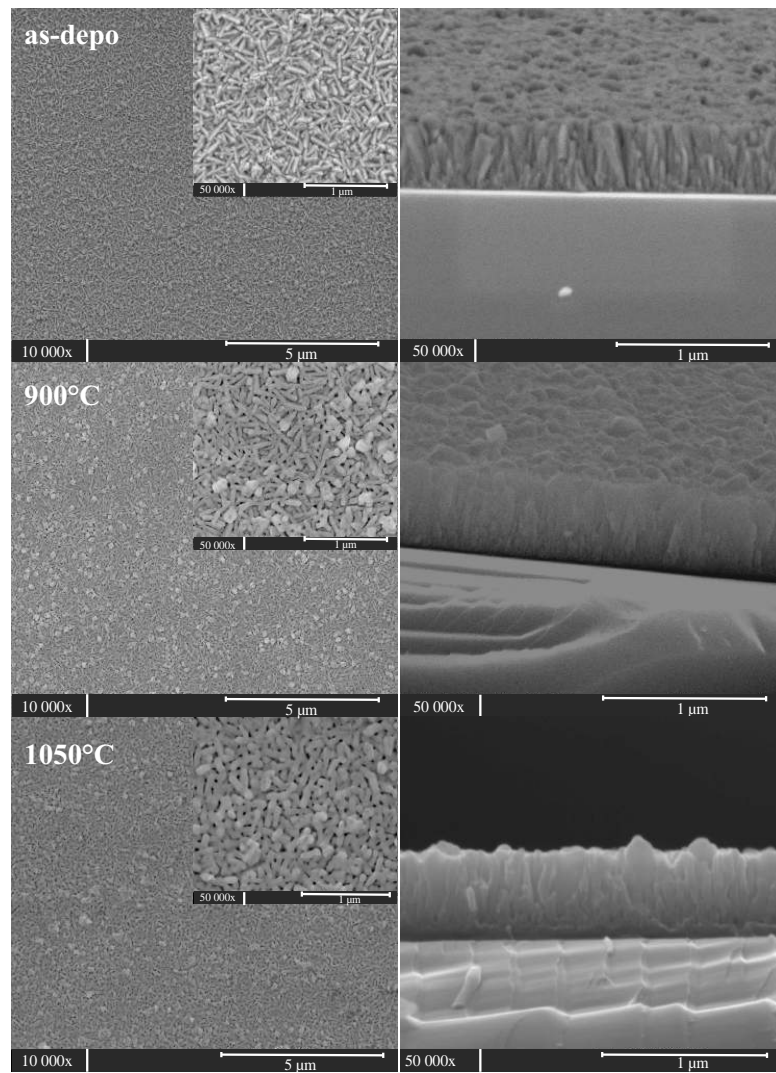


Figure 5.4: Left: Top-view SEM micrographs of Er/Yb:Y₂O₃ on Si(100) as-deposited (at 700 °C) and after post-growth annealing at 900 °C and 1050 °C. Additionally, for a better view, images of higher magnification are inset. Right: Cross-section images of the same.

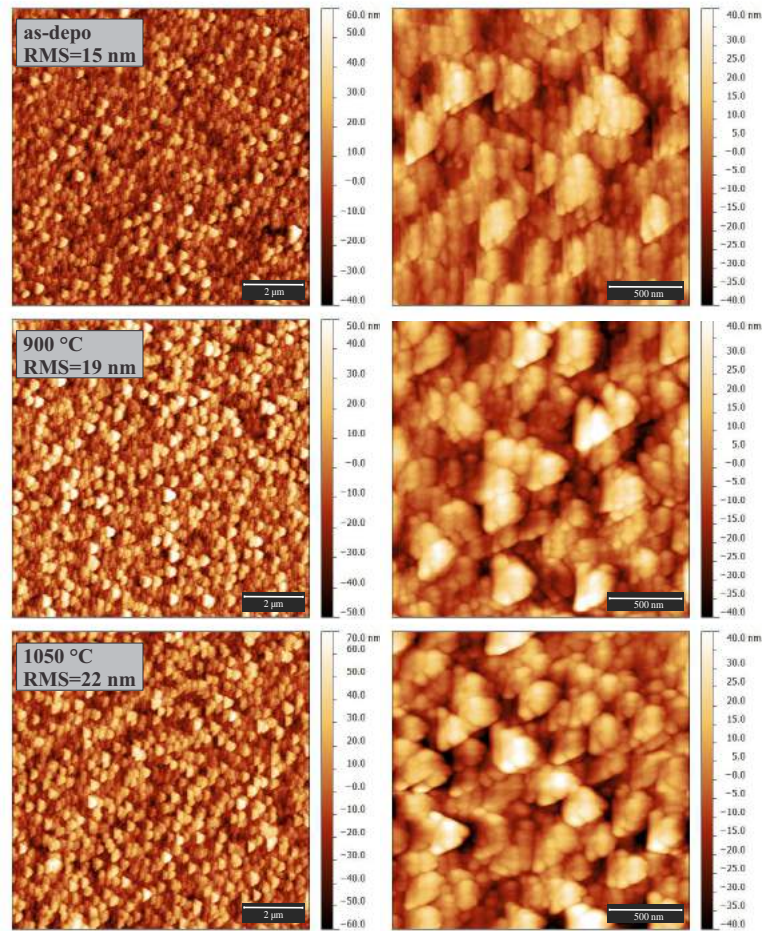


Figure 5.5: AFM height images (left: $10 \times 10 \mu\text{m}^2$; right: $2 \times 2 \mu\text{m}^2$ area) of Er/Yb co-doped Y_2O_3 films as deposited (at 700°C) and after annealing at 900°C and 1050°C ($d_f \sim 500 \text{ nm}$). The corresponding RMS surface roughnesses of a $10 \times 10 \mu\text{m}^2$ area are indicated in the graph.

5.3.1 Dispersion of refractive index and Raman spectra of Er/Yb: Y_2O_3 films

The dispersion of the refractive index for Er/Yb: Y_2O_3 films was determined as a function of the annealing temperature by spectroscopic ellipsometry measurements between 250–800 nm. For the fitting of our ellipsometric data we adopted the Cauchy dispersion function, $n(\lambda) = A + B \cdot 10^4/\lambda^2 + C \cdot 10^9/\lambda^4$, using a multi-layered model consisting of a silicon/ SiO_2 / Y_2O_3 layer.

For each sample, the Cauchy parameters A, B and C were determined by the least mean-square error (MSE) method to obtain a minimization of the fitting residual χ^2 . The three fitting parameters of the Cauchy function for all films are given in Table 5.3.

The refractive index n for the as-deposited film and the films annealed at 900°C and 1050°C at 500 nm is 1.77, 1.81 and 1.88, respectively. The observed changes in the refractive index can be explained on the basis of the increased packing density

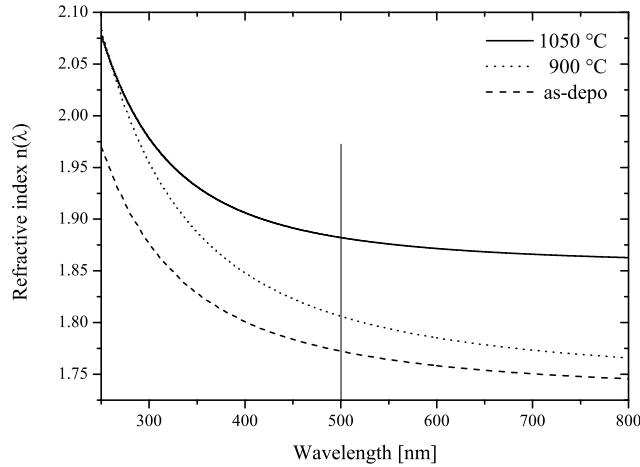


Figure 5.6: Dependence of the dispersion of the refractive index on the annealing temperature of Er/Yb:Y₂O₃. The auxiliary line indicates the refractive indices at 500 nm.

Table 5.3: Fitting parameters A, B and C of the Cauchy dispersion function and refractive index n at 500 nm for Er/Yb:Y₂O₃ films as-deposited and after thermal annealing at 900 °C and 1050 °C.

Er/Yb:Y ₂ O ₃ film	A	B	C	$n(500 \text{ nm})$
as-deposited	1.7310	0.8747	0.3859	1.77
900 °C	1.7430	1.3900	0.4570	1.81
1050 °C	1.8540	0.4721	0.5767	1.88

and crystallinity of the films with higher annealing temperature. The measured refractive index is in good agreement with reference data [168,183], but lower than that for bulk Y₂O₃ (1.939 at 500 nm [148]), because the refractive index is very sensitive to the microstructure, hence film preparation [184]. However, the film annealed at 1050 °C has optical properties closest to the Y₂O₃ bulk material, with a refractive index about 3% below the bulk index data.

Fig. 5.7 shows the room temperature Raman spectra studied over the 50–620 cm⁻¹ range of Er/Yb:Y₂O₃ thin film as-deposited and for films which underwent post-deposition annealing at 900 °C and 1050 °C.

Raman studies are important to obtain knowledge of the phonon cut-off frequency of the host lattice and for predicting the emission in an upconverter. The main bands are located at 369 (w), 404 (w), 469 (s), 542 (m), 558 (s) and 602 cm⁻¹, and are in fairly good agreement with the Raman-active vibrational modes reported for polycrystalline C-type Y₂O₃ [146,177]. From the 22 optically active Raman modes that can be expected for cubic Y₂O₃, only a few are observed in the present spectra, due to the polycrystalline nature of the material, which also may lead to

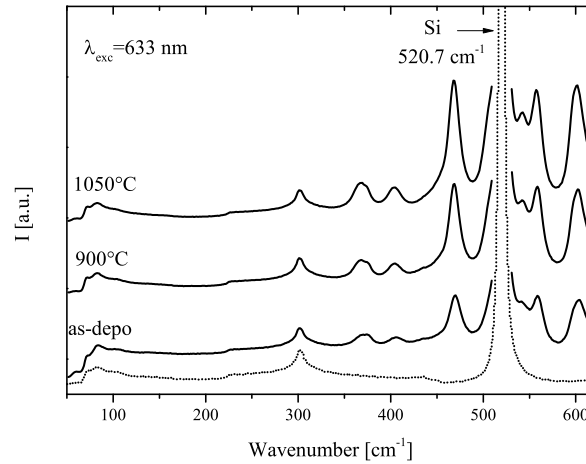


Figure 5.7: Raman spectra of Y₂O₃ thin films doped with Er/Yb, before and after undergoing thermal heat treatment at 900 °C and 1050 °C. Additionally, a reference spectrum of the Si substrate is depicted to identify Raman frequencies originating from the substrate in the sample spectrum.

variations in the Raman band intensities. Moreover, additional peaks are observed in the sample spectra due to the superposition of the Raman spectrum of c-Si on the Y₂O₃ spectrum: a very strong peak at 522 cm⁻¹ due to the first order optical phonon mode of c-Si, which is not recorded in the experimental sample spectra due to its high intensity, and the peak at ~ 300 cm⁻¹ due to overtones of the transverse acoustic 2TA phonons in c-Si [114].

5.4 Three-photon UpC emission and power dependence study on Er/Yb:Y₂O₃ thin films

Fig. 5.8(a) shows the up-converted IR-to-Vis emission recorded from Er/Yb-doped Y₂O₃ thin films after excitation at 972 nm ($P = 0.90$ W). UpC emission was observed for all films, however, post-deposition annealing of the as-grown films is shown to increase the total emission intensity by factors of 2 (annealed at 900 °C) and 6 (1050 °C), respectively. This fact can be mainly attributed to the increase in the grain size due to thermal annealing, which leads to a reduction in defects and hence a reduction in nonradiative recombinations [140, 161].

Moreover, the post-annealing process allows for the organic contamination to be eliminated, and reduces luminescence quenching due to the precursor residues. Groups of high vibrational energy quanta, such as -CO (1500 cm⁻¹) and -OH (3400 cm⁻¹), are able to increase the nonradiative rate and decrease the overall UpC efficiency.

The excitation routes for the population of the higher excited states for the Er/Yb couple upon IR excitation are thoroughly discussed in the literature [119, 185–187] and hence will be only shortly described in the following. The emission bands with

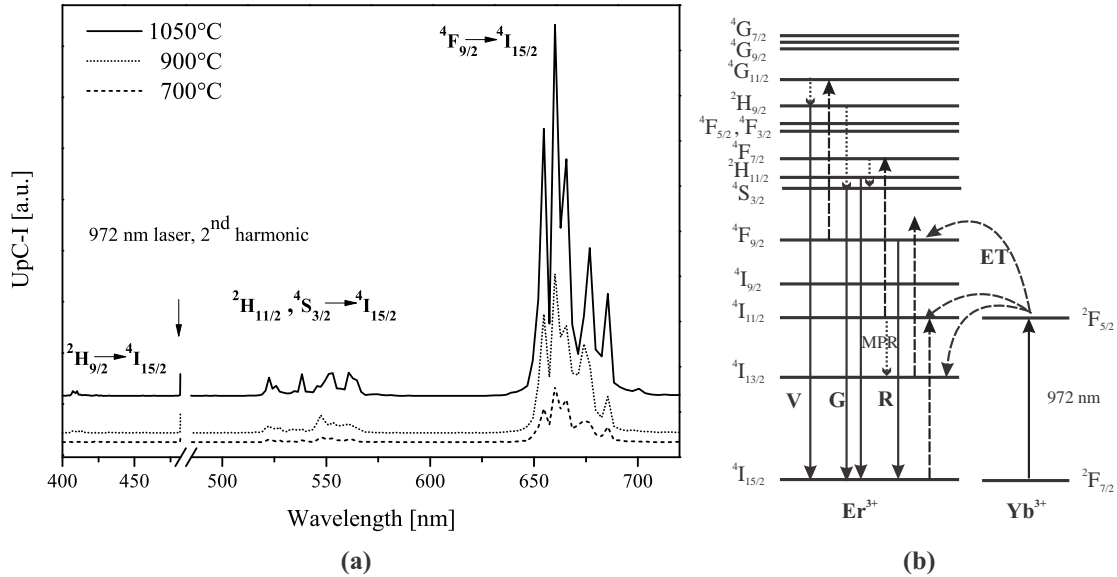


Figure 5.8: (a) UpC emission spectra of Er/Yb co-doped Y_2O_3 films on Si(100) excited at 972 nm, $P = 0.90$ W. (b) Energy level scheme of the Er/Yb couple with the corresponding excitation routes proposed for the green (“G”, 540 nm), red (“R”, 660 nm) and violet (“V”, 410 nm) emission. The excitation routes shown only involve ET steps from Yb^{3+} , indicated by the dashed lines. GSA/ESA in the Er^{3+} ion has been neglected in this scheme. Solid and dotted lines indicate radiative and nonradiative transitions, respectively.

peak maxima at ~ 410 nm, 550 nm and 660 nm correspond to the transitions from the ${}^2H_{9/2}$, ${}^2H_{11/2}$: ${}^4S_{3/2}$ and ${}^4F_{9/2}$ states to the ground state ${}^4I_{15/2}$ of Er^{3+} . In the UpC spectra, the red emission is dominant, which is commonly observed in oxide host lattices and thus the total emission of the samples appears red to the naked eye. As a general rule of thumb, the red emission is dominant considering a material cut-off phonon energy > 500 cm^{-1} , and mainly green emission is observed in case the phonon energy is < 400 cm^{-1} [119]. Most of the incoming 972 nm radiation is absorbed by Yb due to a larger absorption oscillator strength of the $Yb: {}^2F_{7/2} \rightarrow {}^2F_{5/2}$ transition, compared to the ground state absorption of $Er: {}^4I_{15/2} \rightarrow {}^4I_{11/2}$ [119]. Hence, population of the $Er: {}^4I_{11/2}$ state occurs predominantly via a quasi-resonant energy transfer from a nearby Yb^{3+} ion (Fig. 5.8 (b)). As a consequence, we mainly focus on ET and ETU when describing the underlying UpC mechanisms. Excitation via ground state absorption (GSA), followed by excited state absorption (ESA) in the Er^{3+} ion might in any case coexist with the ETU mechanism.

Red emission, corresponding to the ${}^4F_{9/2} \rightarrow {}^4I_{15/2}$ transition, is due to an energy transfer from a nearby excited Yb^{3+} ion to the intermediate level $Er: {}^4I_{13/2}$. The population of ${}^4I_{13/2}$ can occur as a result of a multiphonon relaxation from the upper-lying state ${}^4I_{11/2}$ or radiatively from state ${}^4S_{3/2}$ [149]. Moreover, at a high Yb concentration (as 7 at.%) an Er-to-Yb energy back transfer becomes competitive and enables the population of the ${}^4I_{13/2}$ state due to ${}^4S_{3/2}$ (Er) + ${}^2F_{7/2}$ (Yb) \rightarrow ${}^4I_{13/2}$ (Er) + ${}^2F_{5/2}$ (Yb).

The probability of a nonradiative multiphonon transition between two adjacent energy levels depends exponentially on the energy gap ΔE separating the same. The multiphonon transition rate, W_{MPR} , can be expressed as [41]:

$$W_{\text{MPR}} = W_{\text{MPR}}(0) \cdot \exp^{-\alpha \Delta E} \quad (5.1)$$

with the parameter α determined by the phonon energy and the electron-phonon coupling strength [120]. The number n of phonons which are emitted in the multiphonon relaxation process is expressed as:

$$n = \Delta E / \hbar \omega_{\text{max}} \quad (5.2)$$

with $\hbar \omega_{\text{max}}$ usually the cut-off phonon energy of the material contributing to the process. As mentioned by Güdel and Pollnau in Ref. [42], such multiphonon relaxations are only competitive when $n \leq 6$. Furthermore, it is known, that the controlling factor for the final emission output, i.e. whether the red or green emission is dominant in the spectrum, is the multiphonon relaxation rate (and the phonon-assisted energy transfer rate), which is dominated mainly by the lattice phonons.

In Y₂O₃, the energy gap between the lowest component of ⁴I_{11/2} and ⁴I_{13/2} is $\sim 3600 \text{ cm}^{-1}$ [36], which accounts for 6 phonons to bridge the gap ($\hbar \omega_{\text{max}} = 600 \text{ cm}^{-1}$). Therefore, the internal multiphonon relaxation process is still rather probable and the red emission is predominant over the green one. Kuroda *et al.* reported in Ref. [120] similar results for various Er/Yb-doped phosphor systems, amongst others Er/Yb:Y₃OCl₇, which has a phonon energy comparable to Y₂O₃. This confirms that the multiphonon relaxations are dominated by the phonon energies. An alternate excitation route for the red emission involves the population of ⁴F_{9/2} due to relaxation from ⁴S_{3/2} state towards ⁴F_{9/2} and is accompanied by the emission of phonons [188]. Bearing in mind a phonon cut-off frequency of $\sim 600 \text{ cm}^{-1}$, bridging the energy gap ⁴S_{3/2}-⁴F_{9/2}, $\sim 3000 \text{ cm}^{-1}$, accounts for about 5 phonons [36]. Spectroscopic data for Er:Y₂O₃ nanocrystals however show that, upon 488 nm excitation, the red emission is very weak compared to the green emission output [35]. Based on these results, we can assume that the excitation pathway for the red emission follows most probable ⁴I_{13/2} → ⁴F_{9/2}, and less is likely a result of nonradiative multiphonon transition from the ⁴S_{3/2} state. Our discussion allows us to conclude that two photons are involved in the UpC process which generate the red emission.

In order to affirm our assumptions about the underlying UpC mechanisms, power dependence studies of the UpC emission were performed. Fig. 5.9 shows the results for the measured slopes obtained by a double-logarithmic representation of the pump power P versus the red/green/violet UpC luminescence intensities I . In the case of low UpC rates, we can deduce the number of photons n required in the population of an excited state i according to $I_i = P^n$. The power dependence of the red emission indicates that a 2-photon process is involved, which is consistent with the proposed excitation mechanism and the values reported in the literature.

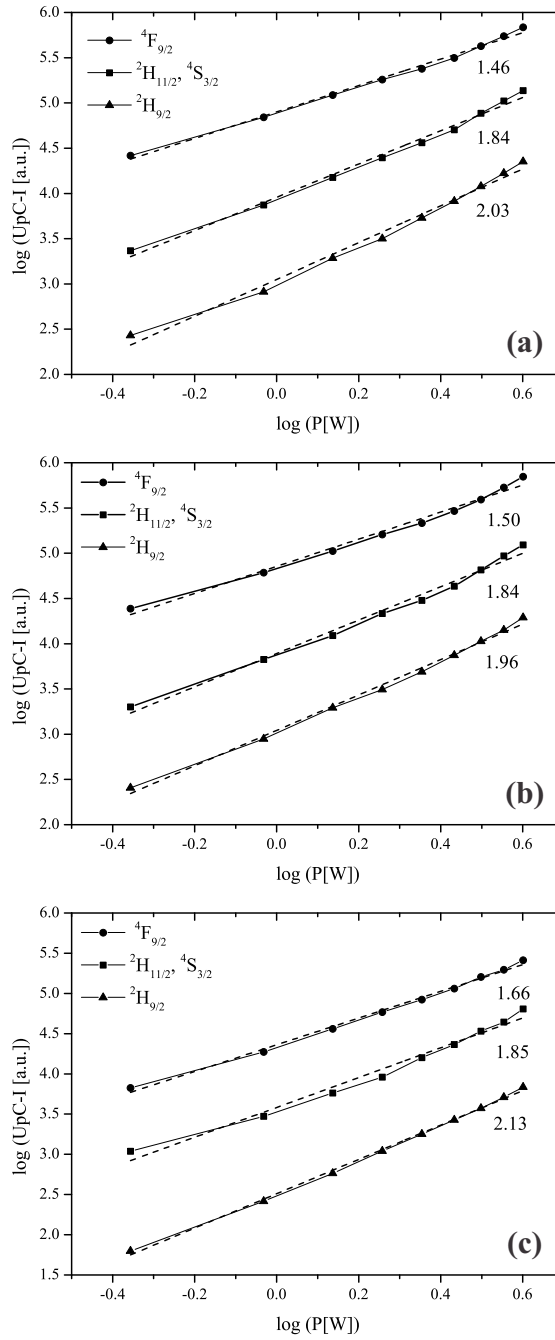


Figure 5.9: Double-logarithmic plot of the dependence of UpC emission intensities on the pump power in 1%Er/7%Yb: Y_2O_3 films annealed at (a) 1050 °C (b) 900 °C and (c) as-deposited (at 700 °C).

Table 5.4 gives some selected examples of experimentally obtained slopes of the dependence of the UpC emission intensities on the excitation power in RE: Y_2O_3 upon ~ 980 nm excitation.

The green emission originates from a successive second energy transfer from Yb: ${}^2F_{5/2}$ to Er: ${}^4I_{11/2}$, promoting the population of Er: ${}^4F_{7/2}$. Followed by a rapid nonradiative multiphonon transitions to the lower-lying states ${}^2H_{11/2}$ and ${}^4S_{3/2}$. Emission

Table 5.4: Literature values for measured slopes of the dependence of the UpC emissions at 410, 550 and 660 nm on the excitation power in Er/Yb:Y₂O₃ upon $\lambda \sim 980$ nm pumping; NC = nanocrystals.

Sample	Violet emission	Green emission	Red emission	Lit.
Yb _{0.20} Er _{0.02} Y _{1.78} O ₃ (NC)	3.02	3.12	2.10	[186]
Y ₂ O ₃ :2%Er/4%Yb (nanospheres)	–	2.21	1.75	[189]
Y ₂ O ₃ :2%Er/1%Yb (NC)	–	2.3	1.9	[190]
Y ₂ O ₃ :5%Er (film)	–	1.37	1.29	[191]
Y ₂ O ₃ :1% Er/10%Yb (NC)	2.32	2.59	1.66	[192]
Y ₂ O ₃ :1% Er/10%Yb (microspheres)	2.02	1.61	1.25	[149]
Y ₂ O ₃ :1% Er/7%Yb	1.93–2.13	1.84–1.85	1.46–1.66	this work

to the ground state from these levels yields the green luminescence. Such an excitation mechanism would show a quadratic behavior in the slope, accounting for a two-photon process, which is in a good agreement for the experimentally obtained slopes of $n = 1.84$ – 1.85 for the films. Therefore, we can exclude a three-photon UpC process to be the underlying excitation mechanism for the green emission. Only a few examples of three-photon processes responsible for green emission in Y₂O₃ are reported in the literature, mostly observed in nanocrystals under large pump powers [186, 192, 193].

For the violet emission at ~ 410 nm, which is due to transition ${}^2\text{H}_{9/2} \rightarrow {}^4\text{I}_{15/2}$, we can state the following three-photon excitation process [186, 193]:

- (1) $\text{Er:}{}^4\text{F}_{9/2} + \text{Yb:}{}^2\text{F}_{5/2} \rightarrow \text{Er:}{}^4\text{G}_{11/2} + \text{Yb:}{}^2\text{F}_{7/2}$
- (2) ${}^4\text{G}_{11/2} \rightsquigarrow {}^2\text{H}_{9/2}$
- (3) ${}^2\text{H}_{9/2} \rightarrow {}^4\text{I}_{15/2}$

with the curled arrows indicating nonradiative multiphonon transitions. The deviation from the cubic law in the emission dependence on the excitation power for the violet emission from the ${}^2\text{H}_{9/2}$ state, yielding $n < 3$, can be ascribed to the enhanced UpC rate at the ${}^4\text{F}_{9/2}$ state [192]. A decrease in n for the ${}^2\text{H}_{9/2}$ state, even down to that of ${}^4\text{F}_{9/2}$, might be observed just due to the enhanced UpC rate at this level [192].

5.4.1 Lifetimes of Er:⁴S_{3/2} and ⁴F_{9/2} states in Er/Yb:Y₂O₃ films

A comparative study of the decay kinetics of the luminescence from Er:⁴S_{3/2} and ⁴F_{9/2} states for Er/Yb:Y₂O₃ was performed at room temperature under 980 nm pulsed laser excitation. The decay profiles were fitted to a single exponential approximation in the far exponential stage of the luminescence decay.

It can be seen from Fig. 5.10 and Fig. 5.11 that the luminescence decay profiles differ slightly from an exponential one and that the excited state decays are lengthened for the annealed samples compared to the as-deposited sample. This and

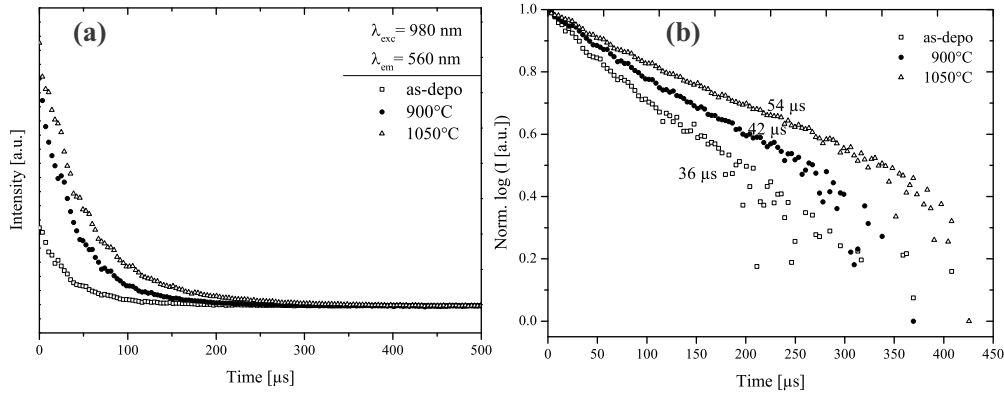


Figure 5.10: Luminescence kinetics of the Er:⁴S_{3/2} state of Er/Yb:Y₂O₃ films upon 980 nm excitation. (a) Measured decay curves and (b) normalized logarithmic representation of decay kinetics for a better comparison with an exponential decay behavior.

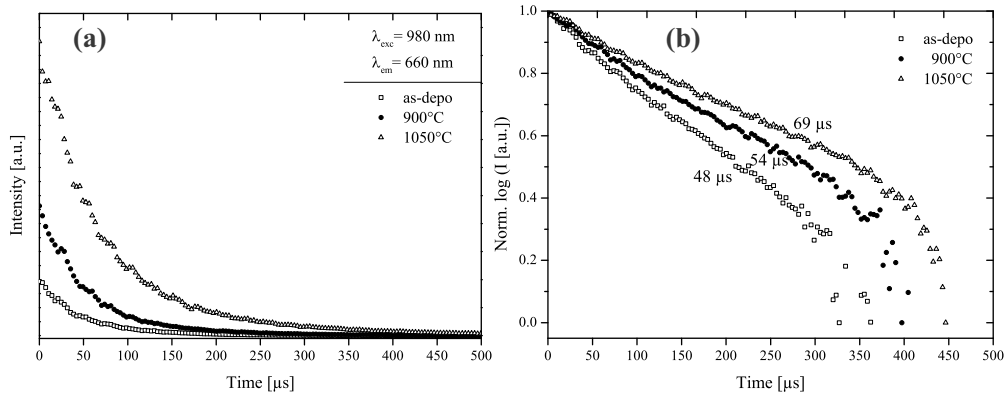


Figure 5.11: Decay kinetics of the luminescence from the Er:⁴F_{9/2} state of Er/Yb:Y₂O₃ films as-deposited and after thermal annealing at 900 °C and 1050 °C, respectively. (a) Measured decay curves and (b) normalized logarithmic representation of decay kinetics for a better comparison with an exponential decay behavior.

the improved UpC emission can be explained by thermal effects, including diffusion, grain growth and elimination of volatile residues acting as quenchers for the emission [140]. However, it has been shown that the main factor for improving the emission intensity and radiative lifetimes is the increase in grain size due to the thermal annealing [140, 170]. This effect can be attributed to a reduction in the grain boundary area with the grain growth, leading to fewer lattice defects which act as quenching centers for radiative emission. The observed lifetime of Er:⁴F_{9/2} in Er/Yb:Y₂O₃ varies from 48 to 69 μs and for the Er:⁴S_{3/2} state from 36 to 54 μs as a result of the thermal annealing. These results are in reasonable agreement with the radiative lifetimes listed in Table 5.5. Er/Yb co-doped samples are expected to exhibit shorter Er lifetimes than singly-doped Er samples, since a Yb concentration dependent quenching occurs due to Er-to-Yb energy back transfer processes [194].

Table 5.5: Lifetimes τ of $\text{Er:}^4\text{S}_{3/2}$ and $^4\text{F}_{9/2}$ states in $\text{Er/Yb:Y}_2\text{O}_3$ films after 980 nm excitation and selected literature values.

Sample	τ $^4\text{S}_{3/2}$	τ $^4\text{F}_{9/2}$	Ref.
1% Er/ 7% Yb:Y ₂ O ₃ film, as-depo.	36 μs	48 μs	this work
film annealed at 900 °C	42 μs	54 μs	this work
film annealed at 1050 °C	54 μs	69 μs	this work
5% Er:Y ₂ O ₃ , film	7.1–87 μs	10.6–114.9 μs	[195]
1% Er/ 20% Yb:Y ₂ O ₃ , NC	~ 8 μs	~ 10 μs	[194]
1% Er:Y ₂ O ₃ , NC	~ 100 μs	~ 100 μs	[194]
1% Er/ 5–10% Yb:Y ₂ O ₃ , NC	< 100 μs	< 100 μs	[119]
0.2% Er:Y ₂ O ₃ , bulk	88 μs	~ 30 μs	[196]
0.5–1.5% Er:Y ₂ O ₃ , bulk	80 μs	–	[197]
Y _{1.8} Er _{0.20} O ₃ , bulk	56 μs	–	[198]
Y _{1.8} Er _{0.20} O ₃ , NC	3.8 μs	–	[198]
1% Er:Y ₂ O ₃ , NC	11.6 μs	4.2 μs	[199]

In general, the observed lifetimes depend strongly on the RE dopant concentration, preparation method and microstructural state of the upconverter material (in form of bulk, nanophosphors or film), hence one has to be cautious when comparing experimentally observed lifetimes. For example, a lengthening of the experimental lifetimes τ is often observed in RE-doped Y₂O₃ films compared to bulk Y₂O₃. In films, larger lifetimes than in the bulk counterpart are attributed to a lower effective refractive index surrounding the RE³⁺ ions, due to a lower packing density compared to the bulk material [195, 200, 201].

5.5 Summary

Er/Yb:Y₂O₃ films of good optical quality were grown onto Si(100) substrates at 700 °C by pulsed LI-MOCVD. A comparative study of films as-deposited and annealed at 900 °C and 1050 °C has been carried out to observe possible changes in microstructural and spectroscopic properties. All films showed a homogeneous grain size distribution and a crack-free microstructure at thicknesses as high as ~ 500 nm. An increase in the UpC emission intensity has been observed with increasing post-deposition annealing temperature. This and a lengthening of the $^4\text{S}_{3/2}$ and $^4\text{F}_{9/2}$ lifetimes in Er/Yb:Y₂O₃ can be attributed mainly to the reduction of lattice defects due to the growth in grain size induced by thermal annealing. Quencher species such as OH and CO groups are removed at annealing temperatures ≥ 900 °C, hence the increased emission intensity and lifetimes of excited states. Power dependence studies on the as-deposited as well as annealed films confirmed a two-photon UpC process for the red and green emission and, that three photons are involved in the UpC mechanism responsible for populating the violet-light emitting state.

Light UpC in RE³⁺-doped Y₂O₃, SiO₂ and TiO₂ thin films by the sol-gel method

We applied wet chemical strategies based on the sol-gel method to deposit dielectric RE-doped oxide thin films. In the present work, we report on the deposition of Y₂O₃, SiO₂ and TiO₂ films onto Si and transparent v-SiO₂ substrates. All these films were subject to an extensive structural and spectroscopic characterization comprising XRD, FTIR, Raman, ellipsometry and UpC emission measurements.

6.1 Sol-gel processing

We describe in the following the fabrication of Y_2O_3 , SiO_2 and TiO_2 thin films by sol-gel processing [71, 165, 202]. The individual processing steps in the film preparation are depicted in Fig. 6.1.

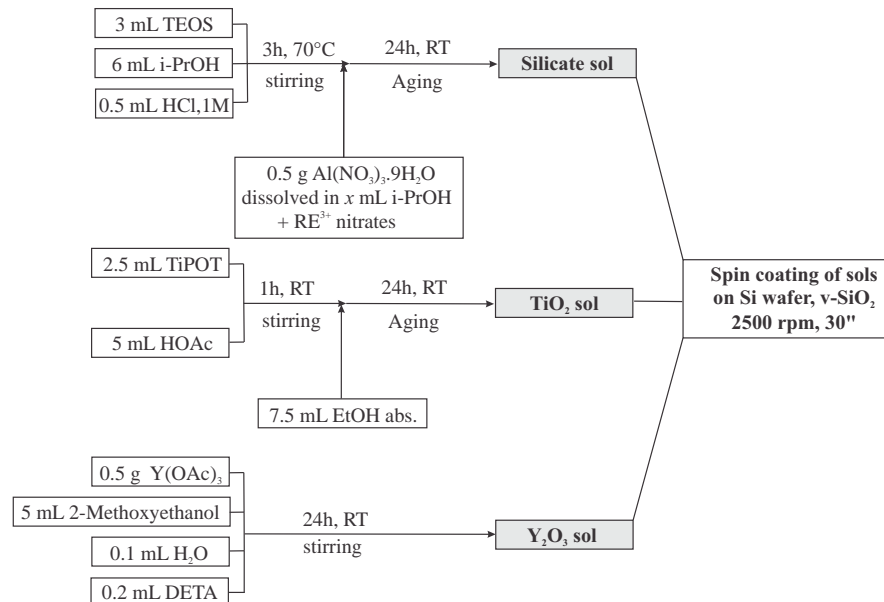


Figure 6.1: Flow chart and process parameters for the sol-gel processing of the prepared oxide thin films.

Er^{3+}/Yb^{3+} -doped Y_2O_3 . A sol was prepared by dissolving 0.5 g yttrium(III) acetate hydrate ($Y(OAc)_3 \cdot x H_2O$, Aldrich, 99.9%, dried overnight at $110^\circ C$) in 0.2 mL diethylenetriamine (DETA, Aldrich, 99%) and 5 mL 2-methoxyethanol. Stoichiometric amounts of Er and Yb nitrates ($RE(NO_3)_3 \cdot x H_2O$, $RE = Er/Yb$, Aldrich, 99.99%) together with 0.1 mL deionized H_2O were added to the prepared yttrium acetate solution and stirred until a homogeneous, transparent solution was formed (24 h at room temperature). The RE concentration was fixed with 1 at.% Er in solution and the Yb concentration was varied between 2 to 14 at.% in order to determine the film composition with the optimal light emission. Before the sol-gel deposition by spin-coating, the solution was filtered through a $0.2 \mu m$ PTFE syringe filter to prevent particulate contamination. The films were spun at 2500 rpm for 30 s on single-side polished Si(100) wafers. The coated substrate was then baked at $900^\circ C$ for 30 s, in air to yield a ~ 50 nm thin film. To obtain a higher film thickness, the number of layers was increased by repeating the whole process. In this fashion, at most 10 layers could be deposited before film cracking started to take effect. After the last deposition cycle, the films were baked at $800^\circ C$, $900^\circ C$ and $1050^\circ C$, respectively, in a muffle furnace for 1.5 h, in air, to assure film densification and a total removal of OH and carbon residues in the as-deposited films. The maximum film thickness after the final annealing step was determined (by SEM) to be ~ 400 nm.

Er^{3+}/Yb^{3+} -doped SiO_2 . The silicate sol (9% $AlO_{1.5}$ and 91% SiO_2) was pre-

pared by mixing 3 mL of tetraethyl orthosilicate with 6 mL of isopropanol and 0.5 mL of 1 M HCl and then stirred at 70 °C for 3 h. The solution was afterwards diluted with another solution of 0.5 g Al(NO₃)₃·9 H₂O in an appropriate volume of isopropanol and was aged at room temperature for 24 h under continuous stirring. The volume of solvent was adjusted in order to obtain the required film thickness. The addition of Al³⁺ ions to the SiO₂ network is beneficial for two reasons: they facilitate the incorporation (solubility) of RE³⁺ ions, and they reduce the rigidity of pure SiO₂ [71]. To fabricate RE-doped silicate films, 0.06 g (1 at.%) of Er(NO₃)₃·x H₂O and appropriate amounts of Yb(NO₃)₃·x H₂O were dissolved in the Al-nitrate solution and added to the silica sol. Spin-coating of the silicate sol was performed in the same manner described for the yttria sol, at 1050 °C, 2500 rpm, for 30 s. If not otherwise mentioned, post-deposition annealing of the silicate films was done at 1050 °C, for 1.5 h, in a muffle furnace.

Er³⁺/Yb³⁺-doped TiO₂. A sol is prepared by dissolving 2.5 mL tetra-*i*-propyl titanate (TiPOT) in 5 mL glacial acetic acid, under continuous stirring for 1 h at room temperature. Added to this solution are 7.5 mL dry ethanol and the solution is stirred for 24 h at room temperature. RE-doped titania sols are prepared by adding the RE³⁺ ions in form of nitrates to the sol. The titania sol was spun onto Si(111) wafers for 30 s at 2500 rpm, and each layer was baked for 30 s at temperatures between 700–1050 °C. After the final sol-gel coating cycle, the TiO₂ films were baked between 700 and 1050 °C, for 1.5 h in air, to further densify the film and eliminate residues of water and organic precursors. Different temperatures were used to elucidate changes in the film microstructure and determine the best processing conditions for achieving a good UpC performance of the films.

6.2 Results: Y₂O₃

6.2.1 Structural characterization

Quantitative elemental analyses by EPMA. Knowledge of the composition of sol-gel derived Er/Yb co-doped Y₂O₃ films was acquired by an electron probe micro-analyzer Cameca SX50, equipped with a wavelength-dispersive spectrometer (WDS). The EPMA data was processed by the Stratagem software and the results are depicted in Fig. 6.2. The Er/Yb co-doped films were prepared with a fixed concentration of 1 at.% Er in the sol and varying contents of Yb. In Fig. 6.2 (a) the cationic concentration of erbium, Er/(Er+Yb+Y) at.%, in Er/Yb co-doped Y₂O₃ thin films, fabricated at 900 °C, is shown as a function of the initial Yb concentration in the solution. The results show values inferior 1 at.%, most probably due to non-avoidable experimental uncertainties. As for the Yb/(Yb+Er+Y) ratios in film and solution, shown in Fig. 6.2 (b), about the same Yb content in the film is found compared to the solution, which assures that no major losses occur during the sol-gel process.

XRD results. The XRD patterns of RE:Y₂O₃ films deposited onto Si(100) substrates at 900 °C, seen in Fig. 6.3, reveal polycrystalline cubic Y₂O₃ as the crystalline phase present (powder diffraction file No. 44-1105). The films are oriented in the [100] direction, as evidenced by the strong 400 reflection at $2\theta \sim 34^\circ$, where the peak intensity of the (400) plane increases with the doping level of Yb

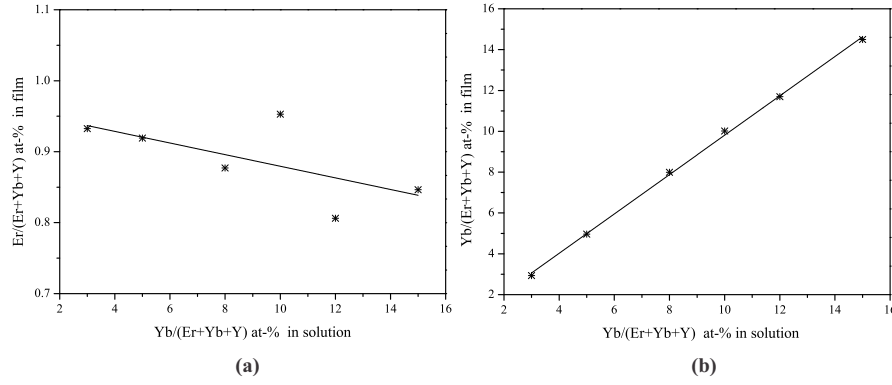


Figure 6.2: Quantitative EPMA of Er/Yb co-doped Y_2O_3 films fabricated by the sol-gel method, using a temperature of $900^\circ C$. (a) Er concentration on cation basis, RE/(RE+Y) at.%, in the film as a function of the Yb concentration in the solution. (b) Yb concentration, Yb/(Yb+Er+Y) at.%, in solution and film for Er/Yb co-doped Y_2O_3 films.

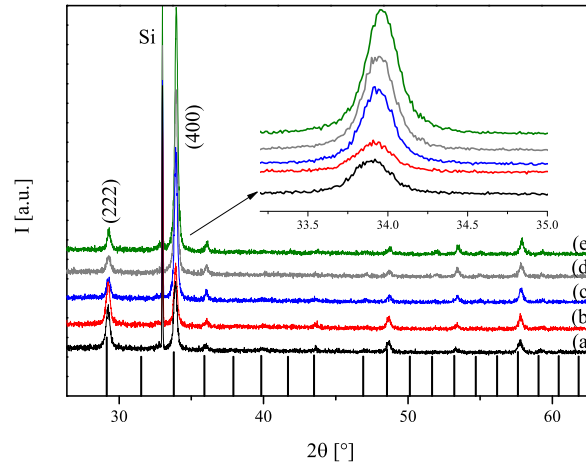


Figure 6.3: XRD patterns of Er/Yb: Y_2O_3 films on Si(100) wafers, deposited and annealed at $900^\circ C$, with 1 at.% Er and varying Yb concentration: (a) 2 at.% (b) 5 at.% (c) 8 at.% (d) 10 at.% and (e) 12 at.%. As reference pattern shown is bcc- Y_2O_3 , ICDD No. 41-1105.

in the film. The crystallite size D was derived from the Scherrer equation, $D = k \cdot \lambda / \beta \cdot \cos\theta$, where $k = 0.9$, $\lambda = 0.154$ nm, β is the full width at half maximum of the diffraction peak, and θ the diffraction angle. The crystallite size of the films fabricated at $900^\circ C$ is about 30 nm, only considering the most intense reflection at $2\theta \sim 34^\circ$.

Film structure and morphology. The sol-gel method requires rather high temperatures for film densification and the elimination of OH groups in the film matrix. However, high temperatures favor the formation of cracks in the film microstructure due to the difference between the CLTE of the substrate and film. Thus the temperature and film thickness have to be chosen carefully to avoid

crack formation. Fig. 6.4 shows the SEM micrographs of an Er/Yb: Y_2O_3 film, annealed at 1050 °C. The film shows a homogeneous surface consisting of fine grains, whereby under high optical magnification, fine isolated microcracks are visible. The cross-section view reveals a dense film microstructure and furthermore, a ~ 100 nm thick thermally grown SiO_2 layer.

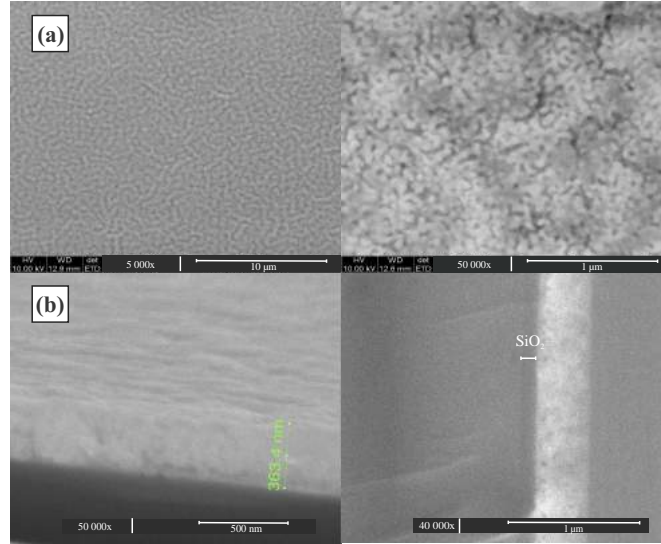


Figure 6.4: (a) Top-view SEM micrographs of an Er/Yb: Y_2O_3 film, annealed at 1050 °C, with 5000 x and 50 000 x magnifications. (b) Cross-section images of the same.

The surface morphology of the sol-gel derived yttria films was additionally investigated by AFM. The AFM measurements reveal a RMS surface roughness of 3.6 nm, and a uniform film surface. The estimated mean grain size from the AFM height image was ~ 70 nm.

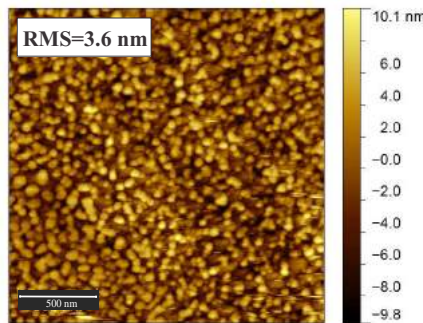


Figure 6.5: AFM morphology of an Er/Yb: Y_2O_3 thin film ($d_f \sim 360$ nm) fabricated by sol-gel processing and annealed at 1050 °C. The RMS surface roughness was estimated with 3.6 nm for a $2 \times 2 \mu m^2$ sampled area.

Raman and FTIR spectroscopy. Micro-Raman spectroscopy was used to determine the cut-off phonon energy of Y_2O_3 (~ 600 cm^{-1}). The spectra were recorded on a Jobin Yvon Horiba Micro-Raman spectrometer with a 100X objective and a 633 nm laser excitation wavelength (14 mW).

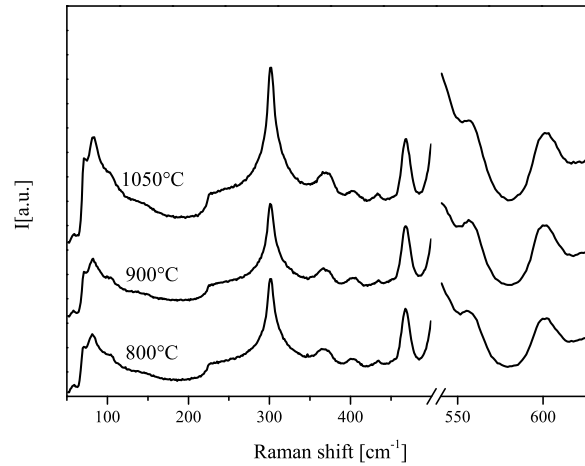


Figure 6.6: Raman spectra of Er/Yb:Y₂O₃ films annealed at 800 °C, 900 °C and 1050 °C. The Raman shift between 500–540 cm⁻¹ was left out, due to the high intensity of the c-Si first order optical Raman mode in this region.

Fig. 6.6 shows the Raman spectra of Er/Yb:Y₂O₃ films baked at 800 °C, 900 °C and 1050 °C, for 1 h, in air. It is evident that all films exhibit Raman modes attributed to C-type Y₂O₃, and that the Raman spectra do not change much with the annealing temperature. The bands at ~370(w), 403(w), 433(w), 468(m), 557(shoulder) and 602(m) are in good agreement with the Raman-active vibrational modes reported for c-Y₂O₃, although slight differences in the band intensities and positions occur due to the polycrystalline nature of the film [146]. The Raman modes in the low frequency range < 350 cm⁻¹ originate from the Si substrate, as does a strong peak at 520 cm⁻¹, the first order optical phonon mode of c-Si, which was left out in the spectra because of its high intensity [114]. The effect of the temperature used in the film preparation can be monitored by FTIR spectroscopy. The absorption spectra were recorded on a Nicolet 5700 FTIR spectrometer (Thermo Electron Corporation) between 4000–100 cm⁻¹. The mid-IR region is important for the detection of traces of OH groups in the film, which are able to quench the luminescence from excited states of the Er³⁺ ion, due to their high energy vibrational modes ($\nu_{\text{stretch}} = 2800\text{--}3600\text{ cm}^{-1}$, $\nu_{\text{bending}} = 1300\text{--}1700\text{ cm}^{-1}$ [203]). The FTIR absorption spectrum of the sample prepared at 800 °C, shown in Fig. 6.7 (a), exhibits a weak OH contamination, while the band intensity of the OH groups decrease with higher temperature. Moreover, the FTIR spectrum of the sample at 1050 °C shows bands of atmospheric water at 1700 and ~3000 cm⁻¹. The remaining bands in the mid-IR region can be attributed to lattice absorption of Si with a strong band at ~600 cm⁻¹ and another at ~1100 cm⁻¹, corresponding to the Si–O–Si vibrational band ($\nu_{\text{stretching}}$) of the thermally oxidized Si wafer. The characteristic lattice vibrations of cubic Y₂O₃ are observed in the 570–100 cm⁻¹ region, see Fig. 6.7 (b), with band maxima at ~563, 509, 462, 370, 330 and 300 cm⁻¹. All these bands can be assigned to lattice absorptions of c-Y₂O₃ [147].

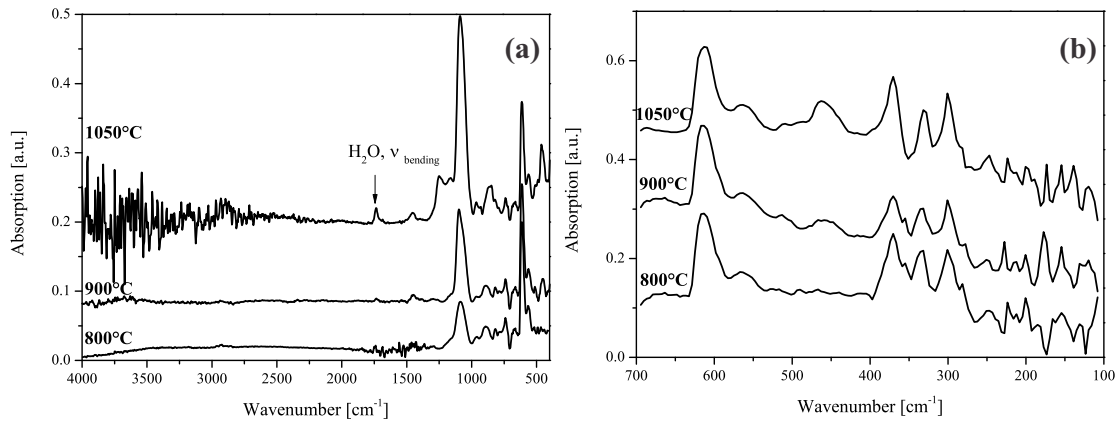


Figure 6.7: (a) FTIR spectra of Er/Yb: Y_2O_3 thin films on Si(100) in the region 4000–500 cm^{-1} , fabricated at 800, 900 and 1050 $^{\circ}C$, respectively. (b) FTIR spectra in the region 700–100 cm^{-1} . All spectra were recorded at room temperature and displayed without subtracting the spectrum of the neat Si substrate.

6.2.2 Optical properties of Er/Yb: Y_2O_3 films

The transmission spectrum of a ~ 300 nm thick RE: Y_2O_3 film, shown in Fig. 6.8 (a), was recorded over the 250–1000 nm wavelength range by a Perkin-Elmer Lambda 950 UV/Vis/NIR spectrophotometer. The transmission in the visible range is clearly reduced, compared to the neat v - SiO_2 substrate, which exhibits a transmittance $< 92\%$ in the visible [204] and several interference fringes are visible. This can be related to light scattering between the interfaces.

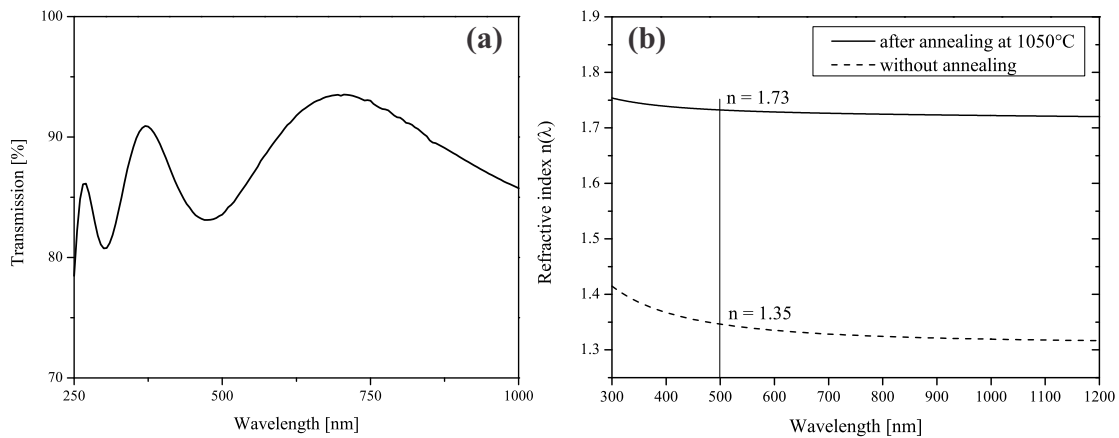


Figure 6.8: (a) Transmission spectrum of RE: Y_2O_3 film on vitreous silica, after baking at 900 $^{\circ}C$, $d_f=300$ nm. (b) Dispersion of the refractive index n as a function of RE: Y_2O_3 thin films, before and after annealing at 1050 $^{\circ}C$.

The dispersion of the refractive index for Er/Yb: Y_2O_3 films was determined by spectroscopic ellipsometry measurements between 300 and 1200 nm. The fitting of the ellipsometric data was done by multi-layer modeling, considering a layered structure of silicon/ SiO_2 / Y_2O_3 , and a three-term Sellmeier dispersion function [71]. Fig. 6.8 (b) shows the dispersion curves of a Y_2O_3 film as-deposited and after undergoing thermal annealing at 1050 $^{\circ}C$. The refractive indices n at 500 nm

for the as-deposited film and the film annealed at 1050°C are 1.35 and 1.73, respectively. The increased refractive index is due to an increased packing density (hence the elimination of the residual porosity) and crystallinity of the films along with the annealing. The measured refractive index is in good agreement with reference data [168, 183], but lower than for bulk Y_2O_3 (1.939 at 500 nm [148]). This is due to the fact, that the refractive index is very sensitive to the film microstructure, hence to the film preparation [184].

6.2.3 Light UpC of Er/Yb-doped yttria sol-gel films at 972 nm

The NIR-to-Vis light conversion of Er/Yb-doped Y_2O_3 thin films processed at 1050°C was studied upon pumping with a 972 nm laser diode. The UpC emission spectra show a typical line profile in the green and red wavelength region originating from the Er^{3+} ion, as depicted in Fig. 6.9 (a). The weak green UpC luminescence is due to the transition ${}^2\text{H}_{11/2}; {}^4\text{S}_{3/2} \rightarrow {}^4\text{I}_{15/2}$ and the strong red emission corresponds to the transition ${}^4\text{F}_{9/2} \rightarrow {}^4\text{I}_{15/2}$ in the Er^{3+} ion. Fig. 6.9 (b) shows the dependence of the Vis-UpC emission on the Yb concentration in the film, when pumped at 972 nm at 4 W excitation power. The sample with the best visible emission corresponds to a film composition of 1 at.% Er and 10 at.% Yb in Y_2O_3 . It is evident that the red emission dominates over the green emission at a Yb concentration > 3 at.%. This is due to the fact that the $\text{Er}: {}^2\text{H}_{11/2}; {}^4\text{S}_{3/2}$ emission is quenched at higher Yb concentration, due to an Er-to-Yb back transfer [119]. The emission characteristics of the Er/Yb couple doped within the Y_2O_3 host lattice has been thoroughly discussed in Chapter 5, where we refer to for details of the excitation mechanisms.

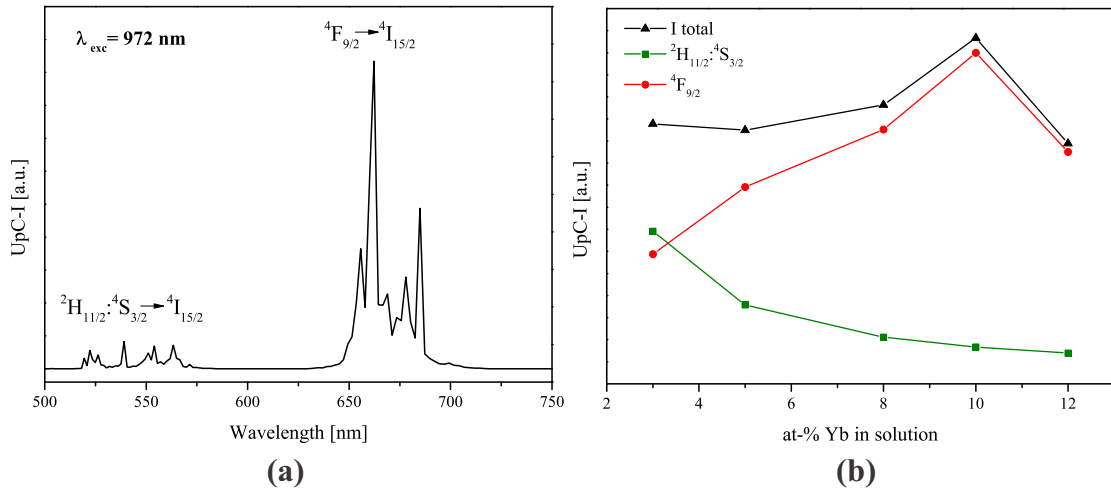


Figure 6.9: (a) Green and red up-converted emission spectrum of Er/Yb: Y_2O_3 obtained upon 972 nm laser pumping ($P = 4$ W). (b) Integrated visible luminescence intensity as a function of the doping concentration of Yb in Er/Yb: Y_2O_3 films, with a fixed Er concentration of 1 at.%.

Fig. 6.10 shows the double-logarithmic representation of the UpC emission versus the excitation power. The number of photons n involved in the UpC process can be estimated by the slope of the line, since the UpC emission intensity, I ,

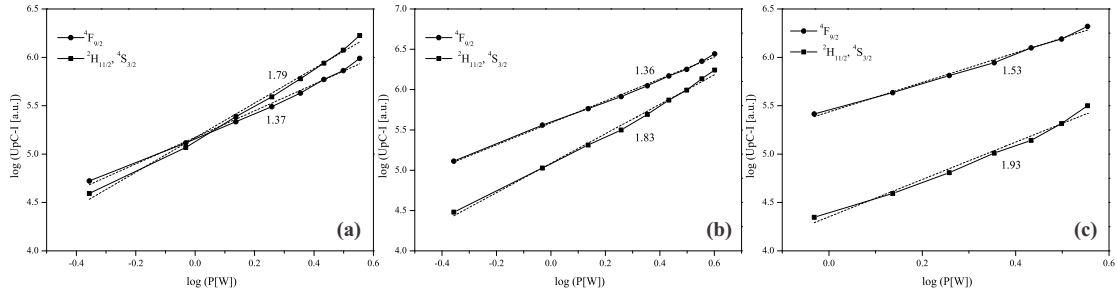


Figure 6.10: Green and red luminescence intensity versus the excitation power in Er/Yb: Y_2O_3 films with different RE doping: (a) 1 at.% Er/3 at.% Yb (b) 1 at.% Er/5 at.% Yb (c) 1 at.% Er/10 at.% Yb.

is proportional to the excitation power, P , according to $I = P^n$, in the specific case that the UpC rates are low compared to the linear decay rate [49]. From the experimentally obtained slopes, we can conclude that both red and green UpC emissions require two photons to populate the excited states in Er^{3+} . The difference from the expected value of 2 can be related to the presence of other depletion mechanisms such as energy back transfer, cross relaxation and multiphonon relaxation [151]. The slope of the green emission shows a slight dependence on the Yb content and converges to 2 with increasing Yb concentration. The same effect was reported by Auzel in Ref. [119].

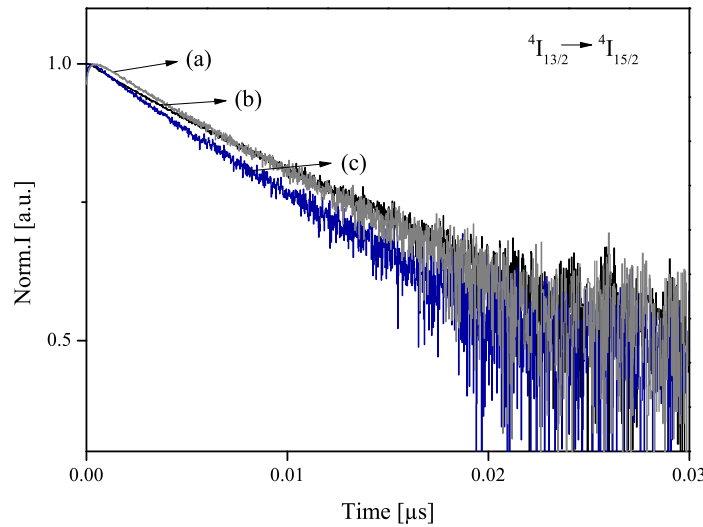


Figure 6.11: Er^{3+} luminescence decay from ${}^4I_{13/2}$ after excitation at ~ 800 nm in Y_2O_3 thin films doped with (a) 1 at.% Er/3 at.% Yb (b) 1 at.% Er/10 at.% Yb and (c) 1 at.% Er/5 at.% Yb.

We studied the luminescence decay kinetics of the level $Er: {}^4I_{13/2}$ upon excitation of the upper-lying excited state ${}^4I_{9/2}$ at ~ 800 nm. Fig.6.11 shows the decay

curves of this level in Er/Yb: Y_2O_3 films, as a function of the Yb concentration. All samples show a single exponential decay behavior and the measured lifetimes, depicted in Table 6.1, are in fairly good agreement with the data reported in the literature [150]. It is evident that the experimental Er: $^4I_{13/2}$ lifetimes do not show a strong dependence on the Yb concentration as expected. This is due to the co-existence of other depopulation processes such as UpC, energy transfer and migration between Yb^{3+} ions, which emerge at high Yb concentrations, and the radiative decay routes [133, 150, 154, 156, 157].

Table 6.1: Lifetimes τ of excited states Er: $^4I_{13/2}$ in Er/Yb: Y_2O_3 films, after NIR excitation and selected values reported in the literature.

Sample	$\tau^4I_{13/2}$	Lit.
1% Er/ 3% Yb: Y_2O_3 film	5.14 ms	this work
1% Er/ 5% Yb: Y_2O_3 film	5.22 ms	this work
1% Er/ 10% Yb: Y_2O_3 film	5.43 ms	this work
0.9% Er/ 7% Yb: Y_2O_3 film	2.4 ms	[150]
0.5% Er/ 2.1% Yb: Y_2O_3 film	4.6 ms	[150]

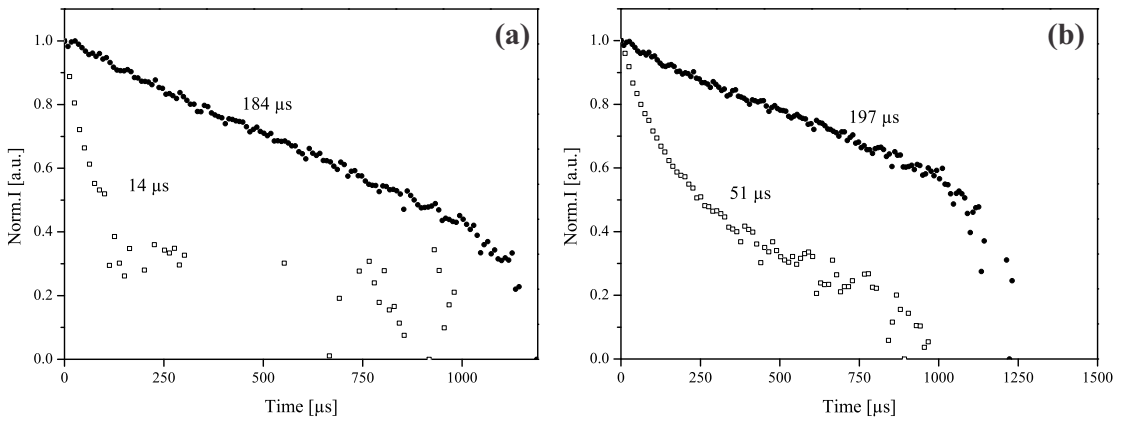


Figure 6.12: Luminescence decay curves from (a) Er: $^4S_{3/2}$ and (b) $^4F_{9/2}$ in 1 at.% Er/3 at.% Yb (black circles) and 1 at.% Er/14 at.% Yb (white squares) doped Y_2O_3 films. The intensities are normalized and represented in a log-scale for a better comparison with an exponential decay behavior.

In contrast to the lifetime of the Er: $^4I_{13/2}$ state, the lifetimes of the states Er: $^4S_{3/2}$ and $^4F_{9/2}$ show a dependence on the concentration of Yb. Yb^{3+} ions influence the nonradiative relaxation of the Er: $^{3+}$ ion, hence a shortening of the lifetime is observed. In Fig. 6.12 the temporal evolution of the green and red UpC luminescence as a function of the Yb concentration is shown. The lifetimes of state Er: $^4S_{3/2}$ are drastically decreased from 184 μs to 14 μs , when increasing the Yb content in the film from 3 at.% to 14 at.%. Analogous is found for the observed lifetimes of state Er: $^4F_{9/2}$. Table 6.2 summarizes the experimental lifetime data and selected reference data from the literature. The luminescence decays of the heavily doped sample show a non-exponential decay behavior, due to the occurrence of energy transfer and migration phenomena.

Table 6.2: Lifetimes τ of Er:⁴S_{3/2} and ⁴F_{9/2} states in Er/Yb:Y₂O₃ films after ~ 980 nm excitation and selected literature values.

Sample	τ ⁴ S _{3/2}	τ ⁴ F _{9/2}	Ref.
1% Er/ 3% Yb:Y ₂ O ₃ film	184 μ s	197 μ s	this work
1% Er/ 14% Yb:Y ₂ O ₃ film	14 μ s	51 μ s	this work
5% Er:Y ₂ O ₃ , film	7.1–87 μ s	10.6–114.9 μ s	[195]
1% Er/ 20% Yb:Y ₂ O ₃ , NC	~ 8 μ s	~ 10 μ s	[194]
1% Er:Y ₂ O ₃ , NC	~ 100 μ s	~ 100 μ s	[194]

6.3 Results: Aluminosilicate glass

6.3.1 Structural characterization

XRD results. The XRD analysis of the silicate films was performed by grazing incidence XRD, using a Bruker-AXS D5000 diffractometer and CuK α radiation. Fig. 6.13 shows, for comparison, the XRD curves of a highly RE-doped film and a weakly-doped one, after annealing at 1050 °C, for 1 h, in air. A broad peak is observed in the 2θ range of 15–30° for films of a low RE doping level, which demonstrates the glassy nature of the film. Films containing a high RE concentration exhibit a polycrystalline reflection pattern which can be attributed to the formation of RE silicates [205].

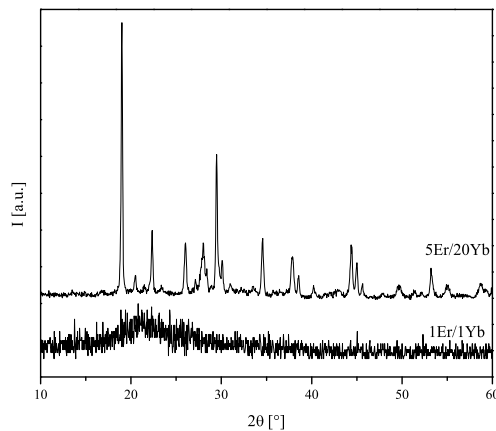


Figure 6.13: XRD patterns of silicate thin films with low and high RE doping level after annealing at 1050 °C, for 1 h, in air. The crystalline phase formed in highly doped films can be attributed to RE silicates, RE₂Si₂O₇.

Raman and FTIR results. Fig. 6.14 (a) displays the FTIR spectra of the samples before and after the final annealing at 1050 °C. The features of the sample spectra are rather similar, however, an increase of the peak intensities is observed due to the increased numbers of Si–O–Si bonds after the heat treatment. The peaks at 468 cm⁻¹ and between 1000 and 1500 cm⁻¹ are typical for SiO₂, corresponding to the Si–O out-of-plane deformation and the Si–O–Si stretching vibra-

tions, respectively [206]. Weaker bands observed at $\sim 810\text{ cm}^{-1}$ correspond to the Si–O bending and the vibrational band at $\sim 960\text{ cm}^{-1}$ can be either attributed to a Si–OH stretching vibration or a Si–O–RE asymmetric mode [207]. Note that the peak at $\sim 600\text{ cm}^{-1}$ is due to the silicon substrate.

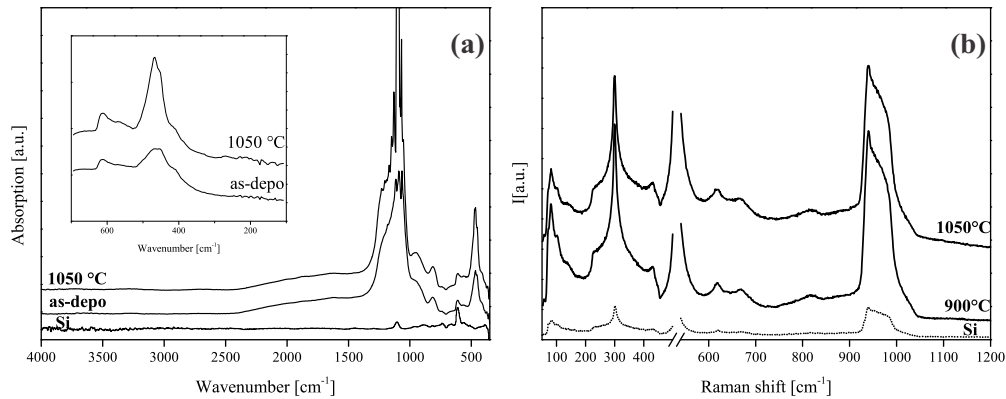


Figure 6.14: (a) FTIR spectra of silicate films, as-deposited and annealed at 1050 °C. (b) Raman spectra of silicate films deposited by the sol-gel method, annealed at 900 and 1050 °C/1 h, in air.

The silicate films were subsequently studied by Micro-Raman spectroscopy using the experimental set-up previously described in Section 6.2. In Fig. 6.14 (b) Raman spectra of pure silicate films fabricated at 900 and 1050 °C are depicted, showing no major differences in their features. The Si–O–Si stretching and bridging modes occur in the range between 850–1100 cm⁻¹ and 400–700 cm⁻¹, respectively. However, the Si phonons contribute to the spectrum, and we cannot certainly attribute the spectral features to the SiO₂ layer. The narrow band at $\sim 430\text{ cm}^{-1}$ may be due to the symmetric motion of oxygen in the Si–O–Si bond [208]. The bands at $\sim 617\text{ cm}^{-1}$, 670 (due to Al–O), 820 and in the 850–1100 cm⁻¹ range, may be attributed to the silica network as well. However, the latter peak consists also of a spectrum superposition of the Si substrate (2TO phonon mode), which partially oxidizes during the annealing process. The strong asymmetric peak at $\sim 940\text{ cm}^{-1}$ might be also assigned to a (Al)Si–OH stretching, or, a deformation vibration due to some hydrolyzation of (Al)Si–O–Si bonds and represents the phonon cut-off energy of the material [209].

The SiO₂ layer thermally grown by oxidation of the substrate is also clearly visible in the SEM micrograph in Fig. 6.15. The estimated layer thicknesses are 180 nm and 90 nm for the RE-doped silicate glass layer, after annealing at 1050 °C, for 1 h, in air. The SEM image also reveals a homogeneous layer thickness and a good film quality with no crack formation visible in the cross section.

Refractive index. Fig. 6.16 shows the refractive index n of silicate films as a function of the wavelength as obtained from spectroscopic ellipsometry measurements. The refractive index was obtained through fitting of the ellipsometric data, using a three-term Sellmeier equation [71]. The refractive index increases for the RE doped samples compared to the neat silicate thin film, and also after the heat treatment. At 500 nm, the indices are 1.47 for a RE-doped film before the

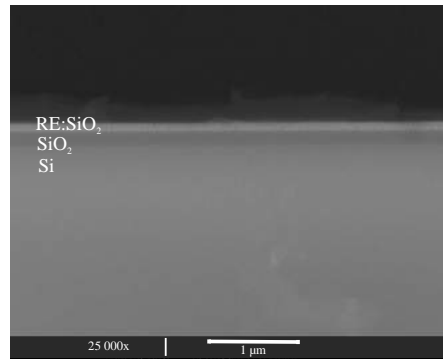


Figure 6.15: FEG-SEM cross-section image in back-scattered electron (BSE) mode of an Er/Yb doped silicate film, deposited and annealed at 1050°C . During the annealing process, a SiO_2 layer is formed due to oxidation of the Si substrate, and the bright layer is the RE-doped silicate film. The estimated layer thicknesses are 180 nm for thermally grown Si and 90 nm for the deposited silicate layer.

heat treatment, and 1.49 and 1.43 for the RE-doped and the pure silicate film, respectively, after annealing at $1050^\circ\text{C}/1\text{ h}$, in air. The observed deviations from the value for pure SiO_2 glass (1.46 at 509 nm [148]) can be attributed to the film microstructure, and to the presence of other species in the film (RE^{3+} , Al^{3+} ions).

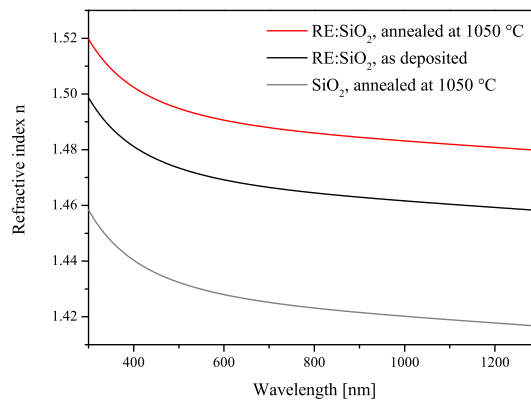


Figure 6.16: Dispersion of the refractive index of an as-deposited and at 1050°C annealed Er/Yb co-doped silicate thin film on Si(111), compared to a pure silicate film, annealed at 1050°C .

6.3.2 Light UpC of Er/Yb-doped silicate sol-gel films at 972 nm

Fig. 6.17 (a) shows the $1.54\ \mu\text{m}$ photoluminescence of a SiO_2 film containing 1 at.% Er and 1 at.% Yb after excitation at the 515 nm argon laser line and in the NIR at 972 nm. Upon 515 nm pumping, the Er^{3+} ion is directly excited, according to the transition $^4I_{15/2} \rightarrow ^4F_{7/2}$, while on the other hand, upon 972 nm excitation, photons are mainly absorbed by the Yb^{3+} ions. This is due to their higher absorption

oscillator strength at this wavelength. The excitation energy is then successively transferred to Er: $^4I_{11/2}$ and furthermore, the emitting state $^4I_{13/2}$ is populated via nonradiative relaxation. The PL spectra exhibit typical $1.54\ \mu\text{m}$ Er luminescence, and are nearly identical at both the excitation wavelengths [210].

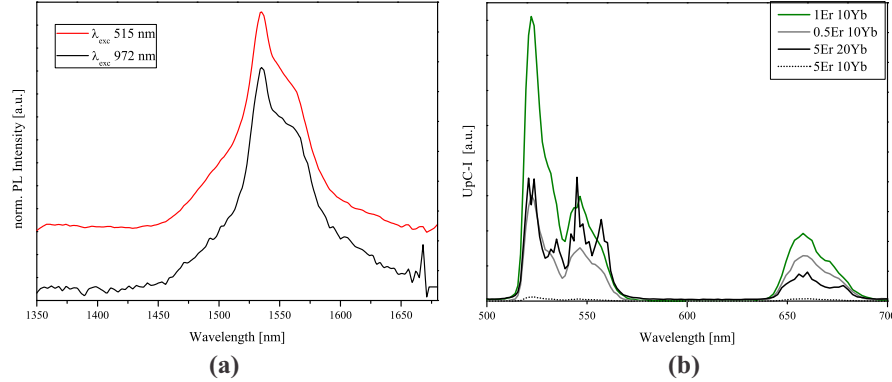


Figure 6.17: (a) PL spectra of Er/Yb:SiO₂ film after 972 nm and 515 nm excitation, normalized to their peak values. (b) Vis-UpC spectra of Er/Yb:SiO₂ films of different RE concentration upon 972 nm excitation, $P = 4\ \text{W}$.

The NIR-to-Vis photon conversion emission spectra in Er/Yb co-doped silicate films are shown in Fig. 6.17 (b), upon 972 nm excitation at 4 W. The UpC emission spectra are shown as a function of the different RE doping concentration in the films, and exhibits a maximum UpC intensity for a film composition of 1 at.% Er and 10 at.% Yb. At high doping level, the Stark splitting changes due to the transition from a glassy SiO₂ into a crystallized RE silicate phase.

To explain the origin of the emission bands, the excitation pathways are schematically depicted in the energy level diagram in Fig. 6.18 (a). The absorption of the incident 972 nm photons provokes mainly the transition $^2F_{7/2} \rightarrow ^2F_{5/2}$ in the Yb³⁺ ions, although GSA in Er³⁺ can in addition occur corresponding to $^4I_{15/2} \rightarrow ^4I_{11/2}$. The higher excited states in Er³⁺ are then populated through successive energy transfer steps from the Yb³⁺ ion. The red emission originates from promoting $^4I_{13/2}$ to $^4F_{9/2}$ by energy transfer from Yb: $^2F_{5/2}$. The green emitting state $^4F_{9/2}$ is populated corresponding to the transitions $^4I_{11/2} + \text{Yb}:^2F_{5/2} \rightarrow ^4F_{9/2} + \text{Yb}:^2F_{7/2}$. Hence, both excitation pathways for the green and red emission require at least two photons. Fig. 6.18 (b) confirms this assumption with the number of photons deduced from the double-logarithmic representation of the emission intensity vs. the pump power, which is equal to ~ 2 .

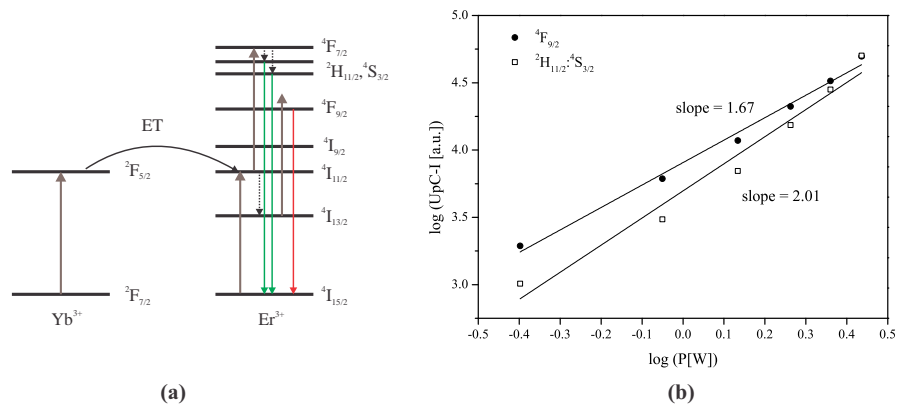


Figure 6.18: (a) Energy level diagram of the Er/Yb couple and the UpC excitation mechanism for the red and green emission in SiO_2 upon 972 nm excitation; the solid lines indicate radiative excitation and emission processes and the dotted lines are nonradiative transitions. (b) Double-log. plot of the red and green emission intensity vs. the excitation power of Er/Yb: SiO_2 film.

6.4 Results: TiO_2

6.4.1 Structural characterization

XRD results. In Fig. 6.19 the XRD patterns of RE: TiO_2 thin films reveal a dependence of the crystalline phases present on the annealing temperature, as well as on the RE^{3+} ion concentration in the films. The inset of Fig. 6.19 shows

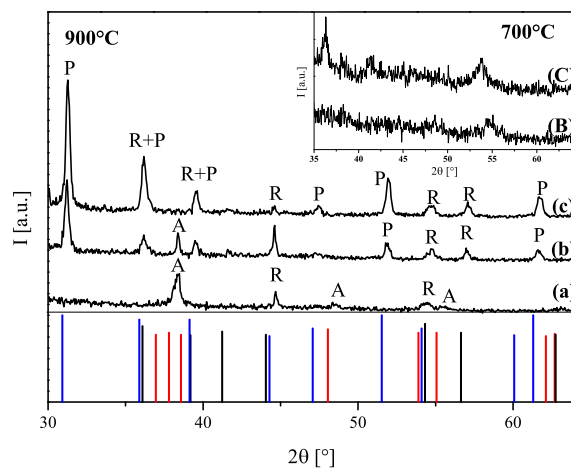


Figure 6.19: X-ray diffractograms of Er/Yb: TiO_2 thin films annealed at 900 °C: (a) 1 at.% Er (b) 1 at.% Er/10 at.% Yb (c) 1 at.% Er/20 at.% Yb. The inset shows, for comparison, the diffraction patterns of two samples deposited and annealed at 700 °C (B) 1 at.% Er/10 at.% Yb and (C) 1 at.% Er/20 at.% Yb. In addition, reference patterns of crystalline phases anatase (A, red line, ICDD No. 21-1272), rutile (R, black line, ICDD No. 21-1276) and ytterbium titanate (P, blue line, ICDD No. 17-0454) are depicted in the figure.

the X-ray diffractograms of titania films fabricated at 700 °C. It is evident that the films exhibit a low degree of crystallinity and few reflections corresponding to anatase (ICDD No. 21-1272) and rutile (ICDD No. 21-1276) phases. A higher temperature of 900 °C for the film deposition and annealing process induces film crystallization. Samples containing a low RE concentration exhibit a mixture of tetragonal anatase and rutile crystalline phases.

However, when the dopant concentration is further increased, the anatase phase is reduced and cubic pyrochlore titanate, RE₂Ti₂O₇ (ICDD No. 17-0454) emerges as a new crystalline phase. For the highest RE concentration in titania films studied, namely 1 at.% Er/20 at.% Yb:TiO₂, the anatase phase disappears and the strongest reflections could be assigned to rutile and crystallites of RE₂Ti₂O₇. The transformation of the crystalline phases in the films was also studied by FTIR and Raman spectroscopy. The FTIR spectra of 1 at.% Er/10 at.% Yb:TiO₂, processed at 700 °C and 900 °C, are shown in Fig. 6.20 (a).

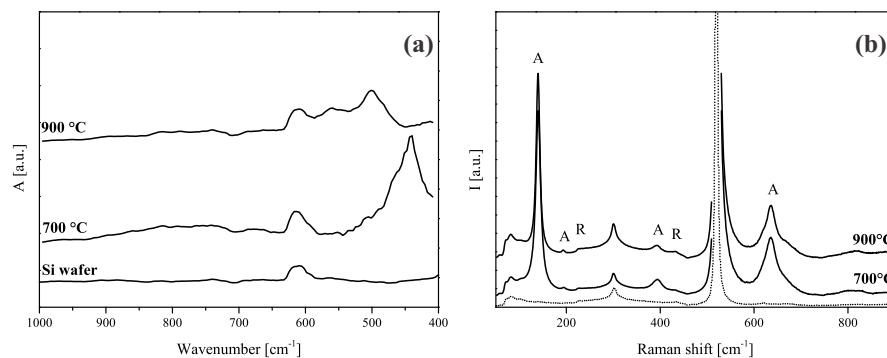


Figure 6.20: (a) Mid-IR absorption spectra of RE:TiO₂ films prepared at 700 °C and 900 °C. For comparison, the IR spectrum of the neat Si substrate is also shown. (b) Raman spectra of the films as a function of the fabrication temperature and the spectrum of the Si substrate without film coating.

At 700 °C, a strong band around 440 cm⁻¹ and a broad peak between 710 and 930 cm⁻¹ are visible, which can be associated to the TO and LO vibrational modes of the anatase phase [211]. The ~677 cm⁻¹ absorption band can be assigned to the Ti–O stretching mode of rutile, even though other rutile modes were unobservable [212]. Increasing the temperature to 900 °C leads to a disappearance of the strong anatase peak at ~440 cm⁻¹, yet another band appears at 498 cm⁻¹, corresponding to the rutile phase. Both crystal phases of anatase and rutile may co-exist at 900 °C, because the spectrum shows the presence of the LO mode of anatase. These results confirm the XRD study as well, affirming the co-existence of the two phases.

The Raman study in Fig. 6.20 (b) confirms the presence of the anatase (A) and rutile (R) phases in samples fabricated at 700 °C and 900 °C. Both Raman spectra exhibit similar features with one well defined peak at ~140 cm⁻¹, as well as peaks at 193, 392, 632 cm⁻¹ due to anatase [212, 213]. The assignment of the rutile phase is more intricate and has to be carefully done due to the superposition of the c-Si Raman signal. The rutile phase has reported Raman modes at 230, 444 and 612 cm⁻¹ [212], which also overlap with the substrate signal.

Ellipsometry. The determination of the dispersion of the refractive index of RE-doped TiO₂ thin films was achieved by spectroscopic ellipsometry. The Cauchy dispersion function was applied to fit the experimental data and the corresponding parameters for films fabricated at 700 °C and 900 °C are listed in Table 6.3. The refractive index at 550 nm increases with increasing temperature, from 2.27 to 2.41, due to film densification. The dispersion curves are very similar compared to the literature [214,215] and the values of n are slightly lower than those reported: 2.75 for rutile and 2.52 for anatase, respectively (av. at 550 nm [216]). These differences in the refractive index can be attributed to the different method of film fabrication, hence, the film microstructure, as well as the presence of porosity.

Table 6.3: Fitting parameters A, B and C of the Cauchy dispersion function and refractive index n at 550 nm for Er/Yb:TiO₂ films as-deposited and after thermal annealing at 700 °C and 900 °C.

Processing temperature	A	B	C	n (550 nm)
700 °C	1.901594	12.39295	-3	2.27
900 °C	2.054903	11.7409	-2.81933	2.41

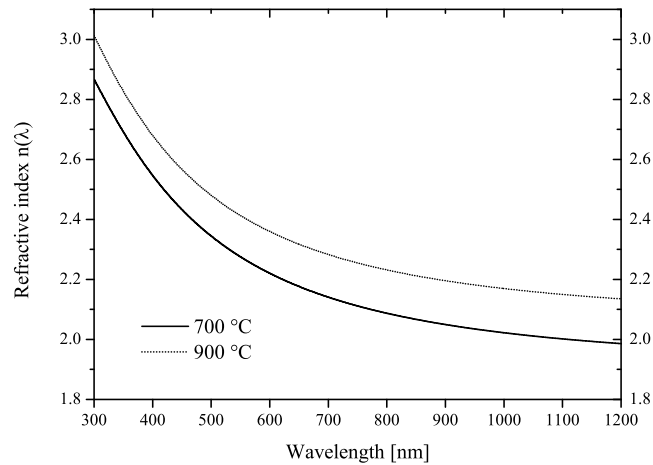


Figure 6.21: Dispersion of the refractive index $n(\lambda)$ of Er/Yb:TiO₂ (1 at.% Er, 10 at.% Yb) thin films fabricated at 700 °C and 900 °C.

6.4.2 Light UpC of Er/Yb-doped titania sol-gel films at 972 nm

Green and red UpC emission at ~ 520 , 550 and 660 nm was observed in Er/Yb-doped TiO₂ films under 972 nm excitation. Fig. 6.22 shows the UpC emission of samples processed at 700 °C and 900 °C, respectively, for two different RE concentrations.

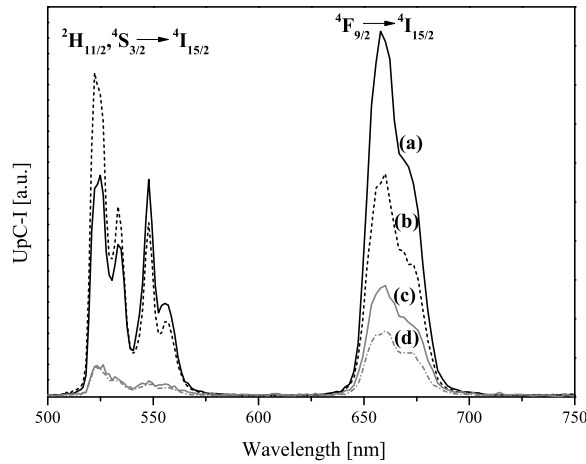


Figure 6.22: UpC emission spectra of ~ 500 nm TiO₂ thin films doped with (a) 1 at.% Er/20 at.% Yb, annealed at 700 °C (b) 1 at.% Er/ 20 at.% Yb, additionally baked at 900 °C (c) 1 at.% Er/ 10 at.% Yb, annealed at 700 °C (d) 1 at.% Er/ 10 at.% Yb, additionally baked at 900 °C, all excited at 972 nm, 4 W.

The maximum UpC emission intensity was found for the film with 1 at.% Er/20 at.% Yb, fabricated at 700 °C. At this temperature, both anatase and rutile phases are present. However, when the film is additionally annealed at 900 °C, the UpC emission is decreased, due to the rutile and pyrochlore phases present in the samples. Patra *et al.* reported a similar behavior for Er-doped TiO₂ and BaTiO₃ nanocrystallites [217].

The origin of the emission bands and the UpC mechanisms are well established for the Er/Yb ion pair in the literature, and hence will not be discussed in detail. The interested reader is referred to Ref. [201, 218]. In the UpC process based on ETU, the 972 nm photons are mainly absorbed by the Yb³⁺ ions, which then subsequently transfer their energy to Er:⁴I_{11/2}. Due to the cut-off phonon energy of ~ 640 cm⁻¹ (for anatase), nonradiative relaxation from ⁴I_{11/2} \rightsquigarrow ⁴I_{13/2} is highly probable, because about 6 phonons are needed to bridge the gap of ~ 3600 cm⁻¹ [218]. Hence, the red emission band is predominant in the UpC spectra.

It is well known that the intensity of the UpC emission is proportional to the exponent n of the pump power, since UpC is a nonlinear optical phenomenon [49]. Fig. 6.23 shows the integrated band intensities of the red and green emission as a function of the excitation pump power. The slopes were estimated with 1.6 and 2.4 for the red and green emission, respectively. The nearly quadratic behavior of the red emission suggests the involvement of two photons in the excitation mechanism. For the green emission, however, a value > 2 is observed, which suggests a three-photon process according to Pollnau [49]: in general a slope of x implies an UpC process involving at least n photons, with n is the smallest integer greater than or equal to x . Similar results were reported in the literature by Singh *et al.*, with slopes of 2.2–2.3 for the green emission. Even though the

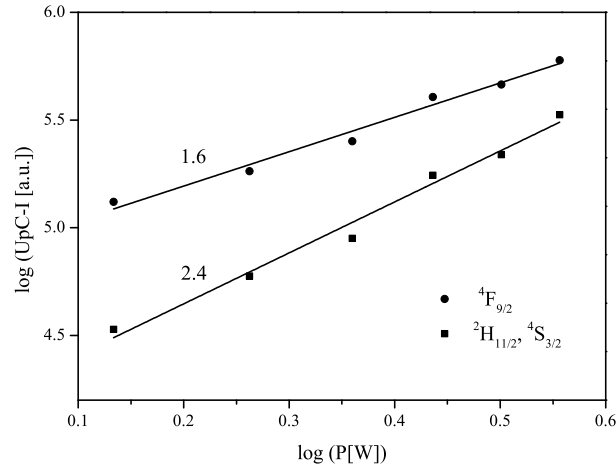


Figure 6.23: Measured emission intensities from the green-emitting levels ${}^2\text{H}_{11/2}$: ${}^4\text{S}_{3/2}$ and red light-emitting level ${}^4\text{F}_{9/2}$ in 1 at.% Er/20 at.% Yb:TiO₂, fabricated at 700 °C, versus the excitation power, upon excitation at 972 nm.

estimated slopes were > 2 , it was referred to a two-photon excitation process. In our case, we believe that in addition to the population via the transition ${}^4\text{I}_{11/2} \rightarrow {}^4\text{F}_{7/2}$, a three-photon process is involved in the population of the green-emitting states. A third energy transfer from Yb: ${}^2\text{F}_{5/2}$ to ${}^4\text{F}_{9/2}$ results in the excitation of the state ${}^4\text{G}_{11/2}$, from where the Er³⁺ ion can relax into lower excited states. Such a mechanism would require three photons and may co-exist with the two-photon process during the UpC process.

6.5 Summary

We have shown that sol-gel processing yields high optical quality RE-doped oxide thin films. The UpC behavior of these films under NIR light excitation, is strongly depend on the nature of host matrix, especially its phonon energy. Even though glassy hosts such as silica, provide a broader absorption ability due to inhomogeneous broadening, the high phonon energy strongly reduces the UpC efficiency. Therefore, the Y₂O₃ host matrix, exhibiting a lower phonon energy compared to the titania and silica hosts, is expected to yield the highest UpC efficiency for Er³⁺. Furthermore, the RE dopant concentration must be adjusted in each host matrix for an optimization of the final emission output. All sol-gel derived films further require a post-deposition annealing step, mainly to reduce the OH contamination. In case of polycrystalline Y₂O₃ thin films, annealing at high temperatures resulted in the formation of micro-cracks, which may be reduced using a different substrate or by depositing films of low thicknesses. At this point it should be mentioned, that the formation of cracks is undesirable concerning the optical quality of the film, however, we expect the light UpC performance not to be reduced due to their presence.

1D-Photonic bandgap structures: Fabry-Pérot microcavities

Fabry-Pérot dielectric microcavities, consisting of an Er/Yb-doped yttria half-wavelength thick layer located between alternating quarter-wavelength thick silicate and titania layers, have been prepared by sol-gel processing. We studied the modifications of the Er^{3+} up-conversion luminescence, when embedded in the cavity layer, compared to the emission properties outside the cavity structure. An enhancement of the green emission, which is attributed to the transition $\text{Er}:^2\text{H}_{11/2};^4\text{S}_{3/2} \rightarrow ^4\text{I}_{15/2}$, was observed in the microcavity samples, at and near their cavity resonance peak. At the same time, the trend towards a reduced red/green emission intensity ratio in the cavity structures suggests a change in the spontaneous emission branching ratios of the Er^{3+} ion.

Finally, we analyzed the influence of the annealing temperature of the cavity samples on their UpC emission properties. An enhancement factor of 2.5 in the total UpC emission was observed in microcavities annealed at 1050 °C compared to the sample annealed at 900 °C. We attributed this emission improvement to thermal effects as well as to a shift in the cavity resonance wavelength towards the center of the green emission band of Er^{3+} .

7.1 Introduction

One-dimensional (1D) photonic bandgap (PBG) structures allow a manipulation of the spontaneous emission by tailoring the electromagnetic environment surrounding the emitter species. This physical phenomenon – by far not trivial – was described by Purcell and is related to an enhancement of the optical mode density of the electromagnetic field of an emitter inside a cavity [219, 220]. This effect can be achieved when the emitter is placed between two distributed Bragg mirrors (DBM), which results in the generation of a pass band (defect mode) inside the stop band. Such structures are known as Fabry–Pérot (F–P) microcavities.

These structures are of interest for realizing a luminescence enhancement in light up-conversion (UpC) processes based on rare earth (RE^{3+}) ions. Significant changes in the luminescence intensity, lifetimes and quantum yields can be achieved by locating the RE^{3+} ions within a cavity. RE^{3+} ions typically show quite narrow and weak emission bands when doped into crystalline host lattices. This is due to the fact that their 4f–4f transitions are electric dipole forbidden and an increase in the absorption and emission intensities can mainly be achieved through increased RE doping. However, the efficiency of UpC processes is limited in terms of the maximum RE doping concentration, due to luminescence concentration quenching and nonradiative relaxation processes which are influenced by ion–phonon (lattice) interactions.

A lot of work has been devoted to the design of microcavities based on semiconductors [221] and dielectric oxide materials as active media. Oxide-based materials have been proven to be particularly interesting for the fabrication of 1D–PBG structures due to their wide range of transparency from the UV to the NIR, and show further a high stability against radiation, corrosion and elevated temperatures [222].

Since the difference in the refractive index, together with the number of distributed Bragg reflector (DBR) periods, control the width of the stop band and the reflectivity within the stop band, the choice of material often falls on SiO_2 ($n \sim 1.45$ [206]), as low refractive index material, and TiO_2 ($n \sim 2.54\text{--}2.75$ [223]), as high refractive index material. Various film deposition techniques are used for the fabrication of oxide-based materials, such as the sol–gel method [67–71, 224–227], rf sputtering [72, 222] and the ion–plating (IP) technique [228, 229]. As far as the sol–gel method is concerned, it is a low cost, versatile technique for the fabrication of good quality F–P microcavities.

In this work, we focus on the fabrication of F–P microcavities by the sol–gel method, to achieve an enhancement of the Er^{3+} green UpC emission centered at ~ 550 nm. Therefore, the microcavities need their resonance wavelength positioned within the green emission band of Er^{3+} . The utilized geometry comprises a 1D–microcavity composed of an Er/Yb–doped Y_2O_3 layer placed between two BMs. The BMs consist of a stack of three pairs of alternating quarter–wavelength thick layers of SiO_2 and TiO_2 , for the low and high refractive index material,

respectively. Reflectance spectra of the microcavities were measured to elucidate the position of the cavity resonance peak. Upon 972 nm laser excitation, all microcavity samples showed visible UpC phenomena, and their emission was compared to non-cavity reference samples, which were fabricated from the same sol and under the same processing conditions as the cavity samples. Finally, we studied the influence of the post-deposition annealing temperature of the microcavities on their luminescent properties.

7.2 Methods and characterization

7.2.1 F-P microcavities

The F-P microcavities, consisting of stacks made of alternating low and high refractive index layers of silicate glass (“L”) and titania (“H”), separated by an Er/Yb:Y₂O₃ cavity layer (“Y”), were deposited on Si(100) substrates by the sol-gel method. Each mirror layer requires a physical thickness $\lambda_f/4n$, with λ_f being the resonance wavelength and n the refractive index, whereas the cavity layer is a one-half wavelength, $\lambda_f/2n$, thick RE:Y₂O₃ layer. The typical cavity structure used consists of a multilayer stack (LH)₃Y(HL)₃, with one BM on each side of the cavity layer, made of three H/L periods, as shown in Fig. 7.1.

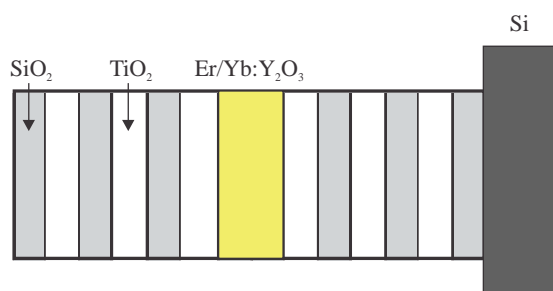


Figure 7.1: Graphic illustration of a F-P microcavity of two BMs made of 3 pairs of alternating TiO₂ ($n \sim 2.5$) and SiO₂ ($n \sim 1.45$) layers. RE:Y₂O₃ ($n \sim 1.7-1.8$) is used as the cavity layer in the center of the structure.

For the positioning of the cavity resonance wavelength at the green emission band of Er³⁺ at ~ 550 nm, the estimated layer thickness for silicate, titania and yttria films should be ~ 90 nm, 60 nm and 150 nm, respectively. The cavity resonance wavelength was only changed by the thickness of the silicate films, which was adjusted by the volume of solvent added to the sol, while the titania and yttria sols were prepared according to the recipes in Chapter 6. The Y₂O₃ cavity layer was the only layer being doped with 1 at.% Er and 10 at.% Yb, while the BMs remained in an undoped form. Two batches of samples were fabricated, using different temperatures during the sol-gel coating and the post-deposition annealing process. Once each layer was densified at 900 °C for 30 s in air and after the last deposition cycle, the microcavities were baked in a muffle furnace at 900 °C for 1.5 h, in air. For the second batch of samples, a temperature of 1050 °C was chosen to study the influence of the annealing temperature on the luminescent properties of the samples.

Additionally to the fabricated F–P microcavities, a reference sample consisting only of RE–doped Y_2O_3 was fabricated from the same initial sol and under the same processing conditions as the cavity samples. This assured, that the measured changes in the Er emission originate from the microcavity structure.

7.2.2 Characterization

Reflectance measurements. Reflectance measurements are an essential tool to elucidate the position of the pass band localized within the stop band of the microcavity. The experimental set–up used for the reflectance measurement is sketched in Fig. 7.2. The illumination of the sample surface was achieved by using a white light emitting tungsten lamp (Cuda products corporation, I-150). The light beam was focused through a lens onto an iris, whose diameter was varied, allowing to adjust the light intensity and spot size of the light reaching the film surface. The spot size on the film surface was of about 5 mm and the sample was positioned in a way that the reflected light coincided with the iris hole.

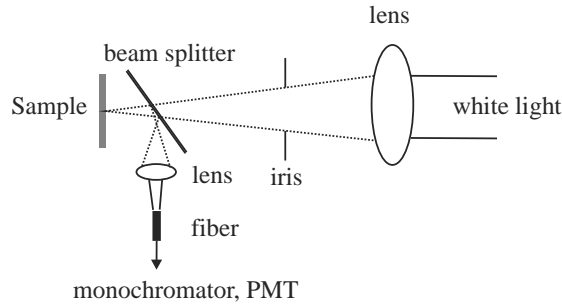


Figure 7.2: Top–view of the experimental set–up for the reflectance measurements used in the characterization of the F–P microcavities. Adapted and slightly modified from [227].

A slide of borosilicate glass acted as the beam splitter, reflecting about 4% of the reflected light onto a second lens. The reflected light was then coupled into a multimode fiber (core diameter: $600\ \mu\text{m}$) and guided into a spectrometer consisting of a 0.85 m double monochromator (Spex 1403) and a photomultiplier tube (PMT, Hamamatsu, R 928). An aluminum mirror was chosen as a reference for a 100% reflectivity, and all reflection spectra measured are corrected by rationing them to the reference spectrum of 100% reflectivity. A simulation of the reflectance spectra was performed by the transfer matrix method (TMM) as has been already described elsewhere in the literature [71, 230].

UpC emission measurements. UpC emission of the F–P cavities as well as the reference samples was observed upon 972 nm continuous laser excitation ($P = 4\ \text{W}$). The experimental set–up was identical to that described prior in Chapter 3. The incident light was about 45° to the sample and the angle of the collected emission was about 90° to the sample.

7.3 Results

7.3.1 Reflectance spectra and UpC emission at 972 nm excitation

The reflectance spectra for the F-P microcavities, annealed at 900 °C, are shown in Fig. 7.3. The incidence of the light was perpendicular for all reflectance measurements. The sharp peak appearing between ~ 550 –600 nm corresponds to the cavity resonance wavelength of the sample and can be adjusted by the thickness of the quarter-wave SiO₂ layer.

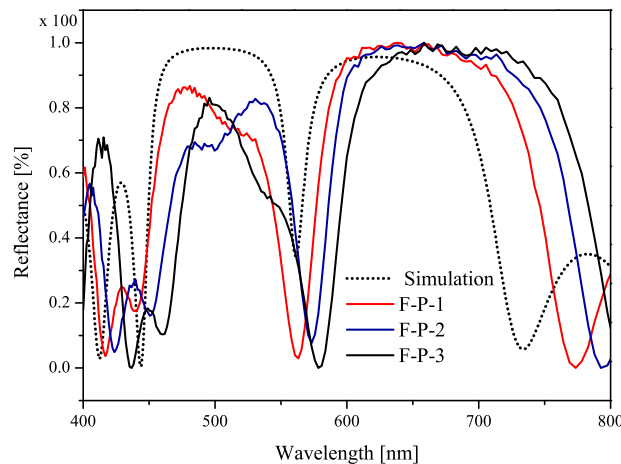


Figure 7.3: The evolution of the reflectance spectra of multilayer stacks consisting of $(LH)_3Y(HL)_3$ with increasing thickness d of the SiO₂ layer, $d(\text{F-P-1}) < d(\text{F-P-2}) < d(\text{F-P-3})$, on Si substrates, baked at 900 °C. The dotted line shows the reflectance spectrum simulated by the TMM, with corresponding layer thicknesses of $L = 90$ nm, $H = 60$ nm and $Y = 150$ nm.

The reflectance of the microcavities shows features similar to the simulated reflectance spectrum, which exhibits a cavity resonance peak at 560 nm. The simulated reflection spectrum was calculated by the transfer matrix method (TMM [145]), using the dispersion of the refractive index from prior results shown in Chapter 6, Sections 6.2, 6.3 and 6.4. The designated layer thicknesses for the simulated spectrum were 90 nm and 60 nm for the quarter-wave thick SiO₂ and TiO₂ layers, respectively, and 150 nm for the Y₂O₃ half-wave layer. A normalization of the reflection spectra with respect to their maximum values was performed to account for the light scattering on the 1-side-polished Si wafer. Larger differences, e. g. in the longer wavelength region, can be attributed to inevitable errors during the sample fabrication and due to the annealing process. The cavity resonance wavelength closest to the simulated reflectance was found for sample F-P-1, with 563 nm.

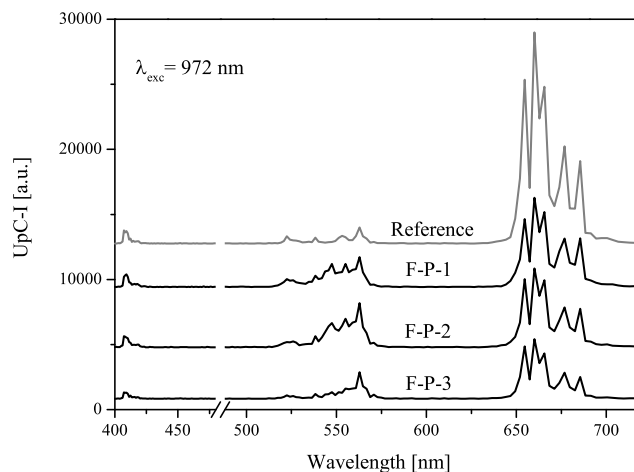


Figure 7.4: UpC emission from the F–P cavities with varying λ_f upon 972 nm excitation, detected at 45° with respect to the normal. Additionally, the emission spectrum of a reference sample without the cavity structure is depicted. For a better view, the 2nd harmonic of the 972 nm laser was left out in the spectra.

For UpC emission measurements, the samples were excited by a 972 nm laser ($P = 4\text{W}$) at a $\sim 45^\circ$ angle and the luminescence was collected in a perpendicular direction to the sample surface. The typical UpC emission of an Er/Yb:Y₂O₃ film outside the cavity structure shows three characteristic emission bands in the visible range: a weak one centered at $\sim 410\text{ nm}$, corresponding to the transition $^2\text{H}_{9/2} \rightarrow ^4\text{I}_{15/2}$, a medium one at $\sim 550\text{ nm}$, due to $^2\text{H}_{11/2}:\text{S}_{3/2} \rightarrow ^4\text{I}_{15/2}$, and another strong band at $\sim 660\text{ nm}$, corresponding to the transition $^4\text{F}_{9/2} \rightarrow ^4\text{I}_{15/2}$. Both green and red emissions exhibited significant Stark splittings. Fig. 7.4 shows, for comparison, the UpC emission spectra of the non-cavity reference sample and of the microcavities with different cavity resonance wavelengths at 563 nm (F–P–1), 573 nm (F–P–2) and 579 nm (F–P–3). It is evident that the reference sample, prepared from the same sol and under the same processing conditions as the PBG structures, has different emission patterns compared to the microcavities. The Er³⁺ emission is enhanced where the wavelength corresponds to, or, is close to the cavity resonance mode. The observed emission enhancement can be ascribed to the Purcell effect, which results in an increased emission rate of the Er³⁺ ions coupled to the resonance optical mode of the cavity [65].

The highest UpC luminescence enhancement compared to the non-cavity layer, depicted in Fig. 7.5, was achieved for the sample F–P–2. An enhancement factor of 3 was obtained for the green light emission peak, and the microcavity emission exhibits a different line profile compared to the typical emission of Er³⁺ in Y₂O₃, outside the cavity.

Moreover, the emission is notably weakened for other wavelengths outside the resonance peak, mainly in the red wavelength domain. Such a redistribution of the emission intensity is a known cavity effect and has been reported in the litera-

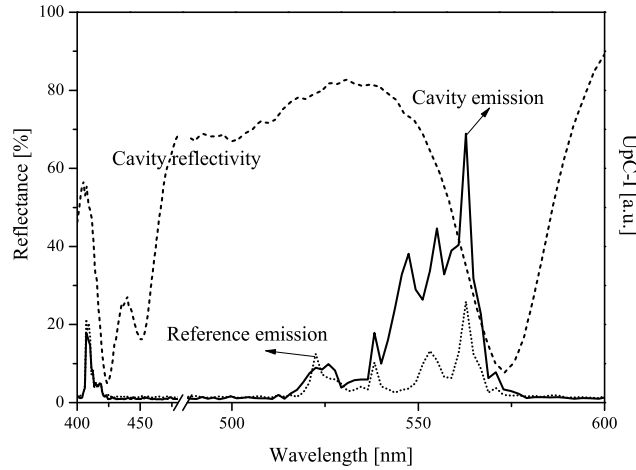


Figure 7.5: UpC emission detected from the microcavity which exhibited the highest light emission, and the reference sample, upon 972 nm excitation. The reflectance spectrum of the microcavity (perpendicular to the incident light) is included in the graph.

ture [231]. Furthermore, the red/green integrated emission ratio decreases from 16 to 2, when the Er/Yb:Y₂O₃ layer is placed between two BMs (for sample F-P-2). The change in the red/green emission ratio, however, could also be a consequence of changes in the spontaneous emission (SE) branching ratios, when the Er³⁺ ion is located inside a microcavity [227]. This might explain the enhancement of the transitions in the Er³⁺ ion which are resonant with the defect peak, while others are reduced. Furthermore, we have to be careful, when we directly compare the emission intensity of the microcavity with the non-cavity sample. An increased light scattering in the microcavity due to its layered structure and higher thickness compared to the reference sample, can also lead to an enhanced luminescence signal. Therefore, the changed ratio of the emission intensity is of a more accurate meaning.

One important factor to be considered in the sol-gel derived microcavities is the temperature used during the sol-gel coating process and in the final annealing. During the sol-gel coating, each individual layer undergoes densification due to a short heat treatment at 900 °C for 30 s. Sol-gel derived films are known to develop internal stresses during the densification process. This favors the formation of cracks and other defects in the film microstructure, in case the elastic energy becomes higher than the cohesion energy. The tensile stress in SiO₂ films transforms into compressive stress at temperatures ≥ 900 °C, whereas for TiO₂ it remains tensile [225]. However these opposite stresses partially compensate each other, and film cracking nonetheless can be avoided. Moreover, a temperature as high as 900 °C is required for the transformation of SiO₂ from the amorphous into the dense glassy state [71]. This temperature also allows for a smooth deposition of the Y₂O₃ films.

In the final post-deposition annealing process, rather high temperatures are required to reduce residual stresses and, importantly, to eliminate OH groups. These act as quencher species for the radiative emission due to their high vibrational energy ($\sim 3200\text{--}3600\text{ cm}^{-1}$ [203]). According to that, we also considered an annealing temperature of $1050\text{ }^\circ\text{C}$, for 1 h, in air at the end of the deposition cycle in the preparation of microcavities.

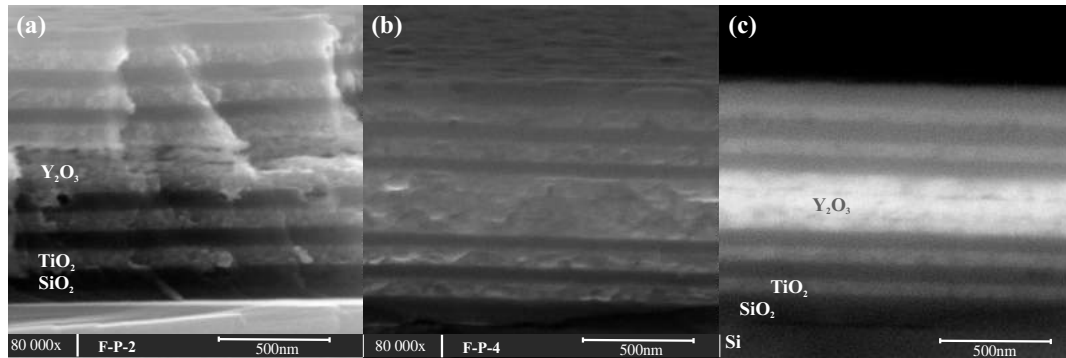


Figure 7.6: SEM cross-section micrographs of microcavities annealed at (a) $900\text{ }^\circ\text{C}$ (F-P-2) in SE mode (b) $1050\text{ }^\circ\text{C}$ (F-P-4) in SE mode and (c) cross section of F-P-4 in BSE mode, respectively. The estimated layer thickness for F-P-2 are: 70 nm and 90 nm for SiO_2 and TiO_2 ; the layer thickness of Y_2O_3 could not be determined due to the weak contrast between Y_2O_3 and TiO_2 . For F-P-4 we estimated the layer thickness of SiO_2 , TiO_2 and Y_2O_3 from the BSE image to be $\sim 80\text{ nm}$, 70 nm and 110 nm .

Fig. 7.6 shows the SEM cross-section images of microcavities annealed at $900\text{ }^\circ\text{C}$ and $1050\text{ }^\circ\text{C}$, respectively. One can easily see the two 3-period BMs made of alternating SiO_2 (dark stripes) and TiO_2 (bright stripes) layers on each side of the RE: Y_2O_3 cavity layer. The cavity layer could not easily be distinguished from the TiO_2 layer, hence the layer thickness was difficult to be determined. The films show a good parallelism and the estimated film thickness for SiO_2 and TiO_2 in F-P-2 was $\sim 70\text{ nm}$ and 100 nm (no Y_2O_3 layer thickness determined); the BSE image of F-P-4, shown in Fig. 7.6 (c), revealed $\sim 80\text{ nm}$, 70 nm and 110 nm thin layers of SiO_2 , TiO_2 and RE: Y_2O_3 .

The increase in the annealing temperature provokes changes in the reflectance spectrum of the microcavities. Fig. 7.7 shows the reflection spectra of a microcavity baked at $900\text{ }^\circ\text{C}$ and, additionally at $1050\text{ }^\circ\text{C}$ in a 2nd annealing process. The position of the defect peak is blue-shifted by $\sim 20\text{ nm}$ due to further film densification at the elevated temperature.

The reflectance spectra of the two best results among the cavity samples which were annealed at $1050\text{ }^\circ\text{C}$ are shown in Fig. 7.8. The cavity resonance wavelengths for the two samples F-P-4 and F-P-5 are 552 nm and 541 nm , respectively, which is due to the difference in the layer thickness of the quarter-wave SiO_2 layer. The simulated reflectance was calculated with a layer thicknesses of $\text{SiO}_2 = 80\text{ nm}$, $\text{TiO}_2 = 60\text{ nm}$ and $\text{Y}_2\text{O}_3 = 150\text{ nm}$, and exhibited the defect peak at 549 nm .

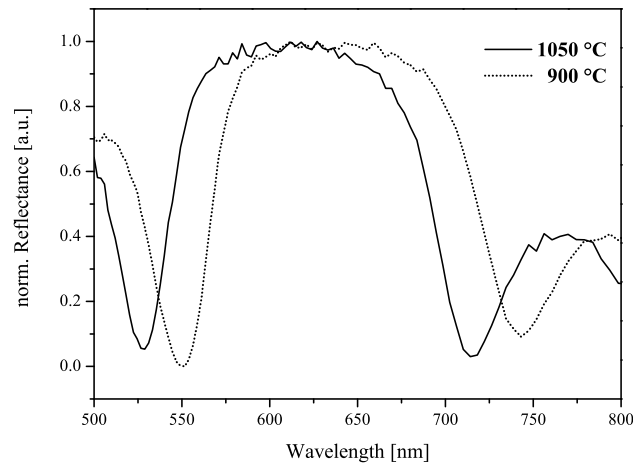


Figure 7.7: Influence of the temperature in the annealing process on the reflectance spectra of microcavities fabricated from the same sol, and annealed at 900 °C (dotted line) and 1050 °C (solid line), respectively, for 1 h, in air.

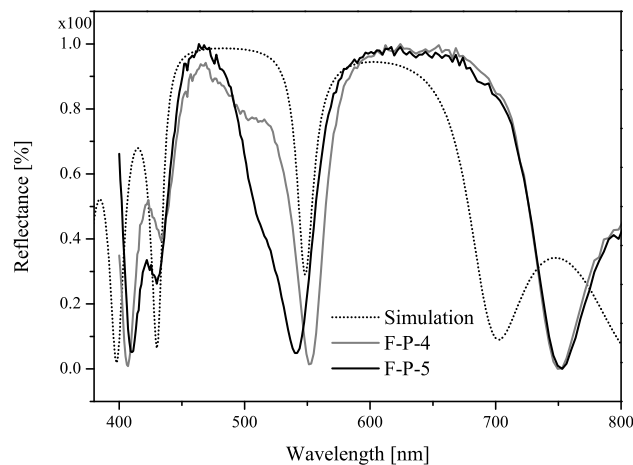


Figure 7.8: Reflectance spectra of two microcavities, annealed at 1050 °C, with cavity resonance wavelengths close to the reflectance spectrum simulated by the TMM. The reflectance spectra were measured perpendicular to the incident light.

Fig. 7.9 shows, for comparison, the UpC luminescence spectra of the microcavities F-P-4 and F-P-5, together with the reference sample without the BMs, which was prepared under the same processing conditions. The green light emission from the microcavity samples is slightly enhanced and the emission line shape is modified in the cavity samples. An enhancement factor of 2 was obtained for the sample F-P-4, which exhibited the strongest emission enhancement for the transition ${}^2\text{H}_{11/2} : {}^4\text{S}_{3/2} \rightarrow {}^4\text{I}_{15/2}$. Furthermore, it is observed that the maximum emission wavelength at ~ 547 nm,

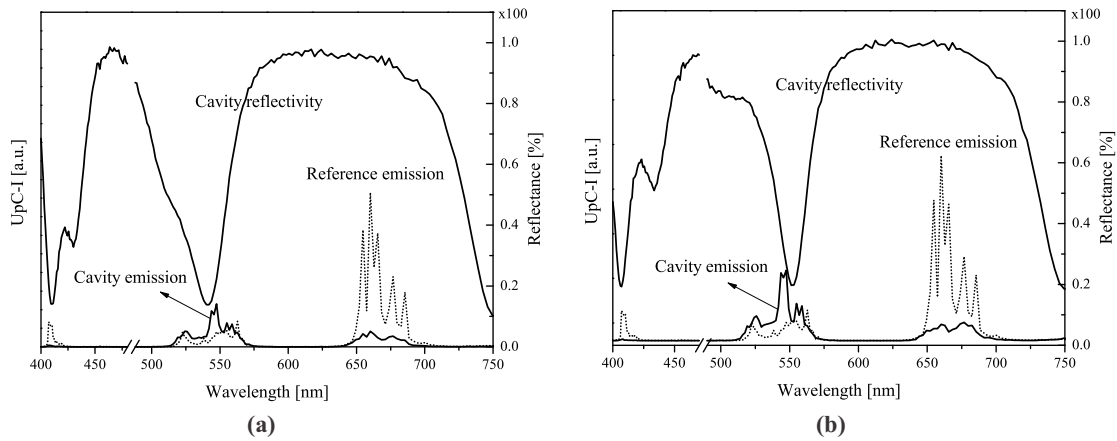


Figure 7.9: NIR-to-Vis UpC emission spectra from the microcavities (a) F-P-4 and (b) F-P-5, with their corresponding reflection spectra. The spectra is cut at ~ 480 – 490 nm to avoid the second harmonic laser line. In both figures, the dotted line represents the emission spectrum of a RE:Y₂O₃ layer, outside the cavity structure.

does not exactly coincide with the cavity resonance wavelength. We assume that this is due to a non-exact 45° angle (with regard to the incident light) in the collection of the emission during the experiments. The cavity resonance position depends strongly on the detection angle, and so do the luminescence spectra. As a consequence, small variations in the detection angle can cause significant changes in the reflection and emission spectra.

The violet and red emission intensities are strongly reduced in the emission spectra of the cavity samples, which can be mainly attributed to changes in the spontaneous emission branching behavior, as was mentioned before. The ratio of the integrated red/green emission intensities decreases from 5 for the RE:Y₂O₃ layer outside the cavity to 0.5 for the microcavity F-P-4.

In Fig. 7.10 the UpC emission spectra of the two microcavities annealed at 900°C and 1050°C , F-P-2 and F-P-4, are compared with each other. The integrated total emission intensity of F-P-4 is about 2.5 times higher compared to sample F-P-2, and the green emission intensity is enhanced by an even higher factor of 5. This can be mainly attributed to two effects: the cavity resonance wavelength of the microcavity F-P-4 is at 552 nm and closer to the center of the green emission band, whereas sample F-P-2 has its resonance peak at 573 nm, located at the lower end of the emission band. Additionally, thermal effects such as a reduction of impurities and grain growth in the matrix, are known to improve the UpC efficiency.

The full width at half maximum (FWHM, $\Delta\lambda$) of the resonance peak for microcavities F-P-2 and F-P-4 is ~ 29 nm. The quality of a microcavity, measured by its quality factor Q , $Q = \lambda_f/\Delta\lambda$, was about 20 for both samples, originating from the rather low number of DBRs in these structures. By increasing the number of DBR pairs on each side of the cavity layer, the reflectivity of the BMs can be enhanced and could lead to a further improvement in the Q factor.

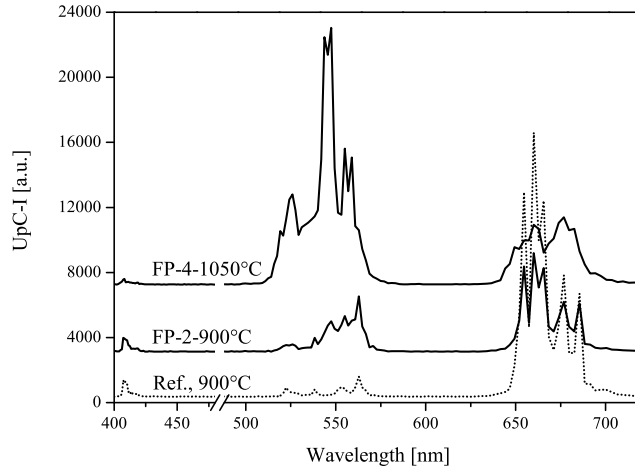


Figure 7.10: Comparison of the UpC luminescence upon 972 nm laser excitation ($P = 4$ W) of microcavities F-P-4, baked at 1050 °C, and F-P-1, baked at 900 °C. In addition the UpC spectrum from an Er/Yb:Y₂O₃ film without the Bragg mirrors, annealed at 900 °C, is shown.

7.4 Summary and Outlook

In a first, preliminary study, we fabricated sol-gel derived F-P microcavities, consisting of an Er/Yb:Y₂O₃ half-wave layer, inserted between two BMs made of three pairs of alternating quarter-wave SiO₂/TiO₂ layers. We investigated the up-converted luminescence enhancement for the green emission in Er/Yb:Y₂O₃, when embedded in a cavity structure. It was shown that the green emission intensity of all prepared F-P microcavities is enhanced when compared to the non-cavity reference sample. The best result showed an emission enhancement factor of 3. However, the direct comparison of the emission intensity of the microcavity with the reference sample is delicate, because the thicker microcavity sample may scatter light stronger than the non-cavity sample, which could change the emission intensity. Therefore, the more meaningful result is the intensity ratio of the green/red up-converted emission. In addition to the emission enhancement for the transition Er:²H_{11/2}:⁴S_{3/2} → ⁴I_{15/2}, a reduced emission intensity in the red wavelength region was observed. The integrated red/green emission ratio decreases from 5 to 0.5 for the RE:Y₂O₃ reference sample and the corresponding cavity sample, both baked at 1050 °C. This change in the emission intensity ratios can be related to a modification of the spontaneous emission branching ratios. Microcavity samples annealed at a post-deposition temperature of 1050 °C, yielded better results in the emitted light intensities. We attributed this mainly to the reduction in OH impurities in the film, which may assist in nonradiative relaxation processes.

A Q factor of 20 was obtained for the best samples and leaves room for further improvement. Increasing the number of DBR periods in the multilayer stack would further improve the Q factor of the microcavity. For further studies, a cou-

pled microcavity structure should be investigated, with the aim to yield a higher luminescence intensity, compared to a single microcavity structure.

Possible application of an upconverter to a solar cell device

We now want to address the questions whether the application of an upconverter to a solar cell device is reasonable, how large the achieved efficiency enhancements are, and what the requirements for the realization of an upconverter–solar cell (UpC–SC) device are.

To date, only lanthanide–based upconverters have been realized for an application to solar cells, mainly to demonstrate the proof of concept that an efficiency enhancement can be achieved. This is due to the fact that the UpC efficiency is low, and so is the resulting efficiency enhancement of the solar cell. For NaYF₄:Er/Yb, the most successful upconverter material known, a luminescence quantum efficiency (LQE) of $\sim 10\%$ at 40 W/cm^2 was reported in Ref. [57]. The full solar spectrum, on the other hand, has an irradiance of 0.1 W/cm^2 [232]; therefore, we can conclude that light concentration is inevitable for measuring any improvements in the cell efficiency. Table 7.1 gives some examples of the reported external quantum efficiencies (EQE) of upconverter solar cells [232].

Table 7.1: Reported external quantum efficiencies *EQE* for UpC–SCs at the power (density) given; excerpt from [232].

Cell type	Upconverter	EQE %	Power (density)	Wavelength [nm]
c–Si	NaYF ₄ :20% Er	3.40	$2.4 \text{ W}\cdot\text{cm}^{-2}$	1523
GaAs	Er/Yb:glass ceramics	2.50	1 W	891
a–Si	NaYF ₄ :18% Yb/2% Er	0.02	$3 \text{ W}\cdot\text{cm}^{-2}$	980
DSSC	UC–TiO ₂	0.002	2.5 W	980

Not only is solar light concentration a requirement, also occurrent optical and electrical losses have to be taken into account for the design of the device structure. Optical losses, such as reflection, absorption and light scattering insight the cell, can be partly minimized by adding an anti–reflection coating and the use of flat solar cells. Three different schemes for UpC–SCs are shown in Fig. 7.11. The electrical losses arise from the fact that the reflected light enters the solar cell from the rear side, which does not optimally generate the current. This is mainly

because the electron hole pairs are generated close to the n-side of the p-i-n junction [232].

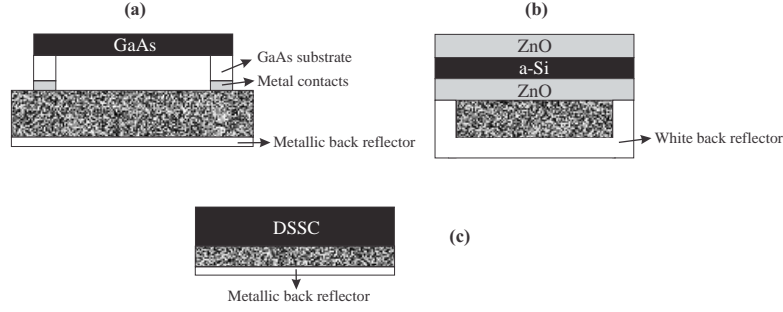


Figure 7.11: UpC-SC device structures, adapted and modified from [232]; the patterned areas are the upconverter layers.

According to Ref. [11, 233] the EQE improvement of the photovoltaic device in the infrared due to an upconverter can be related to the LQE and the optical losses L , as follows:

$$\text{EQE} = (1 - L)(1 - \exp^{-\alpha l})\text{LQE} \propto P_{\text{in}}^{(n-1)} \quad (7.1)$$

with α the absorption coefficient at the excitation wavelength and l the thickness of the UpC layer. Since UpC is a process depending nonlinearly on the incident excitation power, the EQE will also show a dependence on the power of the incident light, $P_{\text{in}}^{(n-1)}$, where n is the number of photons required in the UpC process.

Since we did not perform measurements of LQE and the absorption characteristics of our upconverter films due to lack of appropriate experimental facilities, we can here only make a rough estimation of the efficiency enhancement to be expected for UpC-SC devices.

Assuming an absorption coefficient of 1 cm^{-1} and an upconverter thickness of 1 cm , similar to that reported in Ref. [233], and taking the optical losses L with 0.75 into account [11, 233], we find the relationship $\text{EQE} = 0.16 \text{ LQE}$. Setting a lower and upper limit for the upconverter efficiency with 1% and 10% , we reach an improvement of the $\text{EQE} \sim 0.2\%$ and $\text{EQE} \sim 2\%$, respectively. The main reasons why the calculated efficiency enhancement is that low, is that only part of the solar spectrum is utilized ($900\text{--}1050 \text{ nm}$ for Yb-based upconverter materials), which makes such an application of an UpC-SC device quite unrealistic. To guarantee better results, not only the UpC efficiency of the materials used must be improved, but also their absorption properties in the infrared. Lahoz *et al.* reported, that even with an upconverter LQE of 100% , a c-Si solar cell in combination with an Er-upconverter ($1480\text{--}1580 \text{ nm}$ absorption range), the efficiency enhancement would only be 2.4% , which is too low to justify a practical application.

For a theoretical estimation of the increase of the photo-current due to the upconverter, one has to solve the following equation from [233]:

$$\frac{dI_{UpC}}{d\lambda} = q\Phi(\lambda)EQE(\lambda) \quad (7.2)$$

with q the electron charge ($1.602 \cdot 10^{-19}$ C) and Φ the solar photon flux (measured in photons/m²/s/nm). For example, the reported current density increase due to an Er/Yb:Gd₂O₂S upconverter, attached to an a-Si solar cell, was reported to be 0.002 mA/cm², at 1 sun [26]. The measured photo-current J_{SC} of an a-Si cell was reported with ~ 17 mA/cm² global AM1.5 spectrum (i.e. 1 sun, 1000 W/m²) [8]. Therefore, the efficiency enhancement would be only about 0.01%. Although an IR photo-response can be measured due to the upconverter, the measured efficiencies are too low to justify a practical application in photovoltaics.

We conclude that the efficiency enhancements of an UpC-SC device are to date too low, to justify the financial investment. An improvement can only be achieved using high light concentration, and optimizing the upconverter material itself. An improved luminescence quantum efficiency and absorption ability in the infrared, as well as, e.g. a combination of several RE³⁺ ions to broaden the absorption range, should be considered to make UpC a realistic option in photovoltaics.

General conclusions and outlook

The main questions addressed in this work were: 1.) to find the dominant factors which influence the light up-conversion in rare earth-doped thin films deposited by MOCVD and sol-gel processing 2.) the importance of the film deposition method chosen and its influence on the film microstructure and 3.) the evaluation of the potential applicability of an upconverter layer to a solar cell device.

By dividing the films studied into fluoride- and oxide-based hosts for embedding RE^{3+} ions, it became evident that the UpC emission intensity benefits from a matrix with an intrinsic low phonon energy. The reasons for this stems from the nonradiative decay process becoming uncompetitive when the number of phonon required to dissipate the energy is > 6 , thus as the matrix phonon energy is reduced the likelihood of nonradiative decay is decreased. Er/Yb-doped YF_3 , the most successful upconverter studied in this work, exhibited a strong green up-converted emission upon 972 nm excitation, even under low pump powers. However, it was also found that the relative intensity ratio of red and green emission, hence the final emission output, can be controlled by the Yb doping level in YF_3 : at high Yb concentrations, the red emission intensity increases due to a de-excitation of the green-emitting states $\text{Er}:^2\text{H}_{11/2};^4\text{S}_{3/2}$ towards $^4\text{I}_{13/2}$.

Following the systematic order of the material phonon energy, Er/Yb: Y_2O_3 ($\sim 600 \text{ cm}^{-1}$) is an example for a strong NIR-to-red upconverter material. The three different film deposition methods used in this work allow us some basic conclusions about the relationship between the processing conditions and the resultant changes in the UpC emission. To sum up our findings, Er/Yb-doped Y_2O_3 sol-gel films showed an UpC emission comparable to films deposited by the MOCVD variants. However, the optical properties, such as the refractive index, were shown to be sensitive to the microstructure, thus to the deposition method used. The highest refractive index was measured for the Y_2O_3 film deposited by LI-MOCVD, after annealing at 1050°C , the lowest for the film deposited by sol-gel processing,

before annealing.

Further we found that a processing temperature of 1050 °C for sol–gel derived films, assured the removal of OH contamination, since such contaminants act as luminescence quenchers, hence their removal leads to a high luminescence yield, although micro–crack formation starts to take effect at this temperature. A compromise was found by depositing RE:Y₂O₃ films with a maximum thickness of ~ 500 nm (10 layers) to avoid film crazing. Cracking lowers the optical quality of a film, however, may be prevented by depositing films of a low thickness or by using a different substrate (see below). Taking into consideration that sol–gel is a low–cost process, sol–gel processing of Y₂O₃ films has a principal advantage over MOCVD techniques.

The AA–MOCVD technique enabled Y₂O₃ film growth with a high deposition rate and a rather simple experimental set–up, however, films could not be prevented from forming cracks in their structure after undergoing thermal annealing. This was attributed due to shrinkage cracking (~ 10% film shrinkage after annealing at 1050 °C) and the differences in the CLTE between substrate and film. Even though film cracking does not influence or reduce the UpC efficiency, in terms of optical quality, crack formation is undesirable. One way to go, in case of a large difference in the CLTEs of substrate and film, is the deposition of very thin films, which reduces the formation of tensile stresses.

RE:Y₂O₃ films of high optical and structural quality were obtained by LI–MOCVD, even after high temperature annealing at 1050 °C no cracks were visible, possibly due to the columnar film microstructure. When we compare the Er³⁺ UpC emission in YF₃ and Y₂O₃, we obtained a much higher total emission intensity output for the fluoride host lattice, because the nonradiative multiphonon relaxation rate is lower due to the low cut–off phonon frequency (~ 500 cm⁻¹). Although we were not able to measure the luminescence quantum efficiencies (LQE), we can make a comparison of the lifetimes of Er:⁴S_{3/2}, ⁴F_{9/2} levels in Y₂O₃ and YF₃ films, both grown by LI–MOCVD: we determined $\tau(^4S_{3/2})$ with 54 μ s and $\tau(^4F_{9/2})$ with 69 μ s in Er/Yb:Y₂O₃ films (annealed at 1050 °C), versus $\tau(^4S_{3/2})$ with 442 μ s and $\tau(^4F_{9/2})$ with 714 μ s in Er/Yb:YF₃ films (1.5 at.% Er, 10 at.% Yb). Therefore, the lifetime lengthening (~ 10 x) and visible luminescence intensity makes the fluoride film a promising upconverter material.

The post–deposition annealing of the films plays a key role for the optical and luminescent properties of the films studied: first, high temperature annealing reduces film stresses and eliminates groups of high vibrational quanta, such as organic and OH contamination in the host matrix, which reduce the UpC efficiency. Secondly, annealing has been shown to improve the luminescence intensity, promoted by grain growth. An increased grain size assures a reduction in the grain–boundary area, where defects act as centers of luminescence quenching.

The UpC emission in glassy, amorphous host materials can have the advantage of a broadening of the emission bands compared to crystalline host lattices. The typical emission spectrum of Er/Yb:SiO₂ and TiO₂ films exhibits broader emission bands with less Stark splitting compared to Y₂O₃ and YF₃ matrices. This

can be beneficial regarding the light absorption ability of the upconverter. On the other hand, the high phonon energies of SiO_2 and TiO_2 increase the nonradiative relaxation rate, thus greatly lower the emission intensity.

For sol-gel derived Er/Yb-doped TiO_2 films, the crystal phase present was shown to play an important role for the UpC emission. A mixture of anatase and rutile phases, obtained at a processing temperature of 700°C , showed the highest UpC emission intensities. We have found that the formation of a pyrochlore titanate phase, $\text{RE}_2\text{Ti}_2\text{O}_7$ ($\text{RE} = \text{Yb}, \text{Er}$), at temperatures $\geq 900^\circ\text{C}$ lowers significantly the UpC emission. Since SiO_2 and TiO_2 hosts per se exhibit a low UpC efficiency, another approach for achieving an emission enhancement was realized by 1D photonic bandgap structures.

Fabry-Pérot microcavities, consisting of dielectric layers of $\text{RE:Y}_2\text{O}_3$, SiO_2 and TiO_2 by sol-gel processing were investigated to enhance to green UpC emission of Er^{3+} . In a preliminary study we have shown that the red/green emission ratio of Er^{3+} was changed inside a microcavity structure, which is a known cavity effect, related to a modification of the spontaneous emission branching ratios. An emission enhancement factor of 3 was determined at $\sim 550\text{ nm}$, for a microcavity annealed at 900°C ; however, bearing in mind that the layered microcavity structure shows stronger light scattering than the non-cavity sample, the more reliable meaning is the change of the red/green emission ratio. For further studies, it is necessary to increase the number of DBR periods in the multilayer stack to improve the Q factor, and to investigate coupled microcavity structures aiming for an enhancement of the UpC emission throughout the visible region. For future works, 1D-PBG structures are definitely a promising option to increase the efficiency of RE-doped upconverters.

The future prospects of the application of an upconverter to photovoltaic devices are challenging. Light concentration, and the design of the device structure are important aspects which have to be considered to increase the UpC efficiency. Concerning light concentration, it is necessary to know, how much concentration is needed, since the series resistance limits the overall cell performance. We have discussed that most the upconverter materials used nowadays, are based on phosphor systems and not on films. The different fabrication methods of thin films allow the direct deposition of an UpC layer onto a solar cell. However, still to date, the achieved efficiency enhancements are too low to justify the financial investment using UpC in photovoltaics. The main issues lie in the absorption ability and luminescence efficiency of the upconverter; therefore improving the luminescence quantum efficiency and absorption ability of the upconverter in the infrared, as well as using a combination of several RE^{3+} ions to broaden the absorption range, will play a key role for making UpC a realistic option in photovoltaics. Another promising direction to go would be the use of plasmonic resonance effects and PBG structures to increase the up-conversion efficiency.

References

- [1] Global Market Outlook for Photovoltaics 2013-2017, European Photovoltaic Industry Association.
- [2] Shafiee, S. and Topal, E. *Energy Policy* **37**(1), 181–189 (2009).
- [3] Bruton, T. M. *Solar Energy Materials and Solar Cells* **72**(1–4), 3–10 (2002).
- [4] Green, M. *Journal of Materials Science: Materials in Electronics* **18**(1), 15–19 (2007).
- [5] Green, M. A. *Progress in Photovoltaics: Research and Applications* **9**(2), 123–135 (2001).
- [6] Conibeer, G. *Materials Today* **10**(11), 42–50 (2007).
- [7] Press, W. H. *Nature* **264**(5588), 734–735 (1976).
- [8] Green, M. A., Emery, K., Hishikawa, Y., Warta, W., and Dunlop, E. D. *Progress in Photovoltaics: Research and Applications* **21**(1), 1–11 (2013).
- [9] Shockley, W. and Queisser, H. J. *Journal of Applied Physics* **32**(3), 510–519 (1961).
- [10] Henry, C. *Journal of Applied Physics* **51**(8), 4494–4500 (1980).
- [11] Shalav, A., Richards, B., and Green, M. *Solar Energy Materials and Solar Cells* **91**(9), 829–842 (2007).
- [12] Trupke, T., Green, M. A., and Würfel, P. *Journal of Applied Physics* **92**(7), 4117–4122 (2002).
- [13] Bloembergen, N. *Phys. Rev. Lett.* **2**, 84–85 (1959).
- [14] Auzel, F. *Chemical Reviews* **104**(1), 139–174 (2004).
- [15] Joubert, M.-F. *Optical Materials* **11**(2), 181–203 (1999).
- [16] Xie, P. and Gosnell, T. R. *Opt. Lett.* **20**(9), 1014–1016 (1995).

- [17] Kenyon, A. *Progress in Quantum Electronics* **26**, 225–284 (2002).
- [18] Yang, Z., Feng, Z., and Jiang, Z. *Journal of Physics D: Applied Physics* **38**(10), 1629–1632 (2005).
- [19] Ho, H.-P., Wong, W.-W., Wu, S.-Y., and Pun, E. *Proceedings of SPIE* **4645**, 156–164 (2002).
- [20] Wang, Y. and Ohwaki, J. *Journal of Applied Physics* **74**(2), 1272–1278 (1993).
- [21] Hilderbrand, S. A., Shao, F., Salthouse, C., Mahmood, U., and Weissleder, R. *Chem. Commun.*, 4188–4190 (2009).
- [22] Huang, X., Han, S., Huang, W., and Liu, X. *Chem. Soc. Rev.* **42**, 173–201 (2013).
- [23] Gibart, P., Auzel, F., Guillaume, J.-L., and Zahraman, K. *Japanese Journal of Applied Physics* **35**(8), 4401–4402 (1996).
- [24] Shalay, A., Richards, B., Krämer, K., and Güdel, G. In *Photovoltaic Specialists Conference, 2005. Conference Record of the thirty-first IEEE*, 114–117, (2005).
- [25] Chen, S., Zhou, G., Su, F., Zhang, H., Wang, L., Wu, M., Chen, M., Pan, L., and Wang, S. *Materials Letters* **77**, 17–20 (2012).
- [26] de Wild, J., Meijerink, A., Rath, J., van Sark, W., and Schropp, R. *Solar Energy Materials and Solar Cells* **94**(11), 1919–1922 (2010).
- [27] Yuan, C., Chen, G., Prasad, P. N., Ohulchanskyy, T. Y., Ning, Z., Tian, H., Sun, L., and Agren, H. *J. Mater. Chem.* **22**, 16709–16713 (2012).
- [28] Liu, M., Lu, Y., Xie, Z., and Chow, G. *Solar Energy Materials and Solar Cells* **95**(2), 800–803 (2011).
- [29] Henke, B., Ahrens, B., Johnson, J. A., Miclea, P. T., and Schweizer, S. *Proceedings of SPIE* **7411**, 74110E1–74110E7 (2009).
- [30] Gamelin, D. and Güdel, H. In *Transition Metal and Rare Earth Compounds*, 1–56. (2001).
- [31] Blasse, G. and Grabmaier, B. *Luminescent Materials*. Springer, (1994).
- [32] Lüthi, S. R., Pollnau, M., Güdel, H. U., and Hehlen, M. P. *Phys. Rev. B* **60**, 162–178 (1999).
- [33] Vali, R. *Computational Materials Science* **50**(8), 2391–2396 (2011).
- [34] Van der Ziel, J., Van Uitert, L., Grodkiewicz, W. H., and Mikulyak, R. *Journal of Applied Physics* **60**(12), 4262–4267 (1986).

- [35] Capobianco, J. A., Vetrone, F., Boyer, J. C., Speghini, A., and Bettinelli, M. *The Journal of Physical Chemistry B* **106**(6), 1181–1187 (2002).
- [36] Dammak, M., Maalej, R., Kamoun, M., and Deschanvres, J.-L. *Physica Status Solidi (b)* **239**(1), 193–202 (2003).
- [37] Patra, A., Friend, C. S., Kapoor, R., and Prasad, P. N. *Chemistry of Materials* **15**(19), 3650–3655 (2003).
- [38] Righini, G. C., Forastiere, M. A., Guglielmi, M., and Martucci, A. *Proceedings of SPIE* **3280**, 57–66 (1998).
- [39] Duverger, C., Montagna, M., Roll, i. R., Ronchin, S., Zampedri, L., Fossi, M., Pelli, S., Righini, G., Monteil, A., Armellini, C., and Ferrari, M. *Journal of Non-Crystalline Solids* **280**(1), 261–268 (2001).
- [40] J. Garcia Sole, L. B. and Jaque, D. *An Introduction to the Optical Spectroscopy of Inorganic Solids*. John Wiley & Sons Ltd, (2005).
- [41] Riseberg, L. A. and Moos, H. W. *Phys. Rev.* **174**, 429–438 (1968).
- [42] Güdel, H. U. and Pollnau, M. *Journal of Alloys and Compounds* **303-304**, 307–315 (2000).
- [43] Richards, B. *Solar Energy Materials and Solar Cells* **90**(9), 1189–1207 (2006).
- [44] Hewes, R. A. and Sarver, J. F. *Phys. Rev.* **182**, 427–436 (1969).
- [45] Ohwaki, J. and Wang, Y. *Japanese Journal of Applied Physics* **33**, L334–L337 (1994).
- [46] Ivanova, S., Pelle, F., Tkachuk, A., Joubert, M.-F., Guyot, Y., and Gapontzev, V. *Journal of Luminescence* **128**, 914–917 (2008).
- [47] Xin, F., Zhao, S., Huang, L., Deng, D., Jia, G., Wang, H., and Xu, S. *Materials Letters* **78**, 75–77 (2012).
- [48] Liang, X., Huang, X., and Zhang, Q. *Journal of Fluorescence* **19**(2), 285–289 (2009).
- [49] Pollnau, M., Gamelin, D. R., Lüthi, S. R., Güdel, H. U., and Hehlen, M. P. *Phys. Rev. B* **61**, 3337–3346 (2000).
- [50] Castaneda, J., Meneses-Nava, M., Barbosa-Garcia, O., de la Rosa-Cruz, E., and Mosino, J. *Journal of Luminescence* **102-103**, 504–509 (2003).
- [51] Lahoz, F. *Opt. Lett.* **33**(24), 2982–2984 (2008).
- [52] Tikhomirov, V., Rodriguez, V., Mendez-Ramos, J., del Castillo, J., Kirilenko, D., Tendeloo, G. V., and Moshchalkov, V. *Solar Energy Materials and Solar Cells* **100**, 209–215 (2012).

- [53] Krämer, K. W., Biner, D., Frei, G., Güdel, H. U., Hehlen, M. P., and Lüthi, S. R. *Chemistry of Materials* **16**(7), 1244–1251 (2004).
- [54] Heer, S., Kämpe, K., Güdel, H.-U., and Haase, M. *Advanced Materials* **16**(23-24), 2102–2105 (2004).
- [55] Ostermayer, F. W., van der Ziel, J. P., Marcos, H. M., Van Uitert, L. G., and Geusic, J. E. *Phys. Rev. B* **3**, 2698–2705 (1971).
- [56] Vetrone, F. and Capobianco, J. A. *International Journal of Nanotechnology* **5**, 1306–1339 (2008).
- [57] Page, R. H., Schaffers, K. I., Waide, P. A., Tassano, J. B., Payne, S. A., Krupke, W. F., and Bischel, W. K. *J. Opt. Soc. Am. B* **15**(3), 996–1008 (1998).
- [58] van der Ende, B. M., Aarts, L., and Meijerink, A. *Phys. Chem. Chem. Phys.* **11**, 11081–11095 (2009).
- [59] Boyer, J.-C. and van Veggel, F. C. J. M. *Nanoscale* **2**, 1417–1419 (2010).
- [60] Strümpel, C., McCann, M., Beaucarne, G., Arkhipov, V., Slaoui, A., Svrcek, V., del Canizo, C., and Tobias, I. *Solar Energy Materials and Solar Cells* **91**(4), 238–249 (2007).
- [61] Gamelin, D. R. and Güdel, H. U. *Accounts of Chemical Research* **33**(4), 235–242 (2000).
- [62] Suyver, J., Aebischer, A., Biner, D., Gerner, P., Grimm, J., Heer, S., Krämer, K., Reinhard, C., and Güdel, H. *Optical Materials* **27**(6), 1111–1130 (2005).
- [63] Heer, S., Wermuth, M., Krämer, K., and Güdel, H. *Chemical Physics Letters* **334**, 293–297 (2001).
- [64] Yablonovitch, E. *Phys. Rev. Lett.* **58**, 2059–2062 (1987).
- [65] Vahala, K. J. *Nature* **424**(6950), 839–846 (2003).
- [66] Yamamoto, Y. and Slusher, R. E. *Physics Today* **46**(6), 66–73 (1993).
- [67] Almeida, R. M., Marques, A. C., Chiasera, A., Chiappini, A., and Ferrari, M. *Journal of Non-Crystalline Solids* **353**, 490–493 (2007).
- [68] Zampedri, L., Tosello, C., Portales, H., Montagna, M., Mattarelli, M., Chiappini, A., Righini, G. C., Pelli, S., Conti, G. N., Martino, M., Portal, S., Marques, A. C., Almeida, R. M., Jestin, Y., Ferrari, M., and Chiasera, A. *Applied Surface Science* **248**, 3–7 (2005).
- [69] Almeida, R. and Rodrigues, A. *Journal of Non-Crystalline Solids* **326-327**, 405–409 (2003).

- [70] Almeida, R. M. and Portal, S. *Current Opinion in Solid State and Materials Science* **7**(2), 151–157 (2003).
- [71] Li, Y., Fortes, L. M., Chiappini, A., Ferrari, M., and Almeida, R. M. *Journal of Physics D: Applied Physics* **42**(20), 205104 (2009).
- [72] Boucher, Y., Chiasera, A., Ferrari, M., and Righini, G. *Optical Materials* **31**(9), 1306–1309 (2009).
- [73] Peters, M., Goldschmidt, J. C., Löper, P., Gross, B., Üpping, J., Dimroth, F., Wehrspohn, R. B., and Bläsi, B. *Energies* **3**(2), 171–193 (2010).
- [74] Peters, M., Goldschmidt, J., Löper, P., Bläsi, B., and Gombert, A. *Journal of Applied Physics* **105**(1), 014909–1 – 014909–10 (2009).
- [75] Valeur, B. and Berberan-Santos, M. N. *Excitation Energy Transfer*, 213–261. Wiley-VCH Verlag GmbH & Co. KGaA (2012).
- [76] Auzel, F. *C.R. Acadmie des Sciences (Paris)* **262**, 1016 (1966).
- [77] Förster, T. *Annalen der Physik* **437**(1-2), 55–75 (1948).
- [78] Dexter, D. L. *The Journal of Chemical Physics* **21**(5), 836–850 (1953).
- [79] Turro, N. J. *Modern Molecular Photochemistry*. University Science Books, California, (1991).
- [80] Inokuti, M. and Hirayama, F. *The Journal of Chemical Physics* **43**(6), 1978–1989 (1965).
- [81] Luxbacher, T., Fritzer, H. P., Riehl, J. P., and Flint, C. D. *Theoretical Chemistry Accounts* **103**(2), 105–108 (1999).
- [82] Choy, K. *Progress in Materials Science* **48**(2), 57–170 (2003).
- [83] Hou, X. and Choy, K.-L. *Chemical Vapor Deposition* **12**(10), 583–596 (2006).
- [84] Roger, C., Corbitt, T., Xu, C., Zeng, D., Powell, Q., Chandler, C., Nyman, M., Hampden-Smith, M., and Kodas, T. *Nanostructured Materials* **4**, 529–535 (1994).
- [85] Lang, R. J. *The Journal of the Acoustical Society of America* **34**(1), 6–8 (1962).
- [86] Felten, F., Senateur, J. P., Weiss, F., Madar, R., and Abrutis, A. *J. Phys. IV France* **5**, 1079–1086 (1995).
- [87] Senateur, J.-P., Dubourdiou, C., Weiss, F., Rosina, M., and Abrutis, A. *Adv. Mater. Opt. Electron.* **10**(3-5), 155–161 (2000).
- [88] Brinker, C. J. and Scherer, G. W. *The Physics and Chemistry of Sol-Gel Processing*. Academic Press, Inc., (1990).

- [89] Wright, J. D. and Sommerdijk, N. A. *Sol-Gel Materials: Chemistry and Applications*. Gordon and Breach Science Publishers, (2001).
- [90] Klein, L. *Ann. Rev. Mater. Sci.* **15**, 227–248 (1985).
- [91] Peter Atkins, J. d. P. *Atkins' Physical Chemistry, 7th edition*. Oxford University Press, (2002).
- [92] Tressaud, A. *Functionalized Inorganic Fluorides: Synthesis, Characterization and Properties of Nanostructured Solids*. Wiley & Sons, 1st edition, (2010).
- [93] Pilvi, T., Puukilainen, E., Munnik, F., Leskel, M., and Ritala, M. *Chemical Vapor Deposition* **15**(1-3), 27–32 (2009).
- [94] Lucas, J., Smektala, F., and Adam, J. L. *Journal of Fluorine Chemistry* **114**(2), 113–118 (2002).
- [95] Buchal, C., Siegrist, T., Jacobson, D. C., and Poate, J. M. *Applied Physics Letters* **68**(4), 438–440 (1996).
- [96] Zinchenko, V. *Journal of Fluorine Chemistry* **131**(2), 159–164 (2010).
- [97] Malandrino, G., Perdicaro, L. M. S., and Fragala, I. *Chemical Vapor Deposition* **12**(12), 736–741 (2006).
- [98] Condorelli, G., Anastasi, G., and Fragala, I. *Chemical Vapor Deposition* **11**(6-7), 324–329 (2005).
- [99] Malandrino, G., Incontro, O., Castelli, F., Fragala, I. L., and Benelli, C. *Chem. Mater.* **8**(6), 1292–1297 (1996).
- [100] Lo Nigro, R., Malandrino, G., Fragala, I. L., Bettinelli, M., and Speghini, A. *J. Mater. Chem.* **12**(9), 2816–2819 (2002).
- [101] Pellicori, S. and Colton, E. *Thin Solid Films* **209**(1), 109–115 (1992).
- [102] Barrioz, V., Irvine, S., and Jones, D. *Journal of Materials Science: Materials in Electronics* **14**(9), 559–566 (2003).
- [103] Lide, D. R., editor. *Handbook of Chemistry and Physics*. CRC Press Inc, 77th edition, (1996–1997).
- [104] Yan, R. and Li, Y. *Advanced Functional Materials* **15**(5), 763–770 (2005).
- [105] Xiao, S., Yang, X., and Ding, J. *Applied Physics B: Lasers and Optics* **99**(4), 769–773 (2010).
- [106] Sammelselg, V., Aarik, J., Aidla, A., Kasikov, A., Heikinheimo, E., Peussa, M., and Niinistö, L. *J. Anal. At. Spectrom.* **14**(3), 523–527 (1999).

- [107] Rast, H. E., Caspers, H. H., and Miller, S. A. *Phys. Rev.* **180**, 890–895 (1969).
- [108] Uitert, L. V., O’Bryan, H., Guggenheim, H., Barns, R., and Zydzik, G. *Materials Research Bulletin* **12**(4), 307–314 (1977).
- [109] Okada, Y. and Tokumaru, Y. *Journal of Applied Physics* **56**(2), 314–320 (1984).
- [110] Giusti, G., Langley, D., Jimenez, C., Puyoo, E., Muthukumar, A., Appert, E., Consonni, V., and Bellet, D. *MRS Online Proceedings Library* **1439**, 51–56 (2012).
- [111] Bezuidenhout, D., Clarke, K., and Pretorius, R. *Thin Solid Films* **155**(1), 17–30 (1987).
- [112] Chindaudom, P. and Vedam, K. *Appl. Opt.* **33**(13), 2664–2671 (1994).
- [113] Lage, M. M., Righi, A., Matinaga, F. M., Gesland, J.-Y., and Moreira, R. L. *Journal of Physics: Condensed Matter* **16**(18), 3207–3218 (2004).
- [114] Zhang, S.-L., Wang, X., san Ho, K., Li, J., Diao, P., and Cai, S. *Journal of Applied Physics* **76**(5), 3016–3019 (1994).
- [115] Bünzli, J.-C. G. and Eliseeva, S. V. *Journal of Rare Earths* **28**(6), 824–842 (2010).
- [116] Wang, F. and Liu, X. *Journal of the American Chemical Society* **130**(17), 5642–5643 (2008).
- [117] Chen, G., Qiu, H., Fan, R., Hao, S., Tan, S., Yang, C., and Han, G. *J. Mater. Chem.* **22**, 20190–20196 (2012).
- [118] Wang, H.-Q., Batentschuk, M., Osvet, A., Pinna, L., and Brabec, C. J. *Advanced Materials* **23**, 2675–2680 (2011).
- [119] Auzel, F. *Proceedings of the IEEE* **61**(6), 758–786 (1973).
- [120] Kuroda, H., Shionoya, S., and Kushida, T. *Journal of the Physical Society of Japan* **33**(1), 125–141 (1972).
- [121] Wang, G., Qin, W., Zhang, J., Zhang, J., Wang, Y., Cao, C., Wang, L., Wei, G., Zhu, P., and Kim, R. *Optical Materials* **31**(2), 296–299 (2008).
- [122] Zhang, M., Fan, H., Xi, B., Wang, X., Dong, C., and Qian, Y. *The Journal of Physical Chemistry C* **111**(18), 6652–6657 (2007).
- [123] Yanes, A. C., Santana-Alonso, A., Mndez-Ramos, J., del Castillo, J., and Rodrguez, V. D. *Advanced Functional Materials* **21**(16), 3136–3142 (2011).
- [124] Nunez, N., Quintanilla, M., Cantelar, E., Cusso, F., and Ocana, M. *Journal of Nanoparticle Research* **12**(7), 2553–2565 (2010).

- [125] Rahman, P. and Green, M. *Nanoscale* **1**, 214–224 (2009).
- [126] Wang, F., Han, Y., Lim, C. S., Lu, Y., Wang, J., Xu, J., Chen, H., Zhang, C., Hong, M., and Liu, X. *Nature* **463**(7284), 1061–1065 (2010).
- [127] Ivanova, S. and Pellé, F. *J. Opt. Soc. Am. B* **26**(10), 1930–1938 (2009).
- [128] Reiche, R., Nunes, L., Carvalho, C., Messaddeq, Y., and Aegerter, M. *Solid State Communications* **85**(9), 773–777 (1993).
- [129] Tkachuk, A., Ivanova, S., Joubert, M.-F., and Guyot, Y. *Optics and Spectroscopy* **99**(6), 932–949 (2005).
- [130] Mita, Y., Yamamoto, H., Katayanagi, K., and Shionoya, S. *Journal of Applied Physics* **78**(2), 1219–1223 (1995).
- [131] Weng, F., Chen, D., Wang, Y., Yu, Y., Huang, P., and Lin, H. *Ceramics International* **35**(7), 2619–2623 (2009).
- [132] Chamarro, M. and Cases, R. *Journal of Luminescence* **46**(1), 59–65 (1990).
- [133] Ribeiro, C. T. M., Zanatta, A. R., Nunes, L. A. O., Messaddeq, Y., and Aegerter, M. A. *Journal of Applied Physics* **83**(4), 2256–2260 (1998).
- [134] Martin, I. R., Rodriguez, V. D., Lavin, V., and Rodriguez-Mendoza, U. R. *Journal of Applied Physics* **86**(2), 935–939 (1999).
- [135] Catunda, T., Nunes, L. A. O., Florez, A., Messaddeq, Y., and Aegerter, M. A. *Phys. Rev. B* **53**(10), 6065–6070 (1996).
- [136] Cantelar, E. and Cusso, F. *Journal of Luminescence* **102-103**, 525–531 (2003).
- [137] Deschanvres, J., Langlet, M., and Joubert, J. *Thin Solid Films* **175**, 281–285 (1989).
- [138] Meffre, W., Deschanvres, J.-L., Joubert, M.-F., Abello, L., Joubert, J.-C., and Jacquier, B. *J. Phys. IV France* **9**, 583–588 (1999).
- [139] Hoekstra, T. H., Hilderink, L. T. H., Lambeck, P. V., and Popma, T. J. A. *Opt. Lett.* **17**(21), 1506–1508 (1992).
- [140] McKittrick, J., Bacalski, C. F., Hirata, G. A., Hubbard, K. M., Pattillo, S. G., Salazar, K. V., and Trkula, M. *Journal of the American Ceramic Society* **83**(5), 1241–1246 (2000).
- [141] Gupta, V. and Mansingh, A. *Journal of Applied Physics* **80**(2), 1063–1073 (1996).
- [142] Su, W.-T., Li, B., Liu, D.-Q., and Zhang, F.-S. *Optical Materials* **30**(2), 273–278 (2007).

- [143] Yu, J., Lin, H., Feng, Z., Wang, L., Tripathy, S., and Chua, S. *Thin Solid Films* **498**(1-2), 108–112 (2006).
- [144] Lim, S. M., Kim, H. S., Chung, K. C., Lee, B. S., and Youm, D. *Superconductor Science and Technology* **17**(1), 148–154 (2004).
- [145] Li, Y. and Almeida, R. M. *Optical Materials* **34**(7), 1148–1154 (2012).
- [146] Repelin, Y., Proust, C., Husson, E., and Beny, J. *Journal of Solid State Chemistry* **118**(1), 163–169 (1995).
- [147] McDevitt, N. T. and Davidson, A. D. *J. Opt. Soc. Am.* **56**(5), 636–638 (1966).
- [148] In *Handbook of Optical Constants of Solids*, Palik, E. D., editor, xv – xviii. Academic Press, Burlington (1997).
- [149] Guo, H. and Qiao, Y. M. *Optical Materials* **31**(4), 583–589 (2009).
- [150] Dikovska, A., Atanasov, P., de Castro, M. J., Perea, A., Gonzalo, J., Afonso, C., and Lopez, J. G. *Thin Solid Films* **500**(1-2), 336–340 (2006).
- [151] Martinez, A., Morales, J., Diaz-Torres, L., Salas, P., la Rosa, E. D., Oliva, J., and Desirena, H. *Materials Science and Engineering: B* **174**(1-3), 164–168 (2010).
- [152] Deschanvres, J. L. and Meffre, W. *J. Phys. IV France* **11**, 325–329 (2001).
- [153] Polman, A. *Journal of Applied Physics* **82**(1), 1–39 (1997).
- [154] Laversenne, L., Guyot, Y., Goutaudier, C., Cohen-Adad, M., and Boulon, G. *Optical Materials* **16**(4), 475–483 (2001).
- [155] Peters, V. *Growth and Spectroscopy of Ytterbium-Doped Sesquioxides*. PhD thesis, Universität Hamburg, (2001).
- [156] Orignac, X., Barbier, D., Du, X. M., Almeida, R. M., McCarthy, O., and Yeatman, E. *Optical Materials* **12**(1), 1–18 (1999).
- [157] Li, S., Zhang, M., Peng, Y., Zhang, Q., and Zhao, M. *Journal of Rare Earths* **28**(2), 237–242 (2010).
- [158] Denker, B., Galagan, B., Osiko, V., Sverchkov, S., Balbashov, A., Hellström, J., Pasiskevicius, V., and Laurell, F. *Optics Communications* **271**(1), 142–147 (2007).
- [159] Schaack, G. and Koningstein, J. A. *J. Opt. Soc. Am.* **60**(8), 1110–1115 (1970).
- [160] Jones, S. L., Kumar, D., Singh, R. K., and Holloway, P. H. *Applied Physics Letters* **71**(3), 404–406 (1997).

- [161] Hirata, G., McKittrick, J., Avalos-Borja, M., Siqueiros, J., and Devlin, D. *Applied Surface Science* **113-114**, 509–514 (1997).
- [162] Cho, J. Y., Ko, K.-Y., and Do, Y. R. *Thin Solid Films* **515**, 3373–3379 (2007).
- [163] Bundschuh, K., Schuze, M., Muller, C., Greil, P., and Heider, W. *Journal of the European Ceramic Society* **18**(16), 2389–2391 (1998).
- [164] Berkowski, M., Bowen, P., Liechti, T., and Scheel, H. J. *Journal of the American Ceramic Society* **75**(4), 1005–1007 (1992).
- [165] Lou, L., Zhang, W., Brioude, A., Luyer, C. L., and Mugnier, J. *Optical Materials* **18**(3), 331–336 (2001).
- [166] Pearce, S. J., Parker, G. J., Charlton, M. D. B., and Wilkinson, J. S. *Journal of Vacuum Science & Technology A: Vacuum, Surfaces, and Films* **28**(6), 1388–1392 (2010).
- [167] Pons-Y-Moll, O., Perriere, J., Millon, E., Defourneau, R. M., Defourneau, D., Vincent, B., Essahlaoui, A., Boudrioua, A., and Seiler, W. *Journal of Applied Physics* **92**(9), 4885–4890 (2002).
- [168] Gaboriaud, R. J., Pailloux, F., Guerin, P., and Paumier, F. *Journal of Physics D: Applied Physics* **33**(22), 2884–2889 (2000).
- [169] Hartmanova, M., Jergel, M., Holgado, J. P., and Espinos, J. P. *Vacuum* **85**(4), 535–540 (2010).
- [170] West, G. A. and Beeson, K. W. *Journal of Materials Research* **5**, 1573–1580 (1990).
- [171] Kim, Y. S. and Kim, W. H. *Optical Materials* **14**(3), 229–234 (2000).
- [172] Burmester, P., Huber, G., Kurfiss, M., and Schilling, M. *Applied Physics A* **80**(3), 627–630 (2005).
- [173] Dikovska, A., Atanasov, P., Dimitrov, I., Vasilev, C., Kocourek, T., and Jelinek, M. *Applied Surface Science* **252**(13), 4569–4572 (2006).
- [174] Peeva, A., Dikovska, A., Atanasov, P., de Castro, M. J., and Skorupa, W. *Applied Surface Science* **253**(19), 8165–8168 (2007).
- [175] de J. Morales Ramirez, A., Murillo, A. G., de J. Carrillo Romo, F., Salgado, J. R., Luyer, C. L., Chadeyron, G., Boyer, D., and Palmerin, J. M. *Thin Solid Films* **517**(24), 6753–6758 (2009).
- [176] Guo, H., Zhang, W., Lou, L., Brioude, A., and Mugnier, J. *Thin Solid Films* **458**, 274–280 (2004).

- [177] Husson, E., Proust, C., Gillet, P., and Iti, J. *Materials Research Bulletin* **34**(1213), 2085–2092 (1999).
- [178] Skandan, G., Foster, C., Frase, H., Ali, M., Parker, J., and Hahn, H. *Nanostructured Materials* **1**(4), 313–322 (1992).
- [179] Dimoulas, A., Vellianitis, G., Travlos, A., Ioannou-Sougleridis, V., and Nas-siopoulou, A. G. *Journal of Applied Physics* **92**(1), 426–431 (2002).
- [180] Young, T., Chen, C., Liou, J., Yang, Y., and Chang, T. *Journal of Porous Materials* **7**, 339–343 (2000).
- [181] Alarcon-Flores, G., Aguilar-Frutis, M., Garcia-Hipolito, M., Guzman-Mendoza, J., Canseco, M., and Falcony, C. *Journal of Materials Science* **43**, 3582–3588 (2008).
- [182] Durand, C., Dubourdieu, C., Vallee, C., Loup, V., Bonvalot, M., Joubert, O., Roussel, H., and Renault, O. *Journal of Applied Physics* **96**(3), 1719–1729 (2004).
- [183] Wang, X., Zhang, L., Zhang, J., He, G., Liu, M., and Zhu, L. *Materials Letters* **62**(26), 4235–4237 (2008).
- [184] Santjojo, D. J., Aizawa, T., and Muraishi, S. *Materials Transactions* **48**(6), 1380–1386 (2007).
- [185] Matsuura, D. *Applied Physics Letters* **81**(24), 4526–4528 (2002).
- [186] Song, H., Sun, B., Wang, T., Lu, S., Yang, L., Chen, B., Wang, X., and Kong, X. *Solid State Communications* **132**(6), 409–413 (2004).
- [187] Vetrone, F., Boyer, J.-C., Capobianco, J. A., Speghini, A., and Bettinelli, M. *Journal of Applied Physics* **96**(1), 661–667 (2004).
- [188] Bai, Y., Yang, K., Wang, Y., Zhang, X., and Song, Y. *Optics Communica-tions* **281**(10), 2930–2932 (2008).
- [189] De, G., Qin, W., Zhang, J., Zhang, J., Wang, Y., Cao, C., and Cui, Y. *Journal of Luminescence* **119–120**, 258–263 (2006).
- [190] Pires, A. M., Serra, O. A., Heer, S., and Gudel, H. U. *Journal of Applied Physics* **98**(6), 063529 (2005).
- [191] Qiao, Y. and Guo, H. *Journal of Rare Earths* **27**(3), 406–410 (2009).
- [192] Chen, G., Liu, Y., Zhang, Z., Aghahadi, B., Somesfalean, G., Sun, Q., and Wang, F. *Chemical Physics Letters* **448**(13), 127–131 (2007).
- [193] Li, Z., Zheng, L., Zhang, L., and Xiong, L. *Journal of Luminescence* **126**(2), 481–486 (2007).

- [194] Wittke, J., Ladany, I., and Yocom, P. *Journal of Applied Physics* **43**(2), 595–600 (1972).
- [195] Castro, Y., Julian-Lopez, B., Boissiere, C., Viana, B., Grosso, D., and Sanchez, C. *Microporous and Mesoporous Materials* **103**, 273–279 (2007).
- [196] Weber, M. J. *Phys. Rev.* **171**, 283–291 (1968).
- [197] Kisliuk, P., Krupke, W. F., and Gruber, J. B. *The Journal of Chemical Physics* **40**(12), 3606–3610 (1964).
- [198] Capobianco, J. A., Vetrone, F., D’Alesio, T., Tessari, G., Speghini, A., and Bettinelli, M. *Phys. Chem. Chem. Phys.* **2**, 3203–3207 (2000).
- [199] Chandra, S., Deepak, F. L., Gruber, J. B., and Sardar, D. K. *The Journal of Physical Chemistry C* **114**(2), 874–880 (2010).
- [200] Meltzer, R. S., Feofilov, S. P., Tissue, B., and Yuan, H. B. *Phys. Rev. B* **60**, R14012–R14015 (1999).
- [201] S.-Y., C., Ting, C., and Hsieh, W. *Thin Solid Films* **434**(1), 171–177 (2003).
- [202] Qiao, Y. and Guo, H. *Journal of Rare Earths* **27**(3), 406 – 410 (2009).
- [203] De, G., Qin, W., Zhang, J., Zhang, J., Wang, Y., Cao, C., and Cui, Y. *Solid State Communications* **137**(9), 483–487 (2006).
- [204] Brückner, R. *Journal of Non-Crystalline Solids* **5**(2), 123–175 (1970).
- [205] Miritello, M., Savio, R. L., Iacona, F., Franz, G., Bongiorno, C., and Priolo, F. *Materials Science and Engineering: B* **146**(1-3), 29–34 (2008).
- [206] Gracia, F., Yubero, F., Holgado, J., Espinos, J., Gonzalez-Elipe, A., and Girardeau, T. *Thin Solid Films* **500**(1-2), 19–26 (2006).
- [207] An, Y., Labbe, C., Khomenkova, L., Morales, M., Portier, X., and Gourbilleau, F. *Nanoscale Research Letters* **8**(1), 1–7 (2013).
- [208] Benatsou, M., Capoen, B., Bouazaoui, M., Tchana, W., and Vilcot, J. *Journal of Sol-Gel Science and Technology* **13**, 529–533 (1998).
- [209] McMillan, P., Poe, B., Stanton, T., and Remmele, R. *Physics and Chemistry of Minerals* **19**(7), 454–459 (1993).
- [210] Vanhoutte, M., Wang, B., Michel, J., and Kimerling, L. In *Group IV Photonics, 2009. GFP ’09. 6th IEEE International Conference on*, 63–65, (2009).
- [211] Busani, T. and Devine, R. A. B. *Semiconductor Science and Technology* **20**(8), 870–885 (2005).

- [212] Vitanov, P., Harizanova, A., and Ivanova, T. *Journal of Physics: Conference Series* **356**(1), 012041 (2012).
- [213] Djaoued, Y., Badilescu, S., Ashrit, P., Bersani, D., Lottici, P., and Robichaud, J. *Journal of Sol-Gel Science and Technology* **24**(3), 255–264 (2002).
- [214] Dakka, A., Lafait, J., Abd-Lefdil, M., and Sella, C. *Moroccan Journal of Condensed Matter* **2**, 153–156 (2011).
- [215] Capan, R., Chaure, N. B., Hassan, A. K., and Ray, A. K. *Semiconductor Science and Technology* **19**(2), 198–202 (2004).
- [216] Ting, C.-C., Chen, S.-Y., and Lee, H.-Y. *Journal of Applied Physics* **94**(3), 2102–2109 (2003).
- [217] Patra, A., Friend, C. S., Kapoor, R., and Prasad, P. N. *Chemistry of Materials* **15**(19), 3650–3655 (2003).
- [218] Luo, W., Fu, C., Li, R., Liu, Y., Zhu, H., and Chen, X. *Small* **7**(21), 3046–3056 (2011).
- [219] Purcell, E. *Phys. Rev.* **69**, 681 (1946).
- [220] Rigneault, H., Amra, C., Robert, S., Begon, C., Lamarque, F., Jacquier, B., Moretti, P., Jurdyc, A., and Belarouci, A. *Optical Materials* **11**, 167–180 (1999).
- [221] Björk, G., Machida, S., Yamamoto, Y., and Igeta, K. *Phys. Rev. A* **44**, 669–681 (1991).
- [222] Chiasera, A., Belli, R., Bhaktha, S. N. B., Chiappini, A., Ferrari, M., Jestin, Y., Moser, E., Righini, G. C., and Tosello, C. *Applied Physics Letters* **89**(17), 171910 (2006).
- [223] Chen, S.-Y., Ting, C.-C., and Hsieh, W.-F. *Thin Solid Films* **434**(1-2), 171–177 (2003).
- [224] Jasieniak, J., Sada, C., Chiasera, A., Ferrari, M., Martucci, A., and Mulvaney, P. *Advanced Functional Materials* **18**(23), 3772–3779 (2008).
- [225] Bellessa, J., Rabaste, S., Plenet, J. C., Dumas, J., Mugnier, J., and Marty, O. *Applied Physics Letters* **79**(14), 2142–2144 (2001).
- [226] Bellessa, J., Rabaste, S., Plenet, J.-C., and Mugnier, J. *Proceedings of SPIE* **4944**, 15–22 (2003).
- [227] Li, Y. and Almeida, R. M. *Journal of Physics D: Applied Physics* **43**(45), 455101 (2010).

8 References

- [228] Rigneault, H., Flory, F., Monneret, S., Robert, S., and Roux, L. *Appl. Opt.* **35**(25), 5005–5012 (1996).
- [229] Robert, S., Rigneault, H., and Lamarque, F. *J. Opt. Soc. Am. B* **15**(6), 1773–1779 (1998).
- [230] Almeida, R. M. and Marques, A. C. *Journal of Non-Crystalline Solids* **352**, 475–482 (2006).
- [231] Vredenberg, A. M., Hunt, N. E. J., Schubert, E. F., Jacobson, D. C., Poate, J. M., and Zydzik, G. J. *Phys. Rev. Lett.* **71**, 517–520 (1993).
- [232] de Wild, J., Meijerink, A., Rath, J. K., van Sark, W. G. J. H. M., and Schropp, R. E. I. *Energy Environ. Sci.* **4**, 4835–4848 (2011).
- [233] Lahoz, F., Perez-Rodriguez, C., Hernandez, S., Martin, I., Lavin, V., and Rodriguez-Mendoza, U. *Solar Energy Materials and Solar Cells* **95**(7), 1671–1677 (2011).

List of abbreviations

AA-MOCVD	Aerosol-Assisted Metalorganic Chemical Vapor Deposition
Acac	Acetylacetonate
AFM	Atomic Force Microscopy
BM	Bragg Mirror
CLTE	Coefficient of Linear Thermal Expansion
DBR	Distributed Bragg Mirror
DCCA	Drying Control Chemical Additive
DSSC	Dye Sensitized Solar Cell
EDX	Energy Dispersive X-Ray Spectroscopy
E _g	Energy Band-gap
EPMA	Electron Probe Micro-Analysis
EQE	External Quantum Efficiency
ESA	Excited State Absorption
ET	Energy Transfer
ETU	Energy Transfer Up-conversion
FTIR	Fourier Transform Infrared Spectroscopy
F-P	Fabry-Pérot
FWHM	Full Width at Half Maximum
GSA	Ground State Absorption
ICDD	International Centre for Diffraction Data
IR	Infrared
LI-MOCVD	Liquid-Injection Metalorganic Chemical Vapor Deposition
LQL	Luminescence Quantum Efficiency
MOCVD	Metalorganic Chemical Vapor Deposition
NC	Nano-crystal(s)
NIR	Near-infrared
NP	Nanoparticles
PBG	Photonic Bandgap
PD	Power Dependence
PL	Photoluminescence
RE	Rare Earth
SC	Solar Cell
SEM	Scanning Electron Microscopy
TM	Transition Metal
Tmhd	2,2,6,6-Tetramethyl-3,5-heptanedionate
TMM	Transfer Matrix Method
PTFE	Polytetrafluoroethylene
PV	Photovoltaics
UpC	Up-conversion
UV	Ultraviolet
Vis	Visible
WDS	Wavelength Dispersive Spectroscopy
XRD	X-Ray Diffraction

Résumé

Les questions principales adressées dans ce travail étaient: 1.) déterminer les facteurs dominants qui influent sur les propriétés d'up-conversion (UpC) de la lumière dans des couches minces dopées aux terres rares obtenues par MOCVD et sol-gel 2.) l'importance de la technique d'élaboration de couches minces choisie et son influence sur la microstructure des couches 3.) l'évaluation de l'applicabilité potentielle pour une couche d'UpC à une cellule solaire.

Le chapitre 2 présente l'élaboration de couches minces d' YF_3 dopées Er/Yb sur des substrats de Si(111) et verre de quartz par LI-MOCVD (Figure A1).

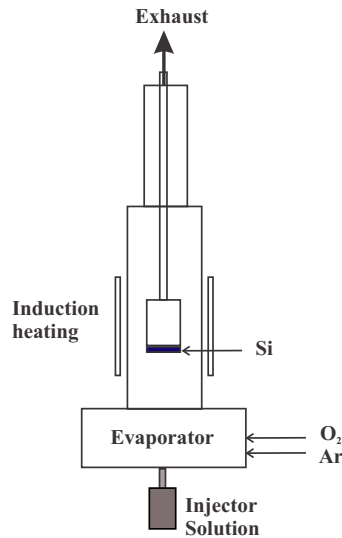


Figure A1: Schéma du réacteur LI-MOCVD.

Il a été montré que la microstructure des couches dépend fortement des conditions d'élaboration utilisées. La pression partielle d'oxygène et la température de déposition ont été déterminées comme étant les facteurs les plus cruciaux pour obtenir des couches d' YF_3 lisses et cristallines. Des couches de fluorure, avec une microstructure dense et homogène, peuvent être facilement déposées à une température de $590\text{ }^\circ\text{C}$ et un taux d'oxygène de 80% dans le flux de gaz vecteur (Table A1).

Par ailleurs, la formation des micro- et macro-fissures apparaît pour des épaisseurs des couches: supérieures à 500 nm, la couche peut alors même se détacher du substrat en raison des trop fortes contraintes.

Le chapitre 3 fait le point sur les propriétés de luminescence des couches minces d' YF_3 mono-dopées Er et co-dopées Er/Yb sous excitation à 488 nm et dans le proche-infrarouge à 972 nm. Les deux longueurs d'ondes différentes ont permis d'élucider les différents mécanismes d'excitation de la luminescence d'ion Er^{3+} et nous a mené à une explication sur la participation d' Yb^{3+} dans les processus de relaxation d' Er^{3+} .

Table A1: Paramètres standards de dépôt des couches minces de RE:YF₃ par LI-MOCVD.

Substrate temperature [°C]	450–650
Evaporation chamber temperature [°C]	250
Carrier gas O ₂ /Ar flow rate [sccm]	560
Oxygen concentration in total gas flow [%]	50–80
Total work pressure [torr]	5
Pulse frequency [Hz]	1
Injector aperture time [ms]	1.5
Concentration precursor solution [M]	0.05
Deposition time [min]	20–40

Avec l'excitation à 972 nm, une émission d'up-conversion forte à ~ 410 nm, 550 nm et 660 nm a été observées (Figure A2) en raison de la faible énergie de phonons principaux d'YF₃ (~ 500 cm⁻¹).

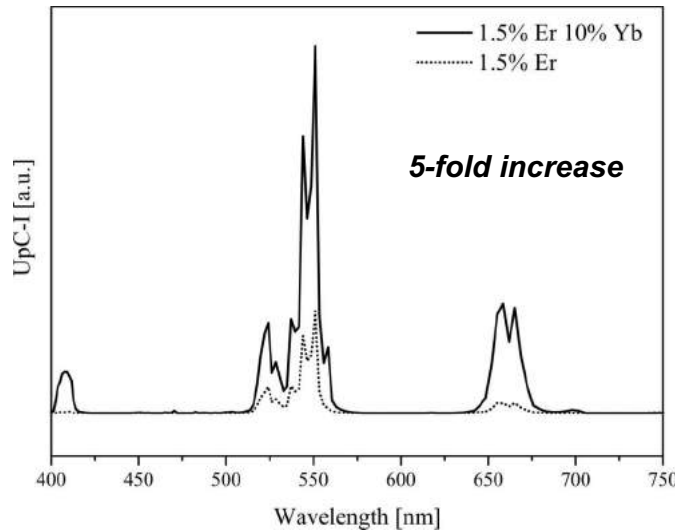


Figure A2: Les spectres d'émission des échantillons Er/Yb:YF₃ excités à 972 nm.

Cette luminescence est même visible à l'œil nu a basse puissance d'excitation. La plus haute intensité de luminescence dans le visible était observé pour une composition de la couche co-dopée avec 1.5 at.% Er et 10 at.% Yb (at.% dans la solution de précurseurs, Figure A3).

Il a été trouvé que le rapport d'intensité relatif de l'émission rouge et verte (R/G) peut être contrôlé par le taux de dopage d'Yb: aux hautes concentrations d'Yb, l'intensité d'émission rouge augmente à cause de la désexcitation non-radiative des niveaux d'émission de lumière verte, Er:²H_{9/2}:⁴S_{3/2} vers le niveau ⁴I_{11/2} (Figure A4).

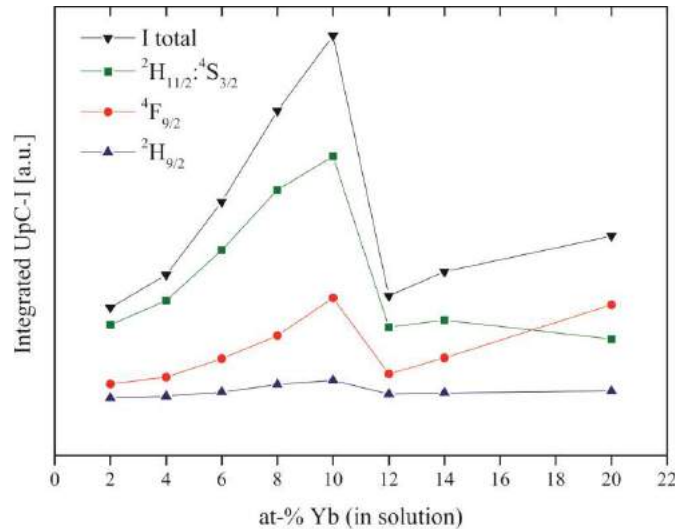


Figure A3: Intensité intégrée de l'émission des couches YF_3 co-dopés Er/Yb excités à 972 nm.

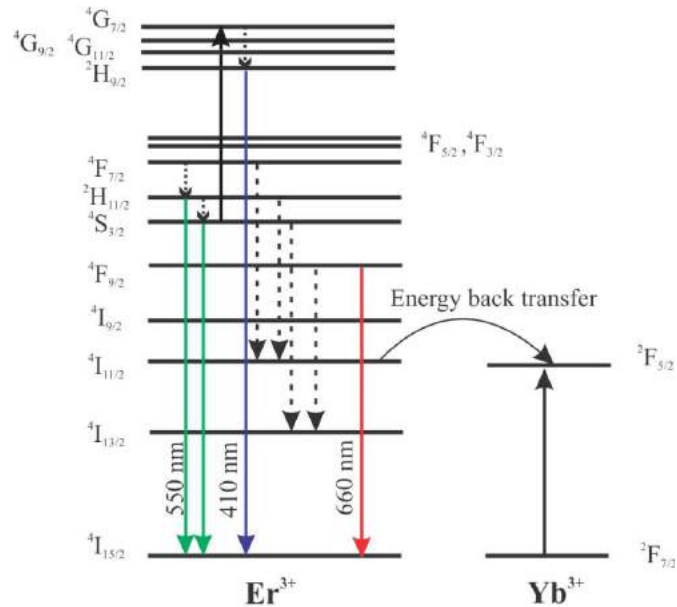


Figure A4: Diagramme du transfert d'énergie inverse entre l' Er^{3+} et l' Yb^{3+} .

Ceci a été attribué à un transfert d'énergie inverse efficace de l'Er-vers-Yb, qui est plus efficace pour les hautes concentrations d'Yb. Les études des cinétiques d'émission des niveaux Er: $^4\text{S}_{3/2}$ et $^4\text{F}_{9/2}$ ont montré une dépendance sur le taux de dopage d'Yb qui ont pour conséquence une réduction des temps de vie des deux niveaux, quand la concentration du sensibilisateur a été augmentée (Figure A5). Les bandes d'émission dans les gammes de longueur d'onde du violet, verte et rouge sont attribuées à des processus d'UpC à trois-et deux-photons, respectivement, pour les deux derniers cas. Pourtant, les pentes mesurées, obtenues par les études de dépendance de puissance, ont montrées une déviation de la relation la

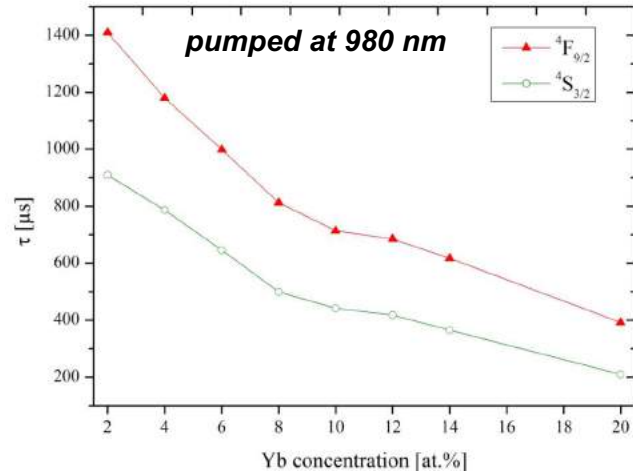


Figure A5: Évolution du temps de vie des couches minces d'YF₃ co-dopés Er,Yb en fonction du taux d'ytterbium dans la solution.

plus simple, $I = P^n$, qui est seulement applicable dans le cas où le taux d'UpC est négligeable comparé à un déclin linéaire.

Donc, nous avons proposé des solutions modèles pour les pentes des intensités d'émission versus la puissance de pompe pour les grands taux d'UpC, et les situations compétitives entre les déclin linéaires et non-linéaires (UpC). Nous avons déterminé les pentes pour suivre la relation $I = P^{i/2}$ à de hautes densités de pompe, avec i le i 'ème niveau excité; et d'autre part, les situations intermédiaires à basse puissance de pompe avec les pentes de convergence à P^i (Figure A6).

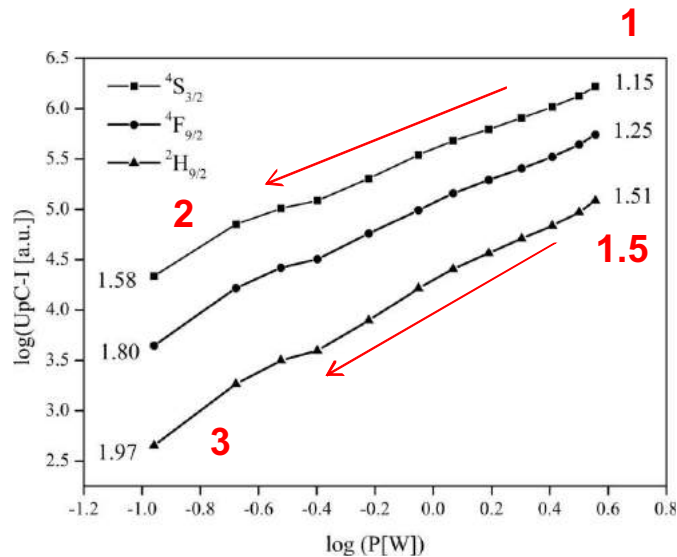


Figure A6: Les pentes des intensités d'émission versus la puissance de pompe pour 1 at.% Er/10 at.% Yb:YF₃ et les pentes proposés par les solutions modèles (valeurs en rouge).

Les pentes expérimentalement obtenues ont confirmé les solutions des équations de taux de notre modèle.

Dans le Chapitre 4, une autre variante de MOCVD a été utilisée pour le dépôt des couches minces Y_2O_3 co-dopée Er/Yb sur des substrats de Si(111) à $540^\circ C$ et à pression atmosphérique à l'aide de précurseurs organo-métalliques et assisté par aérosol (aerosol-assisted MOCVD, Figure A7).

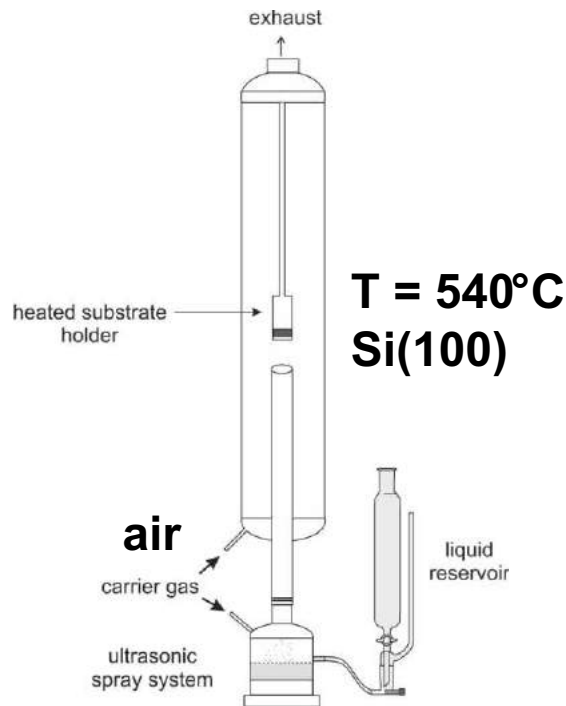


Figure A7: Schéma du réacteur AA-MOCVD pour l'élaboration des couches d' Y_2O_3 .

Bien que cette technique ait un avantage de mise en œuvre expérimentale assez simple comparé à LI-MOCVD, les couches brutes exigent un recuit supplémentaire à de hautes températures ($\geq 900^\circ C$), en raison des résidus organiques dans la matrice (Figure A8).

Ceux-ci proviennent des précurseurs organo-métalliques (*acetylacetonates*) qui agissent comme des quenchers de luminescence. Il a été montré que le recuit améliore la cristallisation de la couche mince et augmente les tailles de grain. Pourtant, avec l'augmentation de la température, des micro-fissures apparaissent dans la microstructure de la couche (Figure A9).

Ceci a été attribué à la rétraction et la densification de la couche et à la grande différence entre le CLTE (Coefficient of Linear Thermal Expansion) de la couche et celui du substrat.

Bien que la présence de micro-fissures ait peu d'influence sur l'efficacité du processus d'UpC, dans certains cas, des couches lisses et non-fissurées sont exigées, un changement vers l'utilisation d'un substrat de CLTE plus grand que le silicium, comme e.g. le saphir, devrait être considéré. Après le recuit, les spec-

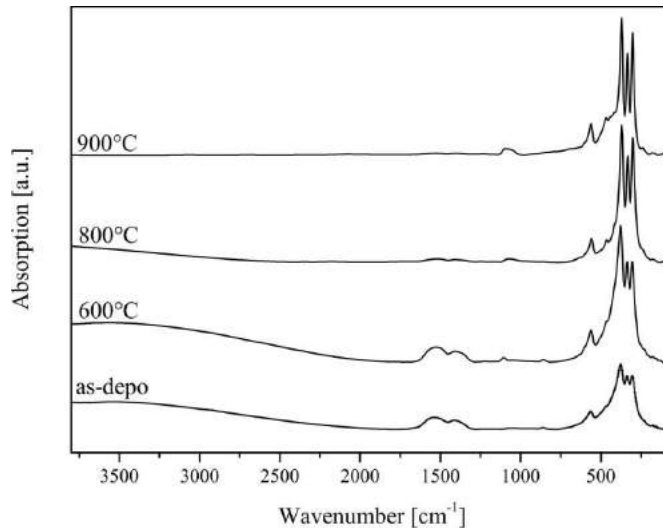


Figure A8: Spectres FTIR sur des couches minces d' Y_2O_3 (par MOCVD) en fonction de la température de recuit.

tres d'émission de conversion spectrale, NIR-vers-IR, ont montré trois bandes d'émission principales à ~ 410 nm, 540 nm et 660 nm.

Une augmentation de l'intensité d'UpC totale ($\times 17$) a été réalisée pour les échantillons recuits à 900°C comparé à ceux recuit à 600°C , pendant 1 h, dans l'air (Figure A10).

En outre, les cinétiques du déclin de fluorescence du niveau $\text{Er}^{:4}\text{I}_{13/2}$ ont révélés, que le temps de vie du niveau intermédiaire s'est révélé dépendre faiblement de la concentration d'Yb, avec une variation de 1.6–1.2 ms.

Nous avons expliqué ce fait par d'autres facteurs d'influence, comme l'UpC et les phénomènes de transfert d'énergie, qui deviennent compétitifs quand la concentration des ions terres rares est assez haute. Pour les couches co-dopées Er/Yb avec des mesures du temps de vie de $\text{Yb}^{:2}\text{F}_{5/2}$, une efficacité de transfert d'énergie entre Yb–Er de $\sim 80\%$ a été déterminé pour une composition de 3 at.% Er/10 at.% Yb (at.% dans la solution).

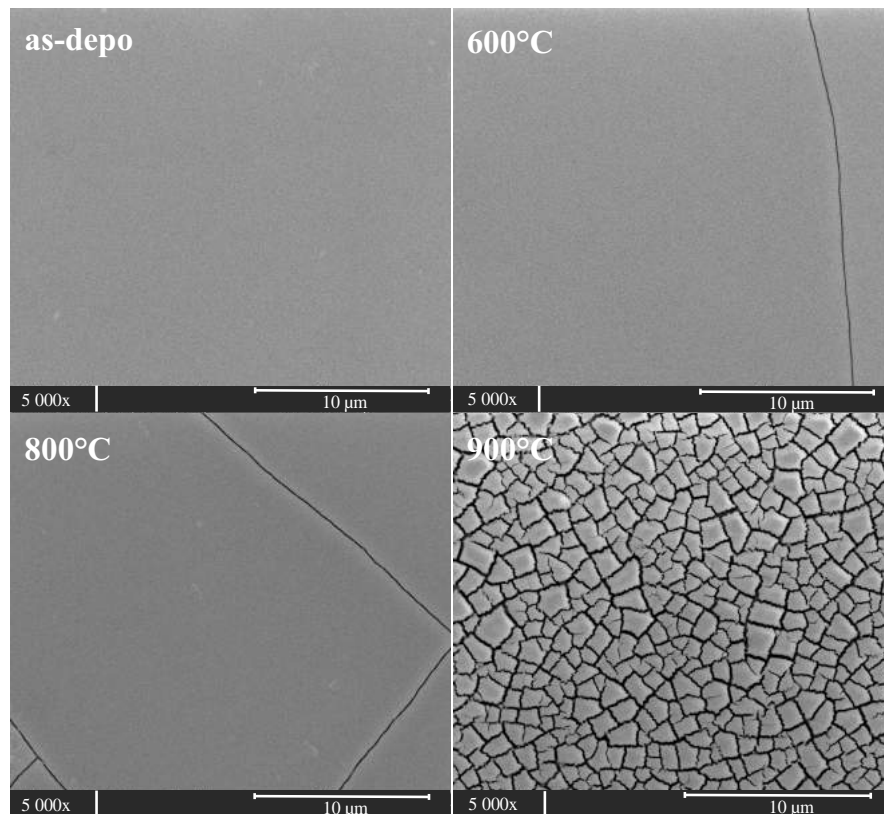


Figure A9: Images MEB de la surface d’une série des échantillons de Er/Yb:Y₂O₃ élaborées par AA-MOCVD en fonction de la température de recuit.

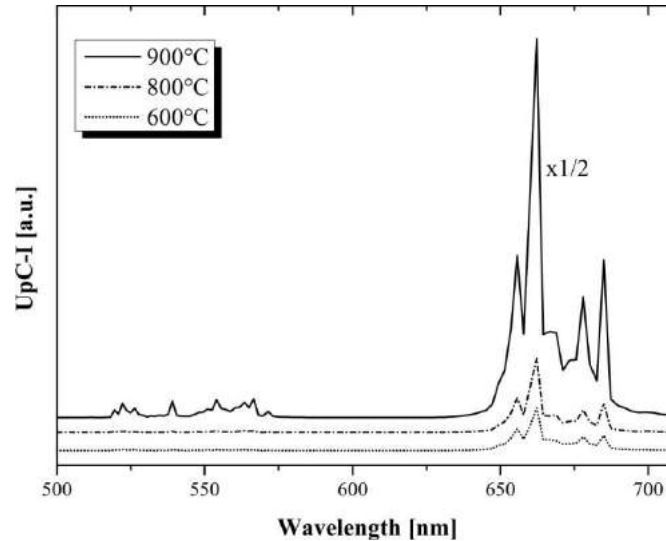


Figure A10: Intensité d’émission d’UpC totale pour les échantillons recuits à 700 °C – 1050 °C, pendant 1 h, dans l’air.

Le chapitre 5 décrit le dépôt des couches minces Er/Yb:Y₂O₃ déposés sur Si(100) à 700 °C par LI-MOCVD. L’influence d’un recuit supplémentaire, après dépôt à 900 et 1050 °C pendant 1 h, sur les propriétés structurales, optiques et de luminescence

de couches minces ont été analysées. Les couches ont montré une structure dense, colonnaire avec une épaisseur de couche de ~ 500 nm (Figure A11).

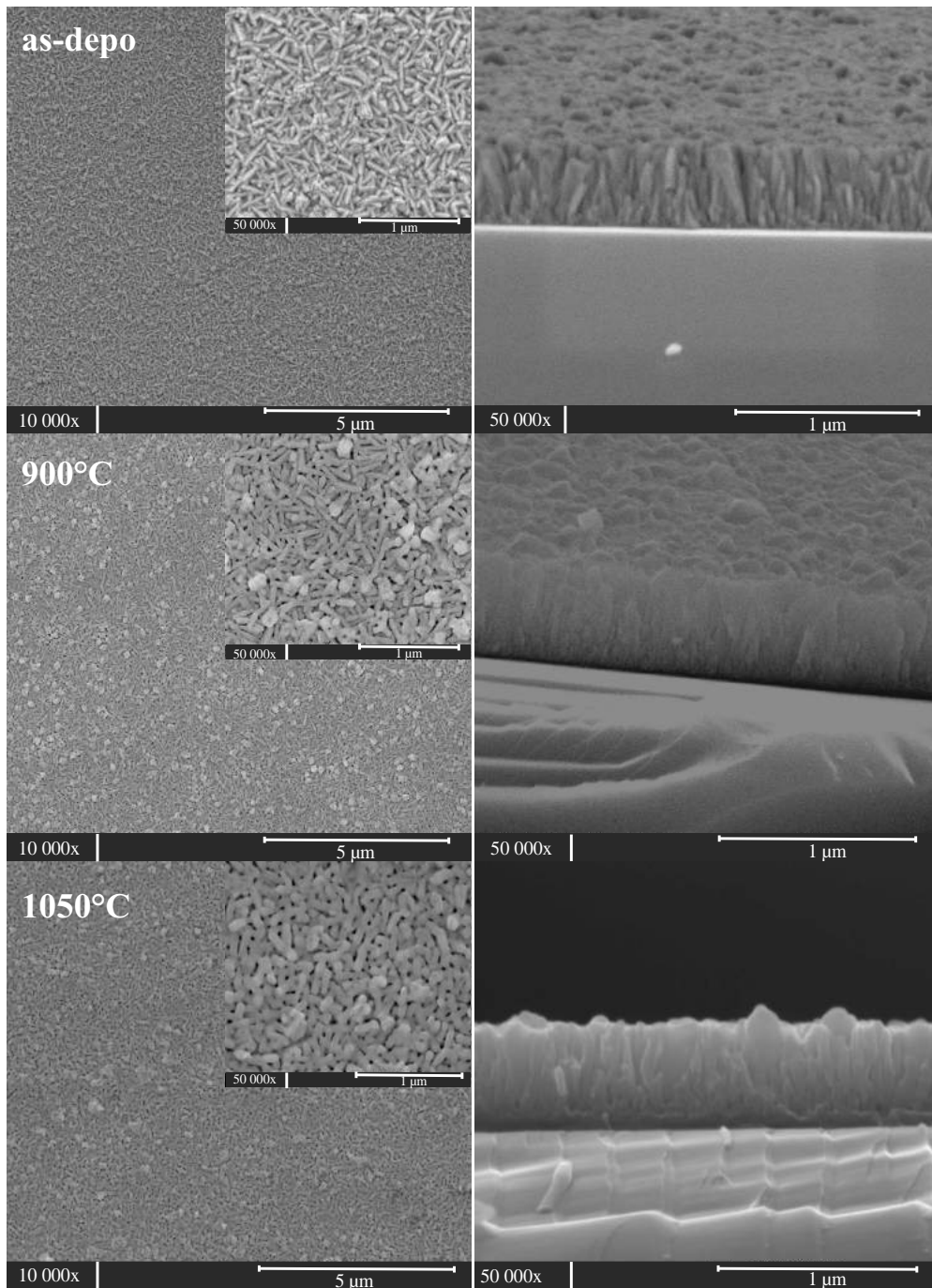


Figure A11: Images MEB de la surface et sur la tranche des couches minces Er/Yb:Y₂O₃ par LI-MOCVD en fonction de la température de recuit.

Pour une excitation à 972 nm, des émissions d'UpC forte rouge, faible verte et violette ont été observées. Les échantillons avant recuit présentent une luminescence faible et une augmentation dans l'intensité d'émission totale (x6) a été obtenue en augmentant la température de recuit à 1050 °C (Figure A12).

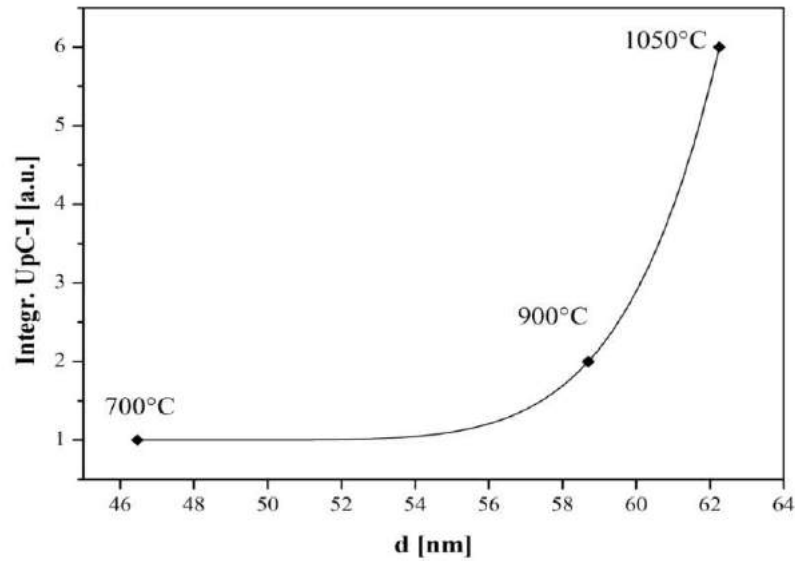


Figure A12: Intensité intégrée d'UpC totale pour les échantillons d' Y_2O_3 dopée Er/Yb (par LI-MOCVD) en fonction de la température de recuit et la taille de grain.

Un prolongement des temps de vie des deux niveaux $^4S_{3/2}$ et $^4F_{9/2}$ dans d' Y_2O_3 dopée Er/Yb ont été également observé et ces deux résultats sont attribués à la réduction de défauts aux joints de grains, en agissant comme des quenchers de luminescence, en raison de la croissance des grains attribuée au traitement thermique. En effet les espèces responsable du quenching, comme les groupes OH et CO, sont éliminées aux températures de recuit ≥ 900 °C.

Le chapitre 6 fait état des procédés sol-gel et des résultats de caractéristiques spectroscopiques, aussi bien que de propriétés structurales des couches minces à base d'oxyde. Le rapport entre la condition de traitement – essentiellement la température de recuit final après le dernier cycle d'enduction – et les changements dans propriétés d'UpC en raison des effets thermiques, sont présentés.

Pour résumer nos conclusions, Y_2O_3 dopé Er/Yb déposé par la méthode de sol-gel, a montré une émission d'UpC comparable avec les couches déposés par les variantes MOCVD. Pourtant, les propriétés optiques, comme l'index de réfraction, ont été montrées pour être sensibles à la microstructure, ainsi qu'à la méthode de déposition utilisée (Table A2).

Table A2: Valeurs de l'indice de réfraction à 500 nm des couches minces d' Y_2O_3 élaborées par des différentes méthodes de dépôt.

n (AA-MOCVD)	n (LI-MOCVD)	n (Sol-gel)
1.80 (as-depo.)	1.77 (as-depo.)	1.35 (as-depo)
1.80 (600 °C)	1.81 (900 °C)	1.73 (1050 °C)
1.81 (800 °C)	1.88 (1050 °C)	-
1.83 (900 °C)	-	-
1.939 (bulk, reference)	-	-

Nous avons constaté qu'une température de traitement de 1050 °C pour les couches dérivées de technique de sol-gel assurait l'élimination de la contamination en OH, et ainsi fournissait un haut taux de rendement de luminescence, bien que la formation de micro-fissures commence à prendre effet à cette température.

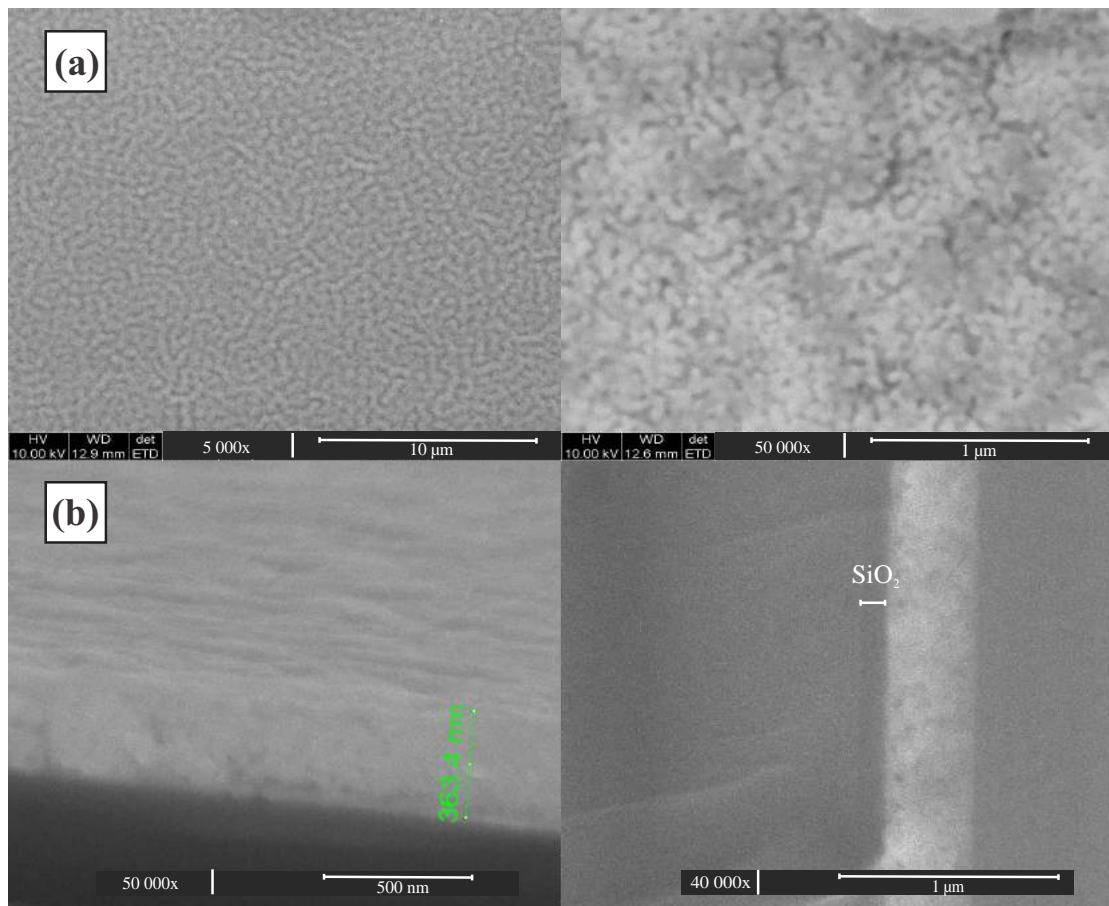


Figure A13: Images MEB (a) de la surface et (b) sur la tranche des couches minces Er/Yb: Y_2O_3 par sol-gel après un recuit à 1050 °C.

Un compromis a été trouvé en déposant des couches minces RE: Y_2O_3 avec une épaisseur maximum de ~ 500 nm (10 couches par spin-coating) pour éviter de décoller de couche.

La technique d'AA-MOCVD a permis la croissance des couches minces RE:Y₂O₃ avec de forte vitesse de croissance et une mise en œuvre expérimentale assez simple, pourtant, on ne pouvait pas empêcher la formation des fissures au sein de la structure des couches après le traitement thermique.

Des couches minces RE:Y₂O₃ de haute qualité optique et structurale ont été obtenues par LI-MOCVD (absence de fissure), même après la haute température de recuit à 1050 °C, en raison de la microstructure de film colonnaire.

Quand nous comparons l'émission d'UpC des matrices d'Y₂O₃ et YF₃, nous avons obtenu une bien meilleur intensité d'émission totale pour la matrice hôte de fluorure, parce que le taux de désexcitation non-radiative par phonons (*multi-phonon relaxation*) est plus basse en raison du cut-off énergie de phonon (~ 500 vs. 600 cm⁻¹).

Bien que nous ne soyons pas capables de mesurer le LQE (rendement quantique, d'efficacité quantique interne), nous pouvons faire une comparaison des temps de vie (τ) des niveaux Er:⁴S_{3/2}, ⁴F_{9/2} dans les couches d'Y₂O₃ et d'YF₃ synthétisées par LI-MOCVD (Figure A14):

Nous avons déterminé $\tau(^4S_{3/2})$ avec 54 μ s et $\tau(^4F_{9/2})$ avec 69 μ s dans Er/Yb:Y₂O₃ (recuit à 1050 °C), versus $\tau(^4S_{3/2})$ avec 442 μ s et $\tau(^4F_{9/2})$ avec 714 μ s dans Er/Yb:YF₃ (1.5 at.% Er, 10 at.% Yb). Donc, la prolongation du temps de vie (~ 10x) et l'intensité de luminescence visible font de la couche de fluorure un matériau prometteur pour une application d'UpC.

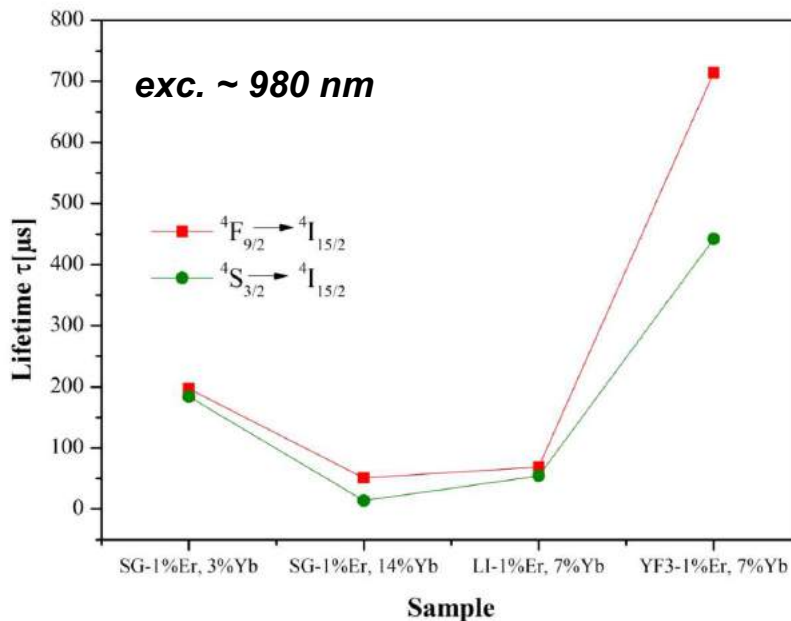


Figure A14: Temps de vie de l'Er³⁺ dans les différentes matrices hôtes pour les transitions ⁴S_{3/2} → ⁴I_{15/2} et ⁴F_{9/2} → ⁴I_{15/2}, pompé à 980 nm.

L'émission d'UpC dans le matériel d'hôte vitreux, amorphe peut avoir un avantage du fait d'élargir des bandes d'émission comparées aux matrices hôte cristallines. Les spectres d'émission typique des couches minces de Er/Yb:SiO₂ et de TiO₂ présentent de plus larges bandes d'émission avec moins de splitting par effet Stark, comparés aux matrices Y₂O₃ et YF₃ (Figure A15).

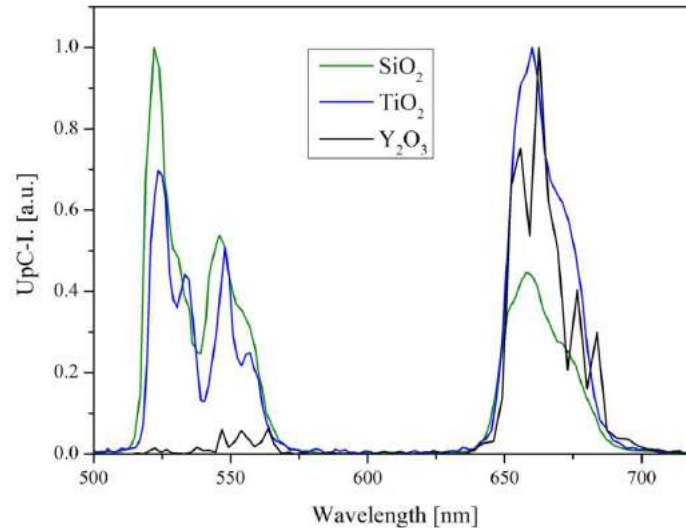


Figure A15: Spectres d'émission d'UpC typiques des couches minces de Er/Yb:Y₂O₃, TiO₂ et SiO₂, élaborées par sol-gel, excitées à 972 nm.

Cela peut être favorable en matière d'absorption de la lumière par le centre actif d'upconversion. Par contre, les hautes énergies de phonon de SiO₂ et de TiO₂ augmentent le taux de relaxation non-radiatif et diminuent ainsi beaucoup l'intensité d'émission.

Pour les couches minces TiO₂:Er/Yb dérivées de sol-gel, la phase cristalline présente a été montré comme jouant un rôle important pour l'émission d'UpC. Un mélange des phases d'anatase et de rutile, obtenues à une température de traitement thermique de 700 °C, a montré les plus hautes intensités d'émission d'UpC. Nous avons trouvé que la formation d'une phase pyrochlore titante, RE₂Ti₂O₇ (RE = Yb, Er), aux températures ≥ 900 °C, diminue significativement l'émission d'UpC (Figure A16). Les études de la dépendance de puissance d'émission d'UpC dans les couches Er/Yb:TiO₂ ont permis de déterminer des pentes de 1.6 et 2.4 pour l'émission rouge et verte, respectivement. Le comportement presque quadratique de l'émission rouge indique un processus de 2-photons, alors que l'émission verte est basée sur un processus de 3-photons, qui est responsable de la population des niveaux excités ²H_{11/2} et ⁴S_{3/2}.

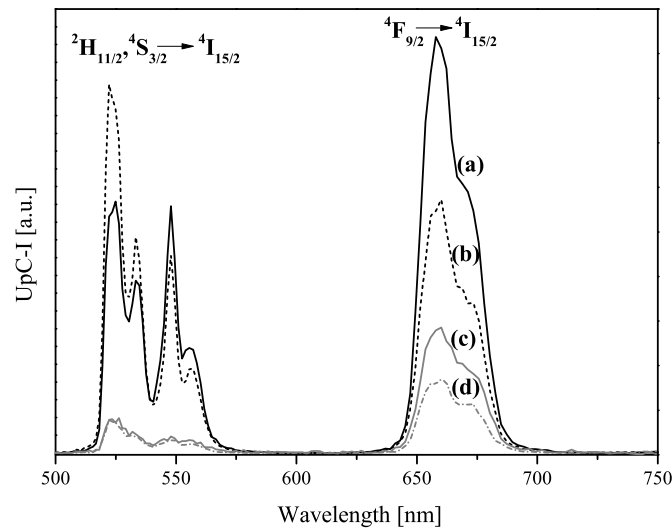


Figure A16: Spectres d'émission d'UpC des couches minces de TiO_2 (~ 500 nm) dopés par (a) 1 at.% Er/20 at.% Yb, recuit à 700°C (b) 1 at.% Er/ 20 at.% Yb, recuit à 700°C et 900°C (c) 1 at.% Er/ 10 at.% Yb, recuit à 700°C (d) 1 at.% Er/ 10 at.% Yb, avec un recuit supplémentaire à 900°C , excités à 972 nm, 4 W.

Le chapitre 7 traite de la fabrication par sol-gel des microcavités de Fabry-Pérot (F-P), formés par des couches diélectriques d' Y_2O_3 , SiO_2 et TiO_2 . Comme étude préliminaire, nous avons étudié sur l'influence de placer une couche d' Y_2O_3 dopé Er/Yb entre deux réflecteurs de Bragg distribués (réseau de Bragg), faits des couches successives de TiO_2 et SiO_2 , qui fonctionnent comme le matériel d'index réfringent haut et bas (Figure A17).

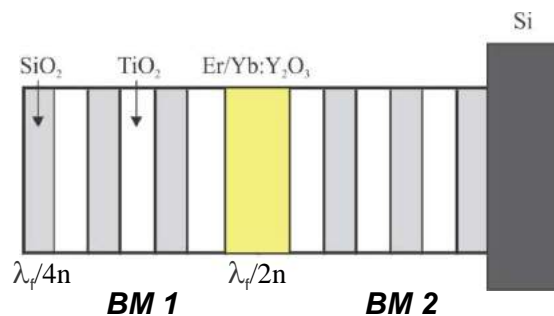


Figure A17: Schéma d'une microcavité de Fabry-Pérot (sur substrat de Si) avec une couche d' Y_2O_3 dopé Er/Yb entre deux réflecteurs de Bragg distribués (réseau de Bragg, BM).

Nous avons montré que la structure de cavité a changé la manière d'émettre d' Er^{3+} : l'émission verte améliorée a été observée quand on la compare à l'échantillon sans cavité. C'est bien – un effet de cavité bien connu – puisque le pic de résonance est placé dans la bande d'émission verte. La meilleure microcavité de F-P a montré un facteur d'augmentation d'émission de 3 (pour une couche élaboré à

900 °C) (Figure A18).

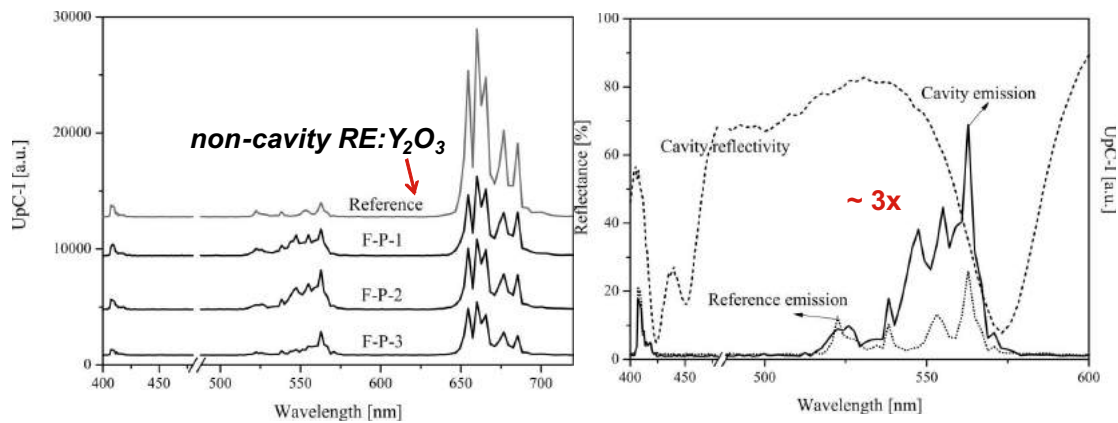


Figure A18: À gauche: Emission d’UpC des microcavités de F–P avec différents λ_f sur 972 nm excitation, et d’un angle de détection de 45°. Par ailleurs, un échantillon de référence, sans la cavité, est montré. À droite: La meilleure microcavité de F–P avec un facteur d’augmentation d’émission de 3, élaboré à 900 °C.

Pourtant, à l’extérieur du pic de résonance de la microcavité, une intensité d’émission réduite dans la région de longueur d’onde rouge a été observée; par ailleurs, le rapport d’émission rouge/verte intégré (rapport R/G) diminue de 5 à 0.5 par rapport à un échantillon de référence RE:Y₂O₃ (sans cavité) et la microcavité correspondante, tous les deux ont été recuit à 1050 °C. Ce changement dans les rapports d’intensité d’émission peut être attribué à une modification de l’émission spontanée, et des rapports de branching.

Un facteur de qualité, Q , de 20 a été obtenu pour les meilleurs échantillons de microcavité et peuvent encore être amélioré. Pour les études futures, nous suggérons d’augmenter le nombre de périodes de DBR (*distributed Bragg reflectors*) dans le stack de multi-couches, pour améliorer le facteur de Q , et de réaliser des microcavités couplées pour une augmentation de l’émission d’UpC partout dans la région visible.

Les perspectives futures de l’application d’un upconverteur aux composantes photovoltaïques constituent un défi. Jusqu’à présent, les améliorations d’efficacité obtenue pour ces systèmes sont trop basses pour justifier un investissement financier. Les problèmes principaux sont dans la capacité d’absorption et le rendement quantique de l’upconverteur. Ainsi l’amélioration du rendement quantique et de la capacité d’absorption de l’upconverteur dans l’infrarouge, aussi bien que, e. g. une combinaison de plusieurs ions terres rares (RE³⁺) pour élargir la gamme d’absorption, peuvent jouer un rôle clé pour faire de l’UpC une option réaliste dans le photovoltaïque de demain. Une autre direction prometteuse, serait l’utilisation d’effets de résonance plasmonique et de structures PBG pour augmenter l’efficacité d’up-conversion.

